RAPID AQUEOUS MINERALISATION OF CARBON DIOXIDE IN A SCALABLE PROCESS WITH BRINES

by

Ning Zhang

A thesis submitted to Newcastle University for the degree of

Doctor of Philosophy

School of Engineering
Newcastle University, UK

August 2020

Abstract

Aqueous mineralisation is a form of mineral carbonation process that reacts CO_2 with reactants in aqueous phase to produce carbonates that fix CO_2 permanently. A target to reach net-zero CO_2 emissions by 2050 has been set, in a bid to control the global surface temperature rise to within 1.5 °C and slow down the rate of climate change. Carbon capture and utilisation (CCU) is a portfolio technology that converts captured CO_2 into products (*e.g. chemicals, fuels, polymers and construction materials*) which can offset the capture and sequestration costs. CO_2 mineralisation processes perform fundamental advantages with thermodynamically favoured and abundant availability of feedstock among these CCU techniques.

The aim of this study is to develop a feasible technology to enable the scale-up design of aqueous mineralisation at optimal processing conditions, to achieve complete carbonation of the calcium content of the brine. An additional goal was to correlate processing conditions to morphological and mineralogical properties of the precipitated carbonates, to aid in scale-up of a process that produces highest value products for specific industries. Compared with the energy-intensive process of gas-solid accelerated mineralisation, aqueous carbonation remains an attractive option requiring milder process parameters, and such processes offer more opportunities for intensification through chemical additives, catalysts, process integration, use of alternative energy sources, reactor design, among other innovations.

This thesis presents a strategy to sequester CO_2 using alkaline desalination brines. Desalination brine is an attractive source of calcium and magnesium for mineral carbonation since the ions are dissolved in the solution which is ready to react with CO_2. An alternative approach to conducting rapid and continuous CO_2 mineralisation process in a tubular reactor is revealed which is favoured for scaling-up for industrial application. Different basic substances were utilised to synergistically boost CO_2 solubility in the brine while neutralising the acidification following precipitation of alkaline earth metals, and blast furnace (BF) slags, sodium hydroxide and low concentration of MEA were implemented in this study. Nickel nanoparticle catalyst is introduced to accelerate the carbonation reaction. Moreover, a three-phase analytical model is established for the scale-up application. A one-dimensional time-dependent plug-flow model is developed to determine CO_2 gas-to-liquid mass transfer rate, aqueous solution chemical speciation, fluid pressure, and carbonation efficiency within the tubular reactor, as a function of reactor length and residence time, under different process conditions.

Moreover, a basic solid substance to replace the alkaline solution was developed, and more importantly, it can be recycled for several cycle usage. Hydrotalcite (HT) treated as a dechlorination agent rather than buffering the mineralisation reaction, and chloride ions were removed from the brine, increasing its pH, and then conducted the mineralisation reaction. It indicates that hydrotalcite can be easily regenerated, and its memory effect property guarantees high efficiency after several cycles. Gaseous CO_2 and Na_2CO_3 solution were tested as the recharging agents, to replace the chloride anions from the spent HT interlayers and intercalate with HCO_3^- or CO_3^{2-}, followed by a calcination process to produce the reusable calcined-HT. Multiple reaction cycles were carried out to evaluate the regenerative and reusable property.

The results showed that the tubular reactor could achieve full (100%) conversion of calcium from the brine and CO_2 from the gas phase by adjusting the parameters to optimum conditions for both NaOH and MEA, thus proving to be an efficient process with high atom economy. Furthermore, calcium conversion efficiency is increased by about 10% in the present of 30 ppm nickel nanoparticles addition. The model explored the mass transfer of CO_2 across the gas-liquid interface in a Taylor flow reactor that can predict the speciation, bubble size and other parameters of the outlet during the reaction in the tubular reactor. The overall mass transfer coefficients were obtained with various CO_2 flowrates and MEA concentrations. Modelled results showed that the bubble length decreased with higher MEA concentration due to the rapid chemical reaction. The overall mass transfer coefficients increased with higher CO_2 flowrates. Modelled data are also in agreement with the experimental data. With the benefit of the model, the ionised species distribution in the carbonation process can be predicted and that can be used to determine the optimal reactor size for scale up.

Compared to previous studies on brine carbonation using NaOH and MEA as pH-buffering additives, the method of using the solid adsorbent calcined hydrotalcite can facilitate the regeneration process, likely reducing processing complexity, cost and energy demand. It was found that the chloride removal efficiency remains over 70% after five cycles, and calcium utilisation efficiency of the brine carbonation process can surpass 90%. In addition, the value-added carbonate produced from this process is pure $CaCO_3$, which can be a commercial product that can offset the operational costs.

This work indicates technical feasibility of the mineralisation process with alkaline brine solutions and represents a first step towards developing a scalable technology that can be used with a variety of brines to achieve sustainable CO_2 mineralisation.

Acknowledgements

I would like to thank my primary supervisor Professor Lidija Šiller for her support throughout my PhD life and accepted me to join her research team and helped me seek for funding to the research and provided the collaborative opportunity to my research project.

My sincere gratitude also gives to Professor Rafael M. Santos in the University of Guelph, Canada, who accepted me conducting part of my PhD work in his laboratory. His expertise in my research field helped me keep my progress on schedule. His willingness to give his precious time to provide valuable and constructive suggestions through my research project has been very much appreciated. His insightful feedback and professional knowledge helped my research to a higher level.

I would like to express my thanks to Newcastle-Singapore Studentship providing the financial support of my PhD study to remove the financial barriers to disrupt my research.

I would also acknowledge the help provided by the technician team, especially Neville Dickman for this technical assistance and equipment installation, who helped me to resemble my reactor and his perfect techniques can exactly transfer the set-up from the design drawing to the reality. Technicians and support team at Department of Chemical Engineering are also appreciated who helped me with data collection, and I must thank Rob Dixon, Ashley Craig, Kevin Brown for their support and maintenance of the instruments and booking management. Furthermore, Dr Isabel Arce Garcia, Maggie White and Steve Ward also provided generous help with samples characterisation. I am also thankful to the IT support team who also makes my research go well.

I am very grateful to the CO2Chem Network for its Seedcorn grant, travel bursaries and various network opportunities which broadens my academic network and increase the impact of my research. I would like to thank the founder and Chair of this organisation Professor Peter Styring, and other administrators for providing their prompt assistants and informative newsletters.

During my PhD research, I achieved two chances to conduct research in Canada, working with Prof Rafael M. Santos and I would like to thank the colleagues in Sheridan

College and the University of Guelph who provided support in the lab work and samples analysis.

I would also like to thank my group members and for the interesting chatting and creating such a comfortable research environment throughout my four years of life.

Last but not least, I would show my great thank to my parents, without their support and understanding, I cannot achieve this degree or even did not have the chance to study abroad. I am very thankful to my Fiancé Dr Xiao Han who always supports and encourages me throughout my study and shows me how to be a patient person. His company makes me go through every difficult time. Words cannot express my feelings and gratitude to their support, without whom I would not have made it complete my PhD.

List of Figures

List of Tables

Nomenclature

List of main abbreviations

AMP	Sterically hindered amine 2-amino-2-methyl-1-propanol
ATR	Attenuated Total Reflection
BF	Blast furnace
CA	Carbonic anhydrase
CHT	Calcined hydrotalcite
CCE	$Ca_{(aq)}$ conversion efficiency
CCS	Carbon capture and storage
CCU	Carbon capture and utilisation
DEA	Diethanolamine
DI	Deionised water
EDX	Energy dispersive x-ray spectroscopy
FTIR	Fourier Transform Infrared
HT	Hydrotalcite
ICP-OES	Inductively coupled plasma atomic emission spectroscopy
IC	Ion chromatography
MDEA	N-methyldiethanolamine
MEA	Monoethanolamine
NETL	National Energy Technology Laboratory
NiNPs	Nickel nanoparticles
PPC	Precipitated calcium carbonate
PZ	Piperazine
QXRD	Quantitative X-ray diffraction
SEM	Scanning electron microscopy
TGA	Thermogravimetric analysis

TRL	Technology Readiness Level
XRD	X-ray diffraction
XRF	X-ray fluorescence

Symbols

A	Debye–Hückel constant
d	Diameter of tubing of tubular reactor
D	Curvature diameter of the helically coiled tube
De	Dean number
$(dp/dz)_{TP}$	Two-phase pressure gradient
f	Friction factor
H	Henry’s law constant
$\triangle_{sol}H$	Enthalpy of dissolution
$\Delta_f G_m^\circ$	Gibbs free energy of formation
I	Ion strength
K	Overall mass transfer coefficient
N_{CO2}	Mass flus of CO_2
Q_G	Superficial flow rate of gas
ρ	Density of the liquid
Re	Reynolds number
μ	Viscosity of the liquid velocity of the liquid
U	Superficial
χ	Lockhart-Martinelli parameter
Z_i	Valence number of the ion
φ_G, φ_L	Two-phase frictional multiplier for gas, liquid

List of Publications and Conferences

Publications

- **N. Zhang**, R.M. Santos, S.M. Smith, L. Šiller. Acceleration of CO_2 mineralisation of alkaline brines with nickel nanoparticles catalysts in continuous tubular reactor, *Chemical Engineering Journal*, 377, (2019) 120479.
- **N. Zhang**, R.M. Santos, L. Šiller. Rapid CO_2 capture-to-mineralisation in scalable reactor*, Reaction chemistry & Engineering*, 5(3), (2020) 473-484; Inside front cover. *Reaction Chemistry & Engineering*, 5(3), 398-398.
- **N. Zhang**, R.M. Santos, L. Šiller. CO_2 mineralisation of brines with regenerative hydrotalcites in a cyclical process, *Chemical Engineering Journal*, 404, (2021) 126450.
- **N. Zhang**, Y.E Chai, R.M. Santos, L. Šiller. Advances in process development of aqueous CO_2 mineralisation towards scalability, *Journal of Environmental Chemical Engineering*, 8, (2020), 104453.

Conference Presentations

- **N. Zhang**, R.M. Santos, L. Šiller. 'Experimental and modelling study of CO_2 sequestration by mineralisation process in tubular reactor', Oral presentation. *CO2Chem 3rd Annual Status Conference*, Sheffield, UK, January 2020.
- **N. Zhang**, R.M. Santos, L. Šiller. 'CO_2 sequestration by precipitating carbonates from aqueous alkaline solution with nickel nanoparticles in tubular reactor', Oral presentation. *17th International Conference on Carbon Dioxide Utilization - ICCDU 2019*, Aachen, Germany, June 2019.
- '**N. Zhang**, R.M. Santos, L. Šiller. Intensified CO_2 sequestration by precipitating carbonates from aqueous monoethanolamine solution in continuous tubular reactor', Oral presentation. *Second International Process Intensification Conference (IPIC)*, Leuven, Belgium, May 2019.
- **N. Zhang**, R.M. Santos, L. Šiller. 'Mineral sequestration of CO_2 with brine in tubular reactor', Poster presentation. *ChemEngDayUK 2019*, Heriot-Watt University, April 2019.

- **N. Zhang**, R.M. Santos, L. Šiller. ‘Investigation of CO_2 mineralization of alkaline brine in continuous tubular reactor’, *International Conference on Chemical Reaction Engineering*, Poster presentation. *ISCRE 25*, Florence, Italy, May 2018.

Table of Contents

Chapter 1. Introduction

1.1 Background

Since the beginning of the industrial revolution, the atmospheric concentrations of greenhouse gases have shown an increasing trend, bringing significant impacts to the environment. The atmospheric CO_2 level of the global marine surface has risen sharply from 340 ppm to 416 ppm over the last 40 years shown in Figure 1.1 (Dlugokencky and Tans, 2020), driven primarily by fossil fuel combustion emissions and a variety of other anthropogenic activities. Extreme weather consequences have occurred frequently in recent years, indicating that the climate on our planet is changing towards a harmful direction, and it has been pointed out that the Earth is approaching the tipping point beyond which irreversible consequences of the climate change become unavoidable (Lenton *et al.*, 2019).

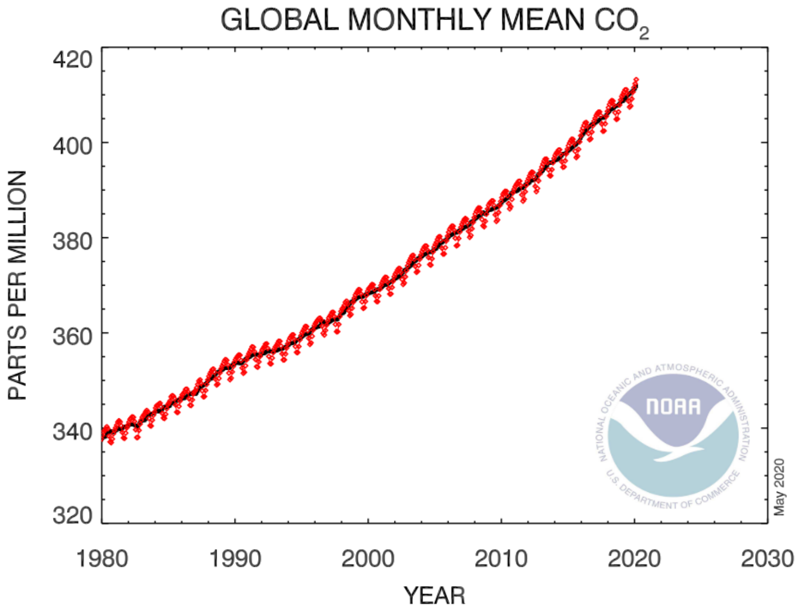

Figure 1.1 Monthly mean carbon dioxide globally averaged over marine surface sites since 1980 (Dlugokencky and Tans, 2020).

Governments, civil society and industrial sectors are working together around the world to slow down the greenhouse gas effect in launching numerous technologies and regulations most appropriate to regional situations. The European Commission has recently set a target to reach net-zero CO_2 emissions by 2050, in a bid to control the global surface temperature rise to within 1.5 °C and slow down the rate of climate change (IPCC, 2018; European Commission, December 2018).

In order to meet the goal of the global climate change mitigation, measures should be taken promptly, including renewable energy usage (Arent *et al.*, 2011), improving the energy efficiency and deploying CO_2 capture, storage and utilisation technologies (Metz B, 2005). Renewable energy, which refers to the low carbon emission energy, such as wind, solar, hydropower, biomass, nuclear power, etc., cannot rapidly replace the current dominant fossil fuel powered energy sources, but rather are looked at as part of a hybrid energy strategy due to their limited capacity and discontinuity of generation (Baños *et al.*, 2011). Moreover, renewable energy implementation processes require high investment (Dicorato *et al.*, 2011) and can pose other environmental concerns. Additionally, nuclear power energy is facing a number of safety issue and public concerns. Traditional CO_2 capture and sequestration technologies are referred to the carbon capture and storage (CCS) (Boot-Handford *et al.*, 2014), and the preferred CCS approaches transfer and store the captured CO_2 underground in saline reservoirs or use the CO_2 for enhanced oil recovery. CCS has been deployed at large-scale in some locations, but its environmental impact, energy efficiency and economic evaluation are still under investigation (Bachu, 2008; Sweatman *et al.*, 2009; Gaus, 2010; De Silva *et al.*, 2015).

Carbon capture and utilisation (CCU) is the portfolio technology that converting captured carbon dioxide to a product by forming or breaking chemical bonds (Styring *et al.*, 2014), such as mineral carbonation, enhanced oil recovery, and chemical feed stocks via electrochemical CO_2 reduction (Garg et al., 2020). Though CCU is treated as complementary alternative to CCS, it can turn CO_2 as a feedstock to lower the burden on the deployment of technologies (Styring *et al*., 2011). CCU can proceed through various feasible techniques that have capabilities to fix CO_2 and convert it to value-added products while mitigating emissions (Markewitz *et al.*, 2012). CCU options include converting CO_2 to chemicals, fuels, bioproducts, polymers and construction materials (Aresta *et al.*, 2014; North and Styring, 2015; Pan *et al.*, 2018a). CCU is in some ways inspired by nature, in closing the carbon cycle (Dunsmore, 1992). Comparing these CO_2 transformation routes, the main advantages of CO_2 mineralisation processes are: (i) carbonates are thermodynamically favoured due to their lower Gibbs free energy; (ii) abundant availability of mineral feedstock; (iii) mineral carbonation reactions are exothermic; and (iv) mineralisation can store CO_2 permanently (Chiang and Pan, 2017). Mineralisation was first introduced by Seifritz (Seifritz, 1990) and Lackner et al. (Lackner *et al.*, 1995) and Lackner (Lackner, 2003) envisioned it to be a feasible process at large-scale. Initially, investigations considered the reaction between CO_2 and minerals directly, similar to ambient geological weathering, however, this process is always kinetically limited, requiring high temperature or pressure to accelerate the reaction. Subsequently, aqueous carbonation was proposed as an option to accelerate the process of mineralisation (Gerdemann *et al.*, 2007). Aqueous mineral carbonation has since developed into a promising candidate to economically sequester CO_2 at large scales (Ron Zevenhoven *et al.*, 2010; Kelly *et al.*, 2011; Matter *et al.*, 2016). The current Technology Readiness Level (TRL) mostly ranges from 3 to 9, depending on different approaches under development (Aines *et al.*, 2018; Carbon8, 2020), accomponied with life cycle assessment and techno-economic assessment to evaluate enviromental and ecomonic impacts (McCord *et al*., 2019; Müller *et al*., 2020; Zimmermann *et al*., 2020).

Aqueous mineralisation processes can be classified into two main categories: direct carbonation and indirect carbonation. Many researchers have been working on this classification of CO_2 mineralisation from different perspectives in recent years (Sanna *et al.*, 2012; Sanna *et al.*, 2014; Romanov *et al.*, 2015; Wang *et al.*, 2017; Pan *et al.*, 2018b; Kelemen *et al.*, 2019) and some of them have focused on aqueous carbonation (Azdarpour *et al.*, 2015; Chakraborty and Jo, 2018) and little emphasis is given to direct aqueous carbonation in the absence of solid minerals (i.e. brines), and to process scalability and process intensification strategies.

Feedstock of mineralisation processes is either a solid phase or an aqueous brine phase. Solid minerals can be either obtained from the natural sources (Bide *et al.*, 2014; Xie *et al.*, 2016), or originate from industrial wastes such as steel slags, fly ashes, red mud, etc. (Gunning *et al.*, 2014; Gad how many desalinationikota *et al.*, 2015; Pan *et al.*, 2015; Ibrahim *et al.*, 2019). Aqueous feedstock for mineralisation refers to liquid solutions that contain high concentrations of alkaline earth metal ions that are available to react with CO_2 without dissolution process, such as brines from desalination plants or saline reservoirs (Druckenmiller and Maroto-Valer, 2005; Bang *et al.*, 2017). According to a report from the International Desalination Association (International Desalination Association, 2017), 92.5 million cubic meters per day of water is desalinated. Assuming 50% recovery, the same volume of brine is produced daily, and assuming 100% rejection of calcium and an average seawater calcium content of 400 $mg \cdot L^{-1}$ Ca, desalination brine typically has 800 $mg \cdot L^{-1}$ Ca. Hence, it can be estimated that 6.75 × 10^{11} mol per year of $Ca_{(aq)}$ can be present in brine. If all this calcium is carbonated, a total of 2.97× 10^7 tonnes of CO_2 can be sequestered; that is 29.7 MT CO_2 per annum. The products of mineralisation processes usually contain solid carbonates, pure or combined with feedstock residues, and in some cases can be processed into construction materials, such as mineral aggregates and bricks (Zevenhoven *et al.*, 2006; Woodall *et al.*, 2019).

The essence of mineralisation technology is to address the challenge of current greenhouse gas emissions; therefore, large-scale deployment is the ultimate purpose. Over the past decade, the commercial deployment of mineral carbonation processes has been slow, and many processes have been shown to suffer from limited reaction rate and poor energy efficiency. Yet, the potential of further improvement of this route and its theoretical capacity to address CO_2 emissions at the global scale still drive efforts from many researchers in academia and industry. Compared with the process of gas-solid accelerated mineralisation, aqueous carbonation can be conducted under milder process parameters through process intensification with novel reactor design and addition of chemical additives.

1.2 Research objective

Driven by the opportunities and challenges revealed from the aqueous mineralisation reaction with brine, the overall aim of this thesis is to propose a scalable process with alkaline brines for CO_2 mineralisation at optimal processing conditions, to achieve complete carbonation of the calcium content of the brine. In addition, aim was to combine experimental and modelling studies provide a better understanding of the multiple-phases reactions and chemical interactions of the reactants. This works represents a first step towards developing a scalable technology that can be used with a variety of brines to achieve sustainable CO_2 mineralisation. In particular, these following processes are implemented:

1) Process development and reactor design were used to conduct continuous aqueous CO_2 mineralisation reactions.

2) Investigation of optimal process parameters was conducted with various experiments and the key parameter is the calcium conversion efficiency (CCE) which shows how much calcium in the brines is converted to carbonates. It is aimed to

achieve complete conversion efficiency to obtain the high atom economy. A nickel nanoparticle catalyst is introduced to accelerate the carbonation reaction through acceleration of hydration reaction of CO_2. Different basic substances (NaOH, MEA and calcined hydrotalcites) are applied to neutralise brine acidification by CO_2 injection, and improvements are developed to make the process cost and energy effective.

3) Followed by experiments outcomes, a one-dimension three-phase model is developed in order to comprehensively understand the mass transfer of the reactions occurred during the integrated process and provide a tool to facilitate the scale-up process by predicting the species distribution and giving an optimal reactor length for reactor design.

4) Moreover, the morphological and mineralogical properties of the precipitated carbonates are analysed, to aid a scale-up process that can produce the highest specific value products to offset the cost.

1.3 Thesis structure

This thesis contains seven chapters, including three key chapters (*i.e. Chapter 4, 5, 6*) on results of experiments and modelling. These are preceded by a literature review and methodology chapter, and finally followed by a chapter of conclusions and future work with summaries and implications of this thesis, plus future potential work. Herein, the content of this thesis is outlined.

The Chapter 2 titled *'State-of-the-Art review of aqueous mineralisation',* this is *a* literature review chapter that discusses up to date progress of the aqueous mineralisation from different perspectives.

The Chapter 3*: Methodology,* this chapter reveals a detailed methodology of this thesis implementation from the experimental and modelling perspectives. The design and installation of reactors are displayed coupled with the process intensification and development, plus data collection. Moreover, the principles of analytical instruments used in the characterisation of solid and liquid samples are also described.

The Chapter 4 titled *'Acceleration of CO_2 mineralisation of alkaline brines with catalysts in continuous tubular reactor'*, describes a continuous tubular reactor that was implemented as the aqueous mineralisation reactor for the first time and this part of research has been published in *Chemical Engineering Journal* (Zhang *et al.*, 2019). In this chapter, a novel strategy to sequester CO_2 using alkaline desalination brine is presented and the novelty is using a tubular reactor with three-phase slug flow pattern, and introducing a nickel nanoparticle catalyst to accelerate the carbonation reaction. The optimal processing conditions in such a system to achieve complete carbonation of the calcium content of the brine are found. This chapter represents a first step towards developing a scalable technology that can be used with brines.

In Chapter 5 titled *'Rapid CO_2 capture-to-mineralisation in a scalable reactor'*, is a subsequent research of Chapter 4. This is a study to sequester CO_2 using alkaline brines in a tubular reactor as previously studied, but different type of basic substances (i.e. low concentrations of monoethanolamine (MEA)) are applied. Moreover, a one-dimensional time-dependent plug-flow model that determines CO_2 gas-to-liquid transfer rate is developed, aqueous solution chemical speciation, fluid pressure, and carbonation efficiency within the tubular reactor, as a function of reactor length and residence time, under different process conditions. The aim of this chapter was to develop a scale-up tool (the experimentally validated model) to enable the scaled-up design at optimal processing parameters, to achieve high conversion efficiency of the calcium content of the brine, and the modelling was run with Excel and MATLAB. Furthermore, specific morphological and mineralogical properties of the precipitated carbonates are produced to offset the processing costs. This chapter has been published in *Reaction Chemistry and Engineering* (Zhang *et al.*, 2020).

The *Chapter 6,* titled *'Cyclical process with regenerative hydrotalcites enabling efficient CO_2 mineralisation of brines',* deals with the issue of the basic agent regeneration. An approach that uses calcined hydrotalcite as a dechlorination agent is presented. That is, rather than buffering the mineralisation reaction with basic additives as used in previous chapters, chloride ions from the brine are removed first, by increasing its pH, and then proceed with the mineralisation reaction can proceed. Hydrotalcite can be easily regenerated, and its memory effect property guarantees a high efficiency conversion after several cycles. This novel cyclical and regenerative approach used on the aqueous CO_2 mineralisation has the potential to be applied in a variety of other mineral carbonation processes that currently require the use of pH buffering agents.

The work of this chapter has been published in *Chemical Engineering Journal* (Zhang *et al.*, 2021).

In Chapter 7, titled *''Conclusions and Future Work''*, provided a detailed summary of the results obtained throughout the thesis. Based on these findings and revealed challenges, future works are proposed to provide further improvements for the aqueous CO_2 mineralisation with alkaline brines in different types of reactors.

References

Aines, R., Friedmann, J., McCormick, C. and Sandalow, D. (2018) 'Paths to Effective CO_2 Utilization: A Roadmap for Several Options'. *14th Greenhouse Gas Control Technologies Conference.* Melbourne, Australia, 21st -25th October 2018.

Arent, D.J., Wise, A. and Gelman, R. (2011) 'The status and prospects of renewable energy for combating global warming', *Energy Economics*, 33(4), pp. 584-593.

Aresta, M., Dibenedetto, A. and Angelini, A. (2014) 'Catalysis for the valorization of exhaust carbon: from CO_2 to chemicals, materials, and fuels. Technological use of CO_2', *Chemical Reviews*, 114(3), pp. 1709-42.

Azdarpour, A., Asadullah, M., Mohammadian, E., Hamidi, H., Junin, R. and Karaei, M.A. (2015) 'A review on carbon dioxide mineral carbonation through pH-swing process', *Chemical Engineering Journal*, 279, pp. 615-630.

Bachu, S. (2008) 'CO_2 storage in geological media: Role, means, status and barriers to deployment', *Progress in Energy and Combustion Science*, 34(2), pp. 254-273.

Bang, J.-H., Yoo, Y., Lee, S.-W., Song, K. and Chae, S. (2017) 'CO_2 Mineralization Using Brine Discharged from a Seawater Desalination Plant', *Minerals*, 7(11), p. 207.

Baños, R., Manzano-Agugliaro, F., Montoya, F.G., Gil, C., Alcayde, A. and Gómez, J. (2011) 'Optimization methods applied to renewable and sustainable energy: A review', *Renewable and Sustainable Energy Reviews*, 15(4), pp. 1753-1766.

Bide, T.P., Styles, M.T. and Naden, J. (2014) 'An assessment of global resources of rocks as suitable raw materials for carbon capture and storage by mineralisation', *Applied Earth Science*, 123(3), pp. 179-195.

Boot-Handford, M.E., Abanades, J.C., Anthony, E.J., Blunt, M.J., Brandani, S., Mac Dowell, N., Fernández, J.R., Ferrari, M.-C., Gross, R., Hallett, J.P., Haszeldine, R.S., Heptonstall, P., Lyngfelt, A., Makuch, Z., Mangano, E., Porter, R.T.J., Pourkashanian, M., Rochelle, G.T., Shah, N., Yao, J.G. and Fennell, P.S. (2014) 'Carbon capture and storage update', *Energy & Environmental Science*, 7(1), pp. 130-189.

Carbon8 Systems (2020). Available at: http://c8s.co.uk/ (Accessed: 20 Apri 2020).

Chakraborty, S. and Jo, B.W. (2018) 'Aqueous-based carbon dioxide sequestration', in *Carbon Dioxide Sequestration in Cementitious Construction Materials*. Woodhead Publishing, pp. 39-64.

Chiang, P.-C. and Pan, S.-Y. (2017) *Carbon dioxide mineralization and utilization*. Taiwan: Springer.

De Silva, G.P.D., Ranjith, P.G. and Perera, M.S.A. (2015) 'Geochemical aspects of CO_2 sequestration in deep saline aquifers: A review', *Fuel*, 155, pp. 128-143.

Dicorato, M., Forte, G., Pisani, M. and Trovato, M. (2011) 'Guidelines for assessment of investment cost for offshore wind generation', *Renewable Energy*, 36(8), pp. 2043-2051.

Dlugokencky, E. and Tans, P. (2020) *Trends in Atmospheric Carbon Dioxide, NOAA/ESRL (www.esrl.noaa.gov/gmd/ccgg/trends/)*. Available at: https://www.esrl.noaa.gov/gmd/ (Accessed: 17 April 2020).

Druckenmiller, M.L. and Maroto-Valer, M.M. (2005) 'Carbon sequestration using brine of adjusted pH to form mineral carbonates', *Fuel Processing Technology*, 86(14-15), pp. 1599-1614.

Dunsmore, H. (1992) 'A geological perspective on global warming and the possibility of carbon dioxide removal as calcium carbonate mineral', *Energy Conversion and Management*, 33(5-8), pp. 565-572.

European Commission. (December 2018) *'2050 long-term strategy'*. Available at: https://ec.europa.eu/clima/policies/strategies/2050_en (Accessed: 15 April 2020).

Gadikota, G., Fricker, K., Jang, S.-H. and Park, A.-H.A. (2015) 'Carbonation of Silicate Minerals and Industrial Wastes and Their Potential Use as Sustainable Construction Materials', in *Advances in CO_2 Capture, Sequestration, and Conversion*. American Chemical Society, pp. 295-322.

Garg, S., Li, M., Weber, A.Z., Ge, L., Li, L., Rudolph, V., Wang, G. and Rufford, T.E. (2020) 'Advances and challenges in electrochemical CO_2 reduction processes: an engineering and design perspective looking beyond new catalyst materials', *Journal of Materials Chemistry* A, 8(4), pp. 1511-1544.

Gaus, I. (2010) 'Role and impact of CO_2-rock interactions during CO_2 storage in sedimentary rocks', *International Journal of Greenhouse Gas Control*, 4(1), pp. 73-89.

Gerdemann, S.J., O'Connor, W.K., Dahlin, D.C., Penner, L.R. and Rush, H. (2007) 'Ex situ aqueous mineral carbonation', *Environmental Science & Technology*, 41(7), pp. 2587-2593.

Gunning, P., Hills, C., Araizi, P., Maries, A. and Wray, D. (2014) 'Carbon capture using wastes: A review'. *7th International Scientific Conference: Science and Higher Education in Function of Sustainable Development*. Uzice, Serbia, 3-4 October 2014.

Ibrahim, M., El-Naas, M., Benamor, A., Al-Sobhi, S. and Zhang, Z. (2019) 'Carbon Mineralization by Reaction with Steel-Making Waste: A Review', *Processes*, 7(2), p. 115.

International Desalination Association (2017) *Desalination by the Numbers* Available at: https://idadesal.org/international-desalination-association-and-global-water-intelligence-release-new-data-in-30th-worldwide-desalting-inventory/ (Accessed: 20 April 2020).

IPCC (2018) ‘Global Warming of 1.5 °C Special Report’. Available at: https://www.ipcc.ch/sr15/ (Accessed: 18 May 2019).

Kelemen, P., Benson, S.M., Pilorgé, H., Psarras, P. and Wilcox, J. (2019) 'An Overview of the Status and Challenges of CO_2 Storage in Minerals and Geological Formations', *Frontiers in Climate*, 1, p. Article 9.

Kelly, K.E., Silcox, G.D., Sarofim, A.F. and Pershing, D.W. (2011) 'An evaluation of ex situ, industrial-scale, aqueous CO_2 mineralization', *International Journal of Greenhouse Gas Control*, 5(6), pp. 1587-1595.

Lackner, K.S. (2003) 'A guide to CO_2 sequestration', *Science*, 300(5626), pp. 1677-1678.

Lackner, K.S., Wendt, C.H., Butt, D.P., Joyce Jr, E.L. and Sharp, D.H. (1995) 'Carbon Dioxide Disposal in Carbonate Minerals', *Energy*, 20, pp. 153-1170

Lenton, T.M., Rockström, J., Gaffney, O., Rahmstorf, S., Richardson, K., Steffen, W. and Schellnhuber, H.J. (2019) 'Climate tipping points - too risky to bet against', *Nature*, 575, pp. 592-595.

McCord, S., Villa Zaragoza, A., Sanderson, P., Armstrong, K., Styring, P., Hills, C., Carey, P., Osbourne, M., Müller, L. and Bardow, A. (2019) 'Global CO_2 Initiative Complete Mineralization Study 2018'. CO_2 Chem Media and Publishing Ltd.

Markewitz, P., Kuckshinrichs, W., Leitner, W., Linssen, J., Zapp, P., Bongartz, R., Schreiber, A. and Müller, T.E. (2012) 'Worldwide innovations in the development of carbon capture technologies and the utilization of CO_2', *Energy & Environmental Science*, 5(6), p. 7281.

Matter, J.M., Stute, M., Snæbjörnsdottir, S.Ó., Oelkers, E.H., Gislason, S.R., Aradottir, E.S., Sigfusson, B., Gunnarsson, I., Sigurdardottir, H., Gunnlaugsson, E., Axelsson, G., Alfredsson, H.A., Wolff-Boenisch, D., Mesfin, K., Taya, D.F.d.l.R., Hall, J., Dideriksen, K. and Broecker, W.S. (2016) 'Rapid carbon mineralization for permanent disposal of anthropogenic carbon dioxide emissions', *Science*, 352(6291), pp. 1312-1314.

Metz B, D.O., de Coninck HC, Loos M, Meyer LA, editors (2005) 'IPCC special report on carbon dioxide capture and storage'. Cambridge (United Kingdom)/New York (NY, USA): Prepared by Working Group III of the Intergovernmental Panel on Climate Change Cambridge University Press.

Müller, L.J., Kätelhön, A., Bachmann, M., Zimmermann, A., Sternberg, A. and Bardow, A. (2020) 'A Guideline for Life Cycle Assessment of Carbon Capture and Utilization', *Frontiers in Energy Research*, 8, p. Article 15.

North, M. and Styring, P. (2015) 'Perspectives and visions on CO_2 capture and utilisation', *Faraday Discuss*, 183, pp. 489-502.

Pan, S.-Y., Chiang, A., Chang, E.E., Lin, Y.-P., Kim, H. and Chiang, P.-C. (2015) 'An Innovative Approach to Integrated Carbon Mineralization and Waste Utilization: A Review', *Aerosol and Air Quality Research*, 15(3), pp. 1072-1091.

Pan, S.-Y., Chiang, P.-C., Pan, W. and Kim, H. (2018a) 'Advances in state-of-art valorization technologies for captured CO_2 toward sustainable carbon cycle', *Critical Reviews in Environmental Science & Technology*, 48(5), pp. 471-534.

Pan, S.-Y., Ling, T.-C., Park, A.-H.A. and Chiang, P.-C. (2018b) 'An Overview: Reaction Mechanisms and Modelling of CO_2 Utilization via Mineralization', *Aerosol and Air Quality Research*, 18(4), pp. 829-848.

Romanov, V., Soong, Y., Carney, C., Rush, G.E., Nielsen, B. and O'Connor, W. (2015) 'Mineralization of Carbon Dioxide: A Literature Review', *ChemBioEng Reviews*, 2(4), pp. 231-256.

Sanna, A., Hall, M.R. and Maroto-Valer, M. (2012) 'Post-processing pathways in carbon capture and storage by mineral carbonation (CCSM) towards the introduction of carbon neutral materials', *Energy & Environmental Science*, 5(7), pp. 7781–7796.
Sanna, A., Uibu, M., Caramanna, G., Kuusik, R. and Maroto-Valer, M.M. (2014) 'A review of mineral carbonation technologies to sequester CO_2', *Chemical Society Reviews*, 43(23), pp. 8049-8080.

Seifritz, W. (1990) 'CO_2 disposal by means of silicates', *Nature*, 345(6275), pp. 486-486.

Styring, P., Jansen, D., De Coninick, H., Reith, H. and Armstrong, K. (2011) ‘Carbon Capture and Utilisation in the green economy’, Centre for Low Carbon Futures New York.

Styring, P., Quadrelli, E.A. and Armstrong, K. (2014) ‘Carbon dioxide utilisation: closing the carbon cycle’, Elsevier.

Sweatman, R.E., Parker, M.E. and Crookshank, S.L. (2009) ‘Industry experience with CO_2-enhanced oil recovery technology’, *SPE international conference on CO_2 capture, storage, and utilization*. Society of Petroleum Engineers. San Diego, California, USA, 2-4 November.

Wang, F., Dreisinger, D.B., Jarvis, M. and Hitchins, T. (2017) 'The technology of CO_2 sequestration by mineral carbonation: current status and future prospects', *Canadian Metallurgical Quarterly*, 57(1), pp. 46-58.

Woodall, C.M., McQueen, N., Pilorgé, H. and Wilcox, J. (2019) 'Utilization of mineral carbonation products: current state and potential', *Greenhouse Gases: Science and Technology*, 9(6), pp. 1096-1113.

Xie, H., Tang, L., Wang, Y., Liu, T., Hou, Z., Wang, J., Wang, T., Jiang, W. and Were, P. (2016) 'Feedstocks study on CO_2 mineralization technology', *Environmental Earth Sciences*, 75(7) p. 615.

Zevenhoven, R., Eloneva, S. and Teir, S. (2006) 'Chemical fixation of CO_2 in carbonates: Routes to valuable products and long-term storage', *Catalysis Today*, 115(1-4), pp. 73-79.

Zevenhoven, R., Fagerlund, J. and Songok, J.K. (2010) 'CO_2 mineral sequestration: developments toward large-scale application', *Greenhouse Gases: Science and Technology*, 1, pp. 48-57.

Zhang, N., Santos, R.M. and Šiller, L. (2020) 'Rapid CO_2 capture-to-mineralisation in a scalable reactor', *Reaction Chemistry & Engineering*, 5(3), pp. 473-484.

Zhang, N., Santos, R.M., Smith, S.M. and Šiller, L. (2019) 'Acceleration of CO_2 mineralisation of alkaline brines with nickel nanoparticles catalysts in continuous tubular reactor', *Chemical Engineering Journal*, 377, p. 120479.

Zhang, N., Santos, R.M. and Šiller, L. (2021) 'CO_2 mineralisation of brines with regenerative hydrotalcites in a cyclical process', *Chemical Engineering Journal*, 404, p. 126450.

Zimmermann, A.W., Wunderlich, J., Müller, L., Buchner, G.A., Marxen, A., Michailos, S., Armstrong, K., Naims, H., McCord, S., Styring, P., Sick, V. and Schomäcker, R. (2020) 'Techno-Economic Assessment Guidelines for CO_2 Utilization', *Frontiers in Energy Research*, Article 8.

Chapter 2. State-of-the-Art review of aqueous mineralisation

Aqueous mineralisation is a process that CO_2 reacts with aqueous ions to produce solid carbonates that can store CO_2 permanently. Compared with other energy-intensive mineralisation processes, aqueous carbonation remains a competitive approach with milder process parameters. This chapter is a part of a review paper titled ‘Advances in process development of aqueous CO_2 mineralisation towards scalability’, to be published in *Journal of Environmental Chemical Engineering*, and it has been accepted.

The scope of this chapter is illustrated in Figure 2.1. Based on the increasing research on aqueous carbonation, the mineralisation process can be subdivided into three main categories: 1) two-step aqueous mineralisation, which contains solid extraction and carbonation processes; 2) single-step aqueous mineralisation solid phase, which represents the reaction of multiphases gas-liquid-solid; and 3) single-step aqueous mineralisation with liquid phase only, which is the liquid-gas reaction and all the active reactants are dissolved in the aqueous media and readily reacted with CO_2. For each category, the progress in the investigation, optimization of process parameters, source of feedstock, process intensification strategies, and products evaluation for utilisation, were reviewed. Feedstocks of mineralisation process are either in solid phase or aqueous phase, and solid minerals could be either obtained from the natural minerals (Bide *et al.*, 2014; Xie *et al.*, 2016), or derived from industrial wastes, such as steel slags, fly ashes, red mud, thermal wastes, etc (Gunning *et al.*, 2014; Gadikota *et al.*, 2015; Pan *et al.*, 2015; Ibrahim *et al.*, 2019). Aqueous feedstock for mineralisation refers to the liquid solution that contains high concentration of alkaline earth metal ions which are ready to react with CO_2 without dissolution process, like brines from desalination plants or saline reservoirs (Bang *et al.*, 2017; Zhang *et al.*, 2019; Zhang *et al.*, 2020). The products of mineralisation process are normally solid carbonates and also can be processed into construction materials (Gunning *et al.*, 2010; Zevenhoven *et al.*, 2006; Woodall *et al.*, 2019).

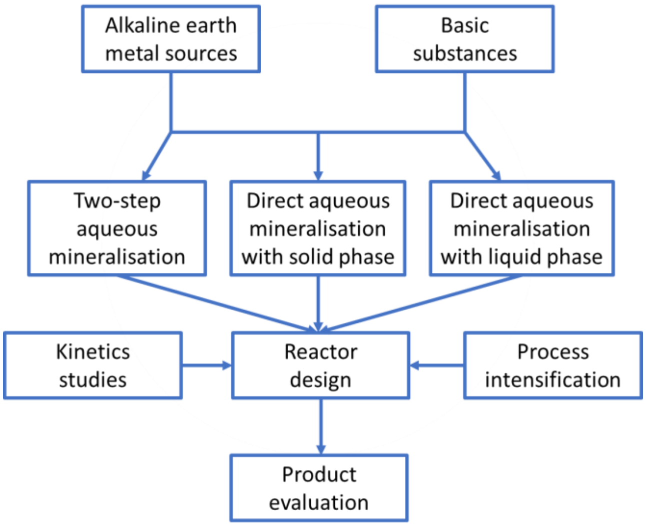

Figure 2.1 Scope of aqueous CO_2 mineralisation literature review.

2.1. Two-step aqueous mineralisation

Here, the conventional two-step mineralisation processes, which involve metal ions leaching from solid resources and carbonation process, are reviewed. The outline is illustrated in Figure 2.2, where the process of leaching and carbonation will be summarised and discussed from the aspects of feedstock, process parameters, process intensification, and products evaluation. The basic chemical reactions of the process are shown in Eq.(2.1-2) (Lackner *et al.*, 1995), where the mineral containing multiple metal oxides is dissolved by acid, base or salt to release metal ions and then react with CO_2 for carbonation process by adding basic substances in order to adjust the pH value.

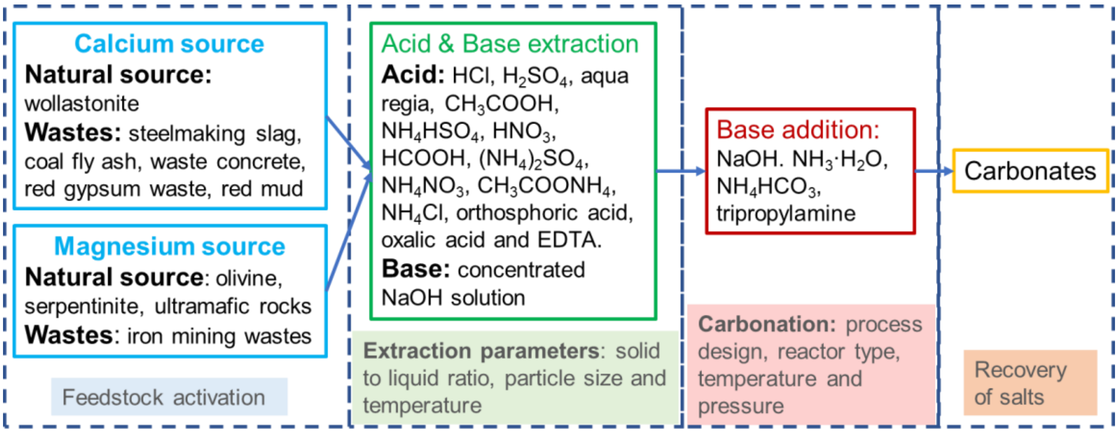

Figure 2.2 Processes involved in the two-step aqueous carbonation.

$$\mathrm{Metal\ Oxide} + \mathrm{Acid} \rightarrow \mathrm{M}^{n+} + \mathrm{Cations} + \mathrm{H_2O} \qquad \text{(E2.1)}$$

$$\mathrm{M}^{n+} + \mathrm{Base} + \mathrm{CO_2} \rightarrow \mathrm{Carbonates} + \mathrm{H_2O} \qquad \text{(E2.2)}$$

Table 2.1 Summary of up-to-date two-step aqueous mineralisation processes with various process parameters.

No.	Metal	Source	Composition	Particle size	Leachate and concentration	Solid/liquid	Temp	Agitation	Time	Efficiency/ Capacity	Reference
1	Mg	Serpentine	MgO 35%	< 60 mesh	HCl 20%	68 g/100 g	100 °C	vigorously	60 min	93.2%	(Barnes and Cunningham, 1950)
2	Mg	Serpentine	MgO 25%	37 µm	7.0 M HCl	3.0 g·L^{-1}	95 °C	Rotating 400 rpm	16 hr	200 mg/cm^2	(Dutrizac *et al.*, 2000)
3	Ca	Wollastonite		75 µm	CH_3COOH 13.72 g/50 g	13.3 g/63.7 g	60 °C	300 rpm	250 min	48%	(Kakizawa *et al.*, 2001)
4	Mg	Serpentine	MgO 27%	< 75 µm	1vol% Orthophosphoric + 0.9 wt.% Oxalic acid + 0.1 wt.% EDTA	3 g/200 mL	Room temp	750 rpm	120 min	80%	(Park *et al.*, 2003)
5	Ca	Waste cement		10-200 µm	Pressurized CO_2 and water	0.29 wt.%	323 K	900 rpm	120 min	50%	(Iizuka *et al.*, 2004)
6	Mg	Serpentine	MgO 27%	< 75 µm	1 vol% orthophosphoric + 0.9wt% oxalic acid + 0.1 wt.% EDTA with internal grinding	2.5 g/80mL	70 °C	Fluidising with 20cm/s air and 20 vol% 2mm glass beads	60 min	65%	(Park and Fan, 2004)
7	Mg	Serpentine		Median 125 µm	5M H_2SO_4				60 min	58.5%	(Alexander *et al.*, 2007)
8	CaO	Blast furnace slag	40.6%	350–500 µm	33.3 wt.% CH_3COOH	4.2 g/300mL	50 °C	–	20 min	100%	(Teir *et al.*, 2007a)
		Steel converter slag	43.6%	350–500 µm					2 hr	90%	

Table 2.1 Summary of up-to-date two-step aqueous mineralisation processes with various process parameters.

No.	**Metal**	**Source**	**Composition**	**Particle size**	**Leachate and concentration**	**Solid/liquid**	**Temp**	**Agitation**	**Time**	**Efficiency/ Capacity**	**Reference**
		Electric arc furnace slag	40.8%	125–350 µm					1 hr	94%	
		AOD process slag	60.7%	<125 µm					20 min	84%	
		Wollastonite	44.5%	<250 µm					1 hr	51%	
9	Mg	Serpentinite	MgO 40%	Median 100 µm	4M HCl 4M HNO_3	100 $g\cdot L^{-1}$	70 °C	650 rpm	2 hr	93% 88%	(Teir *et al.*, 2007b)
10	Mg	Serpentinite	MgO 22%	74 – 125 µm	2M H_2SO_4 2M HCl 2M HNO_3	10 g/500 mL	70 °C	650 rpm	2 hr	100%	(Teir *et al.*, 2007c)
11	Ca	Converter slag	CaO 45%	63–125 µm	1M NH_4Cl	Molar ratio NH_4Cl/CaO= 2	80 °C	300 rpm	1 hr	60%	(Kodama *et al.*, 2008)
12	Mg	Serpentinite		74 – 125 µm	0.5M HCl 0.5M HNO_3	1 g/50 mL	20 °C	100 rpm	1 hr	10% 8%	(Teir *et al.*, 2009)
13	Ca Mg	Steelmaking slag	CaO 38.7% MgO 5%		CH_3COOH mixed with TBP solvent 0.998 mol/L	30 g/400 mL	94 °C	300 rpm	1 hr	Mg & Ca 80%	(Bao *et al.*, 2010)
14	Ca	Steelmaking slag	CaO 40%	38-250 µm	2M NH_4Cl	10 g/100 mL	60 °C	_	120 min	15 $g\cdot L^{-1}$ 4 $g\cdot L^{-1}$	(Sun *et al.*, 2011)
15	Mg	Serpentinite	MgO 40%	75-150 µm	1.4M NH_4HSO_4	20 g/400 mL	100 °C	800 rpm	3 hr	100%	(Wang and Maroto-Valer, 2011)
16	Ca	Coal fly ash	CaO 7wt%		DI water	100 $g\cdot L^{-1}$	Room temp	45 rpm	24 hr	10%	(Jo *et al.*, 2012)
17	Ca	Coal fly ash	CaO 30.5%	< 100 µm	3 M CH_3COONH_4	50 $g\cdot L^{-1}$	25 °C	500 rpm	60 min	58%	(He *et al.*, 2013)
18	Ca	Steelmaking slag	CaO 45%	74–125 µm	1 M NH_4NO_3	5 $g\cdot L^{-1}$	30 °C	600 rpm	1 hr	73%	(Said *et al.*, 2013)
19	Mg	Serpentine	MgO 40%	< 250 µm	2.8 M NH_4HSO_4	100 $g\cdot L^{-1}$	140 °C	800 rpm	1 hr	80%	(Sanna *et al.*, 2013)

Table 2.1 Summary of up-to-date two-step aqueous mineralisation processes with various process parameters.

No.	**Metal**	**Source**	**Composition**	**Particle size**	**Leachate and concentration**	**Solid/liquid**	**Temp**	**Agitation**	**Time**	**Efficiency/ Capacity**	**Reference**
20	Mg	Serpentinite	MgO 39.3%	<57 µm	0.5 M HCl	0.5 g/100 mL	100 °C	_	3 hr	65%	(Steel *et al.*, 2013)
21	Ca	Wollastonite	CaO 42.7%	17 ± 1 µm	0.1 M HCOOH	0.58 g/100 mL	80 °C	_	3 hr	96%	(Ghoorah *et al.*, 2014)
22	Mg	Magnesium silicate ore	MgO 40.7%	< 56 µm	1 M HCl	40 g·L^{-1}	80 °C	600 rpm	2 hr	85%	(Hemmati *et al.*, 2014)
23	Ca	Waste cement	CaO 35.7%	100 mesh	1 M NH_4NO_3	50 g·L^{-1}	20 °C	130 rpm	4 hr	69%	(Jo *et al.*, 2014)
24	Mg	Raw dunite	MgO 48.3%	<63 µm	40 mol/kg NaOH	50 g·L^{-1}	180 °C	_	18 hr	79%	(Madeddu *et al.*, 2014)
25	Mg	Olivine	MgO 48%	75-150 µm	1.4 M NH_4HSO_4	20 g/400 mL	100°C	_	3 hr	77%	(Sanna *et al.*, 2014)
26	Ca	Blast furnace slag	CaO 43.6%	< 200 mesh	20% aqua regia	30 g/300 mL	343 K	Overhead stirring	2 hr	100%	(Bang *et al.*, 2016)
27	Mg	Mining waste	MgO 43%	150 µm	2 M HCl	74 g·L^{-1}	100 °C	650 rpm	2 hr	95%	(Arce Ferrufino *et al.*, 2018)
28	Ca	Cement kiln dust	CaO	< 425 µm	Brine	1 g/50 mL	25 °C	Shaking 250 rpm	1 h	42%	(Jeon and Kim, 2019)
29	Ca	Red mud	CaO		1 M HCl	21 g/300 mL	80 °C	600 rpm	2 hr	85%	(Kashefi *et al.*, 2020)

Comparing the extraction process of solid to solid phase (Koivisto *et al.*, 2016) with solid to liquid phase, researchers from Åbo Akademi University (Erlund *et al.*, 2016) investigated these two routes with ammonia sulphate salt, and they found that the leaching efficiency was improved from typically 60% to 80% with the role of liquid, and lower reaction temperature was required for aqueous extraction. The liquid leaching process takes longer compared to solid/solid thermal extraction, but this can be compensated by reduced energy demand which is essential to solid phase extraction. Indirect aqueous carbonation is also called *ex situ* aqueous carbonation (Gerdemann *et al.*, 2007), National Energy Technology Laboratory (NETL), USA studied this aqueous carbonation reaction with various metal cations based minerals and CO_2 from the perspectives of resource evaluation, process development and energy consumption. Based on the advantages of aqueous carbonation via wet extraction process, processes that utilised various acids, bases, and salts as leaching agents are chronologically summarised.

2.1.1 Leaching process

Table 2.1 demonstrates various leaching agents and the main parameters of the leaching process including particle size and composition of feedstock, type of the leaching agents, liquid to solid ratio, reaction temperature, reaction time and leaching efficiency.

Prior to comparing the effect of leaching agents on extraction efficiency, the properties of feedstock itself can influence the alkaline earth metal dissolution performance even under the same process. Sanna et al. (Sanna *et al.*, 2014) and Wang and Maroto-Valer (Wang and Maroto-Valer, 2011) both used 1.4 M NH_4HSO_4 as the extractant solution for leaching of olivine and serpentine, respectively. As a result, 77% dissolution efficiency was achieved by olivine while 100% was obtained by serpentine. Additionally, Styles et al. (Styles *et al.*, 2014) found that magnesium dissolution efficiency of serpentinite could reach 78%, but only 55% with olivine. The mechanism behind this was investigated by comparing materials before and after leaching reaction through scanning electron microscopy (SEM) and X-ray diffraction (XRD) analysis. It was found that structures of magnesium silicates varied and olivine changed dramatically in post-experiment by the formation of secondary boussingaultite covering up the magnesium leaching sites, and large olivine particles broke down into small pieces from SEM images. However, the crystal structure of serpentinite was maintained well after the dissolution reaction. Zhao et al. (Zhao *et al.*, 2020) investigated extraction of different artificial Ca/Mg-bearing minerals including CaO, MgO, Ca_2SiO_4, $Ca_3MgSi_2O_8$, $Ca_2MgSi_2O_7$, $Ca_2Al_2SiO_7$, and $MgCr_2O_4$ and four different types of leaching agents, HCl, CH_3COOH, NH_4Cl, and CH_3COONH_4 were used. The solubility of these minerals via model simulation was studied and it was found that the solubilities of minerals in HCl and CH_3COOH were higher than those in NH_4Cl and CH_3COONH_4, indicating the mineralogy and properties of minerals influence the leaching process.

Table 2.1 shows the effects of various types and concentrations of acids, bases, and salts on the metal extraction efficiency. The strong acids like HCl, HNO_3, and H_2SO_4 were the most commonly used chemicals to dissolve Mg or Ca from minerals and the efficiency can reach relatively high, up to 100% by adjusting other parameters. On the other hand, utilising bases like NaOH as leaching agent was not widely implemented, but as seen in the research by (Madeddu et al. 2014) (No.24 in Table 2.1), adding NaOH resulted in high extraction efficiency, close to 80%. With the technology developing, the most widely used leaching agents are salts, especially ammonia salts which can be regenerated and reused to reduce the capital cost favoured by the industrial application. Among them, ammonia salts are the best candidate to be recycled (Sun *et al*., 2011; Wang and Maroto-Valer, 2011a). Kodama et al. (Kodama *et al*., 2008) presented an approach of applying NH_4Cl and NH_3 transformation. In this process, NH_4Cl was initially used to extract Ca from the minerals (Eq.(2.3)) and the produced NH_3 reacted with Ca to form precipitates (Eq.(2.4)). As a result, NH_4Cl was regenerated.

$$4\mathrm{NH_4Cl} + 2\mathrm{CaO}\cdot\mathrm{SiO_2} \rightarrow 2\mathrm{CaCl_2} + \mathrm{SiO_2} + 4\mathrm{NH_3} + 2\mathrm{H_2O} \qquad \text{(E2.3)}$$

$$4\mathrm{NH_3} + 2\mathrm{CO_2} + 2\mathrm{CaCl_2} + 4\mathrm{H_2O} \rightarrow 2\mathrm{CaCO_3} + 4\mathrm{NH_4Cl} \qquad \text{(E2.4)}$$

Implementing different leaching agents on the same minerals under same operating parameters could provide information on the role of agents during the extraction process. Teir et al. (Teir *et al.*, 2007c) conducted extraction experiments with various leaching process parameters including acid concentrations. They elucidated that strong acids such as H_2SO_4, HCl and HNO_3 could extract Mg from serpentinite completely within 2 hr with its concentration at 2 M and the extraction rate was in the following order: $HNO_3 < HCl < H_2SO_4$. Other acids, bases, and neutral salt leachates such as HCOOH, $(NH_4)_2SO_4$, NH_4NO_3, NH_3, NaOH, KOH and CH_3COOH were also tested. The results showed that acids have a similar effect on Mg extraction compared to the other three strong acids (HNO_3, HCl and H_2SO_4), but ammonia salts were shown to exhibit very low extraction efficiencies with it being less than 0.5% during 1 hr reaction. In terms of basic solutions, there was no sign indicating Mg extraction even with concentration up to 4 M. Said et al. (Said *et al.*, 2013) compared the Ca extraction efficiencies of aqueous ammonia salts, NH_4NO_3, CH_4COONH_4 and NH_4Cl from steelmaking slags, and the results showed that they have comparable efficiencies. At solid to liquid ratio of 20 $g \cdot L^{-1}$, the extraction efficiency of NH_4Cl was 37-45% with the solvent concentration ranging between 0.5 and 2 M while that of NH_4NO_3 and CH_3COONH_4 were 42-50% and 41-54%, respectively. However, at a lower liquid/solid ratio (5 $g \cdot L^{-1}$), NH_4NO_3 showed the highest efficiency up to 73%, followed by CH_3COONH_4 (72%) and NH_4Cl (58%). He et al. (He *et al.*, 2013) also investigated extraction capabilities of these three ammonia salts with coal fly ash and the highest efficiency was achieved by CH_3COONH_4 at temperatures from 10 to 90 °C and agent concentration up to 3 M. The formation of $Ca(CH_3COO)^+$ complex, which reduces the concentration of Ca, is predicted to have promoted the extraction reaction.

Santos et al. (Santos *et al.*, 2014a) used $MgCl_2$ as a leaching agent to extract several CaO-rich minerals. It was found that the addition of $MgCl_2$ was efficient to extract Ca from CaO at every tested dosage while the performance was not as effective as HCl shown with other feedstock like slags or industrial residues, which required more acidic solvents for extraction due to mineralogy discrepancy of the materials. Particularly, when wollastonite was used as feedstock, extraction efficiency did not improve with the addition $MgCl_2$ because high temperature and pressure are essential for dissolution of wollastonite. They addressed that an effective leaching agent should have high extractant efficiency and less affinity for the alkaline earth metal ions than the carbonate ions. In their later research, they used succinic acid ($HOOC\text{-}(CH_2)_2\text{-}COOH$) as a leaching agent for metal ions extraction of steelmaking blast furnace slag and repeated the experiment with acetic acid (CH_3COOH) as to compare their performances (Santos *et al.*, 2014b). It was found the leaching process of succinic acid surpassed that of acetic acid in both sequential steps by 10%. However, the subsequent carbonation reaction showed that the products from with succinic acid were not calcium carbonates and therefore are not suitable for production of precipitate calcium carbonate (PCC).

The higher extraction efficiency is a significant factor for the leaching process, but selectivity of Ca or Mg dissolution is also a crucial factor for overall improvement. It is known that the stronger the acid is, the higher extraction efficiency is reached. However, the minerals or the industrial wastes do not only contain the desirable cations but also other impurities which can be leached out as well with the function of the strong acid. Therefore, researchers need to compromise between the efficiency and selectivity by adjusting the proper operational conditions.

According to Kodama et al. (Kodama *et al.*, 2008), the selectivity of Ca extraction from silicate waste material with NH_4Cl was 80%, higher than with HCl and CH_3COOH which have higher extraction efficiencies. The selectivity of Ca and Mg were also investigated by Bao et al. (Bao *et al.*, 2010) using steelmaking slag as feedstock and organic solvent tributyl phosphate (TBP) and CH_3COOH solution was applied as leaching agents. They found that the selectivity was strongly influenced by the ratios of TBP to solid and by applying the ratios below 15 mL/g, 100% selectivity could be achieved. Pérez-Moreno et al. (Pérez-Moreno *et al.*, 2015) used NaOH and $NH_3{\cdot}H_2O$ to dissolute red gypsum for carbonation and the results showed that the carbonate conversion for NaOH was 92% which was higher than that of $NH_3{\cdot}H_2O$ (64%).

Solid to liquid ratio, extraction temperature, particle size, and agitation are potential parameters that influence the extraction efficiency (Iizuka *et al.*, 2004; Alexander *et al.*, 2007; Teir *et al.*, 2007c; Jo *et al.*, 2012). Energy requirement and cost of integrated process should also be taken into consideration to figure out the cost- and energy-efficient processes. In most cases, higher dissolution efficiencies can be obtained under lower solid to liquid ratios, small particle size of minerals, and higher extraction temperature. Said et al. (Said *et al.*, 2013) studied the effect of slag size on calcium extraction and they found the extraction efficiency almost doubled, from 30% to 59%, by reducing the slag particle size from 250-500 to 0-250 µm. Higher temperature promoted the metal cations extraction which was observed by (Wang and Maroto-Valer, 2011; Sanna *et al.*, 2014; Arce Ferrufino *et al.*, 2018). The effect of solid to liquid ratio was investigated by (He *et al.*, 2013; Said *et al.*, 2013; Bang *et al.*, 2016) in the extraction process and they all showed lower solid mass in the solution increased the leaching efficiency.

To properly determine the optimal process parameters, the overall cost and energy consumption of the process must be taken into account. The reduction on reaction time can decrease the capital cost (Sanna *et al.*, 2013) by slightly sacrificing the leaching efficiency and it was found that Mg extraction efficiency reached 95% with 3 hr reaction while the efficiency turned to 80% with 1 hr reaction. Also, the energy cost can be reduced by minimising the number of reactors implemented. Besides the experimental investigation, models can also be introduced to simulate the leaching process. For example, Ca leachability from oil shale ash was investigated through modelling and experiments (Velts *et al.*, 2010a; Velts *et al.*, 2010b; Velts *et al.*, 2011). They applied different types of reactors (e.g. batch reactor, packed-bed reactor, multifunctional disintegrator-type reactor) and processes to proceed and optimised the leaching reaction. In general, the high leaching efficiency and selectivity are the key factors to assess the leaching process, but the next stage the carbonation processes should account for the wastewater management and the cost of leaching agents.

2.1.2 Carbonation process

Carbonation process is the subsequent reaction where the extracted alkaline earth metal ions react with CO_2. To adjust the pH value of leachate for the mineralisation reaction, basic substances are needed to buffer the solution (Teir *et al.*, 2009; Wang and Maroto-Valer, 2011; He *et al.*, 2013; Sanna *et al.*, 2013; Bang *et al.*, 2016).

The ‘pH swing’ carbonation process is widely used in indirect two-step mineralisation (Azdarpour *et al.*, 2015). After the dissolution stage, pH of the leachate decreases to a relatively low level which cannot trigger the carbonation reaction and therefore, basic substances are added to elevate the basicity of the solution to neutralise the acidification. The key is to find out the optimal pH for carbonation. Aqueous ammonia solution and sodium hydroxide are the most widely used basic solutions. Park and Fan (Park and Fan, 2004) used NH_4OH solution to increase the pH step by step. They first increased the pH to 8.6 to precipitate iron oxide and they filtered out the precipitate and injected pure CO_2 to the filtrate and then further increased the pH to 9.5 and obtained $MgCO_3 \cdot 3H_2O$ with high purity. In the end, 65% overall magnesium conversion at relatively low temperature and pressure (70 °C and 1 atm) was achieved. Teir et al. (Teir *et al.*, 2007b) (No.9 in Table 2.1) used NaOH to control the pH of carbonation solution. To do so, 50 wt.% NaOH was added in drops to the leachate to reach the optimal pH value of 9. They precipitated hydromagnesite with high purity (99 wt.%), with the highest magnesium conversion of 94% and lowest NaOH mass (0.9 g NaOH/g, precipitate).

Besides the inorganic basic additives elevating the basicity of a solution, organic substances were investigated to increase the pH for carbonation. Steel et al. (Steel *et al.*, 2013) implemented a tertiary amine to buffer the solution to raise the pH to 8 for carbonation. In order to accelerate the carbonation rates and improve the purity of products, a small amount of crystal seeds of $CaCO_3$ (0.05 g in 200 mL solution) was added in the research of Katsuyama et al. (Katsuyama *et al.*, 2005) studied. It was found that taking the advantage of $CaCO_3$ seeds, the purity of carbonates increased from 80 to 98%. Chiang et al. (Chiang *et al.*, 2014) proposed a novel CO_2 sequestration integrated approach by two parallel processes to convert blast furnace slag into two value-added products with zero waste: calcium carbonates and zeolite materials. Acetic acid was used as the leaching agent to limit the dissolution of aluminium which was used to synthesise zeolite, then NaOH and CO_2 were introduced to react with the leachate to form carbonates. In the hydrothermal conversion process, the residue contained silicate and Al_2O_3 were prepared for zeolite materials.

To conclude, the two-step aqueous mineralisation process can leach out desirable metal ions from minerals by applying various agents and CO_2 can be fixed by the subsequent carbonation reaction. However, the application of multiple processes might elevate capital cost and operational cost. Therefore, single-step aqueous carbonation can eliminate this weakness with fewer process steps and shorter reaction time.

2.2 Single-step aqueous carbonation with solid phase

The single step of mineralisation process with gas-solid route was first studied by (Lackner *et al.*, 1995) and further developed by other researchers (Costa *et al.*, 2007; Prigiobbe *et al.*, 2009; Mazzella *et al.*, 2016). Although the process is more mature than the aqueous carbonation with the liquid phase only, high reaction temperature or pressure is required and the massive energy consumption is a barrier to implement it at a commercial-scale. The single-step aqueous carbonation process with solid phase has its fundamental advantages, such as availability of a large amount of feedstock, providing an alternative way to manage the industrial wastes (Bodor *et al.*, 2013), and saving the consumption of acids compared to the two-step carbonation process. The direct aqueous carbonation with solid phase extracts the alkaline earth metal ions and the carbonation process takes place simultaneously with controlled parameters.

The primary advantage of reaction involving water or steam is the mineralisation process can be accelerated in mild conditions compared to the solid-gas process. Ben Ghacham et al. (Ben Ghacham *et al.*, 2015) compared the gas-solid with gas-liquid-solid routes of mineralisation using waste concrete and anorthosite tailings and it was found that the aqueous carbonation performed better than that with dry route. Through aqueous carbonation, 66% CO_2 was removed using waste concrete and 34% CO_2 removed using anorthosite. In the dry carbonation process, the efficiencies did not exceed 15% with both materials. Since 18 vol.% CO_2 of flue gas component was used in this study without any chemical additive, in such short reaction time (15 min), the kinetics of carbonation with the dry route was limited. Also, the differences of two materials were assigned to the different structures leading to different performances of Ca dissolution. This research also provided a cost-effective approach to proceed mineralisation with a very short reaction time and flue gas composition which are favoured by the industrial application. Tamilselvi Dananjayan et al. (Tamilselvi Dananjayan *et al.*, 2016) also studied the direct mineral carbonation with dry and wet conditions with coal fly ash. They found that 50.3 g of CO_2 per kg fly ash was fixed with aqueous carbonation while with a dry route, only 26.3 g of CO_2 per kg fly ash sequestered. Based on these advantages of direct single aqueous mineralisation with the solid phase, the progress of recent technologies is reviewed as below.

2.2.1 Process parameters

Process parameters can influence the carbonation efficiency or morphologies of products. Different feedstocks showed various carbonation performance even at same experimental situations which is mainly due to the mineralogical discrepancy. Recent progress on the aqueous carbonation using different feedstocks is evaluated from the perspective of CO_2 capture capacity or the carbonation conversion efficiency. Georgakopoulos et al. (Georgakopoulos *et al.*, 2016) reviewed multiple parameters that affected the carbonation rate and conversion efficiency of steelmaking slags. In addition to conventional variable parameters, up-to-date process parameters that influence the direct aqueous carbonation reaction with solid phase are summarised, as listed in Table 2.2. The optimal process parameters that contributed in obtaining the highest efficiency in each research are shown.

Given the parameters demonstrated in Table 2.2, the properties of the feedstock, reaction temperature, pressure and CO_2 concentration significantly influence the ultimate efficiency and uptake capacity. Polettini et al. (Polettini *et al.*, 2016) studied a systemic factorial design to figure out the optimal process parameters and each operating condition was designed into three levels, with three various operations, leading to 3^3 factors. With the advantages of these analysis, a more precise model was set up to get an accurate operating parameter. Montes-Hernandez et al. (Montes-Hernandez *et al.*, 2009) stated that the temperature (20-60 °C) and the solid to liquid ratio did not influence the carbonation efficiency significantly. However, in fact, the results listed in Table 2.2 demonstrate that temperature and solid to liquid ratios are important. The effects of CO_2 pressure, temperature, particle size was studied by Zevenhoven et al. (Zevenhoven *et al.*, 2009), and they found that the particle size significantly influenced the conversion of Ca. The efficiency was increased from 40% to over 80% after 3 hr by reducing the particle size from 140 to 17 µm. In terms of temperature, the extraction performance was enhanced by increasing the temperature from 110 to 150 °C and there was no further improvement with a higher temperature.

Researches up to this date were mostly studied with pure CO_2 or with only air or N_2 as a balance gas. Only a few studies used real flue gas or similar component. Reddy et al. (Reddy *et al.*, 2010) studied aqueous carbonation of fly ash with flue gas on a pilot scale. The flue gas was used directly from a real power plant and contained moisture, CO_2, SO_x, Hg, etc. The reaction was conducted with a fluidised bed reactor with pressure of 115 kPa, flue gas flow rate of 300 SCFM, and varying moisture content (2–16%). It was found that the carbonation efficiency was the highest when 16% moisture was applied at 60° C. Mercury was oxidised to ionic form and then reacted with CO_2 to produce $HgCO_3$. Based on their previous research results, it showed that CO_2 concentration decreased from 13% to 9.6% and SO_2 decreased from 107.8 ppmv to 15 ppmv within 2 min (Reddy *et al.*, 2011). This study provided particular data for direct industrial usage of flue gas and fly ash. Also, hazardous components in the flue gas such as SO_2 and Hg were captured during this process. Therefore, there are more factors to consider when using real flue gas as feedstock.

In order to achieve rapid carbonation, several additives and feedstock activation methods are implemented. Various additives such as $NaHCO_3$, NaCl, and Na_2CO_3 have been used to increase the mineralisation reaction rate. Different additives with various concentrations showed diverse performance and the mechanism of the reaction acceleration also varied. Turianicová et al. (Turianicová *et al.*, 2013) compared the reactivity of standard and activated olivine in aqueous carbonation. The selected olivine was mechanically activated through ball milling. It was found that the activated olivine achieved high reactivity due to modified structural and surface properties. Zevenhoven et al. (Zevenhoven *et al.*, 2009) investigated various additives ($NaHCO_3$, NaCl, $NaNO_3$, seawater, sucrose, sorbitol and $Ca(OH)_2$) in an attempt to increase the carbonation or extraction rates. They found that adding nitrous salts like KNO_3 and $NaNO_3$ to calcium silicate mineral, wollastonite, increased Ca solubility by providing high ion activity and ion strength, making them more attractive compared to $NaHCO_3$ and NaCl. When the steelmaking slag was implemented, it was found that sucrose addition promoted the Ca leaching up to 94%. Another additive, such as $Ca(OH)_2$, elevated the pH and promoted carbonation, however, the experimental results showed it did not affect the conversion efficiency due to its inhibiting effect towards Ca leaching (Zevenhoven *et al.*, 2009). Farhang et al. (Farhang *et al.*, 2016) studied the mineralisation process with heat activated serpentine in the aqueous process under high temperature and pressure in the presence of $NaHCO_3$. They found the transformation of magnesium carbonates polymorphs is depended on temperature. Hydromagnesite converted to magnesite under 185 °C in a few minutes while reacting it for longer time (> 90 min) did not exhibit the same transformation at 120 °C.

Table 2.2 Summary of up-to-date direct aqueous mineralisation processes with solid phase under various process parameters.

No.	Metal	Source	Composi-tion	Particle size	Solid/liquid	Addictive	CO_2	Pressure	Temp	Agitation	Time	Efficiency/ Amount	Reference
1	Mg	Serpentine	MgO 45.7%	<37 µm	15% 167g/930g	0.64 M $NaHCO_3$ + 1.0 M NaCl	100%	185 atm	155°C	2,000 rpm	30 min	78%	(O'Connor *et al.*, 2000)
2	Ca Mg	Wollastonite talc	44 wt.% 35 wt.%	440 µm 310 µm	4 mg/mL 4 mg/mL		100%	202 kPa	Room temp	NA	22 days	140kg CO_2/ton wollastonite	(Wu *et al.*, 2001)
3	Ca	Coal fly ash	CaO 4.1%	40 µm	100 $g\cdot L^{-1}$	water	100%	20 bars	30 °C	450 rpm	18 hrs	26kg CO_2/ton fly ash 82%	(Montes-Hernandez *et al.*, 2009)
4	Ca	Wollastonite	CaO 32.4%	15.6 µm	13 kg/kg	0.02% NaCl	100%	4 MPa	150 °C	stir	2h	90%	(Zevenhoven *et al.*, 2009)
5	Ca	Stainless steel slags	CaO 50%	< 878.7 µm	62.5 $g\cdot L^{-1}$		99.5%	9 bars	90 °C	1000 rpm	60 min	60% 0.312g/g, slag	(Santos *et al.*, 2013b)
6	Ca	Fly ash	CaO 40%	0.9 mm	300 g/1.5L		100%	6 MPa	40 °C	NA	1.5 hrs	7.66 kg CO_2/ton fly ash	(Ukwattage *et al.*, 2013)
7	Mg	Rocks tailings	Mg 282 mg/g	< 75 µm	15 wt% pulp density		18.2 vol%	10.5 bars	22 ± 3 °C	stir	30 min	0.28g CO_2/kg residues	(Pasquier *et al.*, 2014)
8	Ca	Waste concrete	CaO 26.8%	< 21 µm	15 wt% pulp density		18.2%	10.3 bars	room	600 rpm	15 min	0.045g CO_2/g, sample	(Ben Ghacham *et al.*, 2015)
9	Mg	Olivine	Mg 65.2%	< 10 µm		0.5M NaHCO3+0.75M NaCl	100%	73 bars	190 °C	NA	4 hrs	100%	(Eikeland *et al.*, 2015)
10	Ca	Ca-bearing mineral	CaO 34.55%	65 – 75 µm	2 g/60 mL		100%	1MPa	75 °C	700 rpm	1h	45%	(Sheng *et al.*, 2015)
11	Ca	Coal fly ash	CaO 24.8%	< 1.18 mm	300 g/90 g		100%	3 MPa	40 °C	60 rpm	10 hrs	27.05 kg CO_2/ton, ash	(Ukwattage *et al.*, 2015)
12	Ca	Basic oxygen furnace slag	Ca 31%	63 -100 µm	1 kg/5 L		40%	5 bars	50 °C	Magnetic stir	4 hrs	53.6% CO_2 uptake	(Polettini *et al.*, 2016)
13	Ca	Coal fly ash (CFA)	CaO 6.74%	<1 mm	1/15		99.99 %	4 bars	30 °C	900 rpm	2 hrs	67.87% 50.3 g/kg ash	(Tamilselvi Dananjayan *et al.*, 2016)
14	Ca	Fly ash	CaO 3.35 wt%		1 g/15 mL		>99%	Atmospheric	30 °C	Stir	Until pH to 8.3	83.5% 32g CO_2/kg ash	(Ebrahimi *et al.*, 2017)

Table 2.2 Summary of up-to-date direct aqueous mineralisation processes with solid phase under various process parameters.

No.	Metal	Source	Composi-tion	Particle size	Solid/liquid	Addictive	CO_2	Pressure	Temp	Agitation	Time	Efficiency/ Amount	Reference
15	Ca	Fly ash	CaO 16.41%		100 $g \cdot L^{-1}$	0.5M Na_2CO_3	15% CO_2	20 bars initial	275 °C	500 rpm	2 hrs	79%, 0.102kg CO_2/kg ash	(Ji *et al.*, 2017)
16	Ca	Cement kiln dust	CaO 47%		100 g/500 g		100%	3 bars	25 °C	Stir	1h	9.45%	(Medas *et al.*, 2017)
17	Ca	Electric arc furnace slag	CaO 56.4%	< 15 µm	1 g/20 mL		100%	Ambient	55 °C	700 rpm rotating	40 min	86.3%, 0.38t CO_2/ton slag	(Pan *et al.*, 2017)
18	Ca	Phospho-gypsum	CaO 32%	< 110 µm	2 g/40 mL		Pure	1 bars	room	stir	90 min	80%	(Romero-Hermida *et al.*, 2017)
19	Ca	Steel slag	CaO 47%	25 – 37 µm	10 g/300 mL		Pure	1 atm	90 °C	700 rpm	240 hrs	70%, 24g of CO_2/100g slag	(Yadav and Mehra, 2017)
20	Ca	Fly ash	CaO 28.42%	125 µm	20% H_2O(g)		15% CO_2	Ambient	600 °C	NA	60 min	28.74%, 60 g CO_2/kg ash	(Liu *et al.*, 2018)
21	Ca	Fly ash	CaO 32.4%		200 $g \cdot L^{-1}$		Pure	20 bars	40 °C	450 rpm	2 hrs	103 g of CO_2/kg ash	(Ji *et al.*, 2019)

2.2.2 Process intensification, reactor design and catalysts

Given the relatively slow rate of mineralisation, several process intensification concepts applicable to mineral carbonation were studied. Santos and Van Gerven (Santos and Van Gerven, 2011) proposed the process intensification routes for the mineralisation and the strategies were classified into four parts: structure, energy, synergy, and time. SMaRT-Pro2 platform based in KU Leuven provided researches on slags carbonation and ultrasound was applied to accelerate the process. Santos et al. (Santos *et al.*, 2013b) studied stainless steel slags carbonation with two different approaches: unpressurized thin-film carbonation and pressurized slurry carbonation and investigated the optimal parameters of the process. Two different slags were selected, Argon Oxygen Decarburization (AOD) and Continuous Casting (CC) slags, and were compared as a carbonation feedstock. Thin-film carbonation was conducted with an incubator with 25 wt.% moisture content and 20% of CO_2, at 30 °C. The maximum conversion efficiencies with 144 hr reaction of AOD and CC slags were 24% and 37%, respectively. The conversion efficiency was significantly improved with slurry carbonation due to mechanical stirring which enhanced the mass transfer. The effect of temperature, CO_2 partial pressure, reaction time and solid to liquid ratio were investigate and the results showed that carbonation conversions of CC slags were higher than those of AOD slags, in almost all conditions tested in this research. The optimal operational parameters were listed in the No.5 row in Table 2.2. (Santos *et al.*, 2013a) investigated application of ultrasound as a tool to intensify mineral carbonation processes. Ultrasound was produced by an ultrasound horn into a slurry where the reaction occurred. It was found that ultrasound effectively enhanced the carbonation process by removing the passivating layers formed by the precipitated calcium carbonates and depleted silica layers. It also broke down mineral particles into smaller pieces, exposing the unreacted core for further carbonation. The carbonation efficiencies increased from 30% to 49% and 61% to 73%, for AOD and CC slag carbonation, respectively. Araizi et al. (Araizi *et al.*, 2016) also used ultrasound technique to enhance the carbonation process with landfills as feedstock. They found that the reaction efficiency can reach four times higher by adjusting high water to solid ratios with ultrasound.

The reactor design is a promising technique that can intensify and accelerate the mineralisation with certain modifications. van Noort et al. (van Noort *et al.*, 2013) studied mineral dissolution and carbonation reaction with different reactor systems:

autoclave and cold-seal batch reactor for peridotite rock. In the autoclave system, the dissolution rate of peridotite decreased slightly due to the fluid penetration across the fracture, increasing the exposed area for dissolution. In the closed batch reactor, the carbonation conversion was high under high temperature and pressure to further confirm the microstructure of boundary function. This mechanism can contribute in *in situ* geological applications as the experiments simulated 3 km deep underground (393 K, 120 °C). Sequestration of 1 MT CO_2 is predicted to be possible with a fracture spacing of 60-70 cm in a 300 by 300 by 100 m^3 volume of peridotite. Ji et al. (Ji *et al.*, 2017) studied direct aqueous carbonation in an open semi-batch reaction system and closed autoclave reactor. The results showed that the open system reached the equilibrium within 90 min and the maximum calcium conversion efficiency was 35%. The efficiency did not increase with higher temperature due to poor dissolution of CO_2. However, increased temperatures effectively promoted the efficiency in the autoclave reactor with better ions diffusion. The elevated initial pressure of CO_2 was beneficial for carbonation as well. Velts et al. (Velts *et al.*, 2013) implemented and summarised various routes of mineralisation with oil shale ash to produce precipitated calcium carbonates by sequestrating CO_2. They demonstrated a rotary drum filter to achieve a continuous mineralisation process. This research conducted in a pilot plant confirmed the feasibility of the process, process development and mechanism. The authors introduced a continuous model to produce calcium carbonates with a novel separation system to filter out the solid residues. The high basicity of ash liquid was introduced into the mineralisation process after filtering out the solid ash by rotary drum filter. After CO_2 injection to the solution, the precipitates were separated with another rotary drum filter and neutral outlet solution was cycled (Velts *et al*., 2013). The carbonates yield and purity were high when the pH of the carbonated solution was over 9. With oil shale ashes containing up to 30% Ca/Mg silicates, up to 290 kg of CO_2 per ton of ash is possible to be sequestered. Besides the conventional reactors, novel reactors and techniques were also designed and implemented to provide an alternative option for mineralisation process intensification (Velts *et al.*, 2014). Santos et al. (Santos *et al.*, 2013c) developed a gravity pressure vessel called 'CO_2 Energy Reactor' to proceed the slurry carbonation. The primary advantages of this vertical plug flow reactor were that it was autothermic and allowed for hydrostatic pressurisation and underground set-up which lowers the risk of having safety issues. Pan et al. (Pan *et al.*, 2013) proposed an integrated process of indirect carbonation with a rotating packed bed. The use of this reactor can enhance the gas-liquid mass transfer by the high speed of the centrifuge. Alkaline wastes were implemented as the feedstock to react with 30% CO_2 for carbonation. With this set up, CO_2 removal efficiency reached up to 99% within 1 min under ambient temperature and pressure and also the pH dropped from 13 to neutral, indicating the carbonation reaction proceeded. A flow-through reactor was studied for CO_2 mineralisation with concrete and the resulting carbonation efficiency was compared to that of conventional pressurised reactor (Kashef-Haghighi and Ghoshal, 2010). The results indicated that the CO_2 residence time was an important factor, as longer CO_2 contact time led to higher CO_2 uptake efficiency. With this 1D flow-through reactor, the average of 18% carbonation efficiency was achieved which is comparable with the previous studies on the acceleration of concrete curing. Moreover, the energy consumption of this process was much lower than the pressurised reactor.

The weathering process in nature is relatively slow and therefore, acceleration of the process had been the focus in mineral carbonation studies. In most cases, the limiting rate of carbonation is CO_2 hydration in the dissolution step (Eq.(2.5)). To address the challenge of limited rate of the mineralisation, catalysts are required to accelerate the process. Carbonic anhydrase (CA) was initially introduced to accelerate this step which is regarded as a suitable catalyst to accelerate CO_2 mineralisation reactions via the transformation of $CO_{2(aq)}$ into bicarbonate (HCO_3^-) (Khalifah, 1971; Silverman and Lindskog, 1988; Dreybrodt *et al.*, 1997).). The core active site in CA is zinc, which is located in the centre of metalloenzyme, and the general mechanism is illustrated in Eq.(2.6). In the presence of CA, CO_2 hydration equilibrium can be rapidly reached, with zinc-bound OH^- reacting with dissolved CO_2 to form bicarbonate (Silverman and Lindskog, 1988). Di Lorenzo et al. (Di Lorenzo *et al.*, 2018)) also studied using CA as a catalyst attempting to accelerate the mineralisation with Ca and Mg silicates and the results showed the CA has very limited effect on the acceleration because the rate-determining step was the dissolution of wollastonite with passive layers, not CO_2 hydration. Therefore, authors explored a new type of catalyst Zr-based MOFs (metal-organic frameworks) material aiming to speed up the dissolution step. It was found UiO -66 MOF could increase the wollostonite dissolution because the functional groups on this catalyst interact with the surface of minerals directly which promotes the hydrolysis of Si-O-Si bonds and consequently increases the dissolution rate.

$$\mathrm{CO_2} + \mathrm{H_2O} \rightarrow \mathrm{HCO_3^-} + \mathrm{H^+} \qquad \text{(E2.5)}$$

$$\mathrm{EZnOH^- + CO_2(aq) \leftrightarrow EZn(OH^-)CO_2(aq) \leftrightarrow EZnHCO_3^- \leftrightarrow EZnH_2O(aq) + HCO_3^-} \quad \text{(E2.6)}$$

Besides the conventional catalyst CA, nickel nanoparticles (NiNPs) have been demonstrated to proceed catalytic activity by accelerating CO_2 hydration reaction as a first wholly inorganic heterogeneous catalyst (Bhaduri and Šiller, 2013; Šiller and Bhaduri, 2013; Bhaduri *et al.*, 2015). NiNPs are photo-catalytically active towards hydration reaction of CO_2 and although they can be extracted magnetically from solutions, they have also been immobilised on the silica support for the better processing (Han *et al.*, 2015). Bodor et al. A study from (Bodor *et al.*, 2014) showed that NiNPs are marginally beneficial for capturing CO_2 from the gas phase when using CaO and steelmaking slags as the source of Ca^{2+}. For example, when solid to liquid ratio is low (7.19 g/1000 mL) it was shown that improvement in the efficiency of mineralisation was significant in the presence of nickel particles (from 56.1% without NiNPs to 98.7% with NiNPs in 15 min) shown in Figure 2.3. With high solid to liquid ratio, the benefit of NiNPs was reduced. One possibility was because of the Ca^{2+} dissolution, rather than the CO_2 hydration, is the rate limiting step. Another possibility is that when solid to liquid ratio is high, some of the NiNPs surfaces gets poisoned by a rapid covering with the formed calcium carbonate, which stops NiNPs to act as catalysts for hydration reaction.

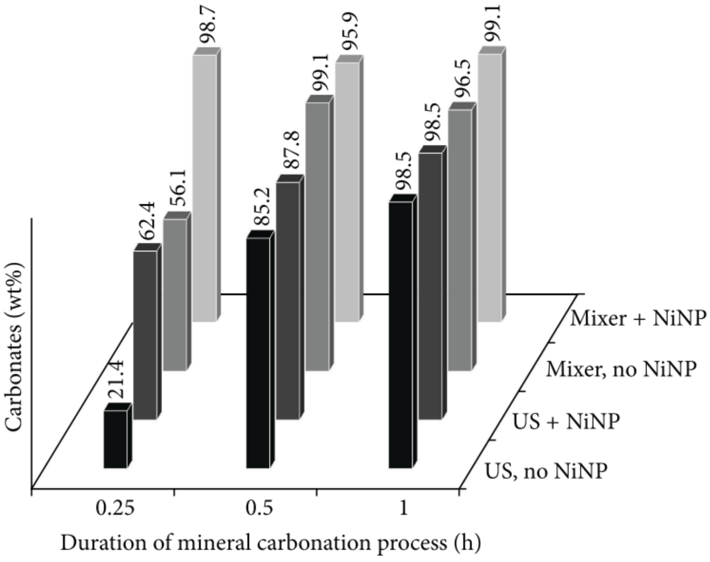

Figure 2.3 Carbonate content after MgO mineral carbonation, using S/L ratio of 7.19 g/1000 mL, determined by QXRD (Bodor et al., 2014).

2.2.3 Product utilisation and scale up

The products of the carbonation process are widely applied in industries including construction, paper making, agricultural and pharmaceutical fields. The carbonated minerals have the potential to benefit the economy and waste management. A high stability of the product is also advantageous in cases in which carbonation occurs underground. Morgan et al. (Morgan *et al.*, 2015) studied thermal stability of nesquehonite ($MgCO_3 \cdot 3H_2O$) in the presence of water stream and CO_2 in the open and closed system *in situ* by X-ray diffraction, thermogravimetric analysis and Fourier-transform infrared spectroscopy. It was found that the stability of nesquehonite was enhanced in the presence of water vapour. The data of water vapour sorption displayed that a thin, hydrous film formed on the surface of nesquehonite inhibits the water molecule leaving the material to delay dehydration process. The stability test of nesquehonite after long-term exposure to CO_2 was required to check the morphology and crystal transformation. It was found the stability was improved only at 50 °C in the closed system due to the low temperature and the help of water vapour existing in the system. The results also showed that the stability of nesquehonite in the closed system was better than in an open system because of the water vapour releasing from the surface of materials which can prevent samples undertake further decomposition.

Santos et al. (Santos *et al.*, 2014a) used $MgCl_2$ to extract Ca from AOD slags and the remaining $MgCl_2$ in the aqueous phase affected the carbonation efficiency and polymorphs of products. The presence of $MgCl_2$ decreased the rate of carbonation by reducing the CO_2 degassing while the carbonation was enhanced when the ultrasound was used in addition to $MgCl_2$ by increasing CO_2 uptake from 0.19 to 0.27g CO_2/g, slag. Also, $MgCl_2$ was incorporated in the forming of carbonates and aragonite was favoured to be formed compared to calcite without $MgCl_2$.

The largest commercial products of the construction material are concrete, aggregates and bricks. The carbonated minerals can replace the binding materials of the construction industry. Salman et al. (Salman *et al.*, 2014) compared two different carbonation processes with Argon Oxygen Decarburisation (AOD) stainless steel slag to produce construction materials: carbonation chamber (ambient pressure) and carbonation reactor (high pressure). In the ambient pressure chamber, the carbonation reaction rate was slower than in the pressurised reactor (a few hours), but the reaction lasted longer time to capture more CO_2 enhancing the mechanical strength of final products. Although higher pressure could obtain higher CO_2 uptake and shorter residence time, the compressive strength of products was decreased because small parts of collapsed or rapidly formed carbonates covered the surface of materials, which limited exposing the unreacted parts of minerals for further carbonation. The highest mechanical strength was achieved after 15 hr in 8 MPa up to 60 MPa which met the criteria for construction materials. If this material is to be applied, more CO_2 could be fixed due to the continuous carbonation reaction. Aggregates are another potential construction material which can be made by carbonates from CO_2 mineralisation with solid wastes (Gunning *et al*., 2009). Bodor et al. (Bodor *et al.*, 2016) tested and compared the mechanical strength of aggregates with cement mortars in the presence/absence of carbonates. The results demonstrated that the particle size played a significant effect on the compressive strength and the value could be higher than the reference mortar when the slags with particles size less than 0.5 mm are used. For instance, by replacing 50% of natural sand in the cement mortar with the carbonated slags that had particle size smaller than 0.5 mm, compressive strength was increased to 27.3 N/mm^2. The mixture composition of carbonated materials significantly influenced the property of the products as well. Ebrahimi et al. (Ebrahimi *et al.*, 2017) prepared Portland cement with carbonated fly ash (CFA) as the cement paste blends and its mechanical strength was tested under ambient conditions. It was found that the compressive strength of 10% CFA component showed poorer performance compared to that of the original pure cement while the compressive strength was significantly reduced with 30% CFA. Pan et al. (Pan *et al.*, 2017) also studied the preparation of cement mortar with carbonated steel slag and evaluated the compressive strength and autoclave soundness. The results showed that mechanical property was enhanced by the adding carbonated slags into the cement because of the mineral composition modified by the interaction between tricalcium aluminate (cement) and calcium carbonate (carbonated slag), which resulted in the formation of calcium carbonaluminate hydrate. The carbonated slags showed better compressive strength than the fresh slags due to its high surface area. The result of autoclave expansion test showed that all cement mortar could meet the ASTM (American Society for Testing and Materials) standard (< 0.8%), with the maximal expansion being 0.076%.

The stability of carbonated products is a significant factor due to its claim of permanent storage of CO_2. Harrison et al. (Harrison *et al.*, 2019) addressed that hydrated magnesium carbonates have the potential for CO_2 storage, and they investigated the optimal process parameters and stability of formed carbonates. The solubility of different morphologies of magnesium carbonates was evaluated and the phase transformation between 5 to 35 °C was studied. The transformation between nesquehonite ($MgCO_3 \cdot 3H_2O$) and dypingite ($Mg_5(CO_3)_4(OH)_2 \cdot (5 \text{ or } 8)H_2O$) depended on temperature variation and it occurred when the temperature was over 25 °C. At higher temperatures, the transformation occurred earlier, while at 5 °C, no transformation happened. This research facilitated the knowledge of stability of magnesium carbonates under ambient conditions.

Although the concept of single-step aqueous carbonation is simple and there have been a number of lab-scale experiments, only a few mature technologies have been implemented on large scale. Due to the massive amount of emitted CO_2 by the anthropogenic activities every year, the technologies cannot remain at lab-scale and the scalability is an essential aspect of mineralisation. Beyond parameter optimisation for the scale-up, the energy consumption of the processes should be also be assessed. Han et al. (Han *et al.*, 2017) studied the aqueous carbonation of bauxite residue in both lab-scale and pilot-scale. With respect to batch reaction, both short term (48 hr) and long term (55 days) experiments were investigated. In their research, the process rate of carbonation was limited by the concentration of Ca, therefore, additional Ca source like desulfurization gypsum and $CaCl_2$ were selected to add in the residue. The results showed that both of these two Ca sources could accelerate the mineralisation by lowering the pH faster. It was estimated that the maximum carbonation capacity would be 0.083 g CO_2/g bauxite residue. In reality, this value will be reduced as it is uncertain if field treatment will allow for thorough mixing, resulting in slower reaction rate. Kemache et al. (Kemache *et al.*, 2017) studied a pilot-scale of aqueous carbonation based on their previous lab-scale research (Ben Ghacham *et al.*, 2015). The test was carried out in an 18.7 L reactor and flue gas with 12-20% CO_2 was used. The maximum carbonation efficiency of 250 kg CO_2/t of residue was obtained under 8 atm in pilot-scale while it was lower than that in lab-scale due to lack of heat activation for a high rate of metal cations leaching. However, this research elucidated the possibility of large-scale aqueous carbonation, even though modification was required. Pasquier et al. (Pasquier *et al.*, 2014) studied not only process development to investigate the optimal parameters but also evaluated the energy demand of the integrated mineralisation process. The ground samples were activated by heat first to accelerate the dissolution process, then transferred to react with CO_2 to form carbonates. The most energy consuming process was the particle size reduction and heat activation because the mineralisation process was conducted under mild conditions. If the capacity of 200 tonne minerals was to be used at an industrial case, energy of 585.55 kWh/t would be required for activation process and 28.44 kWh/t for grinding. However, the energy requirement could be offset by the recovery the heat from flue gas and commercialising the products, such as $MgCO_3$. The integrated process and cost provide the references for future industrial application and it could be optimised and simulated for better development. Carbon8 Systems which is at the highest TRL level of carbonation process company in the UK converts CO_2 to building blocks and reduces the reaction time to 15-20 min (Carbon8, 2020) and they used air pollution control residues (APCr) as the feedstock to react with CO_2 and water to produce aggregates which can be used in construction blocks (Gunning and Hills, 2015). Also, other industrial wastes (Gunning *et al*., 2009) such as cement, paper, metallurgical were implemented to conduct accelerated carbonation. The reactivity with CO_2 relies on the calcium concentration and mineralogy of the wastes. They provided an alternative way to treat hazardous thermal wastes accompanied with carbon capture and production utilisation (Gunning *et al*., 2011).

2.3. Single-step aqueous carbonation with liquid phase only

Aqueous mineral carbonation with existing earth metal cations in single liquid phase was first investigated by Dunsmore (Dunsmore, 1992) inspired by nature from Earth's biogeochemistry. From this idea, the method to transform brine to carbonates was proposed. According to what had been discussed in previous sections, the kinetic rates of the process are mostly limited by the mineral dissolution and these barriers could be removed by the use of intensive energy, concentrated acid, and high temperature or pressure. Also, the process can be broken down into several steps, typically, leaching and carbonation processes are separated, to enhance each step. Even though the sources of mineralisation with solid phase are naturally existing, the grinding process of these minerals is an energy-intensive step because the size of particles showed a significant impact on the carbonation efficiency. Hence, the energetic and economic evaluation are also required to be traded off. A potentially cost-effective route to mineral carbonation is to utilise aqueous solutions that already contain alkaline earth metal ions which can directly react with CO_2. This alternative approach overcomes the limitations caused by carbonation rate and extraction cost by eliminating the procedure of metal ions dissolution/leaching. Table 2.3 presents the current state-of-the-art of CO_2 mineralisation with a single step in which active ions are provided by the liquid phase. In the following context, various principles, process parameters, and process intensification of direct aqueous carbonation with only liquid phase are reviewed. Among three types of aqueous mineralisation processes mentioned before, this is the most recently developed. Therefore, this section bridges the gaps that existed in the previous sections because reactions occur in the liquid phase only carbonation are under mild conditions.

Table 2.3 Summary of up-to-date direct aqueous mineralisation processes under various process parameters.

No	Metal source	Basic agent	Process	CO_2	Temp	Pressure	Agitation	Time	Efficiency	Reference
1	Brine Ca/Mg	KOH	Autoclave Process (B)	Pure	155 °C	6.87 MPa	800 rpm	1 h	Ca 25% Mg 17%	(Soong *et al.*, 2004)
2	Brine, Ca^{2+} 25000 ppm	0.24 M KOH	Process (B)	99.99 %	150 °C	600 psi	400 rpm	6 hr	11%	(Druckenmiller and Maroto-Valer, 2005)
3	Brine	10 wt.% fly ash plus 0.08 M NaOH	Autoclave Process (B)	100%	20 °C	1.36 MPa	NA		29.63 $g\cdot L^{-1}$	(Soong *et al.*, 2006)
4	$MgCl_2$	25% Aqueous ammonia	Batch Process (B)	Pure	20 °C	Ambient	NA		95%	(Ferrini *et al.*, 2009)
5	Artificial brine Ca	Buffer solution $NaCl/NaHCO_3$	Process (B)	Pure	100 °C	1500 psi	NA	24 hr	90%	(Liu and Maroto-Valer, 2010)
6	$MgCl_2$ Simulate industrial waste	25% Aqueous ammonia	Batch Process (B)	Pure	20 °C	Ambient	NA		>95%,	(Mignardi *et al.*, 2011)
7	Mg^{2+} 1350 ppm Ca^{2+} 420 ppm	NH_3/NH_4Cl buffer solution	Open batch Process (B)	15 vol. %	25 °C	0.15 atm	Magnetic	100 min	>90%	(Wang *et al.*, 2011)
8	$MgCl_2$, 13-33 $mL\cdot min^{-1}$	NH_3, 800 $mL\cdot min^{-1}$	MSMPR crystallizer	Pure	353.2 K	Ambient	300 rpm	77 min	116.9 kg/m^3	(Wang and Li, 2012)
9	$CaCl_2$	50 mL Tris – HCl buffer, Bovine carbonic anhydrase	Process (A)	pure	25 °C	Ambient	200 rpm	2 hr	78%	(Chu *et al.*, 2013)
10	$Ca(OOCCH_2CH_3)_2$	10 wt. %, amine 2-amino-2-methyl-1-propanol (AMP)	Process (A)	30% CO_2	25 °C	Ambient	100 rpm	60 min	75%	(Vinoba *et al.*, 2013)
11	Ca 800ppm Mg 1200 ppm	Tributylamine, and n-butyl alcohol	Process (B)	Pure	25 °C	Ambient	500 rpm	pH to 8.3	90% Ca, Mg did not react	(Wang *et al.*, 2013)
12	$CaSO_4\cdot 2H_2O$	6 M NaOH	Process (B)	99.9%	Ambient	Ambient	Agitation	Till pH to 7	100%	(Bang *et al.*, 2014)
13	$MgCl_2$ 0.25 mol/L	25% NH_4OH, pH > 10	Process (B)	99.5%	20 °C	Ambient	150 rpm	30 min	99.9%	(Hao and Al-Tabbaa, 2014)

Table 2.3 Summary of up-to-date direct aqueous mineralisation processes under various process parameters.

No	Metal source	Basic agent	Process	CO_2	Temp	Pressure	Agitation	Time	Efficiency	Reference
14	Ca^{2+}, 3.4 g·L^{-1}	Tributylamine plus diluent	Process (B)	Pure	24 °C	Ambient	500 rpm	Till pH to 8.1	93%	(Liu *et al.*, 2014)
15	$Ca(OH)_2$ slurry 20 wt.%	30% MEA	MEA based CO_2 solution add to $Ca(OH)_2$ slurry	15%	ambient	Ambient	Magnetic	24 hr		(Park *et al.*, 2014)
16	$MgCl_2$, 2 mol·L^{-1}	N235, 2.04mol/L, Volume ratio to aqueous at 2	Ethanol as dilute, volume ratio to N235 at 0.5	Pure	298.15 K	Ambient	300 rpm	120 min	72%	(Chen *et al.*, 2016)
17	Ca^{2+}, 714 ppm Mg^{2+}, 2226 ppm	1 M NaOH, 36 mL	Inject CO_2 intermittently	Pure	Ambient	Ambient	NA	Till pH to 8	Ca: 99% Mg: 86%	(Bang *et al.*, 2017)
18	$CaCl_2$	0.83 mol/L Na_2CO_3	Process (A)	15%	295 K	Ambient		60 min	80%	(Barzagli *et al.*, 2017)
19	Mg/Li ratio brine, $MgCl_2$	Trioctylamine and isoamyl alcohol	Process (B)	Pure	25 °C	Ambient	300 rpm	120 min	67.41%	(Chen *et al.*, 2017)
20	Mg^{2+} 1.24 g·L^{-1}; Ca^{2+} 0.41 g·L^{-1}	$Mg(OH)_2$	Process (B)	10%	Ambient	Ambient	Stir	35 min	70%	(Zhao *et al.*, 2017)
21	$MgCl_2$	Na_2CO_3 obtained from NaOH with CO_2	Mg/Na_2CO_3 = 1.2 molar ratio		30 °C		1000 rpm	30 min	75%	(Baena-Moreno *et al.*, 2019)
22	$CaCl_2$, 800 ppm	1 M NaOH	Tubular reactor	Pure	50 °C	<150 kPa	NA	<5 min	100%	(Zhang *et al.*, 2019)
23	$CaCl_2$, 800 ppm	0.1% MEA	Tubular reactor	Pure	50 °C	<150 kPa	NA	<5 min	100%	(Zhang *et al.*, 2020)

N235: which is a mixture of tertiary amines R_3N (R: ~C8−C10)

Process (A, B, C): illustrated in Section 4.2.

2.3.1 Source of feedstock

Compared to the source of aqueous carbonation with solid phase, which are mainly derived from natural silicates or industrial wastes, the feedstock of single-step aqueous phase only carbonation also comes from nature and wastewater (i.e. brine). Brine is a concentrated saline solution that contains very high concentrations of Ca and Mg and its dominant component is NaCl. Therefore, it is regarded as an attractive source of alkaline earth metals for the mineralisation process. Brines can be obtained from saline aquifers from nature or the wastewater of desalination plants. In addition to mineralization processes utilising brine as the feedstock, other liquid sources that contain Ca and Mg were investigated, as listed in Table 2.3. Vinoba et al. (Vinoba *et al.*, 2013) compared different liquid sources of Ca to proceed mineralisation: $CaCl_2$ (CAC), $Ca(OOCCH_3)_2$ (CAA), and $Ca(OOCCH_2CH_3)_2$ (CAP). The pK_a values of Cl^-, CH_3COO^- and $C_2H_5COO^-$ are 6.3, 4.76 and 4.87, respectively. The results showed CAP got the highest carbonation yield while CAC was the poorest due to the acidity of chloride accumulation. Chen et al. (Chen *et al.*, 2017) tested the brine from lithium ion batteries industry which contains high Mg content. Mg was extracted from the brine by mineralisation process which could separate Mg from Li to get a lower ratio of Mg/Li, which was favoured. Various additives to precipitate Mg were compared and triethylamine was the most effective which could convert 97.4% Mg to carbonates, turning the Mg/Li ratio from 20 to 0.54.

The pH of desalination brines is around 8 which is not high enough to neutralise the acidification of CO_2 during the mineralisation process. Therefore, it is essential to add extra basic substances to increase the pH value for the precipitation. Herein, a couple of basic additive options are presented. Industrial solid wastes containing a high concentration of CaO are potential basic substances to level up pH by forming $Ca(OH)_2$ in the solution. However, the increased value of pH is not sufficient to balance the CO_2 dissolution due to the limited amount of active component. Soong et al. (Soong *et al.*, 2006) studied CO_2 sequestration with brine and fly ashes. The results showed that the pH could be elevated from 4 to 9.2 after stirring for 24 hr for 60 °C, but this value of pH was not high enough to obtain precipitates. Additional alkaline source, NaOH, was added which can increase the pH over 11. Chu et al. (Chu *et al.*, 2013) applied 2-amino 2-(hydroxymethyl)-1,3-propanediol (Tris base) as the absorbent to get CO_2-rich solution. Tris-HCl buffer solution was prepared subsequently to maintain pH of mineralisation process where the CO_2-rich solution and Ca^{2+} source was mixed. Vinoba et al. (Vinoba *et al.*, 2013) used sterically hindered amine 2-amino-2-methyl-1-propanol (AMP) to absorb CO_2 first and then buffered the carbonation solution to get carbonates. Park et al. (Park *et al.*, 2017) compared the effect of adding 30 wt.% NaOH and KOH with 30 wt.% MEA (monoethanolamine) as an alkaline solution to conduct mineralisation of CaO. The first step was to get CO_2-saturated solution with NaOH, KOH, or MEA by bubbling 15% CO_2 and it was mixed with 20 wt.% CaO solution to form carbonates. The CO_2 absorption efficiency was higher with 30 wt.% NaOH than that with 30 wt.% MEA due to NaOH directly reacting with CO_2. Zhao et al. (Zhao *et al.*, 2017) tested $Mg(OH)_2$ as basic substances which was the by-product from Solvay process, providing hydroxyl groups to facilitate carbonation of brines. Ca carbonated forming $CaCO_3$, then concentration of Mg increased due to dissolution in low pH value. Ji et al. (Ji *et al.*, 2018a) tested five different amines to proceed mineralisation. They prepared CO_2 saturated solution with amines which then was transferred to another reactor for carbonation with CaO solution. The amines after reaction was regenerated for the next cycle reaction. MEA, diethanolamine (DEA), piperazine (PZ), N-methyldiethanolamine (MDEA) and 2-amino-2-methy-1-propanol (AMP) were tested and PZ showed the greatest CO_2 absorption and regeneration efficiency up to 91%. Moreover, PZ showed stable CO_2 loading and regeneration performance during five cycles of experiments.

The concentration of the basic solution can influence the carbonation efficiency. Kang et al. (Kang *et al.*, 2016) studied 5, 10 and 30 wt.% aqueous MEA solution to fix Ca from industrial wastewater. The CO_2 saturated solution was prepared with CO_2 and aqueous MEA solution. It was then mixed with Ca-rich solution to form calcium carbonates. The results showed that 25, 37 and 42% mol basis of absorbed CO_2 converted to $CaCO_3$ in total by adding 5, 10 and 30 wt.% MEA, respectively. However, 0.55, 0.27 and 0.16 mol of CO_2 were fixed per mol amine for these three amines concentrations, respectively. The feedstock of metal ions in the process is derived from multiple sources which is mostly treated as wastes, but the basic substances are not easily accessible. Therefore, recycling and reusing the base substances is an attractive approach and will be illustrated in Chapter 6 of this thesis.

2.3.2 Process development

In the aqueous phase carbonation, pH value becomes a significant parameter monitoring the process as it is an indicator of the amount of dissolved CO_2. The pH value of precipitation point varies depending on the components of the solution, reaction temperature, CO_2 flow rate, mixture and so on. Mignardi et al. (Mignardi *et al.*, 2011) studied the pH ranges that enable precipitation reaction under different $MgCl_2$ concentration. The results demonstrated that such pH range was 7.8-8.2 for 7 $g \cdot L^{-1}$ $MgCl_2$ at 20 °C while it turned to 8.0-8.9 for 16 and 32 $g \cdot L^{-1}$. In the high concentration of the salts, CO_2 solubility was decreased due to high ion activity. It was found the high salinity of solution did not influence the carbonation efficiency in long-term reaction even though the initial efficiency varied because the reaction was completed within 1 hr with 7 $g \cdot L^{-1}$ $MgCl_2$ and 14 and 30 days for 16 and 32 $g \cdot L^{-1}$, respectively. The reaction could be continuous in the solution of highly concentrated salts.

CO_2 mineralisation through direct aqueous carbonation can be categorized into three main processes as demonstrated in Figure 2.4: (A) alkaline earth metal ions solution mixed with CO_2-rich solution which is prepared by CO_2 and absorbent prior to the mineralisation, named 'Process (A)'; (B) all-in-one direct carbonation which is the simplest process as all reactants are mixed simultaneously called 'Process (B)', and (C) multi-ions aqueous carbonation which requires multiple steps employed in practice to achieve high purity target product, named 'Process (C)'. In the following context, these three processes are reviewed and discussed. The majority processes listed in Table 2.3 belong to 'Process (B)' if there is no particular illustration. Park et al. (Park *et al.*, 2014) carried out 'Process (A)' using MEA to capture CO_2 obtaining CO_2-rich solution. When it was added to $Ca(OH)_2$ slurry, carbamate, bicarbonate, and carbonate were produced. The absorbed CO_2 solution can rapidly react with $Ca(OH)_2$ to form precipitates.

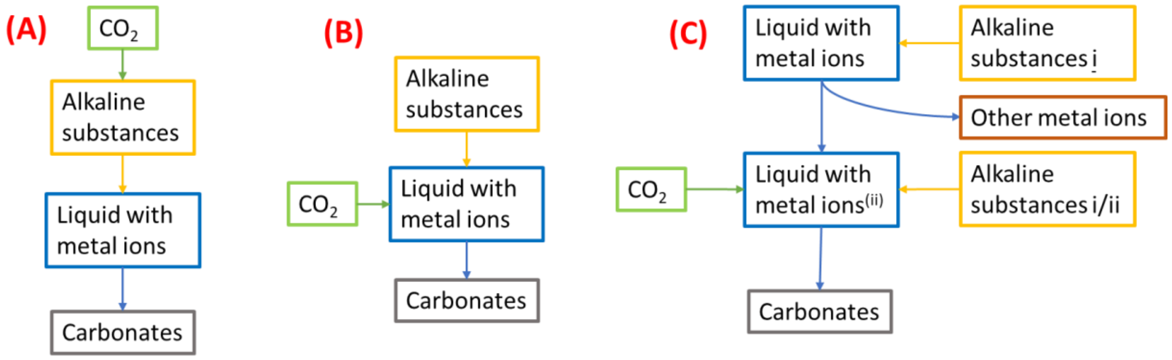

Figure 2.4 Diagram of three categories of direct aqueous carbonation with liquid phase-only.

Bang et al. (Bang *et al.*, 2019) used desalination brines containing Ca and Mg for CO_2 mineralisation with NaOH solution. The process was improved by separating Ca and Mg by separate steps, as Process (C). Firstly, brines were mixed with NaOH to increase pH value to 10.5 and Mg was precipitated as $Mg(OH)_2$ which was filtered out; then the further NaOH was added to the filtrate to increase pH to 12 and obtain $Ca(OH)_2$. CO_2 was bubbled into $Ca(OH)_2$ slurry until pH reduced to 8 to form calcium carbonates and the precipitates were filtered out. The second filtrate was mixed with $Mg(OH)_2$ following by CO_2 bubbles to precipitate magnesium carbonates. Separated sequential steps allowed for increase in CO_2 utilisation efficiency from 12% in previous research (Bang *et al.*, 2017) to 57%, and individually, 99% Ca was fixed and 69% for Mg. The most promising result was that the volume of NaOH solution used decreased by 76% compared to previous research (Bang *et al.*, 2017). Wang et al. (Wang *et al.*, 2015) proposed carbonation of Ca and Mg with insoluble diisobutylamine: Ca^{2+}/Mg^{2+} solution and insoluble amine plus diluent (n-octanol) were mixed first with agitation and then CO_2 was bubbled into the mixture solution to start carbonation process. The experiments were conducted under 28 °C with agitation and bubbled 300 $mL \cdot min^{-1}$ CO_2 till the pH reduced to 8.6. The results showed that Ca was fixed very rapidly within 4 min of 98% conversion efficiency and Mg concentration dropped 91% within 5 min. The different precipitation rates between Ca and Mg are due to their solubility constants. Zhao et al. (Zhao *et al.*, 2019) studied mineralisation with $CaCl_2$ and $MgCl_2$ by using magnesium oxide as alkaline substances to proceed two-step process in which Ca was first carbonated then Mg ions. CO_2 was bubbled into the Ca and Mg containing solution to obtain $CaCO_3$. The filtrate contained a high concentration of Mg and was further mixed with NaOH to precipitate magnesium carbonates. The results showed that Ca conversion efficiency reached 92% under the molar ratio of MgO to Ca at 4:1 at 80 °C. Further addition of NaOH increased OH^- concentration of the solution. When the molar ratio of OH^- and Mg^{2+} reached 1.7, around 75% Mg precipitated as $MgCO_3{\cdot}3H_2O$. Ma and Yoon (Ma and Yoon, 2013) performed a two-step carbonation process to convert $MgCl_2$ to nesquehonite in the liquid phase by degassing the CO_2 from the extra dissolved CO_2. The first step was to inject CO_2 into $MgCl_2$ solution until pH decreased to 5 and then added NaOH solution into the CO_2-rich solution to level up pH to the desired value. Once equilibrium was reached, the solution was agitated to degas the CO_2 to conduct precipitation reaction by increasing the pH due to decomposition of the excess HCO_3^-. It was found the desired pH value was around 6.8 and Mg conversion efficiency over 80% was reached. The final precipitation pH value reached 9 and this process was enhanced by increasing the agitation speed and reaction temperature. The selection of what process to be applied should depend on the property of feedstock and the rate of reaction and comparison between different processes can provide a comprehensive understanding of high conversion efficiency achievement.

2.3.3 Reactor and catalyst – Process Intensification

Mineral carbonation is a cost- and energy-efficient process in the aqueous phase and the principal advantages of this process are thermodynamically favoured and relatively less energy demanding due to mild process parameters implementation. The main challenges are to accelerate the reaction and further minimise energy consumption. In recent years, many novel process intensifications and catalysts were investigated to promote aqueous mineralisation performance. Different advanced approaches those researchers attempted to accelerate the process by novel reactor design or process development and catalysts addition are presented here.

Besides inorganic catalyst NiNPs mentioned in section 2.2, organic catalyst such as carbonic anhydrase is also widely developed for carbonation by other researchers. Chu et al. (Chu *et al.*, 2013) used bovine carbonic anhydrase (BCA) as a catalyst to accelerate the mineralisation process. Tris-HCl was regarded as the buffer solution and the results showed that the amount of precipitates did not increase by the use of BCA in a 120 min reaction, but the rate of mineralisation was enhanced in the initial 30 min. Moreover, the addition of BCA did not change the morphology of carbonates. In the presence of BCA, the crystal nucleation rate was promoted by enhancing Ca bonding with CO_3^{2-}. Vinoba et al. (Vinoba *et al.*, 2011) used SBA-15 as a carrier to immobilise carbonic anhydrase (CA) to test catalytic performance which could help with catalyst separation. The CO_2 hydration and $CaCO_3$ precipitation were studied with this catalyst in which BCA was immobilised by the amine-functionalised SBA-15. The results showed that there was insignificant difference between the free CA and immobilised CA on the biocatalytic activity, however, the thermal stability, cyclic run performance, and storage stability were all enhanced with the support of SBA-15. In terms of CO_2 sequestration reaction, the quantities of $CaCO_3$ obtained from free CA and immobilised CA were almost the same. Later, Vinoba et al. (Vinoba *et al.*, 2013) studied the absorption rate of CO_2 by amine 2-amino-2-methyl-1-propanol (AMP) with stop-flow spectrophotometric method with and without carbonic anhydrase (CA). The catalytic performance was monitored by the colour change of indicator and it was found the CO_2 absorption rate was slow in the absence of CA. The catalytic efficiency was 2.61×10^6 /M·s in the presence of CA while the number turned to 1.35×10^2 /M·s without CA. Furthermore, CA was used to accelerate brucite mineral carbonation by rapidly converting CO_2 to HCO_3^- (Power *et al.*, 2016). The brucite slurry was mixed with BCA and reacted with 10% CO_2 under three different flow rates. It was found there was no catalytic effect when the flow rate was in the very high or very low ranges because at extremely low flow rates, the BCA efficiency decreased substantially and at extremely high flow rates, the reaction was already enhanced by sufficient mass transfer. Therefore, only the moderate flow rate performed desired catalytic effect and brucite carbonation was accelerated by 240%. The products obtained from this process were nesquehonite, which limited collection of hydrated CO_2 and therefore, the overall carbonation rates were influenced.

Moreover, advanced techniques could be used to enhance the mineralisation reaction. Bang et al. (Bang *et al.*, 2014) used microbubble generator to produce CO_2 bubbles into the solution. The $CaCO_3$ precipitation was increased by 39% compared to that of the conventional CO_2 injection method which indicated that the carbonation reaction between $Ca(OH)_2$ and CO_2 was enhanced by the mass transfer. Sun et al. (Sun *et al.*, 2015) studied the mineralisation of NH_3-CO_2-$MgCl_2$ in aqueous phase with a rotating packed bed. The operational parameters, such as rotation speed and flow rates of liquid and gas, influenced carbonation efficiency and morphologies of products.

Barzagli et al. (Barzagli *et al.*, 2017) invented a semi-continuous approach to capture CO_2 from the flue gas with Na_2CO_3 as the absorbent. The diagram is illustrated in Figure 2.5 (left). Two absorbers are connected and CO_2 feeds into absorber (1) where 0.83 mol/L Na_2CO_3 is placed in to capture CO_2 to achieve CO_2-saturated solution following these steps: i) The outlet gas of absorber (1) continuously feeds into absorber (2) for further capture and the effluent gas from absorber (2) was analysed by gas chromatography (GC). The experiments are terminated when the CO_2 absorption is below 65% of the initial value; ii) Absorber (1) is transferred to react with $CaCl_2$ to form precipitates and at the same time another fresh absorber (1) was replaced into the system. iii) The gas direction was reversed from 'red' line to 'blue' line, to saturate the absorber (2) first until the CO_2 absorption decreases to 65%. As shown in Figure 2.5 (right), less time is required to reach 65% due to the existing CO_2-rich solution. The total reaction time was 440 min; iv) The whole cycle was repeated several rounds. ^{13}C NMR (nuclear magnetic resonance) spectra were used to qualify the amount of bicarbonate and carbonate ions. The results indicated that an average 80% absorption efficiency could be achieved by adding Na_2CO_3 in the absorber and high quality of $CaCO_3$ could be formed. To summarise, process intensification is an inevitable step to optimise and achieve compact, energy efficient and environmentally friendly mineral carbonation process. It is important to understand the advantages and limitations of each step of the integrated process and intensify each step according to the overall needs and demands.

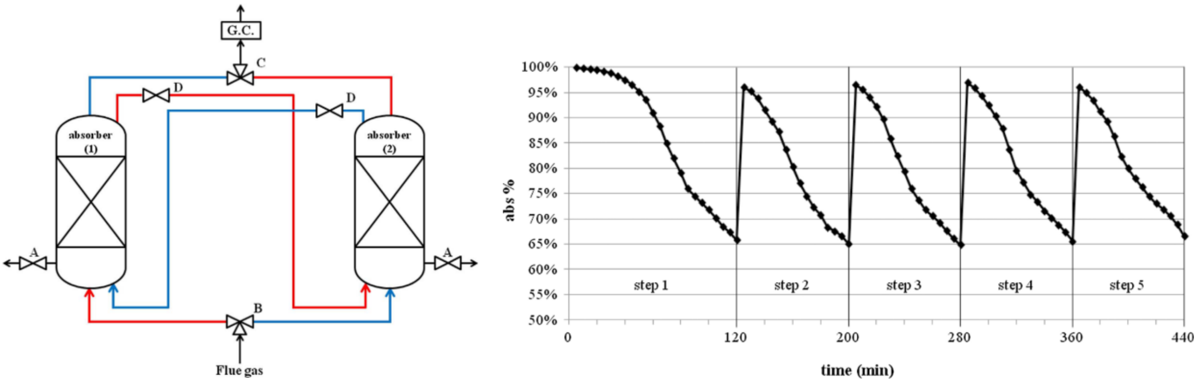

Figure 2.5 Simplified flow diagram of the two absorbers connected to each other for CO_2 absorption (left) (Barzagli et al., 2017); Variation of absorption efficiency during the successive five steps of CO_2 capture (right) (Barzagli et al., 2017).

Furthermore, the novel continuous reactor can be developed eliminating the use of high temperature and pressure and agitation and these parts are illustrated in Chapter 3 and the results are shown in Chapter 4 and Chapter 5 of this thesis.

2.3.4 Basic substances recovery and cyclic carbonation process

Given the fact that supplying basic substances occupies the significant portion of the high cost of the integrated mineralisation process, reusing the chemicals is a trend for recent research as it makes the process more cost and energy competitive as well. Sanz-Perez et al. (Sanz-Perez *et al.*, 2016) reviewed direct air capture (DAC) which is a technology to capture CO_2 from air directly, using liquid or solid sorbents. Direct air CO_2 capture contactor was developed in 2012 by Carbon Engineering with NaOH or KOH as aqueous sorbents for continuous capture process (Holmes and Keith, 2012). CO_2-rich sorbents can be easily regenerated in the next stage with $Ca(OH)_2$ to produce $CaCO_3$ (Keith *et al.*, 2018), as shown in Figure 2.6. There are two loops in the process. One is the CO_2 capture loop with a basic solution and the other is CO_2 regeneration loop which involves calcination of the precipitated $CaCO_3$ to release pure CO_2 and CaO for the cyclic usage.

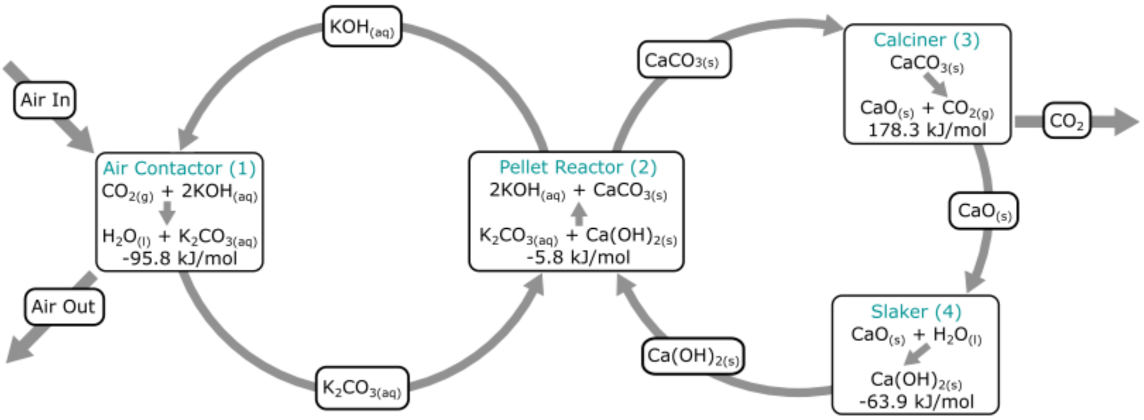

Figure 2.6 Process illustration of direct air capture (Keith et al., 2018).

Wang et al. (Wang *et al.*, 2013) regenerated the insoluble amines tributylamine with ammonia. The mixed solution was separated into two phases rapidly once agitation stopped. HCl was extracted from tributylamine hydrochloride and the regeneration efficiency increased up to 95% with the on-going reaction time. Then they tested diisobutylamine plus n-octanol system to proceed mineralisation and subsequent regeneration of insoluble amines (Wang *et al.*, 2015). 0.1 M NaOH solution was used to extract H^+ from $NH(C_4H_9)_2{\cdot}H^+$ and converted back to $NH(C_4H_9)_2$ for next cycle usage. Compared to the former process (Wang *et al*. 2013b), this system displayed better regeneration performance and Ca fixation rate slightly decreased from 92% to 89% after 7 rounds running. Park et al. (Park *et al.*, 2014) studied mineralisation with amine-based CO_2 solution reacting with $Ca(OH)_2$ slurry and the process consisted of two processes: preparation of CO_2-rich solution with 5 wt.% or 30 wt.% MEA and addition of carbonic solution with $Ca(OH)_2$. The reacted MEA was regenerated via heating to 70 °C to proceed desorption to release CO_2. The CO_2 loading capacity of 5 wt.% was lower than that of 30 wt.% MEA and the absorption in the second cycle with 5 wt.% MEA was slightly lower than that in the first cycle but 30 wt.% MEA exhibited a better performance. One approach to capture and regenerate CO_2 was investigated by Li et al. (Li *et al.*, 2017) and Figure 2.7(left) illustrates the process. In the left column reactor (green), an organic alkali 1-(2-hydroxyethyl) piperazine (HEP) was contained as the agent to capture CO_2 and the right column reactor (red) contained a mixture of K_2CO_3 and $KHCO_3$, which was used as CO_2 stripper. The absorbed CO_2 by amines was transferred to K_2CO_3 to proceed $KHCO_3$ precipitation and by this reaction, fresh K_2CO_3 was regenerated by heat treatment of $KHCO_3$ while pure CO_2 was released. It was found the energy use was reduced by 24% from the stripping process without lowering the absorption efficiency compared to the conventional stripping process.

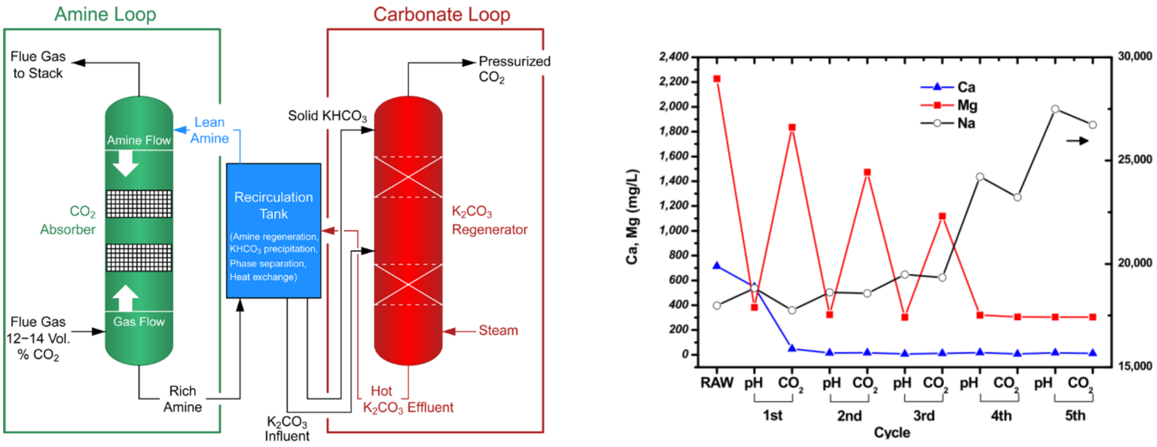

Figure 2.7 Process configuration of the dual alkali solvent system (left) (Li et al., 2017); Changes in the concentrations of Mg, Ca, and Na during the reaction (right) (Bang et al., 2017).

Bang et al. (Bang *et al.*, 2017) investigated a process to precipitate Ca and Mg from RO seawater desalination. Adding NaOH solution to increase the initial pH from 8.2 to 10.5, Ca and Mg were converted to $Ca(OH)_2$ and $Mg(OH)_2$ and CO_2 was injected intermittently into the solution until pH reached 8 for 5 cycles. According to the results, shown in Figure 2.7(right), Ca was first fixed to $CaCO_3$ after the first cycle, which remained constant in the consecutive cycles and then it was collected by filtration. While Mg concentration displayed an oscillating trend, precipitates were collected after each cycle until no more precipitates formed. The concentration of Na increased due to the addition of NaOH. The precipitates were characterised with XRD and they were determined to be calcite, hydromagnesite, and halite (NaCl). According to these results and the initial concentrations of brine, 42,662 tons of CO_2 could be captured after four cycles and achieved 17,770 tons of $CaCO_3$ and 66,816 tons of $MgCO_3$ by 10 Mtons of brines. Kang et al. (Kang *et al.*, 2018) studied the capacity of $CaCl_2$ and $Ca(OH)_2$ to regenerate AMP used as a CO_2 sorbent. The pH of amines after CO_2 absorption was decreased due to the formation of protonated amine. It was found that the addition of $CaCl_2$ cannot elevate the pH to release the H^+ from the protonated amine, therefore, $CaCl_2$ did not demonstrate amine regeneration. However, the addition of $Ca(OH)_2$ not only showed the regeneration function but also captured CO_2 even better than AMP. However, the absorption rate of $Ca(OH)_2$ was slower than that of AMP. Ji et al. (Ji *et al.*, 2018b) investigated the amines regeneration approach by fly ash to form carbonates. It was found that hydroxyl groups released from CaO neutralised hydrogen ions attached to amines to regenerate them back to fresh amines. In this study, 40% regeneration efficiency was achieved for MEA after 15 min of regeneration carbonation, which was similar to the thermal regeneration method. This research team proceeded the following researches with AMP (Yu *et al.*, 2019a) and diamine (Yu *et al.*, 2019b) as CO_2 absorbent to fix CO_2 and regenerated them using fly ash, CaO. The results showed the feasibility of this regeneration process with various amines. As mentioned earlier, recycling the materials within the process is an energy effective way for sustainable and economic development and is favoured by industrial field and this is studied in Chapter 6 of this thesis.

2.3.5 Carbonation product evaluation

The morphology of products highly depends on the operational parameters of the process. The important parameters include the reaction time, temperature, pressure, concentration of alkaline earth metal, and pH. Hänchen et al. (Hänchen *et al.*, 2008) studied how the temperature and pressure influenced the polymorphs of magnesium carbonates in the system of $MgCl_2$-Na_2CO_3-CO_2-H_2O. It was found that nesquehonite ($MgCO_3{\cdot}3H_2O$) precipitated at 25 °C and 1 bar P_{CO2} and hydromagnesite ($(MgCO_3)_4{\cdot}Mg(OH)_2{\cdot}4H_2O$) precipitated at 120 °C and 3 bar $P_{CO2,}$ which transformed to magnesite within 15 hr. Magnesite itself precipitated directly at 120 °C and 100 bar P_{CO2}. Mignardi et al. (Mignardi *et al.*, 2011) studied different concentrations of $MgCl_2$ (7 to 32 $g{\cdot}L^{-1}$) reacting with CO_2 to produce magnesium carbonates. It was found the nesquehonite precipitated in 60 min with 7 $g{\cdot}L^{-1}$ of Mg. With 16 $g{\cdot}L^{-1}$ of Mg, amorphous carbonates precipitated initially (for 2 days) followed by nesquehonite precipitation. With 32 $g{\cdot}L^{-1}$ of Mg, initial precipitation of chlorartinite ($Mg_2(CO_3)Cl(OH){\cdot}3H_2O$) was observed followed by nesquehonite with small amount of lansfordite. By lowering the concentration from 32 to 30 $g{\cdot}L^{-1}$, initial formation of chlorartinite could be avoided. The amorphous carbonates could also be avoided by adjusting the stoichiometry-the molar ratio of Mg to CO_2 at 1. These results elucidated that the morphologies of carbonates were determined depending on various experimental conditions and they transformed during long-term reactions. Wang and Li (Wang and Li, 2012) studied the crystallization kinetics of hydromagnesite with MSMPR (mixed-suspension-mixed-product removal) crystallization method. The temperature affected the morphological transformation and it was found that transformation of nesquehonite to hydromagnesite occurred at 318.2 K while the crystal size increased with the increasing temperature. The nucleation of hydromagnesite was the particle size-limiting process as the negative growth rate order appeared. High supersaturation led to faster nucleation growth and agglomeration. The key factors to influence the reaction rate were the flux of NH_3 and the residence time based on the kinetics correlation.

The effects of reaction temperature, pH, and the ratio between Ca, carbonic acid ions, and other metal ions on the formation of different morphologies of $CaCO_3$ were studied by Chu et al. (Chu *et al.*, 2013). They found vaterite was favoured at the lower mole ratio of Ca^{2+} and CO_3^{2-} (< 1.5) and it shifted to calcite with the increasing ratio. Vaterite polymorphic phase was the main phase at a lower temperature (15 °C) and all three crystalline polymorphs were observed at a temperature ranging from 45 to 60 °C, as higher temperature facilitates calcite. With the addition of Mg (< 10 ppm), more aragonite formed as the calcite and vaterite formation decreased. However, when the Mg concentration was increased to 20 ppm, more amorphous $CaCO_3$ and vaterite formed. The source of Ca^{2+} can also influence the $CaCO_3$ polymorphs under the same experimental conditions. Vinoba et al. (Vinoba *et al.*, 2013) investigated three Ca^{2+} sources: $CaCl_2$ (CAC), $Ca(OOCCH_3)_2$ (CAA), and $Ca(OOCCH_2CH_3)_2$ (CAP). Calcite was the only polymorph observed in CAC while the other two exhibited the mixture of calcite and vaterite. CAP produced the maximum yield of calcium carbonation (75%). Chuajiw et al. (Chuajiw *et al.*, 2014) studied how the organic additive influenced the polymorphs of $CaCO_3$, which was formed by the reaction between CO_2 and $Ca(OH)_2$, and these organic substances included amines, diamines and amino acids. It was observed that only calcite precipitated in the absence of organic additive, while vaterite, aragonite and amorphous $CaCO_3$ precipitated in the presence of the additive. This could be explained by the length of alkyl chain and the van der Waals force between the precipitates and the additive and also the polar interaction from the hydrophilic groups which can transform the polymorphs (Chuajiw *et al.*, 2014).

Zhu et al. (Zhu *et al.*, 2017) studied the $MgCl_2$-NH_3-NH_4Cl system for CO_2 mineralisation with a wetted wall column reactor. It was found that the diffusion of the reactants in the liquid film was the rate-limiting step based on the kinetics study. The results showed that a higher temperature, initial pH and NH_3 concentration result in higher CO_2 absorption. Addition of NH_4Cl changes the polymorphs of the products, and the results showed that only nesquehonite formed when the concentration of NH_4Cl was lower than 2 $mol \cdot L^{-1}$. Otherwise, roguinite was formed. Additionally, nesquehonite and roguinite converted to more basic minerals of magnesium carbonates by washing with hot water over 50 °C. An Aberdeen research team led by Professor Glasser studied the process of CO_2 mineralisation with magnesium to form nesquehonite-based construction materials (Glasser *et al.*, 2016). They separated the process into two steps: the first step was to produce bi/carbonate solution via the reaction of CO_2 and NaOH; the second step was to mix the CO_2-rich solution with $MgCl_2$ to form magnesium carbonates. The precipitated nesquehonite was shaped into cubes and its compressive strength was tested. The yields of recovered Mg were around 75–80%. The compressive strength (8 MPa) of the precipitates indicated its potential as construction materials. Later, they used this process to produce cement under ambient pressure and low temperature (25-65 °C) (Morrison *et al.*, 2016). The cubic nesquehonite product contained 32 wt.% CO_2 as a potential CO_2 sink and the products were non-flammable nor toxic with low cost for the application (Glasser et al., 2016).

De Vito et al. (De Vito *et al.*, 2012) attempted to scale up aqueous carbonation to produce nesquehonite. Their previous studies confirmed the feasibility of process with various concentration of $MgCl_2$ (Mignardi *et al.*, 2011). 9 L reactor with constant mechanic agitation was applied in this study. For the reaction, aqueous ammonia was injected into $MgCl_2 \cdot 6H_2O$ solution at a flow rate of 2 $mL \cdot s^{-1}$ and 130 $mL \cdot min^{-1}$ CO_2 was bubbled for 25 min to reach final pH (5.2 – 5.7). The carbonation reaction was occurred when the pH was adjusted to 8-8.9 by adding ammonia solution. The results showed that 80% CO_2 was fixed as nesquehonite.

Different operating parameters can result in various morphological particle size of solid carbonates and this can be confirmed in Chapter 4, Chapter 5 and Chapter 6. Moreover, the precipitated carbonates can be used in desired field. Also, products obtained from carbonation process require governmental support and legislation regulation to commercialise them and make them competitive to the conventional production process. As a prerequisite, the quality of the products must meet certain criteria and avoid net CO_2 emissions in the integrated process.

Conclusions

Aqueous CO_2 mineralisation process has attracted more and more interest as a significant approach to mitigate the large amount of emitted CO_2 from power plants and other industries. This chapter outlined the most recent progress in the three main classifications of aqueous mineralisation. Mineralisation in the aqueous phase showed its advantages in the process parameters as it allows to reduce the use of extreme conditions, when compared to mineralisation processes that involve solid phase. The aqueous phase mineralisation has shown to have promising advantages such as its ability to accelerate the process and feasibility to be implemented in large-scale. Although parts of the processes are still in their infant phase, the follow-up research is taking place aiming to scale up. Up to this date, there is no single-step aqueous carbonation process with liquid only that is mature enough to be developed into commercial-scale. The feasibility of the process has been proven and the energy penalties of the process could be optimised to remove the barriers for scale-up. This provides an opportunity for researchers to proceed further research to develop the process into a commercial-scale. As studies continue, more reliable energetic analysis, economic evaluation and life cycle assessment will be obtained and contribute the whole picture of the mineralisation process. Furthermore, consistent interest in the topic of aqueous mineralisation will lead to defining the most promising mineralisation process to utilise CO_2.

In the following methodology chapter, the prepared materials, analytical methods and a summary of the applied analytical instruments and techniques are presented, coupled with the designed reactor and process to address the technical problems of carbonation mentioned above.

References

Alexander, G., Maroto-Valer, M. M. and Gafarova-Aksoy, P. (2007) 'Evaluation of reaction variables in the dissolution of serpentine for mineral carbonation', *Fuel*, 86(1-2), pp. 273-281.

Araizi, P.K., Hills, C.D., Maries, A., Gunning, P.J. and Wray, D.S. (2016) 'Enhancement of accelerated carbonation of alkaline waste residues by ultrasound', *Waste Management*, 50, pp. 121-129.

Arce Ferrufino, G.L.A., Okamoto, S., Dos Santos, J.C., de Carvalho, J.A., Avila, I., Romero Luna, C.M. and Gomes Soares Neto, T. (2018) 'CO_2 sequestration by pH-swing mineral carbonation based on HCl/NH_4OH system using iron-rich lizardite 1T', *Journal of CO_2 Utilization*, 24, pp. 164-173.

Azdarpour, A., Asadullah, M., Mohammadian, E., Hamidi, H., Junin, R. and Karaei, M.A. (2015) 'A review on carbon dioxide mineral carbonation through pH-swing process', *Chemical Engineering Journal*, 279, pp. 615-630.

Baena-Moreno, F.M., Rodríguez-Galán, M., Vega, F., Reina, T.R., Vilches, L.F. and Navarrete, B. (2019) 'Converting CO_2 from biogas and $MgCl_2$ residues into valuable magnesium carbonate: A novel strategy for renewable energy production', *Energy*, 180, pp. 457-464.

Bang, J.-H., Chae, S.C., Lee, S.-W., Kim, J.-W., Song, K., Kim, J. and Kim, W. (2019) 'Sequential carbonate mineralization of desalination brine for CO_2 emission reduction', *Journal of CO_2 Utilization*, 33, pp. 427-433.

Bang, J.-H., Kim, W., Song, K.S., Jeon, C.W., Chae, S.C., Cho, H.-J., Jang, Y.N. and Park, S.-J. (2014) 'Effect of experimental parameters on the carbonate mineralization with $CaSO_4{\cdot}2H_2O$ using CO_2 microbubbles', *Chemical Engineering Journal*, 244, pp. 282-287.

Bang, J.-H., Lee, S.-W., Jeon, C., Park, S., Song, K., Jo, W. and Chae, S. (2016) 'Leaching of Metal Ions from Blast Furnace Slag by Using Aqua Regia for CO_2 Mineralization', *Energies*, 9(12), p. 996.

Bang, J.-H., Yoo, Y., Lee, S.-W., Song, K. and Chae, S. (2017) 'CO_2 Mineralization Using Brine Discharged from a Seawater Desalination Plant', *Minerals*, 7(11), p. 207.

Bao, W., Li, H. and Zhang, Y. (2010) 'Selective leaching of steelmaking slag for indirect CO_2 mineral sequestration', *Industrial & Engineering Chemistry Research*, 49(5), pp. 2055-2063.

Barnes, V.E. and Cunningham, W. (1950) *Utilization of Texas serpentine*. Bureau of Economic Geology: The University of Texas.

Barzagli, F., Giorgi, C., Mani, F. and Peruzzini, M. (2017) 'CO_2 capture by aqueous Na_2CO_3 integrated with high-quality $CaCO_3$ formation and pure CO_2 release at room conditions', *Journal of CO_2 Utilization*, 22, pp. 346-354.

Ben Ghacham, A., Cecchi, E., Pasquier, L.C., Blais, J.F. and Mercier, G. (2015) 'CO_2 sequestration using waste concrete and anorthosite tailings by direct mineral carbonation in gas-solid-liquid and gas-solid routes', *Journal of Environmental Management*, 163, pp. 70-7.

Bhaduri, G.A., Alamiry, M.A.H. and Šiller, L. (2015) 'Nickel Nanoparticles for Enhancing Carbon Capture', *Journal of Nanomaterials*, 2015, pp. 1-13.

Bhaduri, G.A. and Šiller, L. (2013) 'Nickel nanoparticles catalyse reversible hydration of carbon dioxide for mineralization carbon capture and storage', *Catalysis Science & Technology*, 3(5), pp. 1234-1239.

Bide, T.P., Styles, M.T. and Naden, J. (2014) 'An assessment of global resources of rocks as suitable raw materials for carbon capture and storage by mineralisation', *Applied Earth Science*, 123(3), pp. 179-195.

Bodor, M., Santos, R., Gerven, T. and Vlad, M. (2013) 'Recent developments and perspectives on the treatment of industrial wastes by mineral carbonation - a review', *Open Engineering*, 3(4), pp. 566-584.

Bodor, M., Santos, R.M., Chiang, Y.W., Vlad, M. and Van Gerven, T. (2014) 'Impacts of nickel nanoparticles on mineral carbonation', *Scientific World Journal*, 2014, p. 921974.

Bodor, M., Santos, R.M., Cristea, G., Salman, M., Cizer, Ö., Iacobescu, R.I., Chiang, Y.W., van Balen, K., Vlad, M. and van Gerven, T. (2016) 'Laboratory investigation of carbonated BOF slag used as partial replacement of natural aggregate in cement mortars', *Cement and Concrete Composites*, 65, pp. 55-66.

Carbon8 Systems (2020). Available at: http://c8s.co.uk/ (Accessed: 20 Apri 2020).

Chen, G., Song, X., Dong, C., Sun, S., Sun, Z. and Yu, J. (2016) 'Mineralizing CO_2 as $MgCO_3 \cdot 3H_2O$ Using Abandoned $MgCl_2$ Based on a Coupled Reaction-Extraction-Alcohol Precipitation Process', *Energy & Fuels*, 30(9), pp. 7551-7559.

Chen, P., Tang, S., Yue, H., Liu, C., Li, C. and Liang, B. (2017) 'Lithium Enrichment of High Mg/Li Ratio Brine by Precipitation of Magnesium via Combined CO_2 Mineralization and Solvent Extraction', *Industrial & Engineering Chemistry Research*, 56(19), pp. 5668-5678.

Chiang, Y.W., Santos, R.M., Elsen, J., Meesschaert, B., Martens, J.A. and Van Gerven, T. (2014) 'Towards zero-waste mineral carbon sequestration via two-way valorization of ironmaking slag', *Chemical Engineering Journal*, 249, pp. 260-269.

Chu, D.H., Vinoba, M., Bhagiyalakshmi, M., Hyun, B., II, Nam, S.C., Yoon, Y., Kim, S.H. and Jeong, S.K. (2013) 'CO_2 mineralization into different polymorphs of $CaCO_3$ using an aqueous-CO_2 system', *RSC Advances*, 3(44), pp. 21722–21729.

Chuajiw, W., Takatori, K., Igarashi, T., Hara, H. and Fukushima, Y. (2014) 'The influence of aliphatic amines, diamines, and amino acids on the polymorph of calcium carbonate precipitated by the introduction of carbon dioxide gas into calcium hydroxide aqueous suspensions', *Journal of Crystal Growth*, 386, pp. 119-127.

Costa, G., Baciocchi, R., Polettini, A., Pomi, R., Hills, C.D. and Carey, P.J. (2007) 'Current status and perspectives of accelerated carbonation processes on municipal waste combustion residues', *Environmental Monitoring and Assessment*, 135(1-3), pp. 55-75.

De Vito, C., Ferrini, V., Mignardi, S., Cagnetti, M. and Leccese, F. (2012) ‘Ex situ CO_2 mineralization via nesquehonite: a first attempt for an industrial application’, *11th International Conference on Environment and Electrical Engineering*. Venice, Italy. IEEE.

Di Lorenzo, F., Ruiz-Agudo, C., Ibañez-Velasco, A., Gil-San Millán, R., Navarro, J., Ruiz-Agudo, E. and Rodriguez-Navarro, C. (2018) 'The Carbonation of Wollastonite: A Model Reaction to Test Natural and Biomimetic Catalysts for Enhanced CO_2 Sequestration', *Minerals*, 8(5), p. 209.

Dreybrodt, W., Eisenlohr, L., Madry, B. and Ringer, S. (1997) 'Precipitation kinetics of calcite in the system $CaCO_3$ - H_2O - CO_2: The conversion to CO_2 by the slow process $H^+ + HCO_3^- \rightarrow CO_2 + H_2O$ as a rate limiting step', *Geochimica et Cosmochimica Acta*, 61(18), pp. 3897-3904.

Druckenmiller, M.L. and Maroto-Valer, M.M. (2005) 'Carbon sequestration using brine of adjusted pH to form mineral carbonates', *Fuel Processing Technology*, 86(14-15), pp. 1599-1614.

Dunsmore, H. (1992) 'A geological perspective on global warming and the possibility of carbon dioxide removal as calcium carbonate mineral', *Energy Conversion and Management*, 33(5-8), pp. 565-572.

Dutrizac, J., Chen, T. and White, C. (2000) 'Fundamentals of serpentine leaching in hydrochloric acid media', *Magnesium Technology 2000*, pp. 40-51.

Ebrahimi, A., Saffari, M., Milani, D., Montoya, A., Valix, M. and Abbas, A. (2017) 'Sustainable transformation of fly ash industrial waste into a construction cement blend via CO_2 carbonation', *Journal of Cleaner Production*, 156, pp. 660-669.

Eikeland, E., Blichfeld, A.B., Tyrsted, C., Jensen, A. and Iversen, B.B. (2015) 'Optimized carbonation of magnesium silicate mineral for CO_2 storage', *ACS Applied Materials & Interfaces*, 7(9), pp. 5258-64.

Erlund, R., Koivisto, E., Fagerholm, M. and Zevenhoven, R. (2016) 'Extraction of magnesium from four Finnish magnesium silicate rocks for CO_2 mineralisation-part 2: Aqueous solution extraction', *Hydrometallurgy*, 166, pp. 229-236.

Farhang, F., Oliver, T.K., Rayson, M., Brent, G., Stockenhuber, M. and Kennedy, E. (2016) 'Experimental study on the precipitation of magnesite from thermally activated serpentine for CO_2 sequestration', *Chemical Engineering Journal*, 303, pp. 439-449.
Ferrini, V., De Vito, C. and Mignardi, S. (2009) 'Synthesis of nesquehonite by reaction of gaseous CO_2 with Mg chloride solution: its potential role in the sequestration of carbon dioxide', *Journal of Hazardous Materials*, 168(2-3), pp. 832-7.

Gadikota, G., Fricker, K., Jang, S.-H. and Park, A.-H.A. (2015) 'Carbonation of Silicate Minerals and Industrial Wastes and Their Potential Use as Sustainable Construction Materials', in *Advances in CO_2 Capture, Sequestration, and Conversion*. pp. 295-322.

Georgakopoulos, E., Santos, R.M., Chiang, Y.W. and Manovic, V. (2016) 'Influence of process parameters on carbonation rate and conversion of steelmaking slags - Introduction of the ‘carbonation weathering rate’', *Greenhouse Gases: Science and Technology*, 6(4), pp. 470-491.

Gerdemann, S.J., O'Connor, W.K., Dahlin, D.C., Penner, L.R. and Rush, H. (2007) 'Ex situ aqueous mineral carbonation', *Environmental Science & Technology*, 41(7), pp. 2587-2593.

Ghoorah, M., Dlugogorski, B.Z., Balucan, R.D. and Kennedy, E.M. (2014) 'Selection of acid for weak acid processing of wollastonite for mineralisation of CO_2', *Fuel*, 122, pp. 277-286.

Glasser, F.P., Jauffret, G., Morrison, J., Galvez-Martos, J.-L., Patterson, N. and Imbabi, M.S.-E. (2016) 'Sequestering CO_2 by Mineralization into Useful Nesquehonite-Based Products', *Frontiers in Energy Research*, 4, p. Article 3.

Gunning, P.J., Hills, C.D. and Carey, P.J. (2009) 'Production of lightweight aggregate from industrial waste and carbon dioxide', *Waste Management*, 29(10), pp. 2722-8.

Gunning, P.J., Hills, C.D. and Carey, P.J. (2010) 'Accelerated carbonation treatment of industrial wastes', *Waste management*, 30(6), pp. 1081-1090.

Gunning, P.J., Hills, C.D., Antemir, A. and Carey, P.J. (2011) 'Secondary aggregate from waste treated with carbon dioxide', *Proceedings of the Institution of Civil Engineers-Construction Materials*, 164(5), pp. 231-239.

Gunning, P., Hills, C., Araizi, P., Maries, A. and Wray, D. (2014) 'Carbon capture using wastes: A review'. *7th International Scientific Conference: Science and Higher Education in Function of Sustainable Development*, Uzice, Serbia 3-4 October 2014.

Gunning, P. and Hills, C. (2015) 'Carbon8: Combined carbon capture and waste treatment-A commercial reality'. In: Book of extended abstracts of WASCON 2015: Resource Efficiency in Construction. WASCON 2015, Santander, Spain, pp. 140-145.

Han, X., Williamson, F., Bhaduri, G.A., Harvey, A. and Šiller, L. (2015) 'Synthesis and characterisation of ambient pressure dried composites of silica aerogel matrix and embedded nickel nanoparticles', *The Journal of Supercritical Fluids*, 106, pp. 140-144.

Han, Y.S., Ji, S., Lee, P.K. and Oh, C. (2017) 'Bauxite residue neutralization with simultaneous mineral carbonation using atmospheric CO_2', *Journal of Hazardous Materials*, 326, pp. 87-93.

Hänchen, M., Prigiobbe, V., Baciocchi, R. and Mazzotti, M. (2008) 'Precipitation in the Mg-carbonate system-effects of temperature and CO_2 pressure', *Chemical Engineering Science*, 63(4), pp. 1012-1028.

Hao, R. and Al-Tabbaa, A. (2014) 'A CCS Mineralization Process: Investigation of the Production of Magnesium Carbonates from Magnesium Chloride Solution', *Energy Procedia*, 63, pp. 8017-8025.

Harrison, A.L., Mavromatis, V., Oelkers, E.H. and Bénézeth, P. (2019) 'Solubility of the hydrated Mg-carbonates nesquehonite and dypingite from 5 to 35 °C: Implications for CO_2 storage and the relative stability of Mg-carbonates', *Chemical Geology*, 504, pp. 123-135.

He, L., Yu, D., Lv, W., Wu, J. and Xu, M. (2013) 'A Novel Method for CO_2 Sequestration via Indirect Carbonation of Coal Fly Ash', *Industrial & Engineering Chemistry Research*, 52(43), pp. 15138-15145.

Hemmati, A., Shayegan, J., Bu, J., Yeo, T.Y. and Sharratt, P. (2014) 'Process optimization for mineral carbonation in aqueous phase', *International Journal of Mineral Processing*, 130, pp. 20-27.

Holmes, G. and Keith, D.W. (2012) 'An air-liquid contactor for large-scale capture of CO_2 from air', *Philosophical Transactions of the Royal Society A*, 370(1974), pp. 4380-403.

Ibrahim, M., El-Naas, M., Benamor, A., Al-Sobhi, S. and Zhang, Z. (2019) 'Carbon Mineralization by Reaction with Steel-Making Waste: A Review', *Processes*, 7(2), p. 115.

Iizuka, A., Fujii, M., Yamasaki, A. and Yanagisawa, Y. (2004) 'Development of a New CO_2 Sequestration Process Utilizing the Carbonation of Waste Cement', *Industrial & Engineering Chemistry Research*, 43, pp. 7880-7887.

Jeon, J. and Kim, M.-J. (2019) 'CO_2 storage and $CaCO_3$ production using seawater and an alkali industrial by-product', *Chemical Engineering Journal*, 378, p. 122180.

Ji, L., Yu, H., Li, K., Yu, B., Grigore, M., Yang, Q., Wang, X., Chen, Z., Zeng, M. and Zhao, S. (2018a) 'Integrated absorption-mineralisation for low-energy CO_2 capture and sequestration', *Applied Energy*, 225, pp. 356-366.

Ji, L., Yu, H., Wang, X., Grigore, M., French, D., Gözükara, Y.M., Yu, J. and Zeng, M. (2017) 'CO_2 sequestration by direct mineralisation using fly ash from Chinese Shenfu coal', *Fuel Processing Technology*, 156, pp. 429-437.

Ji, L., Yu, H., Yu, B., Jiang, K., Grigore, M., Wang, X., Zhao, S. and Li, K. (2018b) 'Integrated absorption-mineralisation for energy-efficient CO_2 sequestration: Reaction mechanism and feasibility of using fly ash as a feedstock', *Chemical Engineering Journal*, 352, pp. 151-162.

Ji, L., Yu, H., Zhang, R., French, D., Grigore, M., Yu, B., Wang, X., Yu, J. and Zhao, S. (2019) 'Effects of fly ash properties on carbonation efficiency in CO_2 mineralisation', *Fuel Processing Technology*, 188, pp. 79-88.

Jo, H., Park, S.-H., Jang, Y.-N., Chae, S.-C., Lee, P.-K. and Jo, H.Y. (2014) 'Metal extraction and indirect mineral carbonation of waste cement material using ammonium salt solutions', *Chemical Engineering Journal*, 254, pp. 313-323.

Jo, H.Y., Kim, J.H., Lee, Y.J., Lee, M. and Choh, S.-J. (2012) 'Evaluation of factors affecting mineral carbonation of CO_2 using coal fly ash in aqueous solutions under ambient conditions', *Chemical Engineering Journal*, 183, pp. 77-87.

Kakizawa, M., Yamasaki, A. and Yanagisawa, Y. (2001) 'A new CO_2 disposal process via artificial weathering of calcium silicate accelerated by acetic acid', *Energy*, 26(4), pp. 341-354.

Kang, D., Jo, H., Lee, M.-G. and Park, J. (2016) 'Carbon dioxide utilization using a pretreated brine solution at normal temperature and pressure', *Chemical Engineering Journal*, 284, pp. 1270-1278.

Kang, J.M., Murnandari, A., Youn, M.H., Lee, W., Park, K.T., Kim, Y.E., Kim, H.J., Kang, S.-P., Lee, J.-H. and Jeong, S.K. (2018) 'Energy-efficient chemical regeneration of AMP using calcium hydroxide for operating carbon dioxide capture process', *Chemical Engineering Journal*, 335, pp. 338-344.

Kashef-Haghighi, S. and Ghoshal, S. (2010) 'CO_2 sequestration in concrete through accelerated carbonation curing in a flow-through reactor', *Industrial & Engineering Chemistry Research*, 49(3), pp. 1143-1149.

Kashefi, K., Pardakhti, A., Shafiepour, M. and Hemmati, A. (2020) 'Process optimization for integrated mineralization of carbon dioxide and metal recovery of red mud', *Journal of Environmental Chemical Engineering*, 8(2), p. 103638.

Katsuyama, Y., Yamasaki, A., Iizuka, A., Fujii, M., Kumagai, K. and Yanagisawa, Y. (2005) 'Development of a process for producing high-purity calcium carbonate ($CaCO_3$) from waste cement using pressurized CO_2', *Environmental Progress*, 24(2), pp. 162-170.

Keith, D.W., Holmes, G., St. Angelo, D. and Heidel, K. (2018) 'A Process for Capturing CO_2 from the Atmosphere', *Joule*, 2(8), pp. 1573-1594.

Kemache, N., Pasquier, L.-C., Cecchi, E., Mouedhen, I., Blais, J.-F. and Mercier, G. (2017) 'Aqueous mineral carbonation for CO_2 sequestration: From laboratory to pilot scale', *Fuel Processing Technology*, 166, pp. 209-216.

Khalifah, R.G. (1971) 'The carbon dioxide hydration activity of carbonic anhydrase', *Journal of Biological Chemistry*, 246(8), pp. 2561-2573.

Kodama, S., Nishimoto, T., Yamamoto, N., Yogo, K. and Yamada, K. (2008) 'Development of a new pH-swing CO_2 mineralization process with a recyclable reaction solution', *Energy*, 33(5), pp. 776-784.

Koivisto, E., Erlund, R., Fagerholm, M. and Zevenhoven, R. (2016) 'Extraction of magnesium from four Finnish magnesium silicate rocks for CO_2 mineralisation - Part 1: Thermal solid/solid extraction', *Hydrometallurgy*, 166, pp. 222-228.

Lackner, K.S., Wendt, C.H., Butt, D.P., Joyce Jr, E.L. and Sharp, D.H. (1995) 'Carbon Dioxide Disposal in Carbonate Minerals', *Energy*, 20, pp. 153-1170

Li, Y., Wang, H.P., Liao, C.Y., Zhao, X., Hsiung, T.L., Liu, S.H. and Chang, S.G. (2017) 'Dual Alkali Solvent System for CO_2 Capture from Flue Gas', *Environmental Science & Technology*, 51(15), pp. 8824-8831.

Liu, Q. and Maroto-Valer, M.M. (2010) 'Investigation of the pH effect of a typical host rock and buffer solution on CO_2 sequestration in synthetic brines', *Fuel Processing Technology*, 91(10), pp. 1321-1329.

Liu, W., Su, S., Xu, K., Chen, Q., Xu, J., Sun, Z., Wang, Y., Hu, S., Wang, X., Xue, Y. and Xiang, J. (2018) 'CO_2 sequestration by direct gas-solid carbonation of fly ash with steam addition', *Journal of Cleaner Production*, 178, pp. 98-107.

Liu, X., Wang, W., Wang, M. and Wang, P. (2014) 'Experimental Study of CO_2 Mineralization in Ca^{2+}-Rich Aqueous Solutions Using Tributylamine as an Enhancing Medium', *Energy & Fuels*, 28(3), pp. 2047-2053.

Ma, J. and Yoon, R.-H. (2013) 'Use of Reactive Species in Water for CO_2 Mineralization', *Energy & Fuels*, 27(8), pp. 4190-4198.

Madeddu, S., Priestnall, M., Kinoshita, H. and Godoy, E. (2014) 'Alkaline digestion of dunite for $Mg(OH)_2$ production: An investigation for indirect CO_2 sequestration', *Minerals Engineering*, 59, pp. 31-38.

Mazzella, A., Errico, M. and Spiga, D. (2016) 'CO_2 uptake capacity of coal fly ash: Influence of pressure and temperature on direct gas-solid carbonation', *Journal of Environmental Chemical Engineering*, 4(4), pp. 4120-4128.

Medas, D., Cappai, G., De Giudici, G., Piredda, M. and Podda, S. (2017) 'Accelerated carbonation by cement kiln dust in aqueous slurries: chemical and mineralogical investigation', *Greenhouse Gases: Science and Technology*, 7(4), pp. 692-705.

Mignardi, S., De Vito, C., Ferrini, V. and Martin, R.F. (2011) 'The efficiency of CO_2 sequestration via carbonate mineralization with simulated wastewaters of high salinity', *Journal of Hazardous Materials*, 191(1-3), pp. 49-55.

Montes-Hernandez, G., Perez-Lopez, R., Renard, F., Nieto, J.M. and Charlet, L. (2009) 'Mineral sequestration of CO_2 by aqueous carbonation of coal combustion fly-ash', *Journal of Hazardous Materials*, 161(2-3), pp. 1347-54.

Morgan, B., Wilson, S.A., Madsen, I.C., Gozukara, Y.M. and Habsuda, J. (2015) 'Increased thermal stability of nesquehonite ($MgCO_3 \cdot 3H_2O$) in the presence of humidity and CO_2 : Implications for low-temperature CO_2 storage', *International Journal of Greenhouse Gas Control*, 39, pp. 366-376.

Morrison, J., Jauffret, G., Galvez-Martos, J.L. and Glasser, F.P. (2016) 'Magnesium-based cements for CO_2 capture and utilisation', *Cement and Concrete Research*, 85, pp. 183-191.

O'Connor, W.K., Dahlin, D.C., Nilsen, D.N., Walters, R.P. and Turner, P.C. (2000) *Carbon dioxide sequestration by direct aqueous mineral carbonation*. Albany, Oregon: Albany Research Center (ARC) Albany Research Center.

Pan, S.-Y., Chiang, A., Chang, E.E., Lin, Y.-P., Kim, H. and Chiang, P.-C. (2015) 'An Innovative Approach to Integrated Carbon Mineralization and Waste Utilization: A Review', *Aerosol and Air Quality Research*, 15(3), pp. 1072-1091.

Pan, S.Y., Chiang, P.C., Chen, Y.H., Tan, C.S. and Chang, E.E. (2013) 'Ex Situ CO_2 capture by carbonation of steelmaking slag coupled with metalworking wastewater in a rotating packed bed', *Environmental Science & Technology*, 47(7), pp. 3308-15.

Pan, S.Y., Chung, T.C., Ho, C.C., Hou, C.J., Chen, Y.H. and Chiang, P.C. (2017) 'CO_2 Mineralization and Utilization using Steel Slag for Establishing a Waste-to-Resource Supply Chain', *Scientific Report*, 7(1), p. 17227.

Park, A.-H.A. and Fan, L.-S. (2004) 'CO_2 mineral sequestration: physically activated dissolution of serpentine and pH swing process', *Chemical Engineering Science*, 59(22-23), pp. 5241-5247.

Park, A.H.A., Jadhav, R. and Fan, L.S. (2003) 'CO_2 mineral sequestration: chemically enhanced aqueous carbonation of serpentine', *The Canadian Journal of Chemical Engineering*, 81(3-4), pp. 885-890.

Park, S., Jo, H., Kang, D. and Park, J. (2014) 'A study of CO_2 precipitation method considering an ionic CO_2 and $Ca(OH)_2$ slurry', *Energy*, 75, pp. 624-629.

Park, S., Song, K. and Jo, H. (2017) 'Laboratory-scale experiment on a novel mineralization-based method of CO_2 capture using alkaline solution', *Energy*, 124, pp. 589-598.

Pasquier, L.-C., Mercier, G., Blais, J.-F., Cecchi, E. and Kentish, S. (2014) 'Parameters optimization for direct flue gas CO_2 capture and sequestration by aqueous mineral carbonation using activated serpentinite based mining residue', *Applied Geochemistry*, 50, pp. 66-73.

Pérez-Moreno, S.M., Gázquez, M.J. and Bolívar, J.P. (2015) 'CO_2 sequestration by indirect carbonation of artificial gypsum generated in the manufacture of titanium dioxide pigments', *Chemical Engineering Journal*, 262, pp. 737-746.

Polettini, A., Pomi, R. and Stramazzo, A. (2016) 'CO_2 sequestration through aqueous accelerated carbonation of BOF slag: A factorial study of parameters effects', *Journal of Environmental Management*, 167, pp. 185-95.

Power, I.M., Harrison, A.L. and Dipple, G.M. (2016) 'Accelerating Mineral Carbonation Using Carbonic Anhydrase', *Environmental Science & Technology*, 50(5), pp. 2610-8.

Prigiobbe, V., Polettini, A. and Baciocchi, R. (2009) 'Gas–solid carbonation kinetics of Air Pollution Control residues for CO_2 storage', *Chemical Engineering Journal*, 148(2-3), pp. 270-278.

Reddy, K.J., John, S., Weber, H., Argyle, M.D., Bhattacharyya, P., Taylor, D.T., Christensen, M., Foulke, T. and Fahlsing, P. (2011) 'Simultaneous capture and mineralization of coal combustion flue gas carbon dioxide (CO_2)', *Energy Procedia*, 4, pp. 1574-1583.

Reddy, K.J., Weber, H., Bhattacharyya, P., Morris, A., Taylor, D., Christensen, M., Foulke, T. and Fahlsing, P. (2010) 'Instantaneous Capture and Mineralization of Flue Gas Carbon Dioxide: Pilot Scale Study', *Nature Precedings*, https://doi.org/10.1038/npre.2010.5404.1.

Romero-Hermida, I., Santos, A., Pérez-López, R., García-Tenorio, R., Esquivias, L. and Morales-Flórez, V. (2017) 'New method for carbon dioxide mineralization based on phosphogypsum and aluminium-rich industrial wastes resulting in valuable carbonated by-products', *Journal of CO_2 Utilization*, 18, pp. 15-22.

Said, A., Mattila, H.-P., Järvinen, M. and Zevenhoven, R. (2013) 'Production of precipitated calcium carbonate (PCC) from steelmaking slag for fixation of CO_2', *Applied Energy*, 112, pp. 765-771.

Salman, M., Cizer, Ö., Pontikes, Y., Santos, R.M., Snellings, R., Vandewalle, L., Blanpain, B. and Van Balen, K. (2014) 'Effect of accelerated carbonation on AOD stainless steel slag for its valorisation as a CO_2-sequestering construction material', *Chemical Engineering Journal*, 246, pp. 39-52.

Sanna, A., Lacinska, A., Styles, M. and Maroto-Valer, M.M. (2014) 'Silicate rock dissolution by ammonium bisulphate for pH swing mineral CO_2 sequestration', *Fuel Processing Technology*, 120, pp. 128-135.

Sanna, A., Wang, X., Lacinska, A., Styles, M., Paulson, T. and Maroto-Valer, M.M. (2013) 'Enhancing Mg extraction from lizardite-rich serpentine for CO_2 mineral sequestration', *Minerals Engineering*, 49, pp. 135-144.

Santos, R.M., Bodor, M., Dragomir, P.N., Vraciu, A.G., Vlad, M. and Van Gerven, T. (2014a) 'Magnesium chloride as a leaching and aragonite-promoting self-regenerative additive for the mineral carbonation of calcium-rich materials', *Minerals Engineering*, 59, pp. 71-81.

Santos, R.M., Chiang, Y.W., Elsen, J. and Van Gerven, T. (2014b) 'Distinguishing between carbonate and non-carbonate precipitates from the carbonation of calcium-containing organic acid leachates', *Hydrometallurgy*, 147-148, pp. 90-94.

Santos, R.M., François, D., Mertens, G., Elsen, J. and Van Gerven, T. (2013a) 'Ultrasound-intensified mineral carbonation', *Applied Thermal Engineering*, 57(1-2), pp. 154-163.

Santos, R.M., Van Bouwel, J., Vandevelde, E., Mertens, G., Elsen, J. and Van Gerven, T. (2013b) 'Accelerated mineral carbonation of stainless steel slags for CO_2 storage and waste valorization: Effect of process parameters on geochemical properties', *International Journal of Greenhouse Gas Control*, 17, pp. 32-45.

Santos, R.M. and Van Gerven, T. (2011) 'Process intensification routes for mineral carbonation*', *Greenhouse Gases: Science and Technology*, 1(4), pp. 287-293.
Santos, R.M., Verbeeck, W., Knops, P., Rijnsburger, K., Pontikes, Y. and Van Gerven, T. (2013c) 'Integrated Mineral Carbonation Reactor Technology for Sustainable Carbon Dioxide Sequestration: ‘CO_2 Energy Reactor”', *Energy Procedia*, 37, pp. 5884-5891.

Sanz-Perez, E.S., Murdock, C.R., Didas, S.A. and Jones, C.W. (2016) 'Direct Capture of CO_2 from Ambient Air', *Chemical Reviews*, 116(19), pp. 11840-11876.
Sheng, H., Lv, L., Liang, B., Li, C., Yuan, B., Ye, L., Yue, H., Liu, C., Wang, Y., Zhu, J. and Xie, H. (2015) 'Aqueous carbonation of the potassium-depleted residue from potassium feldspar–$CaCl_2$ calcination for CO_2 fixation', *Environmental Earth Sciences*, 73(11), pp. 6871-6879.

Šiller, L. and Bhaduri, G.A. (2013) *Carbon Capture, Patent, T/GB2013/051243 (WO 2013171480 A2, WO2013171480 A3,US20150151248 A1, EP2849871 A2, CN104428051 A)*.

Silverman, D.N., Lindskog.S. (1988) 'The catalytic mechanism of carbonic anhydrase: Implications of a rate-limiting protolysis of water', *Accounts of Chemical Research* 21(1), pp. 30–36.

Soong, Y., Fauth, D.L., Howard, B.H., Jones, J.R., Harrison, D.K., Goodman, A.L., Gray, M.L. and Frommell, E.A. (2006) 'CO_2 sequestration with brine solution and fly ashes', *Energy Conversion and Management*, 47(13-14), pp. 1676-1685.

Soong, Y., Goodman, A.L., McCarthy-Jones, J.R. and Baltrus, J.P. (2004) 'Experimental and simulation studies on mineral trapping of CO_2 with brine', *Energy Conversion and Management*, 45(11-12), pp. 1845-1859.

Steel, K.M., Alizadehhesari, K., Balucan, R.D. and Bašić, B. (2013) 'Conversion of CO_2 into mineral carbonates using a regenerable buffer to control solution pH', *Fuel*, 111, pp. 40-47.

Styles, M.T., Sanna, A., Lacinska, A.M., Naden, J. and Maroto-Valer, M. (2014) 'The variation in composition of ultramafic rocks and the effect on their suitability for carbon dioxide sequestration by mineralization following acid leaching', *Greenhouse Gases: Science and Technology*, 4(4), pp. 440-451.

Sun, B., Zhou, H., Arowo, M., Chen, J., Chen, J. and Shao, L. (2015) 'Preparation of basic magnesium carbonate by simultaneous absorption of NH_3 and CO_2 into $MgCl_2$ solution in an RPB', *Powder Technology*, 284, pp. 57-62.

Sun, Y., Yao, M.-S., Zhang, J.-P. and Yang, G. (2011) 'Indirect CO_2 mineral sequestration by steelmaking slag with NH_4Cl as leaching solution', *Chemical Engineering Journal*, 173(2), pp. 437-445.

Tamilselvi Dananjayan, R.R., Kandasamy, P. and Andimuthu, R. (2016) 'Direct mineral carbonation of coal fly ash for CO_2 sequestration', *Journal of Cleaner Production*, 112, pp. 4173-4182.

Teir, S., Eloneva, S., Fogelholm, C.-J. and Zevenhoven, R. (2007a) 'Dissolution of steelmaking slags in acetic acid for precipitated calcium carbonate production', *Energy*, 32(4), pp. 528-539.

Teir, S., Eloneva, S., Fogelholm, C.-J. and Zevenhoven, R. (2009) 'Fixation of carbon dioxide by producing hydromagnesite from serpentinite', *Applied Energy*, 86(2), pp. 214-218.

Teir, S., Kuusik, R., Fogelholm, C.-J. and Zevenhoven, R. (2007b) 'Production of magnesium carbonates from serpentinite for long-term storage of CO_2', *International Journal of Mineral Processing*, 85(1-3), pp. 1-15.

Teir, S., Revitzer, H., Eloneva, S., Fogelholm, C.-J. and Zevenhoven, R. (2007c) 'Dissolution of natural serpentinite in mineral and organic acids', *International Journal of Mineral Processing*, 83(1-2), pp. 36-46.

Turianicová, E., Baláž, P., Tuček, Ľ., Zorkovská, A., Zeleňák, V., Németh, Z., Šatka, A. and Kováč, J. (2013) 'A comparison of the reactivity of activated and non-activated olivine with CO_2', *International Journal of Mineral Processing*, 123, pp. 73-77.

Ukwattage, N.L., Ranjith, P.G. and Wang, S.H. (2013) 'Investigation of the potential of coal combustion fly ash for mineral sequestration of CO_2 by accelerated carbonation', *Energy*, 52, pp. 230-236.

Ukwattage, N.L., Ranjith, P.G., Yellishetty, M., Bui, H.H. and Xu, T. (2015) 'A laboratory-scale study of the aqueous mineral carbonation of coal fly ash for CO_2 sequestration', *Journal of Cleaner Production*, 103, pp. 665-674.

van Noort, R., Spiers, C.J., Drury, M.R. and Kandianis, M.T. (2013) 'Peridotite dissolution and carbonation rates at fracture surfaces under conditions relevant for in situ mineralization of CO_2', *Geochimica et Cosmochimica Acta*, 106, pp. 1-24.

Velts, O., Hautaniemi, M., Kallas, J., Kuosa, M. and Kuusik, R. (2010a) 'Modeling calcium dissolution from oil shale ash: Part 2', *Fuel Processing Technology*, 91(5), pp. 491-495.

Velts, O., Hautaniemi, M., Kallas, J. and Kuusik, R. (2010b) 'Modeling calcium dissolution from oil shale ash: Part 1. Ca dissolution during ash washing in a batch reactor', *Fuel Processing Technology*, 91(5), pp. 486-490.

Velts, O., Uibu, M., Kallas, J. and Kuusik, R. (2011) 'Waste oil shale ash as a novel source of calcium for precipitated calcium carbonate: carbonation mechanism, modeling, and product characterization', *Journal of Hazardous Materials*, 195, pp. 139-46.

Velts, O., Uibu, M., Kallas, J. and Kuusik, R. (2013) 'CO_2 Mineralisation: Concept for Co-utilization of Oil Shale Energetics Waste Streams in $CaCO_3$ Production', *Energy Procedia*, 37, pp. 5921-5928.

Vinoba, M., Bhagiyalakshmi, M., Grace, A.N., Chu, D.H., Nam, S.C., Yoon, Y., Yoon, S.H. and Jeong, S.K. (2013) 'CO_2 absorption and sequestration as various polymorphs of $CaCO_3$ using sterically hindered amine', *Langmuir*, 29(50), pp. 15655-63.

Vinoba, M., Kim, D.H., Lim, K.S., Jeong, S.K., Lee, S.W. and Alagar, M. (2011) 'Biomimetic Sequestration of CO_2 and Reformation to $CaCO_3$ Using Bovine Carbonic Anhydrase Immobilized on SBA-15', *Energy & Fuels*, 25(1), pp. 438-445.

Wang, D. and Li, Z. (2012) 'Gas-Liquid Reactive Crystallization Kinetics of Hydromagnesite in the $MgCl_2$-CO_2-NH_3-H_2O System: Its Potential in CO_2 Sequestration', *Industrial & Engineering Chemistry Research*, 51(50), pp. 16299-16310.

Wang, W., Hu, M., Zheng, Y., Wang, P. and Ma, C. (2011) 'CO_2 Fixation in Ca^{2+}-/Mg^{2+}-Rich Aqueous Solutions through Enhanced Carbonate Precipitation', *Industrial & Engineering Chemistry Research*, 50(13), pp. 8333-8339.

Wang, W., Liu, X., Wang, P., Zheng, Y. and Wang, M. (2013) 'Enhancement of CO_2 Mineralization in Ca^{2+}-/Mg^{2+}-Rich Aqueous Solutions Using Insoluble Amine', *Industrial & Engineering Chemistry Research*, 52(23), pp. 8028-8033.

Wang, W., Wang, M., Liu, X., Wang, P. and Xi, Z. (2015) 'Experiment and Optimization for Simultaneous Carbonation of Ca^{2+} and Mg^{2+} in A Two-phase System of Insoluble Diisobutylamine and Aqueous Solution', *Scientific Report*, 5, p. 10862.
Wang, X. and Maroto-Valer, M.M. (2011) 'Dissolution of serpentine using recyclable ammonium salts for CO_2 mineral carbonation', *Fuel*, 90(3), pp. 1229-1237.

Woodall, C.M., McQueen, N., Pilorgé, H. and Wilcox, J. (2019) 'Utilization of mineral carbonation products: current state and potential', *Greenhouse Gases: Science and Technology*, 9(6), pp. 1096-1113.

Wu, J.C.-S., Sheen, J.-D., Chen, S.-Y. and Fan, Y.-C. (2001) 'Feasibility of CO_2 fixation via artificial rock weathering', *Industrial & Engineering Chemistry Research*, 40(18), pp. 3902-3905.

Xie, H., Tang, L., Wang, Y., Liu, T., Hou, Z., Wang, J., Wang, T., Jiang, W. and Were, P. (2016) 'Feedstocks study on CO_2 mineralization technology', *Environmental Earth Sciences*, 75(7).

Yadav, S. and Mehra, A. (2017) 'Experimental study of dissolution of minerals and CO_2 sequestration in steel slag', *Waste Management*, 64, pp. 348-357.

Yu, B., Li, K., Ji, L., Yang, Q., Jiang, K., Megharaj, M., Yu, H. and Chen, Z. (2019a) 'Coupling a sterically hindered amine-based absorption and coal fly ash triggered amine regeneration: A high energy-saving process for CO_2 absorption and sequestration', *International Journal of Greenhouse Gas Control*, 87, pp. 58-65.

Yu, B., Yu, H., Li, K., Ji, L., Yang, Q., Chen, Z. and Megharaj, M. (2019b) 'Integration of a diamine solvent based absorption and coal fly ash based mineralisation for CO_2 sequestration', *Fuel Processing Technology*, 192, pp. 220-226.

Zevenhoven, R., Eloneva, S. and Teir, S. (2006) 'Chemical fixation of CO_2 in carbonates: Routes to valuable products and long-term storage', *Catalysis Today*, 115(1-4), pp. 73-79.

Zevenhoven, R., Wiklund, A., Fagerlund, J., Eloneva, S., In't Veen, B., Geerlings, H., Van Mossel, G. and Boerrigter, H. (2009) 'Carbonation of calcium-containing mineral and industrial by-products', *Frontiers of Chemical Engineering in China*, 4(2), pp. 110-119.

Zhang, N., Santos, R.M. and Šiller, L. (2020) 'Rapid CO_2 capture-to-mineralisation in a scalable reactor', *Reaction Chemistry & Engineering*, 5(3), pp. 473-484.

Zhang, N., Santos, R.M., Smith, S.M. and Šiller, L. (2019) 'Acceleration of CO_2 mineralisation of alkaline brines with nickel nanoparticles catalysts in continuous tubular reactor', *Chemical Engineering Journal*, 377, p. 120479.

Zhao, Q., Li, J., You, K. and Liu, C. (2020) 'Recovery of calcium and magnesium bearing phases from iron- and steelmaking slag for CO_2 sequestration', *Process Safety and Environmental Protection*, 135, pp. 81-90.

Zhao, Y., Wu, M., Guo, X., Zhang, Y., Ji, Z., Wang, J., Liu, J., Liu, J., Wang, Z., Chi, Q. and Yuan, J. (2019) 'Thorough conversion of CO_2 through two-step accelerated mineral carbonation in the $MgCl_2$-$CaCl_2$-H_2O system', *Separation and Purification Technology*, 210, pp. 343-354.

Zhao, Y., Zhang, Y., Liu, J., Gao, J., Ji, Z., Guo, X., Liu, J. and Yuan, J. (2017) 'Trash to treasure: Seawater pretreatment by CO_2 mineral carbonation using brine pretreatment waste of soda ash plant as alkali source', *Desalination*, 407, pp. 85-92.

Zhu, C., Wang, H., Li, G., An, S., Ding, X., Teng, H. and Zhao, L. (2017) 'CO_2 Absorption and Magnesium Carbonate Precipitation in $MgCl_2$-NH_3-NH_4Cl Solutions: Implications for Carbon Capture and Storage', *Minerals*, 7(9).

Chapter 3. Methodology

This chapter is to provide detailed description on the materials used and process implemented from an experimental and simulation perspective, accompanied by the characterisation techniques applied in this PhD thesis. There are four sections to be demonstrated in this chapter as shown in Figure 3.1. All the analytical techniques to be used in Chapter 4, 5 and 6 for preparation and analysis of the aqueous and solid phase are described in section 3.1. Followed by section 3.2 where the plug-flow tubular reactor is proposed first time as the reactor conducting the mineralisation with sodium hydroxide (NaOH) and industrial waste-Blast Furnace (BF) slag, as the basic substances (results shown in Chapter 4). In section 3.3, the tubular reactor is continued to be implemented in the experimental section with a low concentration of monoethanolamine (MEA) to buffer the acidification of solutions, coupled with a time-dependent one-dimension model that is set to better understanding the comprehensive reactions occurred in the tubular reactor and predict the optimal length for large-scale deployment (results shown Chapter 5). Finally, in section 3.4, a batch reactor is used to proceed the mineralisation with calcined hydrotalcite (CHT) as the medium to exchange the chloride to hydroxyl groups sufficiently elevating pH value of brines to enable the precipitation of carbonates during CO_2 mineralisation. Moreover, the materials are recyclable for multiple usages by taking advantage of the HT's 'memory effect' property (Cavani *et al.*, 1991) (results shown in Chapter 6).

The results of each section presented here will be found in the subsequent chapters, as illustrated in Figure 3.1. For each section in this chapter, the process is described from two aspects:

1) The motivation of experimental design. The concept and the consideration of the current technical problems of the mineralisation process are demonstrated first.

2) The detailed process implementation to address the problems mentioned in the first point.

Overall, all the input materials, equipment and process implementation of this thesis are all presented in this chapter.

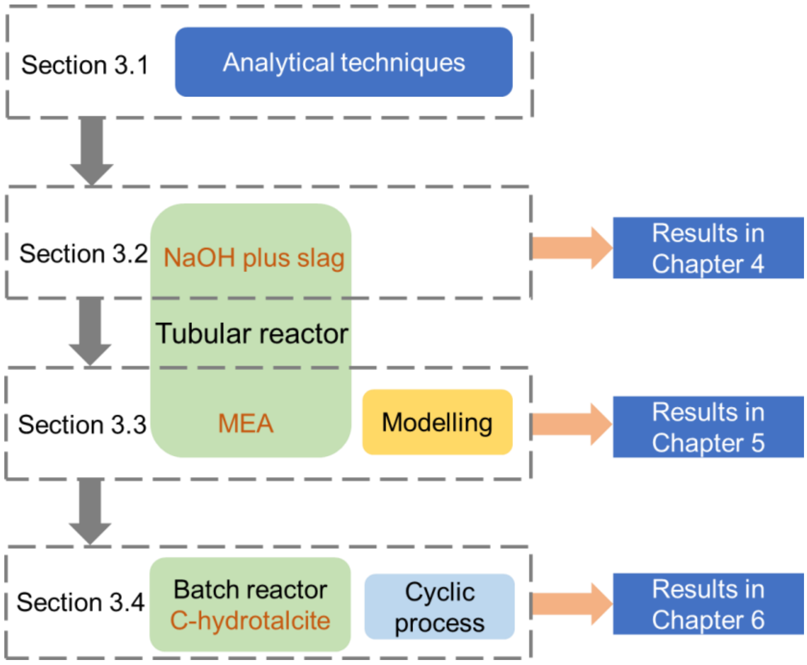

Figure 3.1 The outline of methodology chapter.

3.1 Analytical techniques

The analytical methods used in this thesis including: inductively coupled plasma optical emission spectroscopy, X-ray diffraction, scanning electron microscopy and energy dispersive X-ray spectroscopy, Fourier transform infrared spectroscopy, thermal gravimetric analysis and ion chromatography. For each characterisation technique, the principle of the operation and instrumentation are briefly described below.

3.1.1 Inductively Coupled Plasma Optical Emission Spectroscopy (ICP-OES)

The concentrations of alkaline earth metal cations in the liquid phase are determined by inductively coupled plasma optical emission spectrometry (ICP-OES), mainly for Ca^{2+} measurement. ICP-OES is an analytical technique which is capable of detecting elements at very low concentration (Hill, 1999).

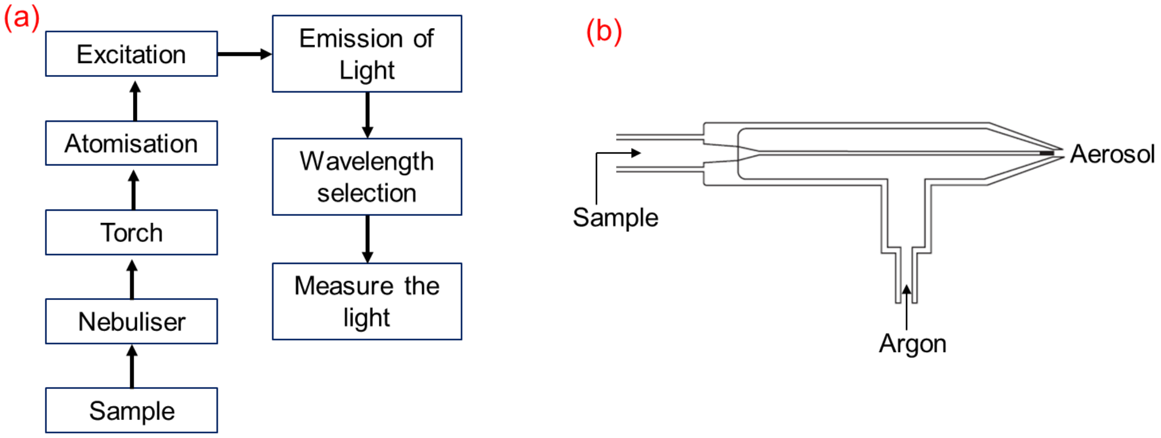

Figure 3.2 (a) Flowchart of ICP-OES analytical process; (b) Schematic diagram of the pneumatic concentric nebuliser (Hill, 1999).

The flowchart of ICP-OES analytical process is presented in Figure 3.2(a). The sample in the liquid phase is introduced into the instrument via a peristaltic pump, then is passed through the nebuliser to produce the aerosol in the atmosphere of argon gas. Aerosol droplets travel into the ICP torch, which produces exceptionally high temperature over 6,000 K, in order to dissociate various components of the sample to atomic level (Dean, 2005). Furthermore, the high temperature also provides the essential energy of excitation. The emitted lights with different wavelengths are separated, then the targeted element with a specific wavelength of emission is detected. Finally, the concentration of the element is listed in the program of the computer (Skoog *et al*., 2017). Figure 3.2(b) shows the detailed nebuliser construction where the sample is converted to the aerosol phase which enters the spray chamber later, and fine aerosol droplets are interacted with plasma, while the remaining large droplets are drained away.

Plasma is one of the fourth state of matter, it is co-existence of the positive ions, electrons and neutral species of inert gas, typically argon or helium (Hill, 1999). Inductively coupled plasma was first applied for spectrochemical analysis in 1964 (Greenfield *et al*., 1964) where gas is ionised by inductively heating it with an electromagnetic coil as indicated in Figure 3.3. The sample in the aerosol state is ionised to the excitation level with plasma under high temperature.

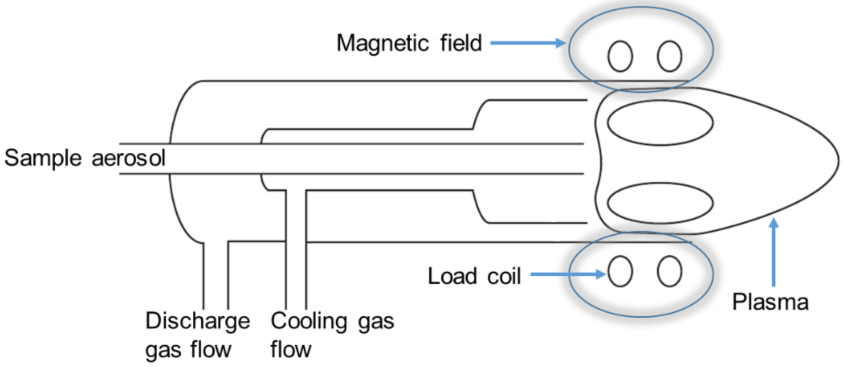

Figure 3.3 Diagram of an ICP torch (Dean et al., 1997).

In most cases, the atom is stable in the ambient condition when it contains low energy with electron configuration at ground state. However, once the thermal energy is applied, electrons are transferred to a higher energy level (excitation state), and this process is called atomic absorption but when it is in a reversed direction, it is called atomic emission as shown in Figure 3.4(a) (Dean, 2005). In this study, calcium cation in the aqueous phase is the aimed element that was detected with ICP-OES. When the calcium atom is exposed to high temperature, it will absorb energy. Calcium has several absorption peaks at 317.933 nm, 315.887 nm, 393.366 nm, 396.847 nm, 422.673 nm and 227.546 nm as listed in Figure 3.4(b) (Tennyson, 2010; Vallapragada *et al.*, 2011). In this work, 422.673 nm was used as the specific wavelength within the instrument by PerkinElmer Optima 8000.

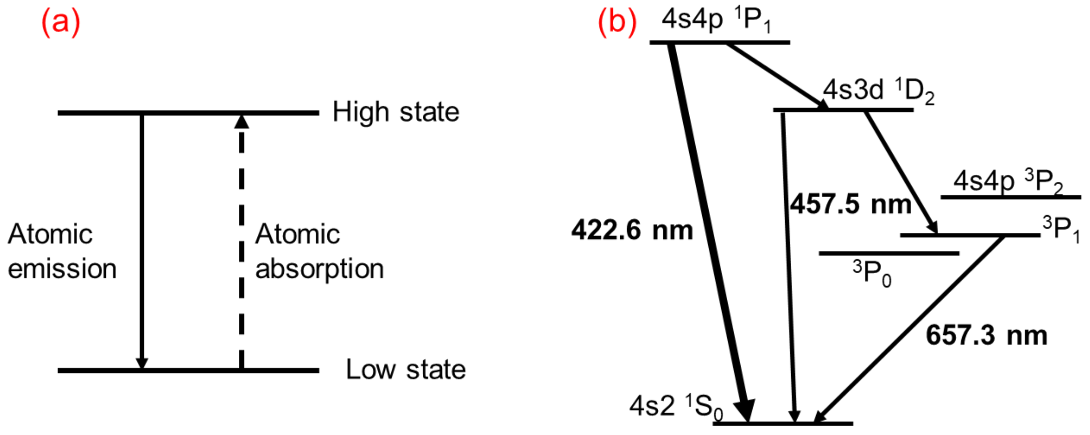

Figure 3.4 (a) Atomic absorption and emission energy transition (Dean, 2005); (b) Energy level diagram for calcium (Tennyson, 2010).

Spectrometers are used to separate the emission lights into different wavelengths with a diffraction grating. The grating equation as shown by Eq.(3.1) is applied to explains how the different light wavelength can be diffracted to different angles when the light hits the grating as detailed in Figure 3.5(a). The grating contains a series of parallel grooves at an angle to the surface of a mirror which can avoid the wavelength overlapping, where n is the order, $\emptyset$ is the angle of a groove, λ is the wavelength and d is the distance between grooves on the grating.

$$\mathrm{n}\lambda = \mathrm{d}\ \mathrm{sin}\emptyset \qquad \text{(E3.1)}$$

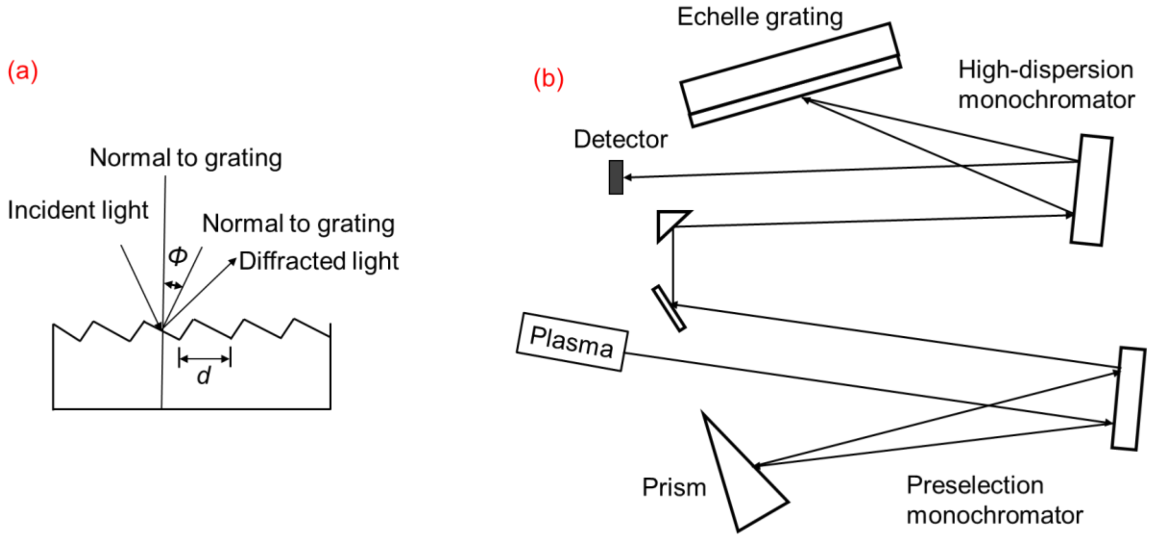

Figure 3.5 (a) A schematic diagram of a blazed grating (Dean, 2005). (b) The optima 8000 ICP-OES double monochromator spectrometer (PerkinElmer, 2020a).

There are two main spectrometers used in ICP, monochromators and polychromators. The ICP of optima 8000 model from PerkinElmer uses preselection dual monochromator technique which can let the purposed element wavelength to go through to the high-resolution echelle monochromator by applying the intermediate slit given in Figure 3.5(b) (PerkinElmer, 2020a). Once the spectrum information has obtained, the detector is ready to analyse it. There are two main detectors that can be used: photomultiplier tube (PMT) and multi-channel detectors based on charge transfer device (PerkinsElmer, 2020). Moreover, Echelle spectrometer always works with a solid-state detector. Charged coupled device is a semiconductor device that is made out from many individual small detectors called pixels and so that they can store electrons under the capacitor. The stored charges in each cell are the indicator of the amount of light. The required volume of the liquid to be analysed per sample by ICP-OES is very little less than 5 mL, and three replications are typically applied for each measurement in order to obtain accurate results. The concentrations of metal ions in the liquid presented throughout Chapter 4-6 are achieved by ICP-OES.

3.1.2 X-ray Diffraction (XRD)

The crystallographic structure of the materials that have been used and products that are obtained from the developed processes in this thesis were analysed by X-ray diffraction (XRD). XRD is a technique that uses X-ray photon beam diffraction to detect the atomic structure of crystals (Warren, 1990). When the high voltage power is applied between two electrodes, the electrons with high energy are released from the cathode and accelerated with high voltage between cathode and anode, then X-rays are generated on the anode side with the electrons decelerated rapidly.

A 3D crystal consists of periodical arrangement of atoms. In terms of crystallography, the crystal is assumed to have a perfect geometry and the lattice, which is one of the extracted repeated unit, also known as the unit cell. The unit cell is containing three vectors a, b and c, which are parallel to the x, y and z direction, respectively. The angles between two vectors are α, β and γ. Another critical parameter for XRD is the indices of the plane developed by W. H. Miller, so called Miller indices. The Miller indices are presented by (hkl) with the intercepts at a/h, b/k and c/l of the each axis and they are satisfy the Eq.(3.2).

$$\frac{hx}{a}+\frac{ky}{b}+\frac{lz}{c}=m \qquad \text{(E3.2)}$$

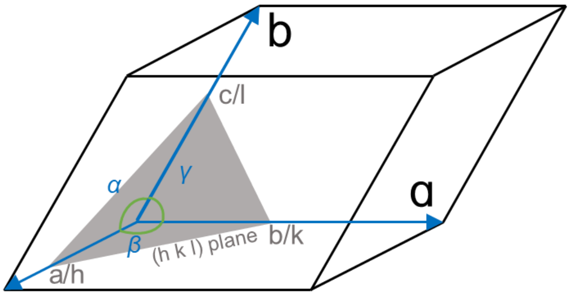

Figure 3.6 A general form of the unit cell (Lee, 2017).

The principle of XRD is based on Bragg's Law and the equation is illustrated as $n\lambda = 2d\sin\theta$, where d is the distance of the two atomic layers in a crystal; λ is the wavelength of the incident X-ray beam; n is the order of the diffraction as an integral value; and θ is the angle of the incident beam. The difference of pathways of two beams is the sum of the length of AB and BC, which is 2dsinθ in total as shown in Figure 3.7(a) (Cullity and Stock, 2001).

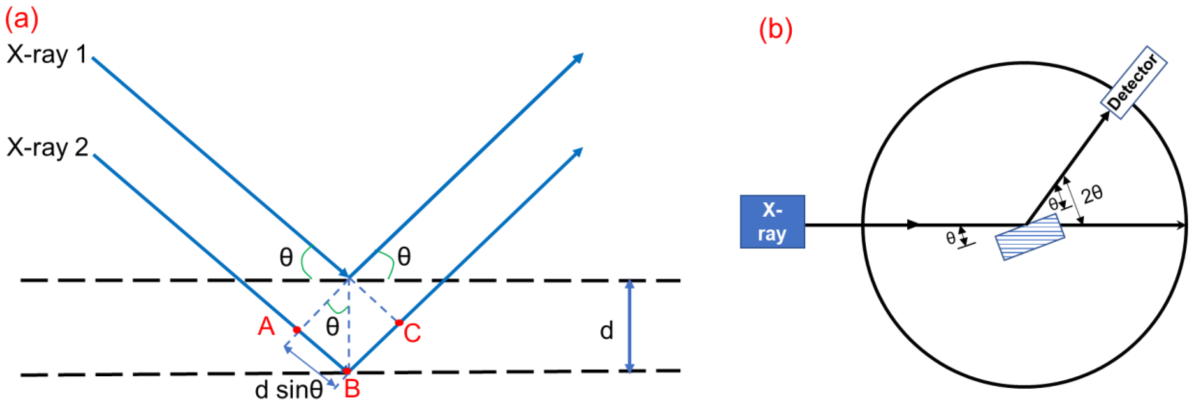

Figure 3.7 (a) Bragg's Law diagram (Cullity and Stock, 2001); (b) The basic layout of XRD instrument (Cullity and Stock, 2001).

The features of X-ray diffraction spectrometer are displayed in Figure 3.7(b) (Cullity and Stock, 2001). X-rays from generator hit the sample to be analysed, and the sample is set at the desired angle to the incident beam and then is rotated around the centre. The diffracted X-rays are captured by the detector which is also rotated around the centre. In practice, the sample is positioned at the angle of θ with the incident X-ray and the detector is placed at the angle of 2θ. Afterwards, the intensity of the beams at the detector are calculated with the formula of Bragg's Law and this process is repeated at each different angle. In this thesis, all the samples measured by XRD are in the form of powder which contains small crystals with their (hkl) planes randomly oriented. Therefore, it is crucial to prepare the homogeneous samples with a large area in the measurement kit to capture the full incident beam. The samples obtained in Chapter 4, 5 and 6 are measured with XRD for the characterisation of precipitates and prepared and regenerated hydrotalcites.

3.1.3 Scanning Electron Microscopy (SEM) and Energy Dispersive X-ray Spectroscopy (EDX)

SEM is a technique to obtain images of the specimen by scanning the electron beam of certain energy depending on the examined samples, typically ranging from 2 to 30 kV (Reed, 2005; Ul-Hamid, 2018). When the electron beam from the electron gun hits the surface of the specimen, several types of electrons are emitted including backscattered, secondary, Auger electrons and photons as illustrated in Figure 3.8(a) (Krinsley *et al*., 2005). Elastic scattering is the way that electrons loose very little kinetic energy and the most of them are scattered directly back out of the specimen, so called backscattered electrons. During the inelastic scattering, the electrons loose significant amount of energy and some of the energy is lost on emission of secondary electrons from the specimen. Due to the low energy of the secondary electrons with only a few electron volts, only the electrons within the nanometre-scale depth from the surface can escape from the specimen (Reed, 2005). Therefore, secondary electrons are used to produce images with detailed surface information. The back scattering highly depends on the atomic number, substantial number of backscattering electrons are scattered on the sample with a large atomic number (Krinsley *et al*., 2005). EDX is the way to identify elements and their concentrations in the specimen via measuring the X-ray signal collected from the dector (Ul-Hamid, 2018).

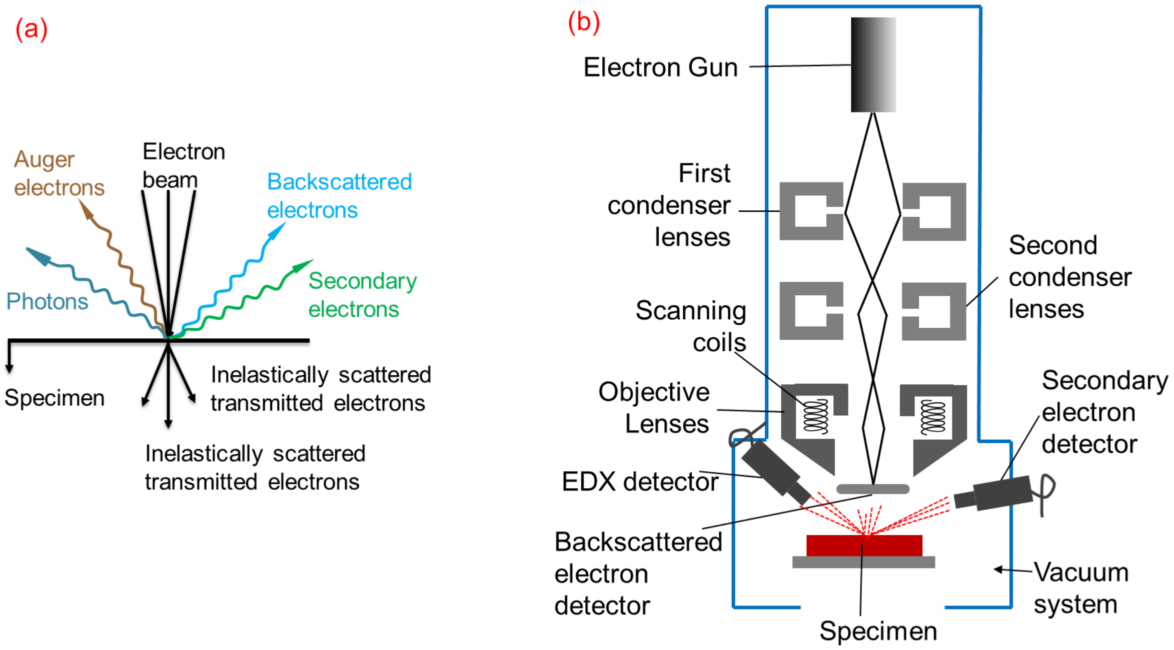

Figure 3.8 (a) Various electrons emission (Reed, 2005); (b) Schematic diagram of the SEM instrument (Ul-Hamid, 2018).

The main elements of an SEM are electron gun, electron lenses, specimen chamber and detectors as described in Figure 3.8(b) (Ul-Hamid, 2018). The source of the electron can be generated and accelerated by an electron gun with high energy to overcome the barrier at the surface (Reed, 2005). To obtain sufficient resolution, three lenses are applied: the first and second lenses are called condenser lenses followed by set of lenses named as objective lenses. The aim of these electro-magnetic electron lenses is to focus the electron beam. When electrons leave the specimen, the signal can be collected with detectors which are typical Everhart-Thornley to form desired images (Goldstein *et al*., 2017). EDX detector can collect the X-ray signal to provide the element and component information by measuring the energy intensity. The instrument is conducted under vacuum condition to maintain the electron conditions without being scattered. The samples obtained in Chapter 4, 5 and 6 are measured with SEM to get detailed morphological information, and part of samples in Chapter 6 are used SEM-EDX to get the element composition.

3.1.4 Fourier Transform Infrared Spectroscopy (FTIR)

With the benefit of FTIR, the information of molecules, chemical bonds and concentrations can be achieved. There are two main properties of the light: electric field and magnetic field. These two vectors are mutually perpendicular and travel along a third direction. The distance between two peaks of electric field vector is called wavelength and is shown in Figure 3.9(a) (Smith, 2011). Wavelength of light is related to light energy and frequency by equation, $\mathrm{E} = \mathrm{h}\gamma = \mathrm{hc}/\lambda$, where E is energy, h is Planck’s constant, γ is frequency, c is the velocity of light and λ is the wavelength.

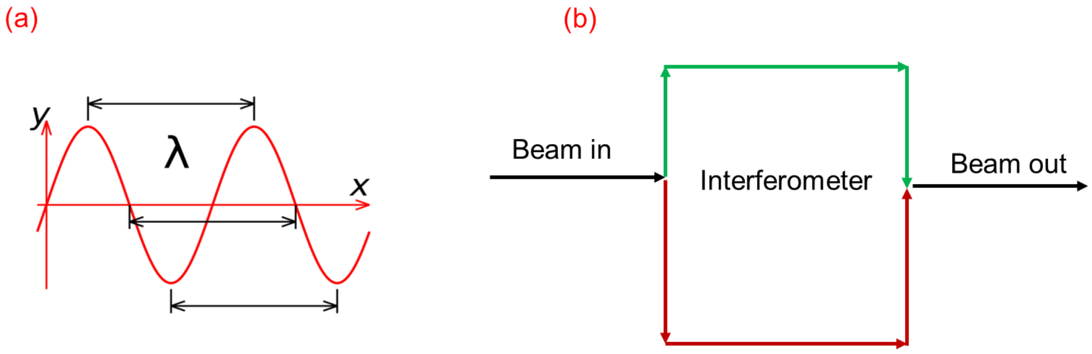

Figure 3.9 (a) An example of the electric vector of a light wave (Smith, 2011); (b) A diagram of an interferometer (Smith, 2011).

Typically, most often the mid-infrared spectrum of sample analysis is taken in wavelength range from 4000 to 400 cm^{-1}. The absorbance spectrum of a sample can be obtained by equation, Eq.(3.3) (Kauppinen and Partanen, 2011), where A is absorbance, I_0 is the intensity of the background and I is the sample spectrum intensity. Another parameter of infrared spectrum is the percentage of transmittance and can be calculated by Eq.(3.4) (Kauppinen and Partanen, 2011).

$$\mathrm{A} = \log(\mathrm{I}_0/\mathrm{I}) \qquad \text{(E3.3)}$$

$$\%\mathrm{T} = 100 \times (\mathrm{I}_0/\mathrm{I}) \qquad \text{(E3.4)}$$

The core part of FTIR spectrometer is the interferometer that splits the single light beam into two beams. These two light beams travel through different path lengths, seen as red and green lines indicated in Figure 3.9(b) (Smith, 2011), and they finally combine into one beam. The most conventional interferometer that is used is the Michelson interferometer. The principle of Michelson interferometer is illustrated as: light strikes the beam splitter that separates light into two beams: one beam goes towards the moving mirror; the other goes towards the fixed mirror. Once these two beams travel back to the beam splitter, they combine into a single beam that hits the detector and then detects the interference between these two beams.

One of the reflectance is called total internal reflectance which is illustrated in Figure 3.10(a). When IR beam hit the crystal with high refractive index that is greater than that of the sample (incidence angle θ_i), the light beam reflects in the internal part of crystal and it never leaves the crystal (Smith, 2011). This phenomenon can create the evanescent wave above the crystal that will enter the sample, and the evanescent wave is attenuated due to the sample absorption. The attenuated beam then returns to the detector to produce IR spectrum. An attenuated total reflectance (ATR) is based on this assumption and it is explained in Figure 3.10(b) (Smith, 2011) displayed and for the solid in powder state should be applied with pressure. This method requires less amounts of sample and can very fast analyse the sample at the ambient conditions as Spectrum Two model FTIR based in the PerkinElmer company (PerkinElmer, 2020b). The precipitates were measured with ATR-FTIR and results are shown in Chapter 4.

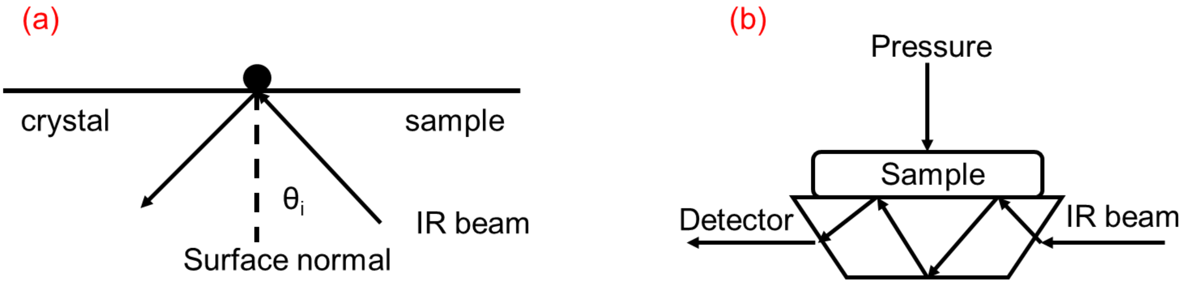

Figure 3.10 (a) Basic illustration of internal reflectance (Smith, 2011); (b) The principle working of ATR (Smith, 2011).

3.1.5 Thermal Gravimetric Analysis (TGA)

Thermal gravimetric analysis is a technique that measures and displays the sample mass alteration as a function of different temperatures (Skoog *et al*., 2017). Thermal analysis instrument consists of a sensitive balance, a furnace, a purge-gas system and a computational operation program. The sensitive balance is so-called thermo balance and it is connected to a sensor to record the mass change with the furnace temperature as illustrated in Figure 3.11 (Gabbott, 2008). The furnace is heated with a specific heat rate to reach the desired temperature and sometimes keeps at this temperature for a while with the carrier and purge gas going through the furnace. In terms of calcium carbonates, in this thesis, the temperature will be heated up to 900 °C under air or N_2 atmosphere to assure that carbonates are decomposed and converted into CaO. The computerised temperature control system can record the changes of thermocouple and the mass of sample.

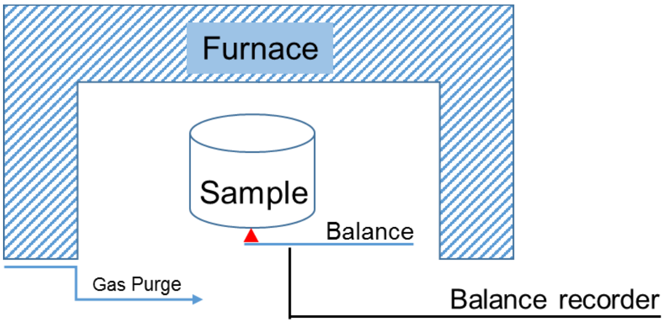

Figure 3.11 The principle operation of thermo-balance (Gabbott, 2008).

3.1.6 Ion Chromatography (IC)

Ion chromatography is a technique to separate mixture of ions (Fritz, 1987), in Chapter 6, chloride anion is the aimed ion to be analysed which could be separated with different retention time among other ions when they pass through the column. The column is the heart of any IC system and the choice of column can have a major impact on the results. The basic principle of separation is based on the ion exchange performance between the mobile phase and ion-exchange groups bonded to the stationary phase, where the stationary phase is typically the resin and the mobile phase is the liquid carrying on the samples. The ion exchange chromatography is based on the phenomenon of attraction of opposite charges component, for example, anion exchanger with positive stationary phase selectively attracts the negatively charged ions (Fritz, 1987).

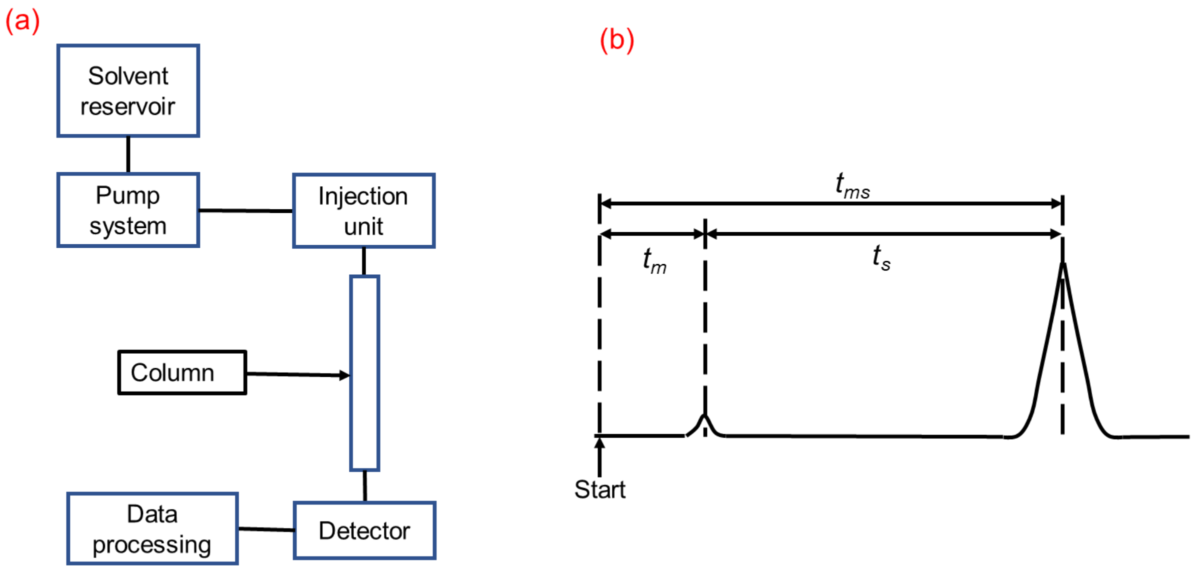

Figure 3.12 (a) The diagram of an ion chromatograph (Fritz, 1987); (b) Definition of retention time (Weiss, 2016).

The main components of the IC are shown in Figure 3.12(a). The solvent reservoir contains eluent which is known as the mobile phase carrying the samples going through the column and for anion analysis, a mixture of sodium carbonation and sodium bicarbonate solution. The eluent is pumped at a desired flow rate with the sample from the injection unit travelling through the column. The column contains a stationary fixed material known as ion-exchange resins and that have the capability to separate the components of samples and perform separation rapidly. A detector is used to measure the outlet conductivity changes of the fluid passing through it. The thermal control of the separation is to confirm the accuracy of the results. The signal obtained from IC is as shown in Figure 3.12(b). Retention time is the time from injection to the aimed anion is detected and it refers to t_s in Figure 3.12(b). The gross retention time t_{ms} can be calculated by the sum of t_s and t_m, where t_m presents the column dead time defined as non-retained component passing through the column (Weiss, 2016). The concentration of Cl^- was measured with ISC-1000 Ion Chromatography System from Thermal Scientific and results are presented in Chapter 6.

3.2 Experimental part of mineralisation process in a tubular reactor

In this section, the brine carbonation process with a continuous plug-flow tubular reactor is investigated. Catalytically active nickel nanoparticles (NiNPs) are applied to improve the mineralisation process. To counter CO_2 acidification effect, the brine was contacted with blast furnace (BF) slags to transfer alkalinity, with sodium hydroxide being used as an additional alkali to achieve the required pH. The effects of reaction temperature, the composition of alkaline brine solution and residence time in the tubular reactor, on the calcium conversion efficiency (CCE) and the mineral composition of the precipitates were investigated and the results of this methodology is discussed in Chapter 4. This has been published in *Chemical Engineering Journal* (Zhang *et al.*, 2019).

3.2.1 Reactor and process design

In this section, the motivation of this study is first illustrated. In order to enhance CO_2 mineralisation process, a novel reactor was designed and the experiments were carried out to evaluate the performance. Various researchers have operated carbonation in different types of reactors as options to reduce CO_2 emissions. The traditional reaction system for CO_2 mineralisation is implemented with batch, semi-batch or semi-continuous (Ukrainczyk *et al*., 2007; Fagerlund *et al*., 2012) reactors, whereby solid carbonates are precipitated by bubbling CO_2 into an aqueous solution or simply contacting a gas phase in the head-space of a reactor with the aqueous phase mixed. Other different reactors have also been summarised in Chapter 2. In this thesis, the focus was on avoiding reactors and processes that rely on high temperatures and pressures, and on mechanical agitation. Therefore, one of the aims of this project is to develop a brine carbonation process using a reactor and process that can enhance and control the reaction under mild operating conditions and flow-induced mixing. Herein, a helical coiled tubular reactor is introduced to proceed continuous gas-liquid carbonation reaction shown in Figure 3.13 with enhanced mixing due to centrifuge force (Kurt *et al.*, 2017). Tubular reactor has been studied for a few decades, such as catalytic reaction (Walker, 1961), pyrolysis reaction (Pütün *et al.*, 1999) and carbonates precipitation (Vacassy *et al.*, 2000). Moreover, continuous processes are favoured for industrial applications, and plug-flow reactors are extensively applied for a variety of gas/liquid/solid systems in the industry, such as production of active pharmaceutical ingredients (Eder *et al.*, 2010) and polyolefin synthesis (Soares and McKenna, 2013). However, the gas-liquid phase reaction of CO_2 mineralisation has never been studied with a tubular reactor and the implemented segmented flow has wide operating window with stable conditions (Kashid *et al.*, 2011). In this thesis, the brine carbonation process with a continuous plug-flow tubular reactor is proposed and developed. This system is easy to be scaled up for industrial applications and enables better process control, optimisation and integration (Zhang *et al.*, 2019).

The carbonation reaction is a homogeneous reaction between alkaline earth metal cations and carbonate anions, producing precipitated carbonates. It is necessary to maintain the pH value of the solution above a certain value, which depends on temperature, CO_2 partial pressure and the type of carbonate forming, to obtain particulate precipitation. There are several methods to prevent a solution from getting overly acidic after injecting CO_2. The most widely used is to add substances into the solution, such as buffer solution (Steel *et al*., 2013), basic inorganic chemicals (e.g. sodium hydroxide, ammonium hydroxide, industrial wastewater (Teir *et al*., 2007; Wang and Li, 2012), and solid industrial wastes such as steelmaking slag (Said *et al*., 2013), red mud and fly ashes (Bodor *et al*., 2013; Ukwattage *et al*., 2013). The approach used in this section was to contact the brine with blast furnace (BF) slag, to transfer alkalinity to the brine, with sodium hydroxide solution being used as an additional alkali substance. The dissolving slag also supplements the brine with additional alkaline earth metal ions, primarily Ca^{2+} (Zhang *et al.*, 2019).

The ultimate goal of the envisioned desalination brine carbonation process in a continuous tubular reactor is the production of commercial-grade PCC (precipitated calcium carbonate). PCC are widely used in various applications, including papermaking, paints, plastics, among others (El-Sherbiny *et al*., 2015; Wang *et al*., 2018). The physical properties of PCC largely determine the potential usage. PCC properties are predominantly determined by process conditions, as it controls the rate of nucleation and crystallisation, and thus the particle size, as well as the mineralogy of the precipitates, which controls particle shape, surface and mechanical properties. The four polymorphs of calcium carbonate ($CaCO_3$) are amorphous, calcite, vaterite and aragonite. In the presence of Mg^{2+}, several magnesium carbonates can also form under mild carbonation conditions (e.g. nesquehonite ($MgCO_3{\cdot}3H_2O$) and hydromagnesite ($Mg_5(CO_3)_4(OH)_2{\cdot}3H_2O$)), as well as magnesian calcite ($Ca_{1-x}Mg_x(CO_3)$)). Therefore, it is necessary in the present study to investigate the influence of experimental conditions in a tubular reactor for precipitated carbonate formation from desalination brine (Zhang *et al.*, 2019).

The last aspect of this section that was investigated in this section was the dissolution and dissociation of CO_2 within the tubular reactor, in particular looking for ways to accelerate the formation of carbonate (CO_3^{2-}) anions, which readily react with dissolved Ca^{2+} and Mg^{2+}. In the literature review Chapter 2, carbonic anhydrase (CA) is regarded as a suitable catalyst to accelerate CO_2 mineralisation reactions via the transformation of $CO_{2(aq)}$ into bicarbonate (HCO_3^-), as the CO_2 hydration reaction is seen as the rate-determining step (in systems with dissolved Ca^{2+} and Mg^{2+}). In the presence of CA, CO_2 hydration equilibrium can be rapidly reached, with zinc-bound OH^- reacting with dissolved CO_2 to form bicarbonate. This will also accelerate the equilibrium-controlled dissolution of gaseous CO_2 into aqueous CO_2, i.e. the carbon capture step. Like zinc, nickel can also be used as a CO_2 capture catalyst, as discussed and tested next.

In the previous work by Bhaduri and Šiller (Bhaduri and Šiller, 2013; Šiller and Bhaduri, 2013; Bhaduri *et al.*, 2015), nickel nanoparticles (NiNPs) have been demonstrated to possess catalytic activity to accelerate CO_2 hydration reaction as a first wholly inorganic heterogeneous catalyst. Therefore, NiNPs catalysts are investigated to check whether they are useful when employed to obtain solid carbonate products from desalination brines in a tubular reactor using different pH-regulating approaches, without the need for a dissolution step (Zhang *et al.*, 2019). The experiments of this section 3.2 were conducted at Sheridan College in Canada in Professor Rafael M. Santos's previous labs.

3.2.2 Process implementation with NaOH and slags

Brine is the concentrated seawater which contains very high concentrations of Ca and Mg ions. Therefore, it is regarded as an attractive source of alkaline earth metals for the mineralisation process which is ready to react with CO_2 without further extraction process. The brine can be obtained from saline aquifers from nature or the wastewater of desalination plants. The simulated brines used in this study were prepared with the identical calcium, magnesium, sodium and chloride composition as the desalination brine obtained and based on the composition from Kuwait desalination plant, which originates from Arabian Gulf seawater desalination. The complete composition of this brine, determined by ICP-OES, is as follows: 38.0 g/L Cl^-; 18.5 g/L Na^+; 4.21 g/L SO_4^{2-}; 2.40 g/L Mg^{2+}; 1.00 g/L K^+; 0.80 g/L Ca^{2+}; 0.13 g/L Br^-.

Sodium hydroxide, calcium chloride dihydrate, magnesium chloride hexahydrate, and sodium chloride were used as received. The nickel nanoparticles were purchased from Nano Technologies, Korea. Deionised water (resistivity over 18 MΩ·cm) was used to prepare solutions. Carbon dioxide (>99.9%) was purchased from Praxair Canada Inc. Solutions were prepared with one or more of the following reagents and concentrations: 0.02 M $CaCl_2$ (all solutions), 1.0 M NaOH, 0.012 M $MgCl_2$, and 0.80 M NaCl (Zhang *et al.*, 2019).

The schematic apparatus of the reactor set-up is shown in Figure 3.13(a) and the image of real set up is in Figure 3.13(b). The tubular reactor consists of a helically coiled tube immersed within a temperature-controlled bath; the reactor length is 20.9 m, with an internal diameter of 5.0 mm, and a total volume of 410 cm^3. Two lines feed the reactor and are mixed in a T-junction: one is for CO_2 coming from a compressed gas cylinder, with inlet pressure controlled by a regulator (set for all runs at 1.5 bar absolute) and volumetric flowrate controlled by a needle valve; the other is for the alkaline brine, pumped by a peristaltic pump from a feed tank where brine, chemical additives and NiNPs are gently mechanically agitated to avoid nanoparticle sedimentation. The flow rate of liquid at each pump setting was calibrated by gravimetrically measuring the exiting flow rate of liquid collected in an impinger trap. The flow rate of gas was set at the beginning of each experiment before commencing liquid flow by using a soap bubble meter connected to the outlet stream. The pattern of the flow in the multi-phase section of the tube, after the T-junction, is illustrated in Figure 3.14; in this segmented slug flow, according to Vacassy et al. (Vacassy *et al*., 2000), poor micromixing can be avoided and the homogeneity in reaction conditions is increased better than in larger volumes, leading to better control of powder characteristics. The effect of process parameters (temperature, gas flow rate, NaOH concentration), NiNPs addition, slags addition, and residence time on the calcium conversion efficiency are investigated, and results are shown in Chapter 4.

The precipitated carbonates were filtered by 0.45 µm nylon syringe filter, washed with DI water and dried at 110 °C for 5 hr. Elemental concentrations ([$Ca_{(aq)}$], [$Mg_{(aq)}$]) in the recovered liquid was tested by inductively coupled plasma optical emission spectrometry (ICP-OES, PerkinElmer Optima 8300); 2 ppm yttrium was used as an internal standard for metal ions analysis, and 0.2 M nitric acid was used as diluent. Eq.(3.5) is introduced to explain $Ca_{(aq)}$ conversion efficiency (CCE); magnesium conversion efficiency can be similarly calculated. The pH value of the exiting slurry and its electrical conductivity were also measured using Fisher Scientific Accumet Research AR20 pH meter, and Hach sension5 conductivity meter, respectively. These instruments were calibrated with standard solutions daily prior to use (Zhang *et al.*, 2019).

$$\mathrm{CCE} = \frac{\text{initial}\left[\mathrm{Ca}_{(\mathrm{aq})}\right] - \text{outlet}\left[\mathrm{Ca}_{(\mathrm{aq})}\right]}{\text{initial}\left[\mathrm{Ca}_{(\mathrm{aq})}\right]} * 100\% \qquad \text{(E3.5)}$$

Thermogravimetric analysis (TGA/DTG) of precipitated carbonates was performed by TA Instruments Q600. TGA analysis was conducted with a heating rate of 10 $°C \cdot min^{-1}$ under 100 $mL \cdot min^{-1}$ air atmosphere up to 900 °C. The chemical bonds of precipitates were investigated by The PerkinElmer Spectrum Two FTIR (Fourier-transform infrared spectroscopy). Attenuated total reflectance (ATR) technique was used. The FTIR spectra were obtained from 4000 cm^{-1} to 400 cm^{-1}. Mineral phases of precipitated products were identified and quantified from X-ray diffraction (XRD) patterns. XRD data were collected by Rigaku MiniFlex 600 with Cu radiation at scanning speed of 1.3 °·min^{-1} and step width of 0.02°. The morphology of precipitated carbonate particles was observed by a scanning electron microscopy (SEM) with Hitachi Tabletop Microscope TM3000 using 15 kV and charge-up reduction mode (Zhang *et al.*, 2019). All characterisation data are presented in Chapter 4.

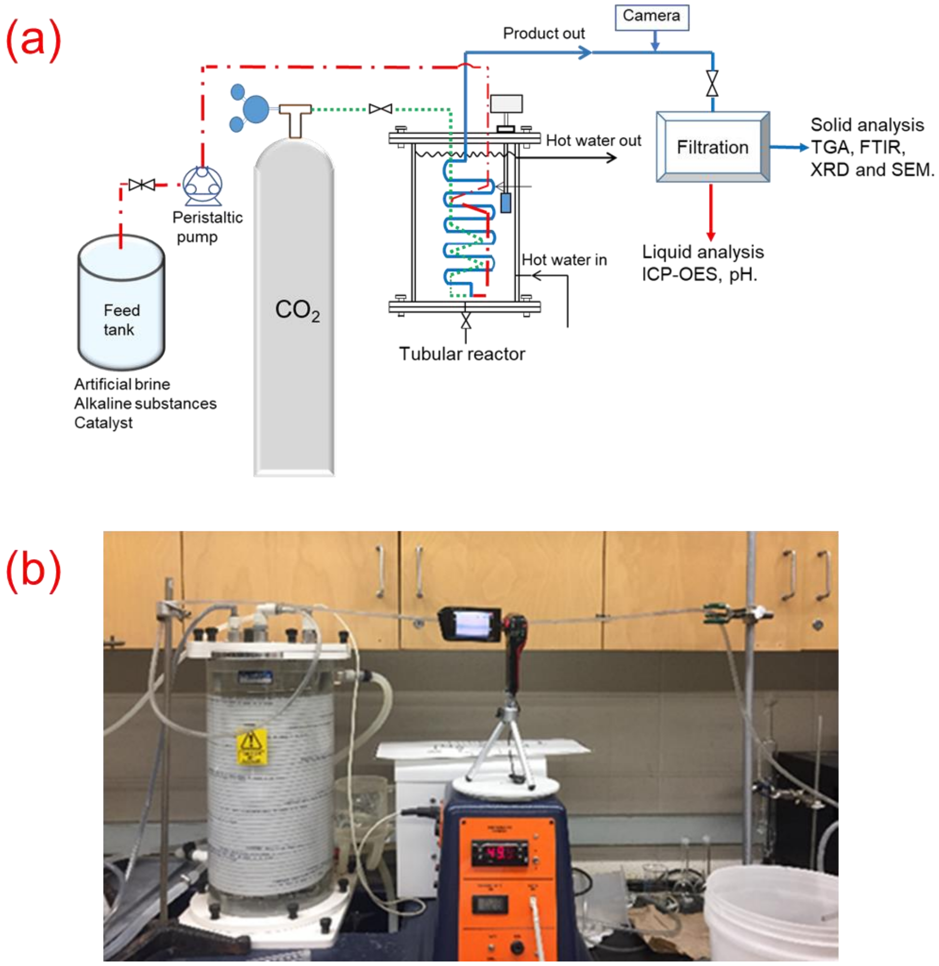

Figure 3.13 (a) The schematic apparatus of the reactor set-up (Zhang et al., 2019); (b) The image of the tubular reactor used in Chapter 4.

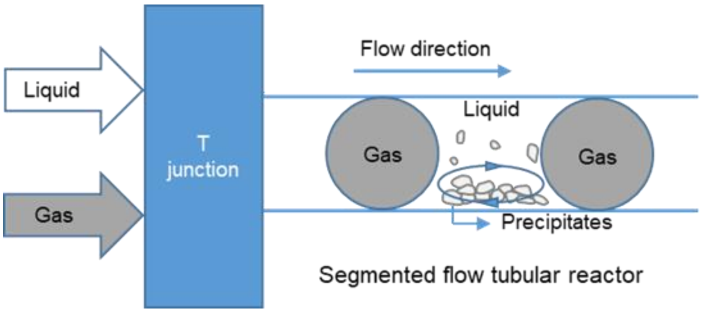

Figure 3.14 Segmented flow tubular reactor (Zhang et al., 2019).

3.3 Rapid CO_2 capture-to-mineralisation in a tubular reactor with MEA

In this section, the similar mineralisation process reactor (tubular reactor) shown in section 3.2 is implemented, and a low concentration of monoethanolamine (MEA) solution is utilised to synergistically boost CO_2 solubility in the brine while neutralising the acidification caused by brine chloride ions left in the solution following the precipitation of alkaline earth metals and relatively low concentrations of MEA, ranging from 0.036 to 0.33 M, were investigated over a temperature range from 303 K to 323 K; these are significantly milder conditions than those used in traditional CO_2 capture processes with MEA. The concentration of Ca is fixed at 0.02 M which is the same value used in section 3.2 based on the real desalination brines. Furthermore, experimental results were used to develop and calibrate a one-dimensional time-dependent plug-flow model that incorporates transport and chemical speciation equations. The model is thus capable of predicting aqueous species and solid carbonate concentrations, fluid pressure and gas slug size as a function of reactor length and the results are shown in Chapter 5. This research is published in *Reaction Chemistry & Engineering* (Zhang *et al*., 2020).

3.3.1 Experimental and modelling design

In section 3.2, carbonation of brine in a tubular reactor was investigated, using sodium hydroxide and ironmaking slag to buffer the carbonation-induced acidification. In this section, alkanolamine has been used in place of the alkali materials, as these amines, have been shown to be effective in CO_2 capture applications (Sartori and Savage, 1983), and can potentially be regenerated from the spent brine, thus reducing the cost associated with unrecoverable NaOH. Several researchers have performed experiments with solubilised alkaline earth metals and amines to form solid carbonates as listed in Chapter 2 of literature review. The process is inherently designed to employ at large-scale, therefore, the tubular reactor is continued to be used as it is favoured for industrial application due to its ease of scaling-up (simple construction and scalable as a function of reactor tube length and diameter) and its better control of product quality (simple control of residence time, and narrow residence time distribution). Other advantages of the helical coiled tubular reactor that we used are its compactness (i.e. footprint area) and more efficient heat transfer (due to high reactor surface-to-fluid volume ratio). Nickel nanoparticles (NiNPs) are introduced due to its acceleration on the mineralisation process, which translates into further energy savings and smaller reactor footprint, so consequently greater net CO_2 sequestration. NiNPs are also applied herein to investigate their effect on CO_2 mineralisation within an amine-containing brine solution. Hence, it is desired to investigate if NiNPs and an amine can synergistically work to further accelerate brine carbonation in a tubular reactor (Zhang *et al*., 2020).

A time-dependent one-dimensional three-phase (gas/liquid/solid) analytical model is developed in the present study to determine CO_2 gas-to-liquid transfer rate, aqueous solution chemical speciation, fluid pressure, and carbonation efficiency within the tubular reactor, as a function of reactor length and residence time, under different process conditions. This model simultaneously solves interfacial CO_2 mass transfer, multi-species chemical equilibria, and two-phase frictional pressure drop calculations, and determines solid carbonate concentration and gas slug size as a function of reactor length. The gas slug size and calcium conversion determined experimentally at the reactor outlet are used to calibrate the overall mass transfer coefficient in the model. Several studies have recently reported multiphase equilibrium models based on batch reactors (Rochelle* *et al*., 1989; McCann *et al*., 2008; Zhang *et al*., 2011), however in terms of CO_2 mineralisation in tubular reactors, to my best knowledge, no research has been studied before. Modelling results are used to mechanistically explain the experimental results under various MEA concentration and gas flow rates and serve for sizing the tubular reactor, thus potentially being useful for scale-up of tubular CO_2 mineralisation processes (Zhang *et al*., 2020) and the set-up and results are illustrated in section 5.6 of Chapter 5.

3.3.2 Experimental section of mineralisation with MEA

Calcium chloride dihydrate and monoethanolamine were used as received. The deionised water (resistivity over 18 MΩ·cm) was used to prepare solutions. Carbon dioxide (> 99.8%, industrial grade) was purchased from the BOC Company (UK). For the purpose of CO_2 mineralisation by calcium carbonate precipitation, the prepared brine had $CaCl_2$ concentration of 0.020 M (Zhang *et al*., 2020).

The tubular reactor consists of a helically coiled metallic tube immersed within a temperature-controlled bath; the stainless-steel reactor length is 6 m, followed by 1 m additional length of transparent tubing that was used for observing and recording the bubble frequency and bubble size, which are used in the model calibration. The internal diameter of both tubes was 5.0 mm. Two lines feed the reactor and are mixed in a T-junction as shown in Figure 3.13. One line is for gas CO_2 coming from a compressed gas cylinder, with inlet pressure controlled by a regulator (set for all runs at 1.5 bar absolute) and the second line is for the brine, pumped by a peristaltic pump from a feed tank, wherein brine, chemical additives and NiNPs catalyst are gently mechanically agitated (to avoid nanoparticle sedimentation). The flow rate of liquid at each pump setting was calibrated by gravimetrically measuring the exiting flow rate of liquid collected in an impinger trap. The flow rate of gas was set at the beginning of each experiment before commencing liquid flow by using a soap bubble meter connected to the outlet stream (Zhang *et al*., 2020).

The precipitated particles at the outlet of the reactor were filtered using a 0.20 μm nylon syringe filter from Fisher Scientific, then washed with DI water and dried at room temperature. Elemental concentration ($[Ca_{(aq)}]$) in the recovered liquid was quantified by inductively coupled plasma optical emission spectrometry (ICP-OES, PerkinElmer Optima 8000); 0.2 M nitric acid was used as diluent. Eq.(3.5) was still utilised for determination of calcite to the calcium conversion efficiency (CCE) based on the ICP-OES results. The pH values of the exiting slurry and the outlet solution were also measured using Hanna HI 2550 meter which was calibrated prior to use daily with standard solutions. Mineral phases of precipitated particles were identified from X-ray diffraction (XRD) patterns. XRD data were collected by Rigaku MiniFlex 600 with Cu radiation at a scanning speed of 1.3 $°\cdot min^{-1}$ and step width of 0.02°. The morphology of precipitated particles was observed by a scanning electron microscopy (SEM) with

Hitachi Tabletop Microscope TM3000, using 15kV and charge-up reduction mode (Zhang *et al*., 2020). The results of this experimental section are shown in section 5.1-5.5 of Chapter 5.

3.4 Cyclical mineralisation process with regenerative hydrotalcites

In the previous sections (3.2 and 3.3), alkaline substances to neutralise the solution, such as sodium hydroxide or amines, are costly to a certain degree, and the processes required to regenerate them (e.g. distillation or electrolysis) are energy intensive, which hinders the feasibility of this CO_2 sequestration approach. Therefore, a process to remove chloride anions from alkaline brines by ion exchange is developed in this chapter, using lamellar structured materials, namely hydrotalcites (HT). HTs are layered double hydroxides prepared by co-precipitation method, releasing hydroxyl groups by ion exchange with chloride, increasing the pH of brines for CO_2 mineralisation. Moreover, the HT materials are recyclable for multiple usage by taking advantage of the HT's 'memory effect' property. Gaseous CO_2 and Na_2CO_3 solution were tested as the recharging agents, to replace the chloride anions from the spent HT interlayers and intercalate with HCO_3^- or CO_3^{2-}, followed by a calcination process to produce the reusable calcined-HT (CHT). Several reaction cycles were conducted to evaluate the reusable property and results are shown in Chapter 6. This section is published in *Chemical Engineering Journal* (Zhang *et al.*, 2021).

3.4.1 Process design of mineralisation with calcined hydrotalcites

Basic substances are demanded to balance the solution acidification that results from CO_2 injection, therefore, NaOH and MEA solutions were tested (section 3.2 and 3.3), and they both performed well in brine carbonation processes, which were optimised by adjusting the operational conditions and results are shown in Chapter 4 and 5. However, these solutions can only be used once, and would require energy intensive regeneration via distillation or electrolysis for further reuse (House *et al.*, 2007). In this present research, an alternative approach is developed to replace these base solutions and to use the materials that can be easily regenerated and recycled, to cut down the cost and energy demand. This approach uses a class of materials known as hydrotalcite (HT) (Zhang *et al.*, 2021).

HT compounds are magnesium aluminium hydroxycarbonates, referring to the form $[\mathrm{M^{2+}}_{1-\mathrm{x}}\mathrm{M^{3+}}_{\mathrm{x}}(\mathrm{OH})_2]\left(\mathrm{A^{n-}_{x/n}}\right)\cdot\mathrm{mH_2O}$, which are composed of double-layered hydroxides, with interlayers containing anions or water molecules, where M^{2+} and M^{3+} represent divalent and trivalent metal ions and x is the ratio of $M^{3+}/(M^{2+} + M^{3+})$, and A^{n-} is the anions that intercalate between the layers (Miyata, 1975). The structure of this compounds is similar to brucite ($Mg(OH)_2$), comprising octahedra of Mg^{2+} cross-linked by OH^-, and each sheet is stacked to form the three-dimensional structure (Reichle *et al.*, 1986). The key feature of HT is that they are formed by sheets that are positively charged with the interlayer occupied by different anions to neutralise the charge, and H_2O molecules filling the interlayer space. The preparation method is classified into the following main categories: precipitation method (Cavani *et al.*, 1991; Li and Guo, 2015), preparation with anions rather than carbonates, hydrothermal treatment (Theiss *et al.*, 2014), anionic exchange method, urea hydrolysis method, among others (Costa *et al.*, 2012). HT have ion exchange property that can remove various anions from aqueous solutions (Duan and Evans, 2006). The interlayers ions can be replaced by other anions depending on the following order (Miyata, 1975): $CO_3^{2-} > SO_4^{2-} > OH^- > F^- > Cl^- > Br^- > NO_3^- > I^-$. This ion exchange property is governed by the ionic radii and the Gibbs free energy of reaction (Kameda *et al.*, 2007). Given the high affinity of CO_3^{2-} for HT, CO_3^{2-} is used as intercalated anion for the sample preparation in this research. Another useful property of HT is their ‘memory effect’ (Cavani *et al.*, 1991). This refers to ability of HT to be reconstructed via reacting with stronger anions in solution, and subsequently undergoing calcination process. The calcination process of regenerated HT is accompanied by an increase in surface area, as the released CO_2 and H_2O can expand the surface of interlayers (Cavani *et al.*, 1991). This can thus be implemented to regenerate the materials after anions removal process. According to the selectivity sequence of anions, carbonate anions are significantly favoured by the interlayers, therefore carbonate anions can replace any other anions in the solution, including chloride as relevant for brines (Zhang *et al.*, 2021). The regeneration of spent HT-Cl can also be implemented with thermal treatment by heating the samples to 550-800 ˚C, to release hydrochloric acid (van der Voet and de Wolff, 1986). However, higher calcination temperatures, over 600 °C, can lead to loss of ion exchange capacity because the layered hydroxide decomposes to MgO and $MgAl_2O_4$ (Hussein *et al.*, 2019).

In Chapter 6, artificial brines are implemented to undergo the chloride removal process with regenerative calcined-HT, thereby producing an alkaline solution to proceed through CO_2 mineralisation reaction. Calcined magnesium and aluminium oxides with different Mg/Al molar ratios were prepared by the thermal composition of synthetic hydrotalcite prepared via co-precipitation method, and optimal operational conditions were evaluated to achieve the highest chloride removal efficiency. The CO_2 mineral sequestration was carried out in a batch reactor, using simulated flue gas (12 vol.% CO_2) and near-ambient temperature (30 °C) to produce calcium carbonates via mineralisation process. In addition, HT was regenerated with two different approaches to investigate the feasibility to recycle this material based on its memory effect. The regeneration process with gaseous CO_2 is newly proposed, providing an approach to cut down the cost on chemicals usage and increase CO_2 utilisation efficiency. The crystal structure of mineral samples before and after different steps of the process were characterised to assess stability and degradation. The integrated process is illustrated in Figure 3.16 (Zhang *et al.*, 2021).

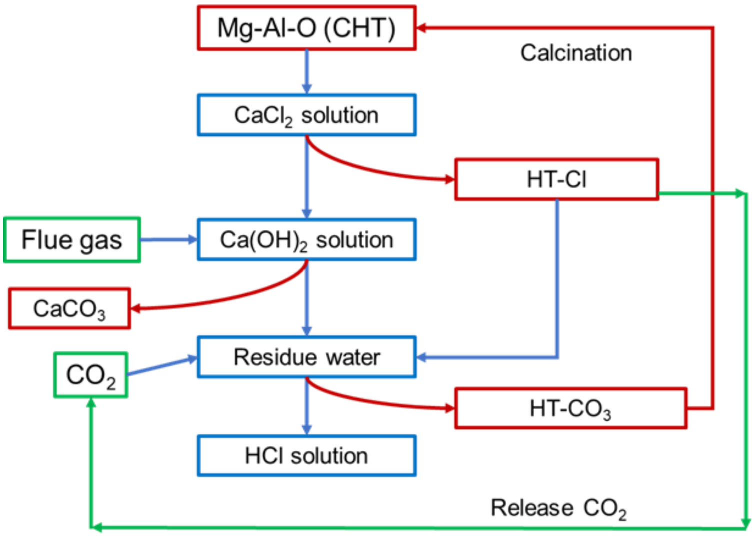

Figure 3.15 Simplified block diagram of the brine mineralisation with calcined hydrotalcite.

3.4.2 Synthesis of calcined hydrotalcite and characterisation

Magnesium nitrate hexahydrate and aluminium nitrate nonahydrate, calcium chloride dihydrate, sodium carbonate and sodium hydroxide were used as acquired. The HT were prepared via standard co-precipitation method (Miyata, 1975; Kovanda *et al.*, 2005). In a five-necked jacketed beaker, 500 mL 0.2 M Na_2CO_3 solution was placed and kept at 40 °C with circulated warm water. Then, a volume of 500 mL mixed solution of $Mg(NO_3)_2 \cdot 6H_2O$ (0.3 M or 0.4 M) and $Al(NO_3)_3 \cdot 9H_2O$ (0.1 M), prepared with the molar ratios of 3 or 4, was slowly injected into the flask using a peristaltic pump (323 series from Watson-Marlow Pumps) set at a very low flow rate. The pH value of the reacting solution was continuously monitored and kept at 10±0.1 via controlling the pumping rate of 1 M NaOH solution, based on the isoelectric point theory that CO_2 absorption is favoured when the preparation pH value is equal to, or higher than 10 (Wang and Wang, 2007). The slurry mixture was stirred vigorously to assure the pH of local portions of the solution is similar to that of the bulk. Stirring lasted for two hours, after which the obtained precipitates were filtered and washed with deionised water until the filtrate was neutral. Then the precipitates were dried at 60 °C for 24 hours to obtain the synthesised HT. It is known that the crystallinity and morphology of HT can be improved via further ageing process or with thermal treatment (Reichle *et al*., 1986). Since we aimed to produce regenerative materials with Cl removal function, it made sense to select a route with short processing time. Thus, calcined-HT (CHT) obtained from synthesised HT by heating at 500 °C for 2 hours in the standard atmosphere (Zhang *et al.*, 2021).

The produced CHT were characterised by X-ray diffraction (XRD), thermogravimetric analysis (TGA), and scanning electron microscopy with energy dispersive X-ray spectroscopy (SEM-EDX). XRD data were collected and analysed using X'Pert Pro Multipurpose from Panalytical, and diffractograms were collected using Cu radiation at scanning speed of 1.3 $°\cdot min^{-1}$ and step width of 0.02°. TGA data were collected under N_2 with the heating rates at 10 $°C\cdot min^{-1}$ using Mettler Toledo TGA 2. The morphological and elemental analyses of samples and precipitates were conducted using a JEOL JSM-5600LV SEM-EDX (Zhang *et al.*, 2021). The characterisation data are presented in section 6.1 of Chapter 6.

3.4.3 Chloride removal process

Artificial brine was prepared with $CaCl_2$ at a concentration of 0.020 M; this concentration is based on a desalination plant in Kuwait, and the main composition of this brine determined by ICP-OES can be found in section 3.1. To more closely simulate desalination brine, some tests were also conducted using solution containing both and 0.020 M $CaCl_2$ and 0.60 M NaCl. Chloride removal performance was conducted using CHT prepared using two Mg/Al molar ratios (3 and 4), under two temperatures (40 °C and 60 °C) and three solid/liquid ratios (0.010 $g \cdot mL^{-1}$ to 0.020 $g \cdot mL^{-1}$). Different removal temperatures were tested to determine the optimal reaction temperature. Another key parameter that influences the removal efficiency is the solid/liquid ratio, which refers to the ratio of CHT to brines. All experiments were performed with constant removal reaction time, 2 hours under magnetic stirring, as it was investigated that this time length is sufficient for the reaction to reach equilibrium (Zhang *et al.*, 2021).

The concentration of Ca^{2+} in the equilibrated solutions was measured by ICP-OES using Vista MPX from Varian Inc., and concentration of Cl^- was measured with ISC-1000 Ion Chromatography System from Thermal Scientific. The chloride removal efficiency is calculated via Eq.(3.5), where $C_{Cl^-(outcome)}$ and $C_{Cl^-(initial)}$ represent the concentration of chloride after reaction and initial condition, respectively and the results are presented in section 6.2 of Chapter 6. The solids recovered after equilibrium are termed HT-Cl, being hydrotalcite containing chloride in its interlayer (Zhang *et al.*, 2021).

$$\text{Chloride removal efficiency}(\%) = \left(1 - \mathrm{C}_{\mathrm{Cl}-_{(\mathrm{outcome})}} / \mathrm{C}_{\mathrm{Cl}-_{(\mathrm{initial})}}\right) \cdot 100 \qquad \text{(E3.28)}$$

3.4.4 HT-Cl regeneration via ion-exchange method

The regeneration method is based on the theory of ion exchange, due to carbonate/bicarbonate ions being more susceptible to attaching to the interlayers of HT compared to the other mono- or divalent anions (Miyata, 1975; Constantino and Pinnavaia, 1995). Two scenarios to release chloride from HT-Cl in aqueous solution were tested in this work: (i) using gaseous CO_2 injection, and (ii) adding Na_2CO_3 to the solution (Zhang *et al.*, 2021).

In the first scenario, we add HT-Cl sample to DI water and inject pure gaseous CO_2 to produce carbonate/bicarbonate ions (ratio between two species depends on the solution pH), thus releasing chloride from the interlayers of HT. Solid to liquid ratio used was 0.025 g·mL^{-1} and the gas flow rate was 160 mL·min^{-1}, which was injected into the solution intermittently to ensure the pH value did not decrease sharply (CO_2 injection stopped when the pH value reduction was over 3.0 compared to initial pH value). The total duration CO_2 of injection depended on the solution volume, with a target time of 0.07 min·mL^{-1}, after which solutions were magnetically stirred until equilibration. In the second scenario, HT-Cl samples were added to 0.1 M Na_2CO_3 solution at a solid to liquid ratio of 0.025 g·mL^{-1}, and magnetically stirred until equilibration. Both of these two experimental scenarios were conducted at room temperature (20 ˚C) and the solutions were stirred for 2 hours to allow for equilibration. After, the solids were recovered by filtration, and dried to achieve carbonate or bicarbonate bonding within the regenerated HT. The calcination process was undertaken at 500 ˚C for 2 hours to obtain regenerated CHT. Several cycles of Cl^- removal experiment and regeneration process were applied to each synthesised HT to determine regeneration efficiency. This is expressed according to Eq.(3.29), which compares the molar amount (M) of chloride was recovered in the regeneration step of the current cycle to the preceding Cl^- removal amount in the same cycle and the results are presented in section 6.3 of Chapter 6. Values lower than 100% suggest irreversible binding or entrapment of Cl^- within the HT structure (Zhang *et al.*, 2021).

$$\text{Regeneration efficiency}(\%) = \left(\mathrm{M}_{\mathrm{Cl^-}_{(\text{recovered,current cycle})}} / \mathrm{M}_{\mathrm{Cl^-}_{(\text{removed,current cycle})}}\right) \cdot 100$$

(E3.29)

3.4.5 CO_2 uptake

The dechlorinated brine solutions were used to fix CO_2 by precipitating carbonates, either for permanent storage or for utilisation in place of natural carbonates. To simulate an industrial implementation without the need for pre-carbonation CO_2 capture, the CO_2 absorption was performed with 12 vol.% CO_2 simulated flue gas, and the temperature used was 30 ˚C, to avoid the need for heating in industrial implementation. Both CO_2 capture and heating of aqueous solutions are energy-intensive processes, and thus have a significant effect on the net CO_2 sequestration of a mineral carbonation process. As such, the present process aims at minimising energy requirements and maximising net CO_2 sequestration. The experiments were conducted with a 200 mL screwed reactor with three ports on the cap to fix the pH probe, thermocouple and bubble generator. Flue gas was bubbled into the solutions obtained from Cl^- removal step, and the pH was monitored in real-time to terminate the process and the pH was 8 in this study when high calcium conversion efficiency is achieved and before further acidification leads to carbonate re-dissolution. The solution was magnetically stirred at the rate of 500 rpm throughout the process. The final Ca^{2+} concentration, post-carbonation, was measured with ICP-OES, and calcium conversion efficiency (CCE) was calculated according to Eq.(3.30) and the results are presented in section 6.4 of Chapter 6. The carbonate precipitates were filtered and dried prior to characterisation (Zhang *et al.*, 2021).

$$\mathrm{Ca^{2+}\ conversion\ efficiency(\%)} = \left(1 - \mathrm{C}_{\mathrm{Ca^{2+}}_{(\mathrm{outcome})}} / \mathrm{C}_{\mathrm{Ca^{2+}}_{(\mathrm{initial})}}\right) \cdot 100 \quad \text{(E3.30)}$$

Reference

Bhaduri, G.A., Alamiry, M.A.H. and Šiller, L. (2015) 'Nickel Nanoparticles for Enhancing Carbon Capture', *Journal of Nanomaterials*, 2015, pp. 1-13.

Bhaduri, G.A. and Šiller, L. (2013) 'Nickel nanoparticles catalyse reversible hydration of carbon dioxide for mineralization carbon capture and storage', *Catalysis Science & Technology*, 3(5), pp. 1234-1239.

Bodor, M., Santos, R., Gerven, T. and Vlad, M. (2013) 'Recent developments and perspectives on the treatment of industrial wastes by mineral carbonation - a review', *Open Engineering*, 3(4), pp. 566-584.

Cavani, F., Trifiro, F. and Vaccari, A. (1991) 'Hydrotalcite-type anionic clays: Preparation, properties and applications', *Catalysis today*, 11(2), pp. 173-301.

Constantino, V.R. and Pinnavaia, T.J. (1995) 'Basic properties of $Mg^{2+}{}_{1-x}Al^{3+}{}_{x}$ layered double hydroxides intercalated by carbonate, hydroxide, chloride, and sulfate anions', *Inorganic Chemistry*, 34(4), pp. 883-892.

Costa, D.G., Rocha, A.B., Souza, W.F., Chiaro, S.S.X. and Leitão, A.A. (2012) 'Comparative Structural, thermodynamic and electronic analyses of Zn - Al - A^{n-}

hydrotalcite-like compounds ($A^{n-} = Cl^-, F^-, Br^-, OH^-, CO_3^{2-}$ or NO_3^-): An ab initio study', *Applied Clay Science*, 56, pp. 16-22.

Cullity, B.D. and Stock, S.R. (2001) *Elements of X-ray Diffraction*. Prentice hall New Jersey.

Dean, J. (2005) *Practical Inductively Coupled Plasma Spectroscopy*. John Wiley & Sons, Ltd.

Dean, J.R., Ando, D.J. and Metcalfe, E. (1997) *Atomic absorption and plasma spectroscopy*. John Wiley & Son Ltd.

Duan, X. and Evans, D.G. (2006) *Layered double hydroxides*. Springer Science & Business Media.

Eder, R.J., Radl, S., Schmitt, E., Innerhofer, S., Maier, M., Gruber-Woelfler, H. and Khinast, J.G. (2010) 'Continuously seeded, continuously operated tubular crystallizer for the production of active pharmaceutical ingredients', *Crystal growth & design*, 10(5), pp. 2247-2257.

El-Sherbiny, S., El-Sheikh, S.M. and Barhoum, A. (2015) 'Preparation and modification of nano calcium carbonate filler from waste marble dust and commercial limestone for papermaking wet end application', *Powder Technology*, 279, pp. 290-300.

Fagerlund, J., Nduagu, E., Romão, I. and Zevenhoven, R. (2012) 'CO_2 fixation using magnesium silicate minerals part 1: Process description and performance', *Energy*, 41(1), pp. 184-191.

Fritz, J.S. (1987) 'Ion chromatography', *Analytical Chemistry*, 59(4), pp. 335A-344A.

Gabbott, P. (2008) *Principles and applications of thermal analysis*. John Wiley & Sons.

Goldstein, J.I., Newbury, D.E., Michael, J.R., Ritchie, N.W., Scott, J.H.J. and Joy, D.C. (2017) *Scanning electron microscopy and X-ray microanalysis*. Springer.

Greenfield, S., Jones, I.L. and Berry, C. (1964) 'High-pressure plasmas as spectroscopic emission sources', *Analyst*, 89(1064), pp. 713-720.

Hill, S.J. (1999) *Inductively coupled plasma spectrometry and its applications*. Wiley Online Library.

House, K.Z., House, C.H., Schrag, D.P. and Aziz, M.J. (2007) 'Electrochemical acceleration of chemical weathering as an energetically feasible approach to mitigating anthropogenic climate change', *Environmental Science & Technology*, 41(24), pp. 8464-8470.

Hussein, A.M.A., Burra, K.G., Bassioni, G., Hammouda, R.M. and Gupta, A.K. (2019) 'Production of CO from CO_2 over mixed-metal oxides derived from layered-double-hydroxides', *Applied Energy*, 235, pp. 1183-1191.

Kameda, T., Yoshioka, T., Watanabe, K., Uchida, M. and Okuwaki, A. (2007) 'Dehydrochlorination and recovery of hydrochloric acid by thermal treatment of a chloride ion-intercalated hydrotalcite-like compound', *Applied clay science*, 37(1-2), pp. 215-219.

Kashid, M.N., Renken, A. and Kiwi-Minsker, L. (2011) 'Gas–liquid and liquid–liquid mass transfer in microstructured reactors', *Chemical Engineering Science*, 66(17), pp. 3876-3897.

Kauppinen, J. and Partanen, J. (2011) *Fourier transforms in spectroscopy*. John Wiley & Sons.

Kovanda, F., Koloušek, D., Cílová, Z. and Hulínský, V. (2005) 'Crystallization of synthetic hydrotalcite under hydrothermal conditions', *Applied Clay Science*, 28(1-4), pp. 101-109.

Krinsley, D.H., Pye, K., Boggs Jr, S. and Tovey, N.K. (2005) *Backscattered scanning electron microscopy and image analysis of sediments and sedimentary rocks*. Cambridge University Press.

Kurt, S.K., Warnebold, F., Nigam, K.D.P. and Kockmann, N. (2017) 'Gas-liquid reaction and mass transfer in microstructured coiled flow inverter', *Chemical Engineering Science*, 169, pp. 164-178.

Lee, M. (2017) *X-ray diffraction for materials research: from fundamentals to applications*. Apple Academic Press.

Li, M. and Guo, Q. (2015) 'The preparation of the hydrotalcite-based composite phase change material', *Applied Energy*, 156, pp. 207-212.

McCann, N., Maeder, M. and Attalla, M. (2008) 'Simulation of enthalpy and capacity of CO_2 absorption by aqueous amine systems', *Industrial & Engineering Chemistry Research*, 47(6), pp. 2002-2009.

Miyata, S. (1975) 'The Syntheses of Hydrotalcite-Like Compounds and Their Structures and Physico-Chemical Properties-I: the Systems Mg^{2+}-Al^{3+}-NO_3^-, Mg^{2+}-Al^{3+}-Cl^-, Mg^{2+}-Al^{3+}-ClO_4^-, Ni^{2+}-Al^{3+}-Cl^- and Zn^{2+}-Al^{3+}-Cl^-', *Clays and Clay Minerals*, 23(5), pp. 369-375.

PerkinElmer (2020a) *The Optima 8000 ICP-OES: A Unique DoubleMonochromator Optical System*. Available at: https://www.perkinelmer.com/lab-solutions/resources/docs/TCH_Optima8000DoubleMonochromator.pdf (Accessed: 8 May 2020).

PerkinElmer (2020b) *Spectrum Two FT-IR Spectrometer*. Available at: https://www.perkinelmer.com/uk/product/spectrum-two-ft-ir-sp10-software-l160000a (Accessed: 8 May 2020).

PerkinsElmer (2020) *Optima 8000 ICP-OES Spectroscopy Custom-Designed SolidState Detector*. Available at: https://www.perkinelmer.com/CMSResources/Images/44-130617TCH_Optima8000Solid-StateDetector.pdf (Accessed: 8 May 2020).

Pütün, A., Özcan, A. and Pütün, E. (1999) 'Pyrolysis of hazelnut shells in a fixed-bed tubular reactor: yields and structural analysis of bio-oil', *Journal of Analytical and Applied Pyrolysis*, 52(1), pp. 33-49.

Reed, S.J.B. (2005) *Electron microprobe analysis and scanning electron microscopy in geology*. Cambridge university press.

Reichle, W., Kang, S. and Everhardt, D. (1986) 'The nature of the thermal decomposition of a catalytically active anionic clay mineral', *Journal of Catalysis*, 101(2), pp. 352-359.

Rochelle*, D.M.A.a.G.T., Peng, X. and Chen, C.-C. (1989) 'Model of Vapor-Liquid Equilibria for Aqueous Acid Gas-Alkanolamine Systems Using the Electrolyte-NRTL Equation', *Industrial & Engineering Chemistry Research*, 28, pp. 1060-1073.

Said, A., Mattila, H.-P., Järvinen, M. and Zevenhoven, R. (2013) 'Production of precipitated calcium carbonate (PCC) from steelmaking slag for fixation of CO_2', *Applied Energy*, 112, pp. 765-771.

Sartori, G. and Savage, D.W. (1983) 'Sterically hindered amines for carbon dioxide removal from gases', *Industrial & Engineering Chemistry Fundamentals*, 22(2), pp. 239-249.

Šiller, L. and Bhaduri, G.A. (2013) *Carbon Capture, Patent, T/GB2013/051243 (WO 2013171480 A2, WO2013171480 A3,US20150151248 A1, EP2849871 A2, CN104428051 A)*.

Skoog, D.A., Holler, F.J. and Crouch, S.R. (2017) *Principles of instrumental analysis*. Cengage learning.

Smith, B.C. (2011) *Fundamentals of Fourier transform infrared spectroscopy*. CRC press.

Soares, J.B. and McKenna, T.F. (2013) *Polyolefin reaction engineering*. John Wiley & Sons.

Steel, K.M., Alizadehhesari, K., Balucan, R.D. and Bašić, B. (2013) 'Conversion of CO_2 into mineral carbonates using a regenerable buffer to control solution pH', *Fuel*, 111, pp. 40-47.

Teir, S., Kuusik, R., Fogelholm, C.-J. and Zevenhoven, R. (2007) 'Production of magnesium carbonates from serpentinite for long-term storage of CO_2', *International Journal of Mineral Processing*, 85(1-3), pp. 1-15.

Tennyson, J. (2010) *Astronomical spectroscopy: an introduction to the atomic and molecular physics of astronomical spectra*. World Scientific.

Theiss, F.L., Couperthwaite, S.J., Ayoko, G.A. and Frost, R.L. (2014) 'A review of the removal of anions and oxyanions of the halogen elements from aqueous solution by layered double hydroxides', *Journal of Colloid and Interface Science*, 417, pp. 356-68.

Ukrainczyk, M., Kontrec, J., Babić-Ivančić, V., Brečević, L. and Kralj, D. (2007) 'Experimental design approach to calcium carbonate precipitation in a semicontinuous process', *Powder Technology*, 171(3), pp. 192-199.
Ukwattage, N.L., Ranjith, P.G. and Wang, S.H. (2013) 'Investigation of the potential of coal combustion fly ash for mineral sequestration of CO_2 by accelerated carbonation', *Energy*, 52, pp. 230-236.

Ul-Hamid, A. (2018) *A Beginners' Guide to Scanning Electron Microscopy*. Springer.
Vacassy, R., Lemaître, J., Hofmann, H. and Gerlings, J.H. (2000) 'Calcium carbonate precipitation using new segmented flow tubular reactor', *AIChE Journal*, 46(6), pp. 1241-1252.

Vallapragada, V.V., Inti, G. and Ramulu, J.S. (2011) 'A Validated Inductively Coupled Plasma-Optical Emission Spectrometry (ICP-OES) Method to Estimate Free Calcium and Phosphorus in In Vitro Phosphate Binding Study of Eliphos Tablets', *American Journal of Analytical Chemistry*, 02(06), pp. 718-725.

van der Voet, G.B. and de Wolff, F.A. (1986) 'Intestinal absorption of aluminium from antacids: a comparison between hydrotalcite and algeldrate', *Journal of Toxicology: Clinical Toxicology*, 24(6), pp. 545-553.

Walker, R. (1961) 'Chemical reaction and diffusion in a catalytic tubular reactor', *The Physics of Fluids*, 4(10), pp. 1211-1216.

Wang, D. and Li, Z. (2012) 'Gas-Liquid Reactive Crystallization Kinetics of Hydromagnesite in the $MgCl_2$-CO_2-NH_3-H_2O System: Its Potential in CO_2 Sequestration', *Industrial & Engineering Chemistry Research*, 51(50), pp. 16299-16310.

Wang, J., Kong, Y., Liu, F., Shou, D., Tao, Y. and Qin, Y. (2018) 'Construction of pH-responsive drug delivery platform with calcium carbonate microspheres induced by chitosan gels', *Ceramics International*, 44(7), pp. 7902-7907.

Wang, S.-L. and Wang, P.-C. (2007) 'In situ XRD and ATR-FTIR study on the molecular orientation of interlayer nitrate in Mg/Al-layered double hydroxides in water', *Colloids and Surfaces A: Physicochemical and Engineering Aspects*, 292(2-3), pp. 131-138.

Warren, B.E. (1990) *X-ray Diffraction*. Courier Corporation.
Weiss, J. (2016) *Handbook of Ion Chromatography, 3 Volume Set*. John Wiley & Sons.

Zhang, N., Santos, R.M. and Šiller, L. (2020) 'Rapid CO_2 capture-to-mineralisation in a scalable reactor', *Reaction Chemistry & Engineering*, 5(3), pp. 473-484.

Zhang, N., Santos, R.M., Smith, S.M. and Šiller, L. (2019) 'Acceleration of CO_2 mineralisation of alkaline brines with nickel nanoparticles catalysts in continuous tubular reactor', *Chemical Engineering Journal*, 377, p. 120479.

Zhang, N., Santos, R.M. and Šiller, L. (2021) 'CO_2 mineralisation of brines with regenerative hydrotalcites in a cyclical process', *Chemical Engineering Journal*, 404, p. 126450.

Zhang, Y., Que, H. and Chen, C.-C. (2011) 'Thermodynamic modeling for CO_2 absorption in aqueous MEA solution with electrolyte NRTL model', *Fluid Phase Equilibria*, 311, pp. 67-75.

Chapter 4. Acceleration of CO_2 mineralisation of brines in a continuous tubular reactor

In this chapter, the results of brine carbonation process with a continuous plug-flow tubular reactor are shown here. The experimental methodology is shown in section 3.2 of Chapter 3. To neutralise the acidification effect by dissolving CO_2, the brine was mixed with blast furnace (BF) slags, with sodium hydroxide being used as an additional basic substance to increase the required pH for mineralisation. Nickel nanoparticles (NiNPs) are applied as catalysts to accelerate the mineralisation process. The effects of reaction temperature, composition of alkaline brine solution and residence time in the tubular reactor, on the calcium conversion efficiency (CCE) and the mineral composition of the precipitates were investigated. The results of this chapter have been published in *Chemical Engineering Journal* (Zhang *et al.*, 2019).

4.1 Effects of process parameters

The first set of investigations herein presented pertains to studying the effect of several process parameters (gas flow rate, temperature, and NaOH concentration) on the CCE and properties of the precipitated carbonate products. Figure 4.1 shows how gas flow rate between 20 to 40 $mL\cdot min^{-1}$ affects the CCE, pH and conductivity at a fixed flow rate of liquid (80 $mL\cdot min^{-1}$). The residence time of the slurry moderately differed between these runs given that the total flow rate differs; effect of residence time is separately studied in section 4.4 of this chapter. The aim here was to determine if an excess of CO_2 leads to more complete conversion. The CCE increased with G/L ratio (i.e. gas flow rate) up to a maximum, while higher ratios of G/L resulted in lower CCE due to the markedly lower pH (< 7.5), which partially prevents precipitation of carbonates (Zhang *et al.*, 2019).

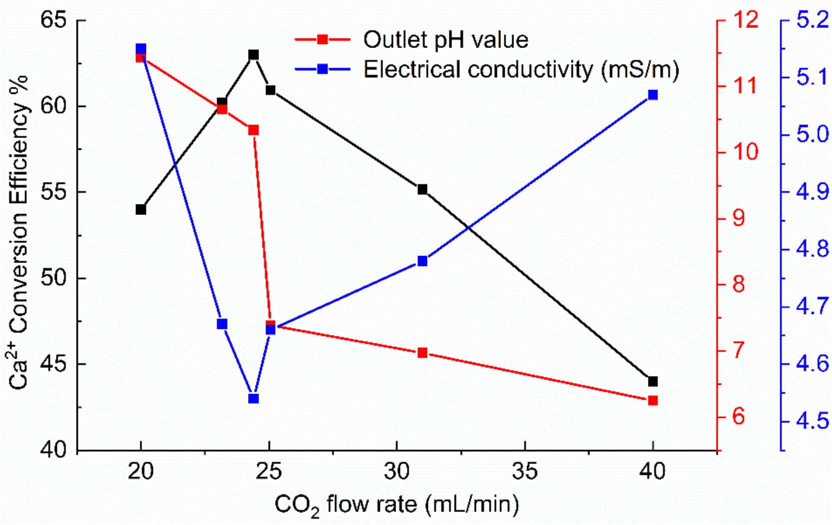

Figure 4.1 Effect of CO_2 flow rate on changes in Ca^{2+} conversion efficiency, pH value and electrical conductivity. The experiment was conducted at 50 °C and the brine pumping rate was 80 $mL{\cdot}min^{-1}$ (Zhang et al., 2019).

The pH value decreased continually with greater amounts of gaseous CO_2 introduced, but there is a sharp decrease between 23-25 $mL{\cdot}min^{-1}$ gas flow rate. Carbon dioxide enters the water phase via an equilibrium reaction to form carbonic acid. It is understood from this data that when the carbonation reaction is faster than CO_2 dissolution, at low G/L ratio, the pH remains high, but when CO_2 dissolves faster, the pH is driven lower as the carbonation reaction is not able to consume carbonate ions fast enough. At higher G/L two mechanisms can cause faster CO_2 dissolution (i.e. faster CO_2 flux ($mol{\cdot}m^{-2}{\cdot}s^{-1}$) across the gas-liquid interface): (i) higher gas phase pressure, resulting from the higher pressure drop at greater total flow rate going through the tube, and (ii) greater gas-liquid contact area (Zhang *et al.*, 2019).

The electrical conductivity showed an opposite trend to CCE. At low G/L ratio, more precipitates were formed, causing the conductivity of the solution to decrease as ions are removed, up to a minimum value. At higher G/L, the excess amount of dissociated carbonic acid and lack of carbonate precipitation resulted in increasing conductivity.
According to Figure 4.1, at a flow rate of 24.4 $mL{\cdot}min^{-1}$, the highest conversion efficiency was achieved in this set of experiments: 63%. To optimise the process to obtain 100% CCE, at an elevated brine flow rate of 30 $mL{\cdot}min^{-1}$, greater alkali concentration in solution is needed to balance the extra CO_2 being dissolved. It was

found, according to Table 4.1, that when the NaOH volume (1 M solution) added to the brine is 50 mL (3.2 vol.%), the CCE increased to 81.4%, compared to only 57.3% when using 40 mL NaOH (2.6 vol.%). Yet, the outlet pH was still low, therefore, more alkali solution was added into the brine, as Table 4.1 shows, and at 60 mL (3.8 v%) NaOH addition, 89.3% CCE was achieved, while the outlet pH is relatively high at 11.23. This means that the amount of CO_2 can still be increased further (to achieve a closer to neutral outlet pH that is still supportive of carbonate precipitation). Therefore, a higher flow rate of CO_2 at 35 $mL \cdot min^{-1}$ was selected, with 60 mL NaOH (3.8 vol.%) in the brine, and 100% CCE was achieved under this condition. The key to maximizing CCE of brine is to balance the amount of alkali with the flux of CO_2 from the gas slugs to the liquid film and plugs within the tubular reactor (Zhang *et al.*, 2019).

Table 4.1 Conversion of Ca^{2+} in experiments using various NaOH concentrations in the brine; CO_2 flow rate was 30 $mL \cdot min^{-1}$, brine flow rate was 80 $mL \cdot min^{-1}$, and temperature was 50 °C (Zhang et al., 2019).

NaOH solution volume (mL), concentration (vol.%)	40 (2.6 vol.%)	50 (3.2 vol.%)	60 (3.8 vol.%)
CCE (%)	57.3	81.4	89.3
Outlet pH value	7.07	7.72	11.23

It is also essential to investigate the effect of reaction temperature. The higher reaction temperature can benefit the mass transfer of ions, and shifts the carbonate precipitation equilibrium towards the product side, but it also reduces the solubility limit of CO_2. The latter becomes a process limitation when the rate of CO_2 mineralisation is much faster than the rate of CO_2 dissolution, in which case the residence time in the reactor may not be enough to fully carbonate the available alkaline earth metal ions. In the present system, with the liquid and gas flow rate at 80 $mL \cdot min^{-1}$ and 24.4 $mL \cdot min^{-1}$, the CCE is slight improved at 25 °C by 1.5%, which implies that greater CO_2 solubility has a benefit over the slower rate of carbonate crystallization at lower temperature. The more significant effect of temperature was on the morphology and mineralogy of the carbonate particles (Zhang *et al.*, 2019).

The ATR-FTIR spectra of calcium carbonates are illustrated in Figure 4.2. The bands at around 1080 and 850 cm^{-1} are assigned to the symmetric carbonate stretching and out-of-plate bending vibrations (Nan *et al.*, 2008) and the peaks at around 1400 cm^{-1} are the carbonate asymmetric stretching vibration. The characteristic spectra of calcite is 713 cm^{-1} (Vagenas *et al.*, 2003). The products analysed were obtained at temperature 25 °C and 50 °C, and both contain calcite. The absorption band at 745 cm^{-1} is attributed to vaterite, and the ones at 700 cm^{-1} and 713 cm^{-1} are indicative of aragonite (Vagenas *et al.*, 2003). These results suggest that the precipitates formed at 25 °C are the mixture of calcite and vaterite, while at 50 °C they are calcite and aragonite (Zhang *et al.*, 2019).

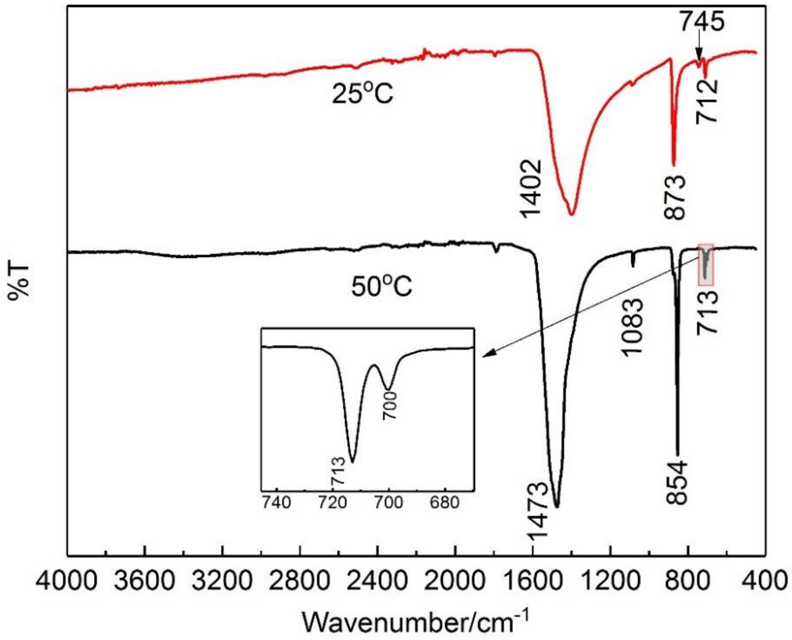

Figure 4.2 ATR-FTIR spectra of products obtained at different temperatures (Zhang et al., 2019).

The XRD results in Figure 4.3 identifies the different crystalline phases of calcium carbonates in the diffractograms of the precipitates formed at different temperatures. The XRD results are in agreement with the FTIR data. The strong peak at 29.4° is assigned to the 104 plane of the calcite, and the products formed at both temperatures contain calcite. The reaction product formed at 25 °C revealed calcite and vaterite, corresponding to DB card files 01-078-4615 (calcite) and 01-074-1867 (vaterite). The quantitative analysis results indicated the component of various CaCO$_3$ phases: calcite (42.8%) and vaterite (57.2%) at 25 °C, and calcite (59.8%) and aragonite (40.2%) at

50 °C. Thus, it is observed that the crystallization of $CaCO_3$ is depended on reaction temperature, and more $CaCO_3$ is transformed to calcite and aragonite at higher temperature due to these being more stable phases compared to vaterite (Spanos and Koutsoukos, 1998).

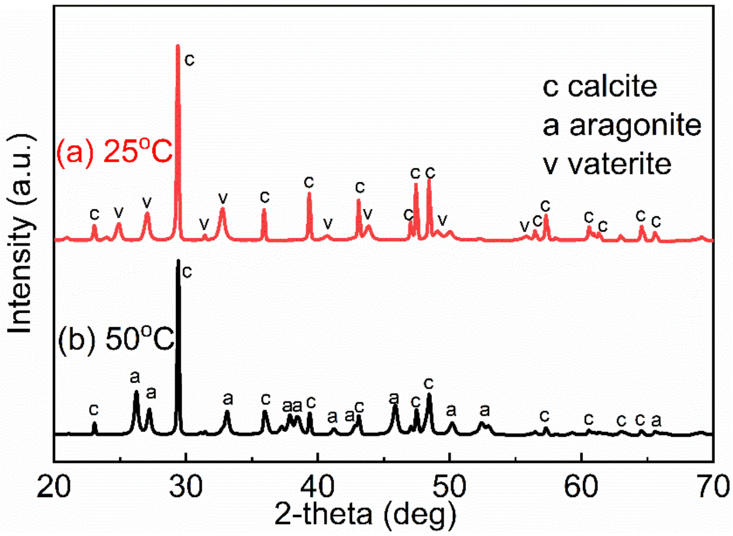

Figure 4.3 XRD patterns (b) of calcium carbonates precipitates obtained at different temperatures. The experiments were conducted with 2.6 vol% NaOH solution and liquid to gas flow rate ratio (mL/mL) was 80/24 (Zhang et al., 2019).

SEM images (Figure 4.4) also showed the different morphologies of precipitated products obtained at 25 °C and 50 °C. The size of most of particle produced at 50 °C is smaller than those obtained at 25 °C. Spherical vaterite particles are evident in the low temperature powder (Chu *et al.*, 2013), while needle-like aragonite is visible in the high temperature sample and cubic rhombohedral calcite particles are found in both samples (Shen *et al.*, 2006), though particle size of calcite clearly differs. The results of SEM imaging are in accord with FTIR and XRD results (Zhang *et al.*, 2019).

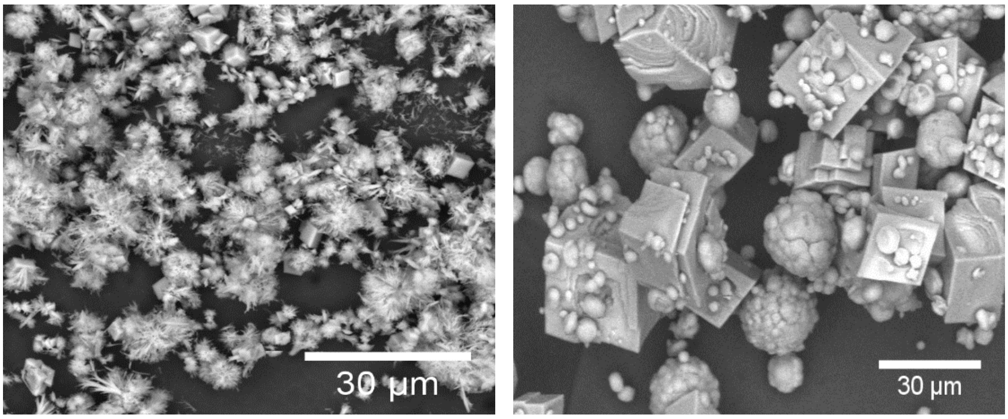

Figure 4.4 SEM images of calcium carbonates powders (left) 50 °C, (right) 25 °C. The experiments were conducted with 2.6 vol% NaOH solution and liquid to gas flow rate ratio (mL/mL) was 80/24 (Zhang et al., 2019).

4.2 Effect of slag addition to brines

In order to reduce the required amounts of NaOH in the brine, the industrial waste Blast Furnace (BF) slag was added to the brine feed tank to transfer alkalinity to the brine and to concurrently offer extra alkaline earth metal ions in the solution. The elemental components of the slag are shown in Table 4.2, characterizing a material that is primarily an amorphous calcium silicate. First, coarse slag (2.75-4.25 mm) was mixed with the brine on the hot plate at 50 °C under magnetic stirring at 400 rpm for 1 hour. ICP-OES analysis of the brine at this stage showed that 80 $mg \cdot L^{-1}$ more calcium ions were added to the solution. The particle size was chosen not to maximize slag dissolution, but rather to ensure that slag particles remained in the feed tank rather than flow into the tubular reactor. This was achieved by gently mixing the feed tank contents and placing the pump inlet tube high enough above the bottom of the tank (Zhang *et al.*, 2019).

Table 4.2 Chemical composition of BF slag (wt.%) as determined by XRF analysis (Zhang et al., 2019).

K_2O	Na_2O	TiO_2	S	Fe	CaO	Mn	SiO_2
0.46	0.34	1.33	1.22	0.29	38.9	0.23	36.8

At the gas flow rates of 20 and 30 $mL \cdot min^{-1}$ (Figure 4.5), there is a little improvement for $CaCO_3$ production because the amount of alkali solution is enough to balance the introduced CO_2. However, at the gas flow rate of 40 $mL \cdot min^{-1}$, there is a relatively significant increase in CCE, which can be attributed to the benefit of OH^- introduction from Eq.(4.1-4.2). The calcium oxide in the slag reacted with water forming $Ca(OH)_2$, and dissociating to Ca^{2+} and OH^-. Even though the initial calcium concentration in the brine is much higher (0.020 M) than that leached from the slag (0.002 M), and under these conditions only partial carbonation is achieved, slag addition results in improved CCE (the CCE calculated only takes into account the brine Ca^{2+} concentration). This reveals that the influence of hydroxyl concentration in the brine is stronger than that of Ca^{2+} (Zhang *et al.*, 2019).

$$\mathrm{CaO} + \mathrm{H_2O} \rightarrow \mathrm{Ca(OH)_2} \qquad \text{(E4.1)}$$

$$\mathrm{Ca(OH)_2} \leftrightarrow \mathrm{Ca^{2+}} + 2\mathrm{OH^-} \qquad \text{(E4.2)}$$

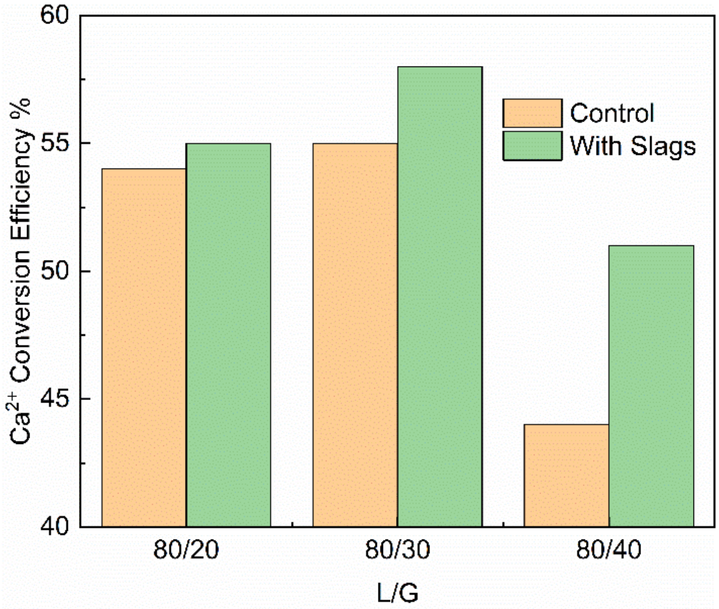

Figure 4.5 Effect of slag addition with various liquid/gas flow rate ratios (mL/mL). The experiments were conducted with 2.6 vol.% NaOH solution and reaction temperature was 50 °C (Zhang et al., 2019).

4.3 Effect of nickel nanoparticles addition

The objective of adding nickel nanoparticles to the alkalinised (NaOH-containing) brine was to promote the CO_2 hydration reaction. Figure 4.6(a) shows the measured benefit of NiNPs addition. As previously illustrated, we need to control the pH value to be higher than 8 to promote the precipitation of $CaCO_3$. At the brine-to-CO_2 flow rate ratio of 80/23.15, reacted at 50 °C, the CCE was 60.4% without NiNPs, and 66.5% with the addition of 30-ppm NiNPs to the brine. Assuming a gas phase pressure of 150 kPa (value measured at the inlet pressure gauge) and disregarding pressure drop along the tube length, the molar volume of CO_2 in these experiments was 15.5 L·mol^{-1} (a gas phase temperature of 43 °C is used as measured at the slurry outlet, while the nominal 50 °C is the water bath set-point temperature). Using the volumetric flow rates of gas and liquid, and the CCE value measured, it is thus possible to estimate the CO_2 gas utilization efficiency (i.e. how much of the injected CO_2 gas is converted to solid carbonate). The CO_2 gas utilization efficiency is calculated to be 64.7% without NiNPs and 71.2% with NiNPs (Zhang *et al.*, 2019).

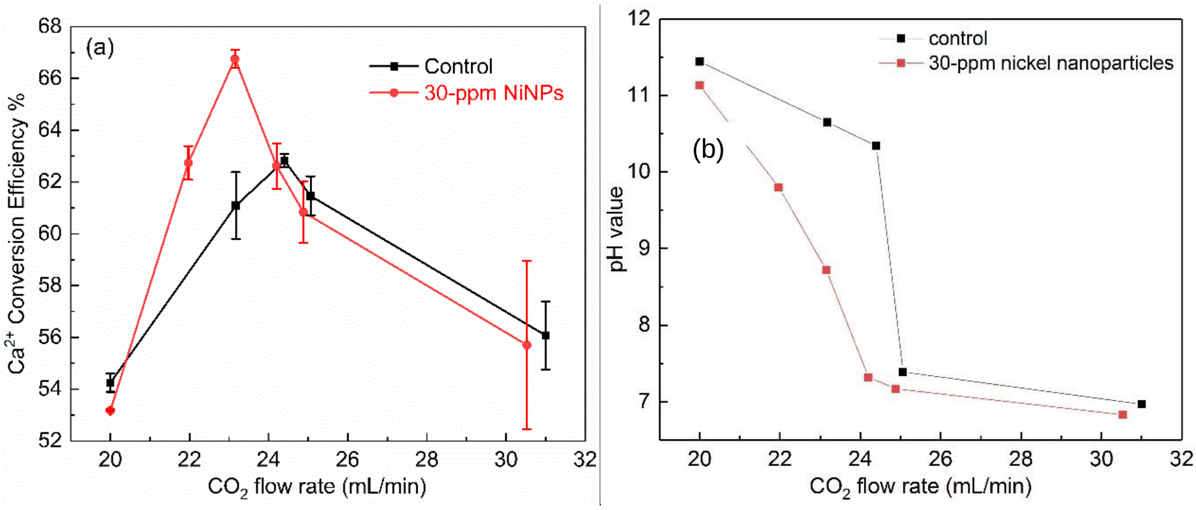

Figure 4.6 Ca^{2+} conversion efficiency (a) and outlet pH (b) varied with and without NiNPs catalyst; temperature was 50 °C and alkalinised brine flow rate was 80 mL·min^{-1} (Zhang et al., 2019).

At the CO_2 flow rate of 20 mL·min^{-1} (Figure 4.6 (a)), due to the outlet pH being over 11 (Figure 4.6 (b)), the benefit of NiNPs is not seen. At the CO_2 flow rate of 30 mL·min^{-1}, where the pH is below optimal, and more so with NiNPs, the CCE is even lower with NiNPs than without nickel nanoparticles. It was between roughly from 21 to 26 mL·min^{-1} that the reactions with NiNPs showed advantages to mineralise more CO_2. The pH curves (Figure 4.6(b)) suggest that NiNPs maintain a lower brine pH value during reaction compared to the control conditions, and this effect is predominant in the range where the best CCE values were obtained (Figure 4.6(a)). In the absence of NiNPs, the pH shift is more gradual up until the buffering capacity of the solution is lost. Dissolved CO_2 in the form of H_2CO_3 may lose up to two protons through the acid equilibria, and while the dissociation of proton is an instant reaction (Ho and Sturtevant, 1963), the kinetics to form H_2CO_3 from $CO_{2(aq)}$ are relatively slow. The hydroxyl groups that form on the surface of NiNPs act to accelerate the $CO_{2(aq)}$ hydration reaction (Bhaduri and Šiller, 2013), leading to more rapid acidification, and in this case of the tubular reactor and its relatively short residence time (~4 min), this results in lower pH of the carbonating brine even before its buffering capacity, from the alkalinisation, is spent (Zhang *et al.*, 2019).

Figure 4.7 shows the TGA and DTG data of obtained precipitates with and without NiNPs. Although the samples were dried, 1 wt.% mass loss observed before 200 °C, corresponding to the loss of water. From 200 °C onwards the sample masses remain stable until 620 °C, after which CO_2 mass is lost and the DTG peak occurs at 800 °C. The measured mass loss from both samples essentially equals the theoretical mass of 44 wt.% of pure $CaCO_3$ into CaO, indicating that both samples have high levels of PCC purity. This set of data indicates that NiNPs has no effect on the thermal stability of the precipitated carbonates (Zhang *et al.*, 2019).

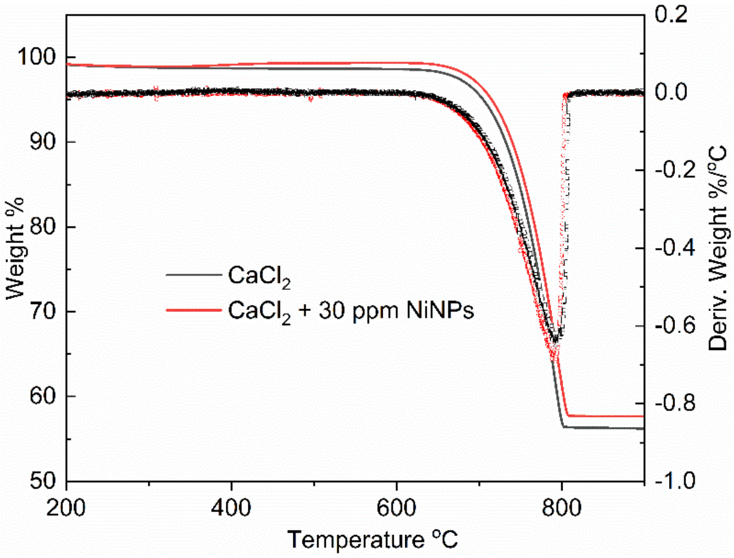

Figure 4.7 Weight loss (wt.%) and derivative weight loss (wt.%/°C) as a function of temperature in TGA/DTG analyser, for $CaCO_3$ obtained under control conditions and in the presence of NiNPs catalyst (Zhang et al., 2019).

The CO_2 mineralisation with and without NiNPs was also studied at a lower temperature of 25 °C. Figure 4.8 illustrates the XRD diffractograms of the obtained precipitates. In the presence of NiNPs, calcite is the only crystalline phase present, compared to a mixture of calcite (42.8%) and vaterite (57.2%) without NiNPs. This indicates that an additional benefit of NiNPs may be more mineralogically homogeneous PCC, perhaps with the nanoparticles aiding in the nucleation/crystallization of the more stable polymorph (Zhang *et al.*, 2019).

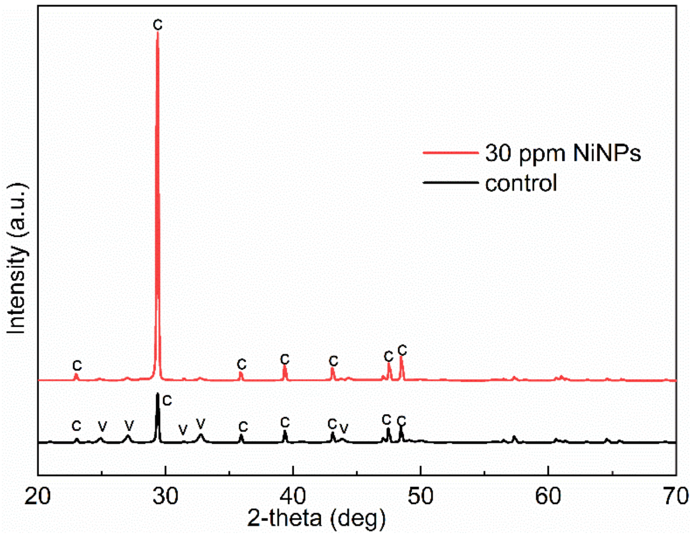

Figure 4.8 XRD patterns of precipitated $CaCO_3$ in the presence of NiNPs catalyst and in control experiment (Zhang et al., 2019).

4.4 Effect of residence time in tubular reactor

The residence time (defined as ratio of reactor volume over total volumetric flow rate) is a significant parameter that affects the reaction conversion, and also determines the capacity of a reactor. The effect of residence time was studied at 50 °C, at the volumetric flow rate ratio ($mL \cdot mL^{-1}$) of L/G equalling to four, ranging from 40/10 (longest residence time) to 320/80 (shortest residence time). The L/G ratios were set at 40/10, 80/20, 160/40, and 320/80. Residence time thus ranged, in reverse order, from 1.02 min to 8.20 min. Collected data in Table 4.3 shows the residence time decrease lead to moderate decline of CCE; experimental conditions for this set of experiments were chosen to result in partial conversion, to magnify the effect of residence time. The CCE with NiNPs addition remained essentially constant with varying residence time, which suggests that the CO_2 mineralisation reaction with catalyst reaches in a shorter time, due to improved CO_2 hydration, the rate-limiting step (Zhang *et al.*, 2019).

Table 4.3 Ca^{2+} conversion efficiency with and without NiNPs as a function of residence time (Zhang et al., 2019).

L/G ratio (mL·min^{-1}/mL·min^{-1})	40/10	80/20	160/40	320/80
Control CCE (%)	55.8	54.4	51	51.3
With NiNPs CCE (%)	52.8	53.3	52.5	52.2

The morphologies of precipitates obtained at various residence time, with and without NiNPs, were detected with SEM analysis. From Figure 4.9, the crystal phase without NiNPs transfers from aragonitic (needle-like) to calcite (cubic) with shorter residence time, which indicates that the shorter residence time can promote more uniform product. With NiNPs, though the CCE of the reactions are very similar, the morphologies were clearly different. Only calcite is observed under the L/G ratio of 160/40 with NiNPs (Figure 4.10(b)), unlike in the absence of NiNPs (Figure 4.9(b)), which means the crystallisation process preferentially forms the most stable polymorph phase with NiNPs, even when the residence time is longer, which can help with less stable phases co-forming (Zhang *et al.*, 2019).

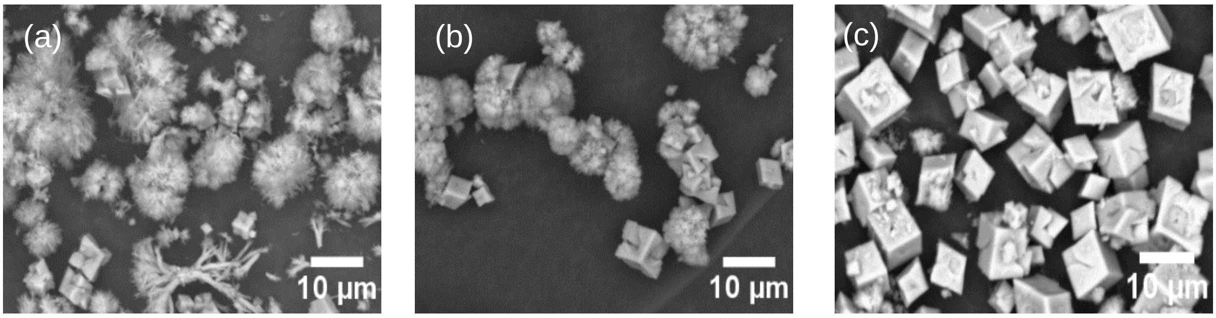

Figure 4.9 The SEM images of precipitates obtained at various residence times by varying liquid to gas volumetric flow rate ratio at (a) 40/10 (b) 160/40 (c) 320/80. Experiments were conducted at 50 °C with 2.6 vol.% NaOH (Zhang et al., 2019).

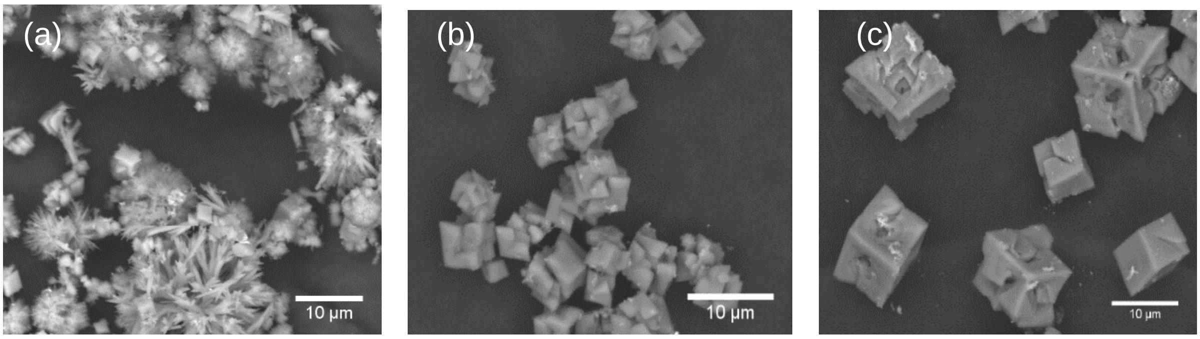

Figure 4.10 SEM images of precipitates obtained at with catalysts at various residence times, liquid to gas ratio at (a) 40/10 (b) 160/40 (c) 320/80. Experiments were conducted at 50 °C with 2.6 vol.% NaOH (Zhang et al., 2019).

The crystalline components obtained at the L/G ratio of 160/40 was analysed by XRD (Figure 4.11), and the results show that calcite (94.4%) is the major crystalline phase of the sample prepared with NiNPs. The remaining sample mass being the nickel nanoparticles (Ni) (Bhaduri *et al.*, 2015), due to partial incorporation of catalyst particles with the carbonate precipitate. The sample prepared without NiNPs was more heterogeneous, containing calcite (66.9%) and aragonite (33.1%) as illustrated in Figure 4.9(b) (Zhang *et al.*, 2019).

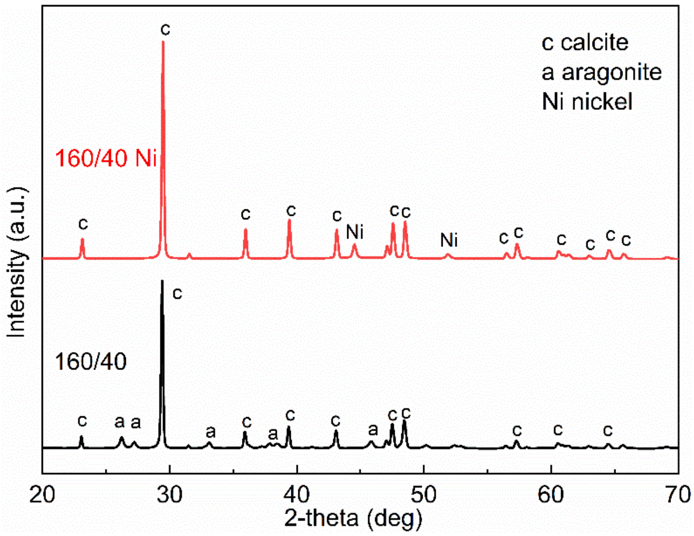

Figure 4.11 XRD patterns of products formed at liquid to gas volumetric flow rate ratio of 160/40, with (top) and without (bottom) NiNPs (Zhang et al., 2019).

4.5 Effects of other salts in brine

There is a high concentration of sodium chloride in desalination brine, so it is necessary to explore the effect of other salts on the CO_2 mineralisation reaction in the tubular reactor. In the presence of 0.8 M NaCl, the salt caused a slightly CCE decrease of about 5%, and one possible reason maybe the solubility of $CaCO_3$ increases with adding NaCl (Duan and Li, 2008).

The SEM, XRD and TGA/DTG results are shown in Figure 4.12 (a-c). NaCl addition affected the precipitate morphology and quantitative distribution of crystalline phases. Precipitates obtained under control conditions and with NaCl are both mixtures of calcite and aragonite, but the calcite content increased from 40.2% to 64.7% with NaCl addition, and the aragonitic particles were larger in the presence of NaCl. From the results of TGA/DTG analysis (Figure 4.12 (c)), the CO_2 mass loss in the temperature range of 630 °C to 800 °C occurs sooner for the sample prepared with NaCl, as indicated by the DTG peaks of the control experiment and the one with NaCl occurring at 794 °C and 745 °C, respectively (Zhang *et al.*, 2019).

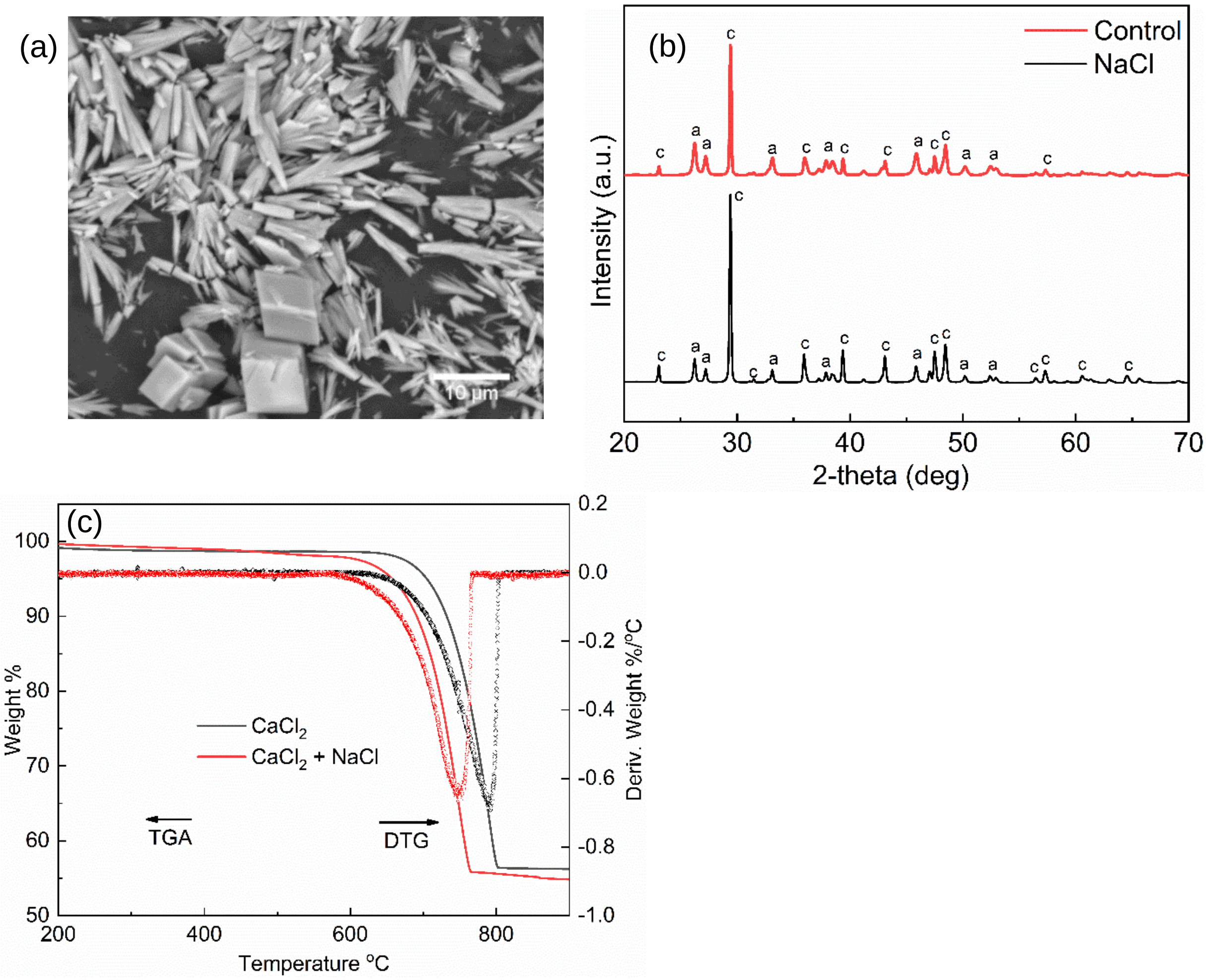

Figure 4.12 SEM image (a), XRD patterns (b), and TGA/DTG analysis (c) of the precipitates formed in the presence of NaCl (compared to control without NaCl) (Zhang et al., 2019).

At the process condition, aforementioned in section 4.1, that resulted in 100% CCE (with 35 mL·mL^{-1} CO_2 flow rate), $MgCl_2$ was added at a concentration of 0.012 M (as found in desalination brine also containing 0.020 M $CaCl_2$), and the CCE dropped to 83% (Table 4.4). Increasing CO_2 flow rate from 35 mL·min^{-1} to 50 mL·min^{-1}, CCE decreased further to 78%. In term of mineralisation, Ca^{2+} and Mg^{2+} will compete with available carbonate anions for precipitation. However, magnesium carbonates are not as readily formed compared to calcium carbonates due to the difference in ionic radius (Chu *et al.*, 2013); the radius of Mg^{2+} is smaller than that of Ca^{2+}, so waters of hydration are more strongly attached to Mg^{2+}, slowing the carbonation reaction. At the higher gas flow rate, the CCE decreased to 78% also due to lower pH value (Table 4.4) (Zhang *et al.*, 2019).

Table 4.4 CO_2 mineralisation experiments with $MgCl_2$ added to alkalinised $CaCl_2$ brine, compared to control (Zhang et al., 2019).

CO_2 flow rate (mL·min^{-1})	$MgCl_2$ (M)	Mineral phases	CCE	Outlet pH
35	NA	--	100%	8.0
35	0.012	calcite	83%	9.5
50	0.012	calcite/aragonite	78%	7.0

Comparing the particle morphologies of two samples formed in the presence of $MgCl_2$ by SEM (Figure 4.13 (a) and (b)) uniform calcite is seen at CO_2 flow rate of 50 mL·min^{-1}, while brucite ($Mg(OH)_2$) particles can be seen in the samples formed at higher CO_2 flow rate of 35 mL·min^{-1}. The outlet pH of slurry from 35 mL·min^{-1} and 50mL·min^{-1} experiments was 9.5 and 7.0, respectively. At flow rate of 35 mL·min^{-1} with $MgCl_2$, the outlet pH of 9.5 is higher than in absence of $MgCl_2$, which means it forms $Mg(OH)_2$ and does not produce carbonates. It is observed that the solution turned to milky by adding $MgCl_2$, and that is a sign of $Mg(OH)_2$ formation. Therefore, more CO_2 is needed to produce acidic solution to keep Mg^{2+} in solution. This can be detected from the FTIR analysis (Figure 4.14 (a)), where the spectrum peak at 3698 cm^{-1} is assigned to the O-H band in crystal structure (Botha and Strydom, 2003), and the TGA/DTG analysis (Figure 4.14 (b)), where brucite decomposes in the temperature range of 300 to 400 °C) (Dong *et al.*, 2018). There was no hydroxyl group appearing in the 80/50 ratio sample, and its thermal decomposition was indicative of only calcium carbonate being present, which means neither magnesium hydroxide nor carbonate were formed with increasing CO_2 flow rate, though it is possible the magnesium co-precipitates with calcium to form magnesian calcite (Hosseini *et al.*, 2015), which is not easily identifiable by SEM, TGA, FTIR or XRD (diffractogram indicative of only calcite and aragonite; not shown) (Zhang *et al.*, 2019).

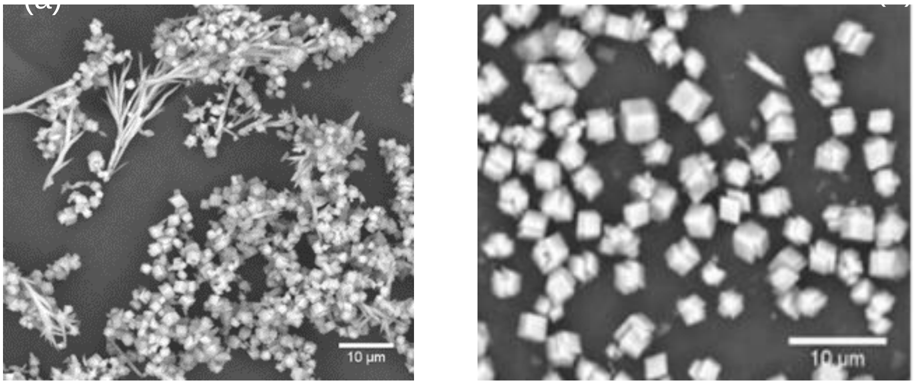

Figure 4.13 SEM images (a) 80/35 (b) 80/50 of precipitates formed under different CO_2 gas flow rates (35 and 50 mL·min^{-1}) with alkalinised brine (80 mL·min^{-1}) containing $MgCl_2$ (0.012 M) (Zhang *et al.*, 2019).

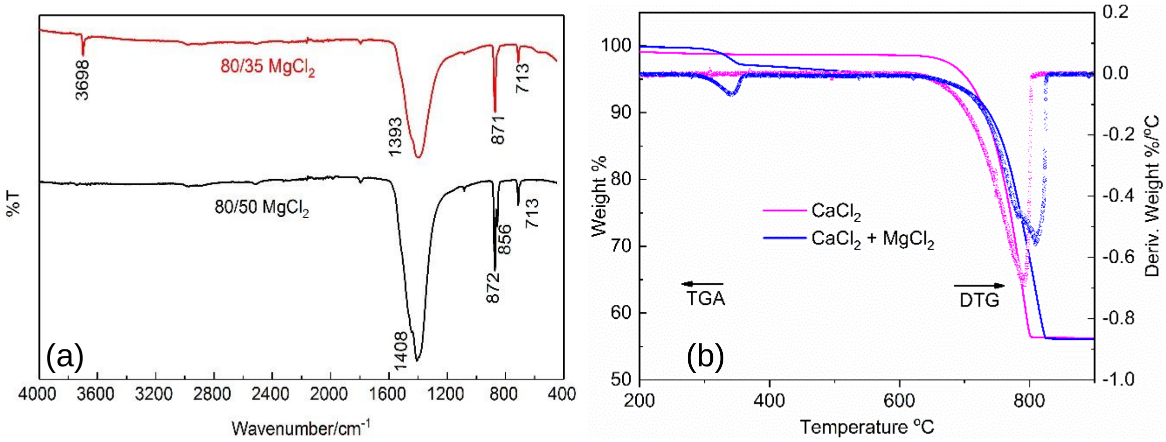

Figure 4.14 FTIR spectra (a) and TGA/DTG analysis (b) of precipitates formed under different CO_2 gas flow rates (35 and 50 mL·min^{-1}) with alkalinised brine (80 mL·min^{-1}), with and without $MgCl_2$ (0.012 M) (Zhang et al., 2019).

Conclusions

This continuous reactor design can be suitable to remove calcium from brine by forming carbonates at large-scale application. In the present tubular reactor, the L/G ratio at 80/35 with 3.8 vol.% NaOH (1 M) can achieve 100% CCE. The precipitates were confirmed to be calcium carbonates by XRD and TGA analyses. The SEM images and FTIR peaks can also detect the polymorphs of $CaCO_3$. The polymorph composition depended on the pH, temperature, residence time and salts addition. The advantage of BF slag addition was that less NaOH solution needs to be added and higher CCE can be obtained. The catalysts NiNPs can accelerate the rate of mineralisation process with a concentration of 30 ppm, and CCE can be increased up to 10%. The precipitates produced with catalyst favoured stable crystalline phase of calcite, with a slight amount of nickel detected in the carbonates (Zhang *et al.*, 2019).

References

Bhaduri, G.A., Alamiry, M.A.H. and Šiller, L. (2015) 'Nickel Nanoparticles for Enhancing Carbon Capture', *Journal of Nanomaterials*, 2015, pp. 1-13.

Bhaduri, G.A. and Šiller, L. (2013) 'Nickel nanoparticles catalyse reversible hydration of carbon dioxide for mineralization carbon capture and storage', *Catalysis Science & Technology*, 3(5), pp. 1234-1239.

Botha, A. and Strydom, C.A. (2003) 'DTA AND FT-IR ANALYSIS OF THE REHYDRATION OF BASIC MAGNESIUM CARBONATE', *Journal of Thermal Analysis and Calorimetry*, 71, pp. 987–995.

Chu, D.H., Vinoba, M., Bhagiyalakshmi, M., Hyun, B., II, Nam, S.C., Yoon, Y., Kim, S.H. and Jeong, S.K. (2013) 'CO_2 mineralization into different polymorphs of $CaCO_3$ using an aqueous-CO_2 system', *RSC Advances*, 3(44), pp. 21722–21729.

Duan, Z. and Li, D. (2008) 'Coupled phase and aqueous species equilibrium of the H_2O-CO_2-NaCl-$CaCO_3$ system from 0 to 250°C, 1 to 1000 bar with NaCl concentrations up to saturation of halite', *Geochimica et Cosmochimica Acta*, 72(20), pp. 5128-5145.

Dong, H., Unluer, C., Yanga, E.-H. and Al-Tabbaa, A. (2018) 'Recovery of reactive MgO from reject brine via the addition of NaOH', *Desalination*, 429, pp. 88-95.
Ho, C. and Sturtevant, J.M. (1963) 'The kinetics of the hydration of carbon dioxide at 25', *Journal of Biological Chemistry*, 238, pp. 3499-3501.

Hosseini, T., Selomulya, C., Haque, N. and Zhang, L. (2015) 'Investigating the Effect of the Mg^{2+}/Ca^{2+}Molar Ratio on the Carbonate Speciation during the Mild Mineral

Carbonation Process at Atmospheric Pressure', *Energy & Fuels*, 29(11), pp. 7483-7496.

Nan, Z., Chen, X., Yang, Q., Wang, X., Shi, Z. and Hou, W. (2008) 'Structure transition from aragonite to vaterite and calcite by the assistance of SDBS', *Journal of Colloid and Interface Science*, 325(2), pp. 331-6.

Shen, Q., Wei, H., Zhou, Y., Huang, Y., Yang, H., Wang, D. and Xu, D. (2006) 'Properties of Amorphous Calcium Carbonate and the Template Action of Vaterite Spheres', *The Journal of Physical Chemistry B*, 110, pp. 2994-3000.

Spanos, N. and Koutsoukos, P.G. (1998) 'The transformation of vaterite to calcite: effect of the conditions of the solutions in contact with the mineral phase', *Journal of Crystal Growth*, 191(4), pp. 783-790.

Vagenas, N., A., G. and C, K. (2003) 'Quantitative analysis of synthetic calcium carbonate polymorphs using FT-IR spectroscopy', *Talanta*, 59(4), pp. 831-836.

Zhang, N., Santos, R.M., Smith, S.M. and Šiller, L. (2019) 'Acceleration of CO_2 mineralisation of alkaline brines with nickel nanoparticles catalysts in continuous tubular reactor', *Chemical Engineering Journal*, 377, p. 120479.

Chapter 5. Rapid CO_2 capture-to-mineralisation in a scalable reactor

This chapter presents CO_2 mineralisation process with MEA from the experimental and modelling perspective. The multiphase flow process uses alkaline brine solution to capture gaseous CO_2 and form carbonate particles in a continuous tubular reactor. In this chapter, monoethanolamine (MEA) solution is utilised to synergistically boost CO_2 solubility in the brine while neutralising the acidification caused by brine chloride ions left in solution following precipitation of alkaline earth metals. Short residence time, in the order of few minutes, is made possible by the high gas-liquid surface area for mass transfer, and the rapid kinetics of aqueous phase carbonation reactions. Nickel nanoparticles (NiNPs) were tested as a catalytic additive to further accelerate the rate limiting step. Experimental results were used to develop and calibrate a one-dimensional time-dependent plug-flow model that incorporates transport and chemical speciation equations. The model is thus capable of predicting aqueous species and solid carbonate concentration, fluid pressure and gas slug size as a function of reactor length. These in turn yield carbonation conversion, total pressure drop, and provide mechanistic insight into the reactor processes that can be used for scale-up. All content of this chapter has been published in *Reaction Chemistry & Engineering* (Zhang *et al.*, 2020).

5.1 MEA concentration, flow rate and L/G ratio effects

The evaluation of optimal MEA concentration and gas flow rate with the continuous tubular reactor was carried out. The experiments were conducted with MEA concentration ranging from 0 vol.% to 5 vol.%, with CO_2 flow rate from 40 to 120 $ml{\cdot}min^{-1}$, calcium concentration in brine of 0.020 M, and at a set reactor temperature of 50°C. The CCE increases in the presence of MEA (in Figure 5.1(a)) up to a certain point, after which it decreases. Lower L/G ratio, achieved by increasing the gas flowrate at constant liquid flowrate, causes greater CO_2 dissolution, which is beneficial for higher CCE at a large range of MEA concentrations (Figure 5.1(a)). However, higher MEA concentrations cause lower CCE at all three L/G ratios (Zhang *et al.*, 2020).

This is a different result compared to our previous research carried with NaOH solution, where the CCE increase has continued at high alkali concentrations in section 4.1 of Chapter 4. It is observed that more CO_2 is dissolved into the MEA solution at higher

MEA concentrations observing from the frequency and size of the bubble, even though CCE values are lower, which means the solution contains more CO_2. The reason why the CCE is reduced might be due to i) higher concentration can attribute high conversion efficiency to form carbamate; ii) the solvation effect (Huertas *et al.*, 2015), whereby the calcium ions cannot combine with the ionised CO_2 (which in this system include carbamate and carbonic acid) due to excess of MEA molecules present, thus restricting the crystallisation reaction.

In Figure 5.1(a) and (b), it is found that the calcium conversion efficiency was reduced when the MEA concentration higher than 1 vol.%, so this can be avoided by utilising MEA concentration below 1 vol.%. However, since the goal of the process is to sequester CO_2, it is desirable to utilize the MEA concentration that gives the highest CCE, and this occurred at MEA concentrations from 1 vol.% to 2 vol.% (Figure 5.1(b)). Moreover, the reactor can be optimized for two scenarios: consuming the greatest fraction of the gas volume introduced, or consuming the most amount of CO_2 in the least time. The former is achieved at the lowest CO_2 flowrate for which high CCE is obtained, namely at 40 $mL \cdot min^{-1}$ using 0.3 vol.% to 0.5 vol.% MEA, reaching CCE of 96% (Figure 5.1(b)). The latter is achieved at the highest CO_2 flowrate for which high CCE is obtained, namely at 120 $mL \cdot min^{-1}$ using 1.5 vol.% MEA, reaching CCE of 98% (Figure 5.1(b)). Given the small CCE difference between these two scenarios, the lower gas flowrate scenario is seen as optimal, since it achieves a simultaneous high rate of CO_2 and calcium utilization, thus being the most atom efficiency process condition for this reactor. However, the highest gas flowrate scenario minimizes the required reactor volume per unit of sequestered CO_2 (Zhang *et al.*, 2020).

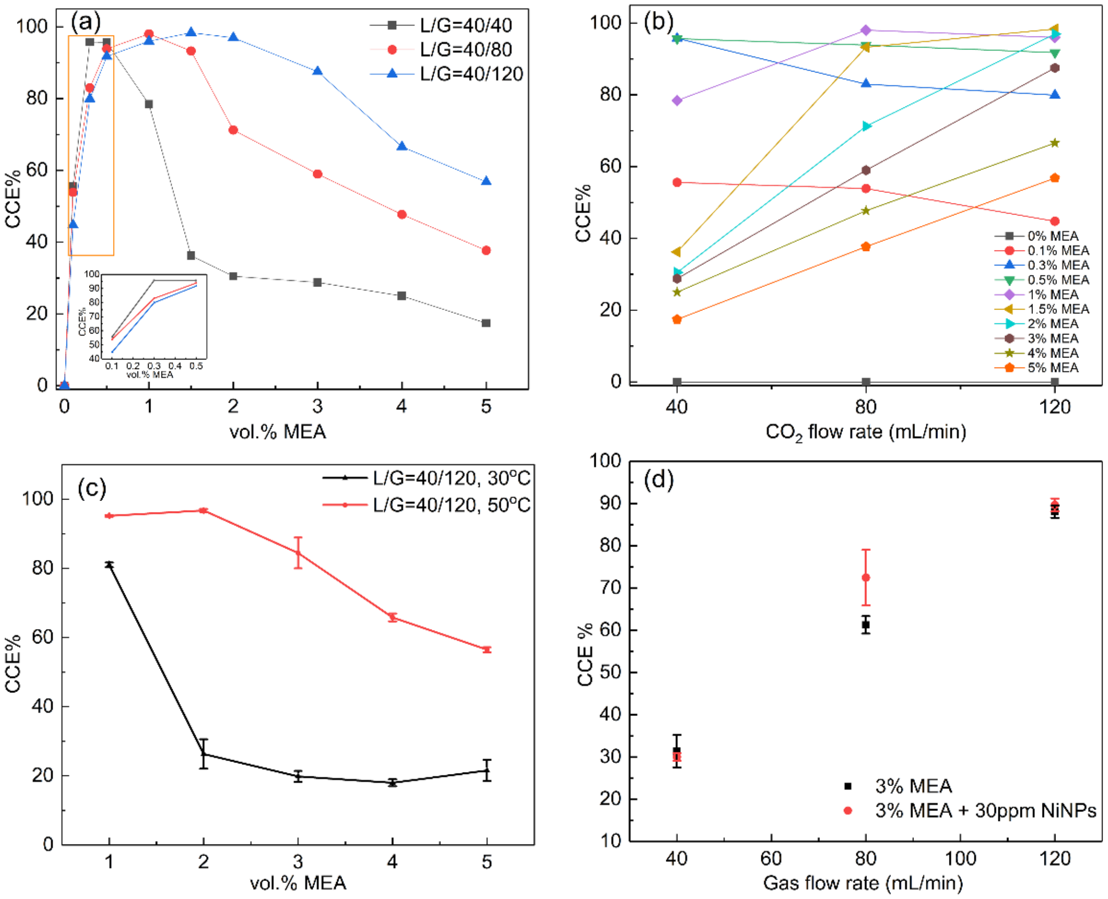

Figure 5.1 (a) The effect of MEA concentration and liquid-to-gas flowrate ratio on the calcium conversion efficiency (CCE), from MEA concentration perspective; (b) The effect of MEA concentration and CO_2 flow rate on CCE, from gas flow rate perspective; (c) The effect of MEA concentration and temperature on CCE, at a fixed L/G ratio of 40/120; (d) The effect of gas flow rate and NiNPs on CCE, using 3 vol.% MEA, 50 °C, and liquid flow rate of 40 mL·min^{-1} (Zhang et al., 2020).

5.2 Temperature effects

The temperature played an important role on the calcium conversion efficiency. Typical flue gas temperature ranges from 35 to 50 °C, (Aaron and Tsouris, 2005) therefore two temperatures were investigated. The experiments were conducted at 30 and 50 °C, using a fixed L/G flowrate ratio of 40/120, calcium concentration in brine of 0.020 M, and a range of MEA concentrations (1 vol.% to 5 vol.%). A higher gas-to-liquid ratio than the optimal determined in section 5.1 was selected since it showed in the previous test (Figure 5.1(a)) to achieve high CCE under a wider range of MEA concentrations. Hence, the aim here is to find out if lower reactor temperature lowers and/or narrows the maximum CCE achievable. Figure 5.1(c) shows that the lower reactor temperature both reduces the maximum CCE achievable and prevents the high CCE range from extending beyond 1 vol.% MEA, with a drastic decrease already at 2 vol.%. This result contrasts with the previous study using NaOH in section 4.1 of Chapter 4, where there was no large effect of temperature on the CCE, though the CCE was slightly higher at higher temperature. The solubility of CO_2 in aqueous solution is known to be favoured at lower temperatures, but conversely the precipitation of carbonates is more favourable (i.e. faster) at higher temperatures (Vučak *et al.*, 1997). The higher reaction temperature can enhance the precipitation reaction due to lower values for the activation energies (Koutsoukos and Kontoyannis, 1984).

The present results suggest that in MEA solution, the carbonation reaction effect is predominant, so higher temperatures are needed to achieve high conversion during the short residence time in the reactor. At a combined 160 $mL\cdot min^{-1}$ total fluid flow rate, and given a total tubular volume of 137.4 mL, based on 7 m length, the residence time is a mere 51.5 seconds, thus rapid reaction aids in achieving high atom efficiency and units of CO_2 sequestered per unit of reactor volume. Another important factor that is temperature dependent, and very important in a plug flow configuration with short residence time, is the mass transfer rate of CO_2 from the gas phase to the liquid phase (Zhang *et al.*, 2020).

As the carbonation products can be commercialised in specific industry, to add value to this process and hence offset the costs of sequestering CO_2, it is also important, in addition to maximising the CCE and atom efficiency and minimizing reactor volume, to assess the purity and morphology of the products. In particular, temperature is well reported (Koutsoukos and Kontoyannis, 1984) to influence the morphology and the particle size of $CaCO_3$ crystals. The morphologies of precipitates obtained at both tested temperatures as characterized by SEM and XRD analyses are shown in Figure 5.2. SEM images show that spherical vaterite crystals are predominantly present in the product prepared at 30 °C (Figure 5.2(b), left), while needle-like aragonite crystals are more visible in the higher temperature specimen (Figure 5.2(b), right); rhombohedral calcite crystals are found in both samples (Trushina *et al.*, 2014). The quantitative XRD analysis, performed by Rietveld refinement of the diffractograms (Figure 5.2(a)), confirms the interpretation of the SEM images. At both temperatures, the predominant phase is vaterite, but the purity is markedly improved at lower temperature. A purer product is likely to offset the process cost, so operation of the reactor at lower temperature using the optimum MEA concentration for that condition (1 vol.%) could be seen as being the more feasible scenario (Zhang *et al.*, 2020).

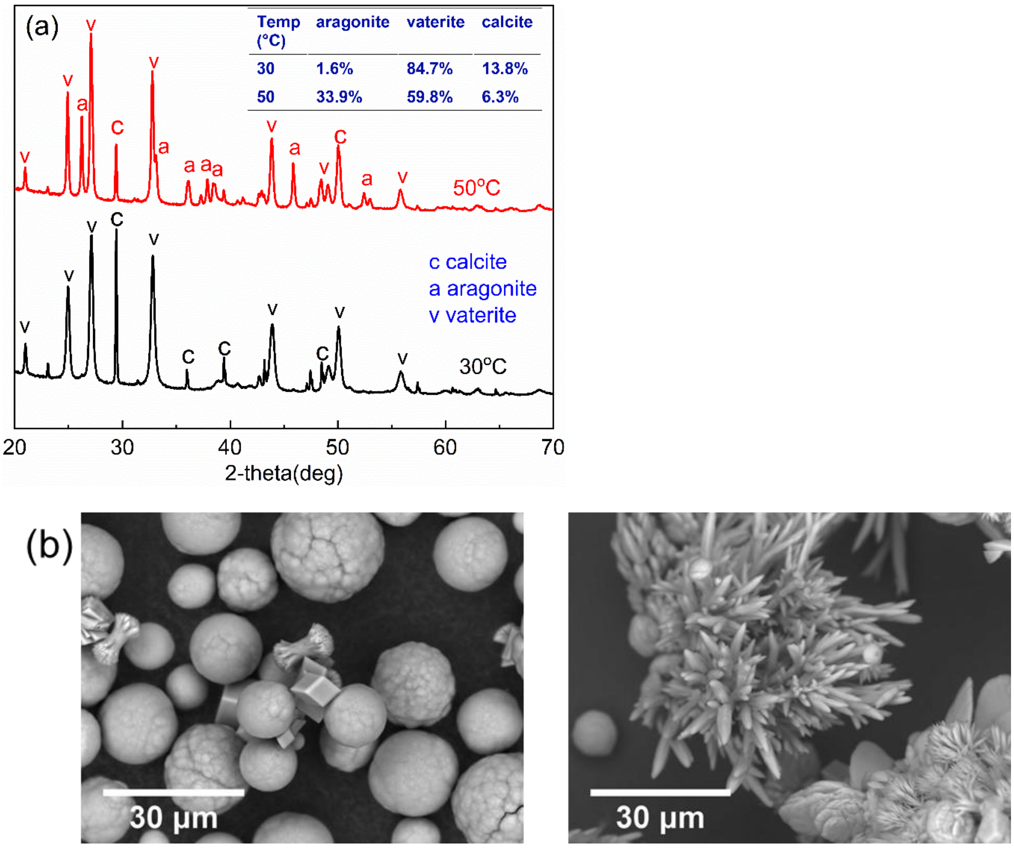

Temp (°C)	aragonite	vaterite	calcite
30	1.6%	84.7%	13.8%
50	33.9%	59.8%	6.3%

Figure 5.2 (a) XRD patterns of carbonated products obtained at different temperatures (QXRD data of carbonated products obtained at different temperatures was listed on the right top corner); (b) SEM images of products obtained at 30 °C (left) and 50 °C (right) (scale bar 30 μm) (Zhang et al., 2020).

5.3 Nickel nanoparticles effects

Mineralisation rate can be limited by the kinetics of the CO_2 hydration reactions. In order to speed up the formation of carbonated precipitates, nickel nanoparticles known as catalysts for hydration reaction (Bhaduri and Šiller, 2013; Šiller and Bhaduri, 2013) were implemented in the tubular reactor process. The effect of nickel nanoparticles is investigated at temperature of 50 °C, 3 vol.% MEA, calcium concentration in brine of 0.020 M, with addition of 30 $mg \cdot L^{-1}$ of NiNPs (Bhaduri and Šiller, 2013). This value was selected in an attempt to magnify the effect of NiNPs, by selecting a condition outside, but not too far, from the optimal range seen in Figure 5.1(a). Liquid flow rate was kept constant at 40 mL·min^{-1}, and gas flow rate was varied. At the gas flow rate of 80 mL·min^{-1}, CCE increased from 59% to 68% (Figure 5.1(d)), but there was no change at the higher and lower gas flow rates tested. At the lowest gas flow rate, the conversion suffers from slow gas and liquid interaction, hence the NiNP is unable to further assist in the reaction. Conversely, at the highest gas flow rate tested, the conversion is already high without NiNP, and the residence time is short, hence the hydration reaction is not rate limiting, and NiNP again offers no advantage. Where NiNP presented an advantage, the catalyst managed to enhance gaseous hydration, via nickel core binding with hydroxyl to produce HCO_3^- (Bhaduri and Šiller, 2013; Šiller and Bhaduri, 2013). NiNPs may also act as a nucleation seed for carbonate precipitation, enhancing reaction rate at conditions where other process effects are not rate limiting (Zhang *et al.*, 2020).

5.4 Effect of residence time

The residence time is a critical parameter to influence the calcium conversion efficiency. This study investigates the effect of residence time of CO_2 at 50 °C, calcium concentration in brine of 0.020 M, and 3 vol.% MEA concentration, using a constant liquid-to-gas flowrate ratio of 0.5, ranging from 20/40 for the longest residence time to 80/160 for the shortest residence time. The results in Table 5.1 show that longer residence time of CO_2 leads to the greater CCE, which is beneficial for maximizing CO_2 uptake from the gas phase. Of course, the greater residence time, also increases the reactor size and footprint, for a given unit of CO_2 sequestration. Hence, the MEA optimization of section 5.1, coupled with residence time optimization, is needed to find the conditions that synergistically results in high conversion efficiency, high CO_2 uptake, and compact reactor size (Zhang *et al.*, 2020).

Table 5.1 The effect of residence time on CCE (Zhang et al., 2020).

L/G ratio (mL·min^{-1}/ mL·min^{-1})	20/40	40/80	80/160
Residence time (min)	2.3	1.15	0.58
CCE (%)	92.4%	59.2%	35.9%

5.5 Effect of other ions concentration

Different concentrations of calcium (as $CaCl_2$) are also applied in MEA solution, ranging from 0.010 M to 0.040 M, to investigate the influence of initial calcium concentration on precipitation rate. This investigation is useful given that different brine sources will have different calcium concentrations. Experiments are conducted with 3 vol.% MEA, L/G flowrate ratio of 40/80, and at 50 °C. The results of CCE and reacted calcium amounts are shown in Table 5.2. CCE declined with higher initial calcium concentration, while the reacted calcium amount actually increased, meaning that more CO_2 was actually sequestered with higher calcium concentration. This shows that excess amount of CO_2 transfers from the gas phase to the liquid phase, and that by providing more calcium ions, more carbonates form. The conversion likely drops due to insufficient residence time to carbonate the extra amount of calcium, as was investigated in section 5.4, but here caused by changes in solution chemistry rather than flowrate. It thus becomes evident that brine concentration affects the reactor size (length) needed to achieve a desired conversion efficiency and/or CO_2 uptake, depending on how the process is optimized (Zhang *et al.*, 2020).

Table 5.2 Effect of calcium concentration on CCE and reacted calcium (Zhang et al., 2020).

Ca^{2+} concentration ($mol \cdot L^{-1}$)	0.01	0.02	0.04
CCE (%)	85.6%	38.9%	38.9%
Reacted calcium ($mg \cdot L^{-1}$)	342.4	472.0	713.6

There are multiple ions in real brine solution besides $CaCl_2$; the major species are typically $MgCl_2$ and NaCl. Therefore, the effects of $MgCl_2$ and NaCl on conversion efficiency were also investigated in this study. The concentrations used of these two species were selected based on the brine composition from Kuwait Desalination Plant: 0.80 M NaCl and 0.10 M $MgCl_2$, with $CaCl_2$ maintained at 0.020 M as in previous experiments. The experiments were carried out using 2 vol.% MEA at 50°C, and L/G flowrate ratio of 40/120. The results in Table 5.3 show that the influence of $MgCl_2$ on CCE is stronger than that of NaCl. In the presence of $MgCl_2$, magnesium ions competed for carbonate/bicarbonate ions from solution, resulting in lowering the CCE.

Table 5.3 CO_2 mineralisation experiments with other ions, compared to control (Zhang et al., 2020).

Source	0.02 mol·L^{-1} $CaCl_2$	0.02 mol·L^{-1} $CaCl_2$ + 0.1 mol·L^{-1} $MgCl_2$	0.02 mol·L^{-1} $CaCl_2$ + 0.8 mol·L^{-1} NaCl
CCE%	96.9%	72.8%	93%

Moreover, with greater amount of chloride in solution, the pH buffering effect of MEA is partly compromised, which also limits the possible CCE before the pH becomes too low for the precipitation of carbonates. The CCE was only slightly declined in the presence of NaCl. Precipitation rate is not expected to be affected by the NaCl addition (Sheikholeslami and Ong, 2003), but solubility of $CaCO_3$ slight increases with higher ionic strength (Duan and Li, 2008), hence likely preventing as high CCE as in the case with lower ionic strength (Zhang *et al.*, 2020).

5.6 Tubular reactor model set-up and results

A one-dimensional three phase plug-flow model is developed and used to comprehensively understand the interfacial mass transfer and the aqueous phase chemical speciation in a tubular reactor for the carbonation of brine using MEA additive. The objective is to divide the plug flow reactor into discrete, inter-connected, reaction volumes, wherein thermodynamic modelling can be used to determine the concentration of all relevant species in the aqueous solution (Zhang *et al*., 2020).

Given that the flow pattern of the tubular reactor is a Taylor slug flow, each discrete reaction volume is sized to contain one whole liquid plug whose surface is in contact with one whole gas bubble. Mass transfer of CO_2 across the gas-liquid interface is modelled as a function of time, and given that the plug and bubble travel down the reactor, as a function of reactor length. The assumption here is that that mass transfer area is equal to the surface area of the gas bubble (modelled as a cylinder), and that the mass transfer driving force (partial pressure difference) is uniform over the whole bubble surface. The model is also designed to predict how bubble volume, and thus bubble length and two-phase flow rate, change over time as more and more CO_2 dissolves in the liquid, and also tracks fluid pressure over the length of the reactor. Another assumption made in the model is that all aqueous and solid (carbonate) species reach equilibrium within the residence time that each fluid element spends in each reactor volume, which also assumes that each fluid element is well-mixed. The chemical equilibrium assumption is made in view that it is understood that mass transfer from the gas phase is much slower than reaction kinetics, and thus is a rate-limiting step (Zhang *et al*., 2020).

The primary calibration parameter of the model is the interfacial overall mass transfer coefficient. The calibration procedure consists of adjusting the overall mass transfer coefficient to match certain modelled parameters with experimentally measured values: bubble size at the reactor outlet, outlet pH (defined as $-\log(\gamma_1[H^+])$), outlet dissolved calcium concentration, and outlet pressure. These three parameters pertain to mass transfer modelling (the bubble size), chemical thermodynamic modelling (the pH) and the fluid mechanics modelling (the pressure drop). The hypothesis of the modelling approach is that the suitability of the model assumptions can be verified by assessing how well these three independent parameters, that are calculated by several sets of non-linear equations, can be fitted to experimental data (Zhang *et al*., 2020).

The conceptual process of the tubular reactor model is schematised in Figure 5.3. The overall aim of the model is to optimise the overall mass transfer coefficient such that the modelled data matches experimentally measured values. The modelling starts by firstly inputting initial pressure (i.e. the fluid pressure at the tubing inlet, where the liquid and gas streams first meet), reactor temperature, and an initial estimate of the overall mass transfer coefficient; these inputs are shown in Figure 5.3 as green boxes. Secondly, the modelling equations (presented in subsequent sections) carry out calculations using the input parameters to calculate all the parameters shown in transparent boxes in Fig. 5.3. Eventually, the length of gas bubble, and the aqueous phase speciation (including the pH value and the Ca^{2+} concentration) are obtained from the model, and are shown in Figure 5.3 as orange boxes. In the presence of CO_2 absorption, aqueous phase chemical reactions, and solids precipitation, the following 13 chemical species are assumed to be present in the liquid phase: H^+, HCO_3^-, CO_3^{2-}, RNH_2, RNH_3^+, $RNHCOO^-$, $CaCO_{3(s)}$, OH^-, Cl^-, $CaOH^+$, $CaHCO_3^+$, $CO_{2(aq)}$, Ca^{2+}. The model is run on Excel using Visual Basic and MATLAB programming (Zhang *et al*., 2020).

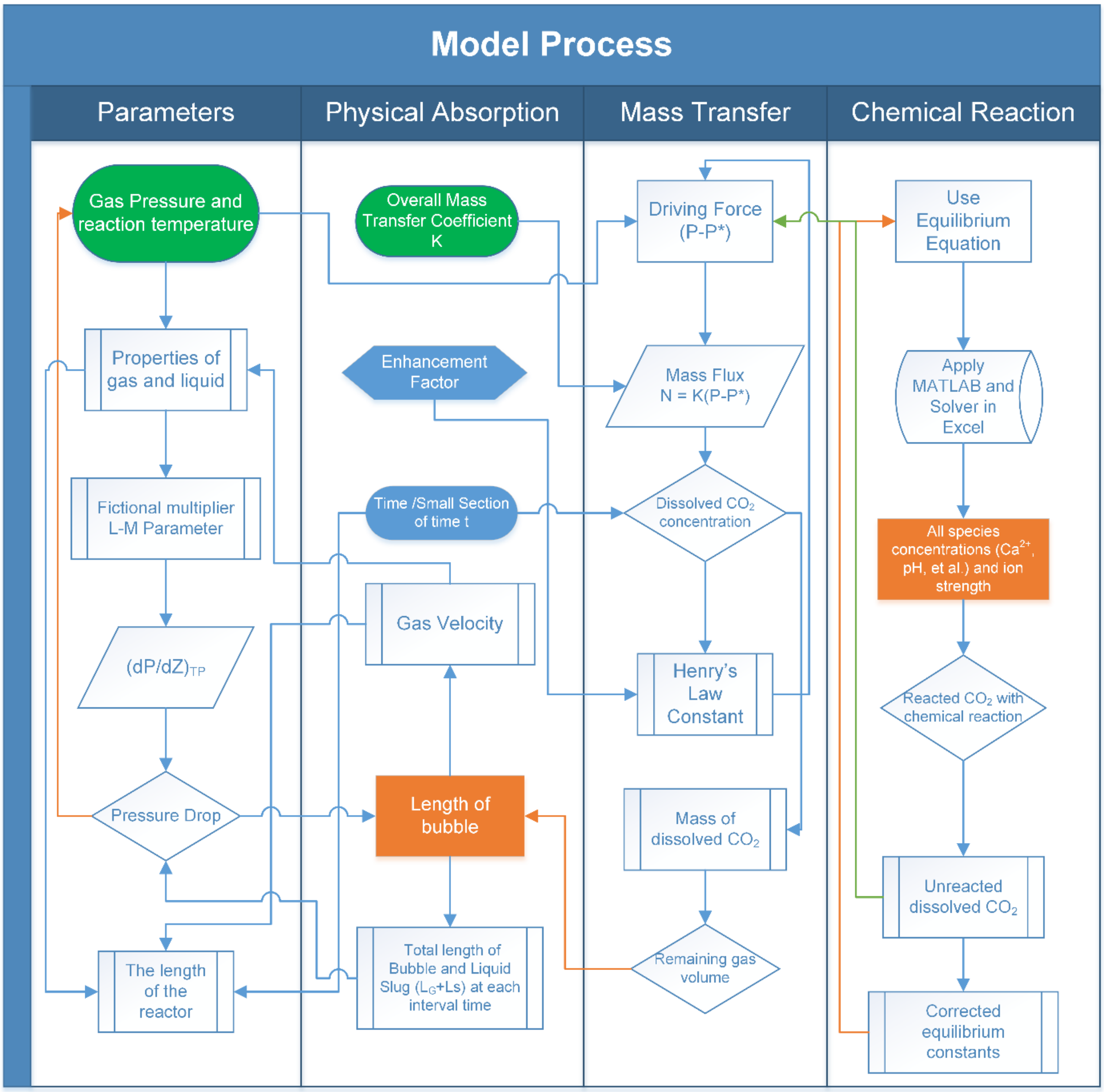

Figure 5.3 Schematic diagram of tubular reactor model (Zhang et al., 2020).

The pH value was experimentally measured by pH meter, the Ca^{2+} concentration was experimentally measured by ICP-OES, and the outlet bubble length was measured from the video recording. The outlet pressure modelled is also compared to the atmospheric pressure. The modelling is then repeated using slightly different values of initial pressure and overall mass transfer coefficient, and this iteration has continued until satisfactory matching of modelled and experimental data (±0.1% to ±10%) was achieved. The main reactor tubing is made of stainless steel to avoid high pressure drop caused by precipitates attached to the internal wall of the tubing. To observe the initial bubble size and the outlet bubble size, a transparent silicone tubing is used to assemble the T-junction where the two phases meet (Zhang *et al*., 2020).

The viscosity and density of the liquid and gas phases are obtained from the literature for different reaction temperatures (Lee and Lin, 1995). With these properties, the Reynolds number ($Re = \rho U d/\mu$) and Dean number ($De = Re(d/D)^{1/2}$) can be calculated, and used in the determination of the two-phase pressure drop of reactor. The tube diameter is d, and the curvature diameter of the helically coiled tube is D. The helical tubular reactor pressure drop is assumed to results from frictional resistance, and thus the two-phase pressure drop for the Taylor slug flow regime can be obtained by the Lockhart-Martinelli method (R.C. Xin *et al*., 1996). The pressure drop multipliers, φ_G and φ_L representing two-phase frictional multiplier for gas alone and flow two-phase frictional multiplier for liquid alone flow, and the Lockhart-Martinelli parameter, χ, is defined with the following formulae:

$$\varphi_G^2 = \frac{(dp/dz)_{TP}}{(dp/dz)_G} \qquad \text{(E5.1)}$$

$$\varphi_L^2 = \frac{(dp/dz)_{TP}}{(dp/dz)_L} \qquad \text{(E5.2)}$$

$$\chi^2 = \frac{(dp/dz)_L}{(dp/dz)_G} \qquad \text{(E5.3)}$$

The two-phase pressure gradient is $(dp/dz)_{TP}$. The single phase pressure gradients above from the gas side as $(dp/dz)_G$ and from the liquid side $(dp/dz)_L$, which are determined assuming that each phase flows in the helicoid tubing alone (i.e. using the superficial velocity of each phase), are determined using the following equations:

$$(dp\ /\ dz)_G = \frac{2f_G \rho_G U_G^2}{d} \qquad \text{(E5.4)}$$

$$(dp\ /\ dz)_L = \frac{2f_L \rho_L U_L^2}{d} \qquad \text{(E5.5)}$$

μ, ρ and U is the viscosity, the density and the superficial velocity of the fluid in the gas and liquid phase, respectively (Zhang *et al*., 2020). The friction factor (f) for laminar flow in a helicoid tubing is obtained using the empirical correlation below (Manlapaz and Churchill, 1980):

$$\frac{f}{fs} = \left[\left(1 - \frac{0.18}{\left[1+\left(\frac{35}{De}\right)^2\right]^{1/2}}\right)^m + \left(1.0 + \frac{\frac{d}{D}}{3}\right)^2 \left(\frac{De}{88.33}\right)\right]^{1/2} \qquad \text{(E5.6)}$$

In Eq.(5.6): d is the tubing inner diameter and D is the coil diameter, f_s=16/Re, which is the friction factor for straight tube; when De<20, m=2; when 20<De<40, m=1, and for other De, m equals 0. In the present case, De is less than 20, so m used is 2. The overall speed of fluids is mild; therefore, the centrifugal force was not taken into consideration in the model (Zhang *et al*., 2020).

The two-phase frictional pressure drop is used to calculate the pressure drop at each time step interval of the model, when the modelled element consisting of a liquid plug and a gas bubble travels a certain distance, depending on the total flow rate (i.e. the sum of liquid and gas superficial flowrates). The total pressure drop across the reactor is then determined based on the number of time steps needed for the liquid plug and gas bubble (if still present) to reach the reactor outlet (Zhang *et al*., 2020).

To model the CO_2 absorption process (i.e. mass transfer from gas phase to liquid phase), the Two Film Theory based equations are applied (Danckwerts, 1951). This film theory divides the liquid and gas phases into two bulk sources/sinks, and a permeable interface. Several assumptions need to be complied: (i) the liquid phase is well mixed (which is the case for liquid plugs moving in Taylor Flow regime), hence bulk gradients are negligible; (ii) the reactions of CO_2 in the liquid phase are fast, such that the liquid phase can reach the equilibrium rapidly; (iii) the driving force is determined by the CO_2 pressure difference between the gas and liquid phases (where the liquid phase concentration is converted into a pressure equivalent); (iv) the resistance of the interface to mass transfer is represented by a single overall resistance, meaning that boundary layers resistance, actual interface resistance, and any charge resistance are coupled into a single resistance. In the case of the absorption process (without chemical reaction), the mass flux can be expressed by:

$$N_{CO_2} = K\left(P_{[CO_2]_i} - P^*_{[CO_2]_i}\right) \qquad \text{(E5.7)}$$

where K is the overall mass transfer coefficient; $P_{[CO2]i}$ represents the pressure of the gas within the gas phase (i.e. bubble), and $P^*_{[CO2]}$ is the pressure that is in equilibrium with the liquid phase concentration; hence the difference between these two pressures is the driving force of CO_2 absorption (Zhang *et al*., 2020).

The obtained flux (N_{CO2}) is multiplied by the duration of the time step to determine the change in concentration in the liquid phase during that time step, and subsequently, taking also into account bubble size and pressure drop, the change in mass and volume of the gas bubble during that time step. According to the Henry's Law, the equilibrium pressure can be obtained by the equation Eq.(5.8), where H is Henry's Law constant; and $C^*_{CO2(L)}$ is the concentration of dissolved (and unreacted) CO_2 in the liquid phase (Zhang *et al*., 2020).

$$P^*_{CO_2} = C^*_{CO_{2(L)}}/H \qquad \text{(E5.8)}$$

Henry's Law constant in the water can be calculated from Eq.(5.9) (Sander, 2015); $T^\ominus$ is 298.15 K and all other parameters are obtained from the reference (Sander, 2015), and $\triangle_{sol}H$ is the enthalpy of dissolution, thus the Henry's Law constant in water at 313.15 K is 1.73E-04 mol/(m^3.Pa) (Zhang *et al*., 2020).

$$H_{(T)} = H^\ominus \times \exp\left[\frac{-\triangle solH}{R}\left(\frac{1}{T} - \frac{1}{T^\ominus}\right)\right] \qquad \text{(E5.9)}$$

This constant is accurate under water condition, and our experiments occurred in the presence of MEA solution, which means that in practice this pressure/concentration relationship requires a constant of higher value than that in water, due to higher solubility of CO_2 in MEA solution. On the other hand, aqueous MEA solution also influences the rates of absorption of CO_2 into solution, due to reactivity of CO_2 with MEA, increasing the mass transfer driving force. To account for these effects, a Henry's Law constant enhancement factor is introduced in the model, and the value is obtained from the literature based on the experimental temperature (Liu *et al*., 1999). In this case, the enhancement factor is adjusted to 2. Finally, these equations lead to determining the mass of dissolved CO_2 in the liquid plug (within the reactor element being modelled), before any chemical reaction occurs, which is then taken into account using equations below (Zhang *et al*., 2020).

In terms of modelling chemical reactions in the tubular reactor, when CO_2 is absorbed into the liquid phase, it dissolves in the liquid and is partially consumed by chemical reaction; thus, the concentration of dissolved but unreacted CO_2 in the bulk liquid decreases. Since the driving force for mass transfer is the difference between the CO_2 pressure in the gas phase and the CO_2 concentration-equivalent pressure in the liquid phase, chemical reaction leads to a higher driving force for mass transfer compared to a non-reacting system. This was experimentally verified in the tubular reactor by comparing gas bubble size at outlet between more reacting (i.e. with more calcium and/or MEA) and less reacting (i.e. with less calcium and/or MEA) fluids. The main reactions occurring in the MEA-CO_2-$CaCl_2$ aqueous solution can be written as follows:

Hydration of carbon dioxide and first dissociation (Aboudheir *et al*., 2003):

$\mathrm{H_2O + CO_{2(aq)} \leftrightarrow H^+ + HCO_3^-}$ (E5.10)

This reaction represents the hydration of unreacted CO_2 ($CO_{2(aq)}$) and the subsequent dissociation of carbonic acid, which follows a two-step mechanism. CO_2 reaction with H_2O to form carbonic acid is the slower reaction, while carbonic acid dissociation to bicarbonate, by donating a proton to water, is the faster reaction; but in this model the CO_2 absorption is assumed to be rate determining, thus both of these reactions are assumed to reach equilibrium with each time step. Additional reactions modelled are:

Dissociation of bicarbonate ion: $\mathrm{HCO_3^- \leftrightarrow H^+ + CO_3^{2-}}$ (E5.11)

Water dissociation: $\mathrm{H_2O \leftrightarrow H^+ + OH^-}$ (E5.12)

First calcium speciation reaction: $\mathrm{CaOH^+ \leftrightarrow Ca^{2+} + OH^-}$ (E5.13)

Second calcium speciation reaction: $\mathrm{CaHCO_3^+ \leftrightarrow Ca^{2+} + HCO_3^-}$ (E5.14)

Carbamate/bicarbonate/amine conversion reaction: $\mathrm{RNHCOO^- + H_2O \leftrightarrow RNH_2 + HCO_3^-}$ (E5.15)

Amine protonation reaction: $\mathrm{RNH_3^+ + OH^- \leftrightarrow RNH_2 + H_2O}$ (E5.16)

Carbonate precipitation: $\mathrm{Ca^{2+} + CO_3^{2-} \leftrightarrow CaCO_{3\,(s)}}$ (E5.17)

Table 5.4 shows the equilibrium constants obtained from literature for each of the aforementioned reactions, and K is the equilibrium constant in different reaction, and ɣ the activity coefficient of monovalent ($ɣ_1$) and divalent ions ($ɣ_2$). The species HCO_3^-,

CO_3^{2-}, $RNHCOO^-$ $CaHCO_3^+$ and $CaCO_{3(s)}$ are obtained from a chemical reaction with dissolved CO_2. The starting unreacted CO_2 concentration for the next time step is then determined by deducting these species from the initial dissolved CO_2 concentration for the present time step, thus the driving force for CO_2 absorption will be increased compared to the non-reacting system (Zhang *et al.*, 2020).

Table 5.4 Chemical equilibrium constants used in the reaction model.

Species	**Equilibrium constants**	**K value (313K)**	**Activity corrections**	**References**
RNH_3^+	$K_1 = [RNH_3^+][OH^-]/[RNH_2]$	3.41E-05	K_1/γ_1^2	(Bates and Pinching, 1951)
$RNHCOO^-$	$K_2 = [HCO_3^-][RNH_2]/[RNHCOO^-]$	6.47E-02	K_2	(Aboudheir *et al.*, 2003)
HCO_3^-	$K_a = [H^+][HCO_3^-]/[CO_{2(aq)}]$	5.01E-07	K_a/γ_1^2	(Edwards, 1978)
CO_3^{2-}	$K_b = [H^+][CO_3^{2-}]/[HCO_3^-]$	6.00E-11	K_b/γ_2	(Edwards, 1978)
$CaOH^+$	$K_3 = [CaOH^+][Ca^{2+}]/[OH^-]$	9.10E-02	$K_3 \times \gamma_2$	(Bates *et al.*, 1959)
$CaHCO_3^+$	$K_4 = [CaHCO_3^+]/[Ca^{2+}]\,[HCO_3^-]$	6.64E-02	$K_4 \times \gamma_2$	(Jacobson and Lanqmuir, 1974)
$CaCO_{3(s)}$	$K_{sp} = [Ca^{2+}][CO_3^{2-}]$	8.92E-09	K_{sp}/γ_2^2	(Plummer and Busenberg, 1982)
H^+/OH^-	$K_w = [H^+][OH^-]$	2.86E-14	K_w/γ_1^2	(Edwards, 1978)

The corresponding chemical equilibrium constant of each equation is corrected to account for activity coefficients not equal to unity. The activity coefficients used in this work are based on the Davies model (Millero, 1992), and accounts for the high ionic strength of the solutions (Vučak *et al*., 2002), according to:

$$\log(\gamma_{zi}) = -A \times Z_i^2 \left(\frac{\sqrt{I}}{1+\sqrt{I}}\right) - 0.3I \qquad \text{(E5.18)}$$

where A is Debye–Hückel constant, and Z_i is the valence number of the ion, and ionic strength I is described as:

$$I = 2[Ca^{2+}] + 1/2\,[RNH_3^+] + 1/2\,[CaOH^+] + 1/2\,[H^+] + 1/2\,[CaHCO_3^+] + 1/2\,[RNHCOO^-] + 1/2\,[HCO_3^-] + 2[CO_3^{2-}] + 1/2\,[OH^-] + 1/2\,[Cl^-] \qquad \text{(E5.19)}$$

In addition to the set of equilibrium equations, mass balance and charge balance equations are needed to solve all species concentrations. Mass balance is performed on carbon dioxide species and amine species. These balances are performed using the following equations:

Amine mass balance: $[MEA]_{TOT} = [RNH_2] + [RNH_3^+] + [RNHCOO^-]$ (E5.20)

Carbon dioxide mass balance: $[CO_2]_{TOT} = [HCO_3^-] + [CO_3^{2-}] + [RNHCOO^-] + [CaHCO_3^+] + \left[CaCO_{3\,(s)}\right] + \left[CO_{2(aq)}\right]$ (E5.21)

Charge balance: $2[Ca^{2+}] + [RNH_3^+] + [CaOH^+] + [H^+] + [CaHCO_3^+] = [RNHCOO^-] + [HCO_3^-] + 2[CO_3^{2-}] + [OH^-] + [Cl^-]$ (E5.22)

The model is run with various MEA concentrations and CO_2 flow rates to predict the distribution of species and demonstrated to facilitate large-scale reactor design by providing optimal length of the reactor (Zhang *et al*., 2020).

The model was run with various MEA concentrations. Figure 5.3 shows speciation plots for the experimental conditions at 40 ˚C with L/G flowrate ratio of 40/80, 0.020 M $CaCl_2$, and 0.1-0.5 vol.% MEA solution. The concentrations of all species are plotted against the length of reactor (Zhang *et al.*, 2020).

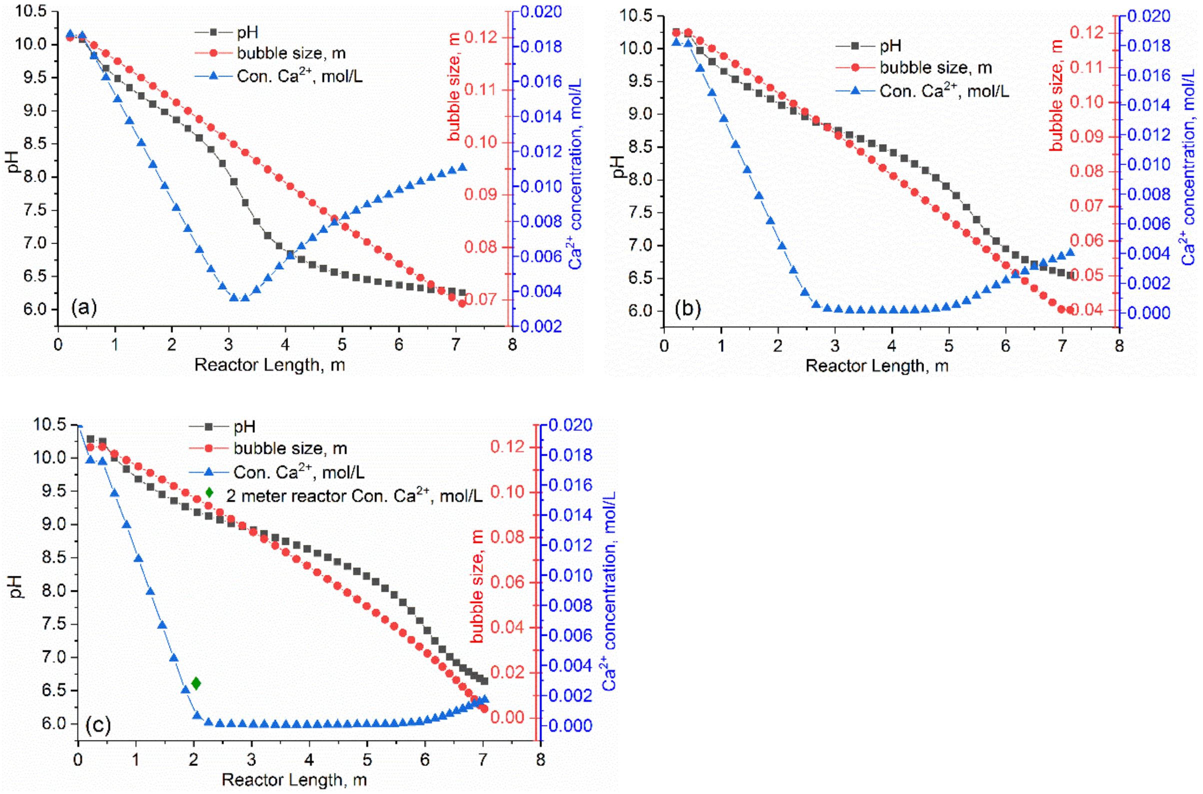

Figure 5.4 Model results of bubble size, pH value and Ca^{2+} concentration changes with various MEA concentrations: (a) 0.1 vol.% MEA (b) 0.3 vol.% MEA (c) 0.5 vol.% MEA. (the green symbol refers to the 2-meter (optimal reactor length) experimental result and validation of the model prediction for 2-meter reactor length) (Zhang et al., 2020).

In Figure 5.4(a), which shows the pH change, bubble size and Ca^{2+} concentration curves as a function of reactor length, the process can be divided into two stages. In the earlier precipitation stage, the Ca^{2+} concentration steeply decreased, and at the same time pH also decreased, both of which can be attributed to the dissolution and subsequent hydration of CO_2, which consumes OH^-, and the $CaCO_3$ precipitation. In the redissolution stage, the calcium carbonate concentration gradually decreased, releasing back Ca^{2+} ions, since the pH value decline beyond the point that leads to partial dissolution of the $CaCO_3$ particles, and this can be confirmed from the HCO_3^- concentration profile in Figure 5.5 (Zhang *et al.*, 2020).

In Figure 5.4(b) and (c), the calcium concentration reaches a plateau, and remains stable close to zero for much of the remaining reactor length, and this is due to the sufficient pH buffering effect of the higher MEA concentrations used. Closer to the reactor outlet, some $CaCO_3$ still dissolved back to the solution, as a result on the continued dissolution of CO_2 into the liquid phase, despite absence of calcium ions, resulting in the pH value eventually dropping below the stability limit of calcium carbonate. The CO_2 dissolution is verified by the ever decreasing bubble length in all cases. The bubble size at the reactor outlet decreased with the increasing MEA concentration, which confirms that MEA aids in CO_2 dissolution. The results from experiments and the model are almost identical, and slight errors seen in the comparisons shown in Table 5.5 can be acceptable due to the measurement inaccuracy or model simplifications. The right column indicated the differences between the experiments and the model with different parameters, including final bubble size, outlet H^+ concentration, outlet Ca^{2+} concentration and outlet pressure. The experiments conditions at 40 ˚C with L/G flowrate ratio of 40/80, 0.020 M $CaCl_2$, and 0.1-0.5 vol.% MEA solution (Zhang *et al.*, 2020). Percentage differences of pH values are calculated based on $[H^+]$, and the measured pH values have uncertainty of +/- 0.02 units, which is equivalent approximately to +/- 4.6% $[H^+]$ at the median pH value here reported (Schmitz, 1994).

Table 5.5 Experimental and model data comparison of final bubble size, outlet pH/Ca^{2+} concentration/pressure as a function of MEA concentration (Zhang et al., 2020).

		Experiment	Model	% Different
0.1 vol.% MEA	Final bubble size (m)	7.00E-02	6.89E-02	1.57%
	Outlet pH	6.26	6.29	6.67%
	Outlet Ca^{2+} conc. ($mol \cdot L^{-1}$)	9.6E-03	1.04E-02	8.33%
	Outlet Pressure (kPa)	101.325	101.304	0.02%
0.3 vol.% MEA	Final bubble size (m)	4.00E-02	4.03E-02	0.75%
	Outlet pH	6.28	6.25	7.15%
	Outlet Ca^{2+} conc. ($mol \cdot L^{-1}$)	4.00E-03	3.8E-03	5.0%
	Outlet Pressure (kPa)	101.325	101.404	0.078%
0.5 vol.% MEA	Final bubble size (m)	4.26E-03	4.64E-03	8.92%
	Outlet pH	6.61	6.58	7.15%
	Outlet Ca^{2+} conc. ($mol \cdot L^{-1}$)	8.00E-04	8.29E-04	3.62%
	Outlet Pressure (kPa)	101.325	101.535	0.2%

Figure 5.5(a) and (b) shows all the species concentration varying with the reaction length, when MEA is 0.5 vol.%, temperature is 50°C, and L/G flowrate ratio is 40/80. The figure shows opposite trends of concentrations of MEA (RNH_2) and protonated

MEA (RNH_3^+), since MEA reacts with water. The carbamate concentration rises and later drops, but at all times remains much lower than that of the other two amine species. This may seem like an inefficient use of amine, but it is important to note that protonation reaction produces hydroxyl groups, which are vital for buffering the reaction and permitting extensive carbonate formation. The concentrations of $CaOH^+$, $CaHCO_3^+$, and $CO_{2(aq)}$ (which is essentially H_2CO_3) are very low compared to the other species, therefore, they are plotted in log scale. The incline of the concentration of HCO_3^- was sharply up, but only after $CaCO_3$ reached a maximum value, signifying that carbonate anion consumption by the carbonate precipitation reaction is balanced by carbonate formation from the dissociation of bicarbonate anion. The carbonic acid concentration eventually rises, once the system is saturated with carbonates and nearly saturated with bicarbonates, and once no free amine is available to react with CO_2. Figure 5.5(c) shows the driving force in the system, which agrees with this trend. It declined gradually for most of the reactor length, and then dropped sharply once dissolved unreacted CO_2 concentration started to build-up. The sharp drop in the very beginning is due to the initial contact of the liquid and gas phases, as the liquid is modelled to initially not contain any CO_2 species (Zhang *et al.*, 2020).

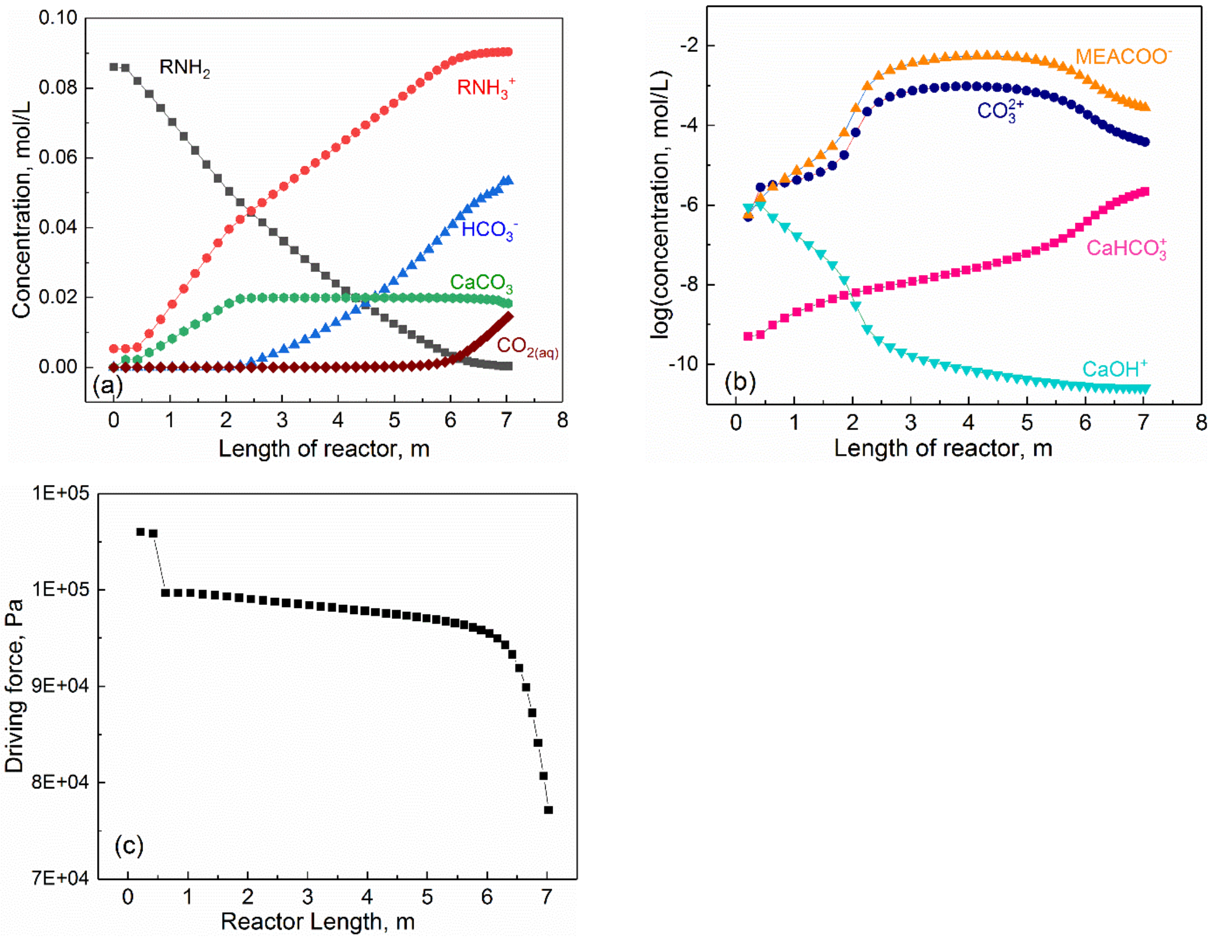

Figure 5.5 (a) and (b) Species concentration in liquid phase as a function of tubular reactor length; (c) Driving force change along with the reactor length. (0.5% MEA, 50 ˚C, L/G=40/80) (Zhang et al., 2020).

Figure 5.6 illustrates the relationship between overall mass transfer coefficients, gas flow rate and MEA concentration. In the 0.1 vol.% MEA solution, the K values are linearly correlated with the gas flow rate (Figure 5.6(a)), whereby the higher flow rate of the gas lead to improved mass transfer. Given that the liquid flowrate was kept constant in this comparison, it can be said that a higher gas-to-liquid ratio produces longer bubbles, which have greater surface area, aiding in the mass transfer. Also, high total flow rate with higher gas flow rate and constant liquid flow rate leads to higher two-phase flow velocity, which in turn leads to greater recirculation within the gas bubbles and liquid plugs according to Taylor Flow regime, thus also aiding in mass transfer by reducing boundary layers across the interface. The MEA concentration increase also resulted in a higher overall mass transfer coefficient. Here, the effect is likely due to insufficient correction of the Henry's Law constant for the presence of MEA, as it is not expected that MEA will result in physical effects that improve mass transfer, so a chemical effect that is not captured in the Henry's Law constant correction is likely the cause (Zhang *et al.*, 2020).

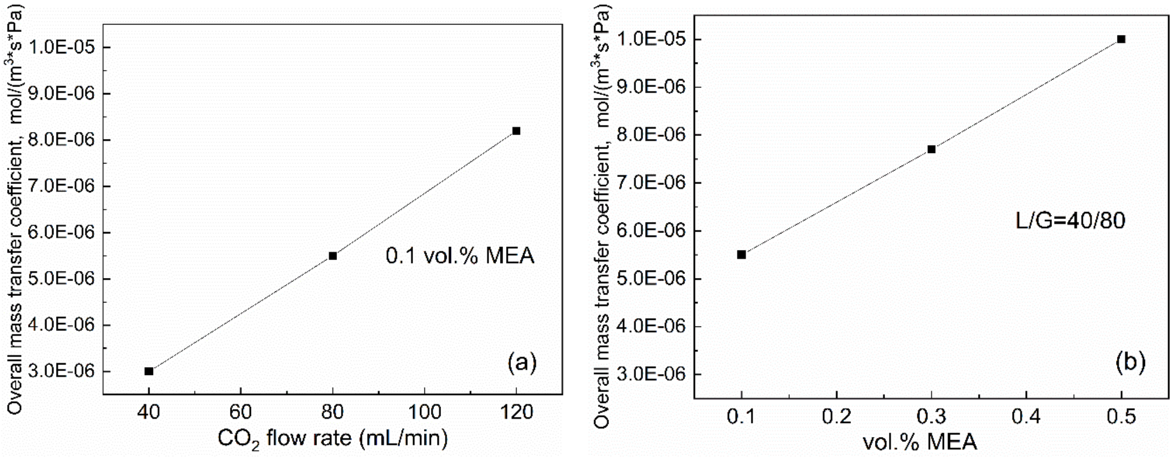

Figure 5.6 The relation between overall mass transfer coefficient and (a) gas flow rates and (b) MEA concentrations (Zhang et al., 2020).

With the benefit of the model, we can predict the species changing in the tubular reactor and then can design the reactor length to be only long enough to maximize carbonate formation and thus CO_2 sequestration. For example, the $CaCO_3$ concentration reached a maximum stable value around 2 meter in Figure 5.5(a), which means that the extra reactor length was not necessary in this case. In order to validate our model, we rebuilt 2-meter reactor to check the results as shown as green symbol in Figure 5.4(c), and the result is close to the model prediction. Such optimization, which is made possible by having a model that shows speciation as a function of tubing length, will contribute to cost reduction and reactor compactness in large-scale design (Zhang *et al.*, 2020).

Conclusion

This chapter demonstrated CO_2 mineralisation process in continuous tubular reactor from the perspective of experimental and model phase. The carbonates can be produced under mild operational process. This study focused on CO_2 sequestration with low concentration MEA solution to reduce the material cost. The calcium conversion efficiency can reach nearly 100% with very low MEA concentrations 0.1vol.% and low CO_2 flowrate which was found to be most atom efficient to utilise the brine source. CCE can also be increased with higher CO_2 flowrates to reduce the residence time. The catalysts 30 mg·L^{-1} NiNPs can accelerate the carbonation reaction up to around 10% at optimal experimental conditions. The morphologies of precipitates can be varied under different reaction temperatures and lower temperature favoured purer spherical vaterite, while partially carbonates transformed to aragonite under higher temperature. The effects of $MgCl_2$ and NaCl on CEE were also tested, indicating that Mg^{2+} competed for carbonate ions and CCE was slightly influenced in the presence of NaCl due to higher ionic strength.

The model explored the mass transfer of CO_2 across the gas-liquid interface in a Taylor flow reactor which can predict the speciation, bubble size and other parameters adjustments during the reaction in the tubular reaction and can be applied in large-scale design. The overall mass transfer coefficients were obtained with different CO_2 flowrates and MEA concentrations. The results of modelling showed that bubble length decreased with higher MEA concentration due to the rapid chemical reaction. The overall mass transfer coefficients increased with higher CO_2 flowrates. Modelled data are also in agreement with the experimental data and validated with experiments. With the benefit of model, the ionised species distribution in carbonation process can be predictable and be capable to achieve the optimal process conditions (Zhang *et al.*, 2020).

References

Aaron, D. and Tsouris, C. (2005) 'Separation of CO_2 from Flue Gas: A Review', *Separation Science and Technology*, 40(1-3), pp. 321-348.

Aboudheir, A., Tontiwachwuthikul, P., Chakma, A. and Idem, R. (2003) 'Kinetics of the reactive absorption of carbon dioxide in high CO_2-loaded, concentrated aqueous monoethanolamine solutions', *Chemical Engineering Science*, 58(23-24), pp. 5195-5210.

Bates, R., Bower, V., Canham, R. and Prue, J. (1959) 'The dissociation constant of $CaOH^+$ from 0 to 40 ˚C', *Transactions of the Faraday Society*, 55, pp. 2062-2068.

Bates, R.G. and Pinching, G.D. (1951) 'Acidic dissociation constant and related thermodynamic quantities for monoethanolammonium ion in water from 0 ˚C to 50 ˚C', *Journal of Research of the National Bureau of Standards*, 46(5), p. 349352.

Bhaduri, G.A. and Šiller, L. (2013) 'Nickel nanoparticles catalyse reversible hydration of carbon dioxide for mineralization carbon capture and storage', *Catalysis Science & Technology*, 3(5), pp. 1234-1239.

Danckwerts, P. (1951) 'Significance of liquid-film coefficients in gas absorption', *Industrial & Engineering Chemistry*, 43(6), pp. 1460-1467.

Duan, Z. and Li, D. (2008) 'Coupled phase and aqueous species equilibrium of the H_2O–CO_2–NaCl–$CaCO_3$ system from 0 to 250°C, 1 to 1000 bar with NaCl concentrations up to saturation of halite', *Geochimica et Cosmochimica Acta*, 72(20), pp. 5128-5145.

Edwards, J.T., Maurer, G., Newman, J., Prausnitz, J.M. (1978) 'Vapor-liquid equilibria in multicomponent aqueous solutions ofvolatile weak electrolytes', *AIChE. Journal*, 24(6), pp. 966–976.

Huertas, J.I., Gomez, M.D., Giraldo, N. and Garzón, J. (2015) 'CO_2 Absorbing Capacity of MEA', *Journal of Chemistry*, 2015, pp. 1-7.

Jacobson, R.L. and Lanqmuir, D. (1974) 'Dissociation constants of calcite and $CaHCO_3^+$ from 0 to 50 °C', *Geochimica et Cosmochimica*, 88, pp. 301-318.

Koutsoukos, P.G. and Kontoyannis, C.G. (1984) 'Precipitation of calcium carbonate in aqueous solutions', *Journal of the Chemical Society, Faraday Transactions 1: Physical Chemistry in Condensed Phases*, 80(5), pp. 1181-1192.

Lee, M.-J. and Lin, T.-K. (1995) 'Density and Viscosity for Monoethanolamine + Water, + Ethanol, and + 2-Propanol', *Journal of Chemical & Engineering Data*, 40(1), pp. 336-339.

Liu, Y., Zhang, L. and Watanasiri, S. (1999) 'Representing Vapor−Liquid Equilibrium for an Aqueous MEA−CO_2 System Using the Electrolyte Nonrandom-Two-Liquid Model', *Industrial & Engineering Chemistry Research*, 38(5), pp. 2080-2090.

Manlapaz, R.L. and Churchill, S.W. (1980) 'FULLY DEVELOPED LAMINAR FLOW IN A HELICALLY COILED TUBE OF FINITE PITCH', *Chemical Engineering Communications*, 7(1-3), pp. 57-78.

Millero, F.J. (1992) 'Stability constants for the formation of rare earth-inorganic complexes as a function of ionic strength', *Geochimica et Cosmochimica Acta*, 56(8), pp. 3123-3132.

Plummer, L.N. and Busenberg, E. (1982) 'The solubilities of calcite, aragonite and vaterite in CO_2-H_2O solutions between 0 and 90 °C, and an evaluation of the aqueous model for the system $CaCO_3$-CO_2-H_2O', *Geochimica et cosmochimica acta*, 46(6), pp. 1011-1040.

R.C. Xin, A. Awwad, Z.F. Dong, M.A. Ebadian and Soliman, H.M. (1996) 'An investigation and comparative study of the pressure drop in air-water two-phase flow in vertical helicoidal pipes', *International Journal of Heat and Mass Transfer*, 39(4), pp. 735-743.

Sander, R. (2015) 'Compilation of Henry's law constants (version 4.0) for water as solvent', *Atmospheric Chemistry and Physics*, 15(8), pp. 4399-4981.

Schmitz, G. (1994) 'The uncertainty of pH', *Journal of chemical education*, 71(2), p. 117.

Sheikholeslami, R. and Ong, H. (2003) 'Kinetics and thermodynamics of calcium carbonate and calcium sulfate at salinities up to 1.5 M', *Desalination*, 157(1-3), pp. 217-234.

Šiller, L. and Bhaduri, G.A. (2013) *Carbon Capture, Patent, T/GB2013/051243 (WO 2013171480 A2, WO2013171480 A3,US20150151248 A1, EP2849871 A2, CN104428051 A)*.

Trushina, D.B., Bukreeva, T.V., Kovalchuk, M.V. and Antipina, M.N. (2014) '$CaCO_3$ vaterite microparticles for biomedical and personal care applications', *Materials Science Engineering: C*, 45, pp. 644-58.

Vučak, M., Perić, J. and Krstulović, R. (1997) 'Precipitation of calcium carbonate in a calcium nitrate and monoethanolamine solution', *Powder Technology*, 91(1), pp. 69-74.

Vučak, M., Perić, J., Žmikić, A. and Pons, M.-N. (2002) 'A study of carbon dioxide absorption into aqueous monoethanolamine solution containing calcium nitrate in the gas–liquid reactive precipitation of calcium carbonate', *Chemical Engineering Journal*, 87(2), pp. 171-179.

Zhang, N., Santos, R.M. and Šiller, L. (2020) 'Rapid CO_2 capture-to-mineralisation in a scalable reactor', *Reaction Chemistry & Engineering*, 5(3), pp. 473-484.

Chapter 6. Cyclical process with regenerative hydrotalcites

In this chapter, a novel process is developed to remove chloride anions from alkaline brines by ion exchange using hydrotalcites (HT), releasing hydroxyl groups in exchange for chloride, sufficiently raising the pH of brines to enable the precipitation of carbonates during CO_2 mineralisation. The preparation and characterisation of HT is shown in section 3.4.2 of Chapter 3. Moreover, the HT materials are recyclable for multiple usage by taking advantage of the HT's 'memory effect' property illustrated in section 3.4.4 of Chapter 3. Gaseous CO_2 and Na_2CO_3 solution were used as to exchange the chloride anions from the reacted HT interlayers and intercalate with HCO_3^- or CO_3^{2-}, followed by a calcination process to produce the regenerated calcined-HT (CHT). Several reaction cycles were conducted to evaluate the reusable property. The results of this chapter have been published in *Chemical Engineering Journal* (Zhang *et al*., 2021).

6.1 Characterisation

The XRD diffractograms of calcined and not-calcined HT, prepared with different ratios of Mg/Al, are shown in Figure 6.1. The samples before calcination are well crystallised and layered materials, attributing to magnesium aluminium hydroxycarbonate, while they turn to amorphous phases and less crystallised materials after calcination. The poorly crystallised condition is due to the disorder of the interlayers and lack of symmetry of the structures. The crystallinity increased with the higher Mg/Al ratio of 4. The interatomic distance of the d_{003} layer, which represents the basal spacing of two host layers (Wang and Wang, 2007), also became shorter with higher Mg/Al ratio. The same trend was also obtained for d_{006}. The characteristic diffraction peaks for such HT material appear at 2θ values of 11.02˚, 23.55˚, 34.84˚, 39.03˚, 46.29˚, 60.96˚ and 62.26˚ (Reichle *et al.*, 1986). After calcination process, the structure of hydrotalcite was collapsed and converted to a mixture of oxides of magnesium and aluminium. It has been reported that the physically absorbed water does not interrupt the layered structure of HT when the temperature is up to 100 ˚C, while the basal spacing starts to decrease at 200 ˚C with the disappearance of (006) from XRD patterns (Tichit *et al*., 1998). The layered structure remains up to 300 ˚C, beyond which it shifts to MgO-like structure with the occurrence of decomposition of anions at 400 ˚C (Tichit *et al*., 1998).

However, the lattice parameters are smaller than that in brucite, because HTs are a mixture of oxides with Al (Gazzano *et al*., 1997).

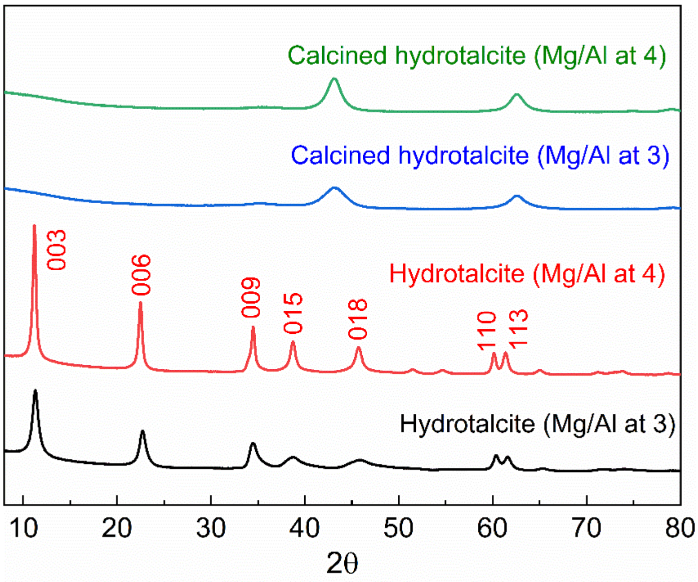

Figure 6.1 XRD patterns of hydrotalcites and calcined hydrotalcites with different Mg/Al ratios (Zhang et al., 2021).

The morphologies of these samples were characterised by SEM/EDX. The rosette-shaped hydrotalcite, produced under pH value of 10, is shown in Figure 6.2. It has been reported that coprecipitation preparation method can lead to particles agglomerated in clusters due to high base supersaturation conditions, and the structure can be very stable (Adachi-Pagano *et al*., 2003). The porous sponge-like morphology still maintains after calcination, which means that the micro-scale layered structure is not affected by thermal decomposition as much as the atomic-scale crystalline structure (Zhang *et al*., 2021).

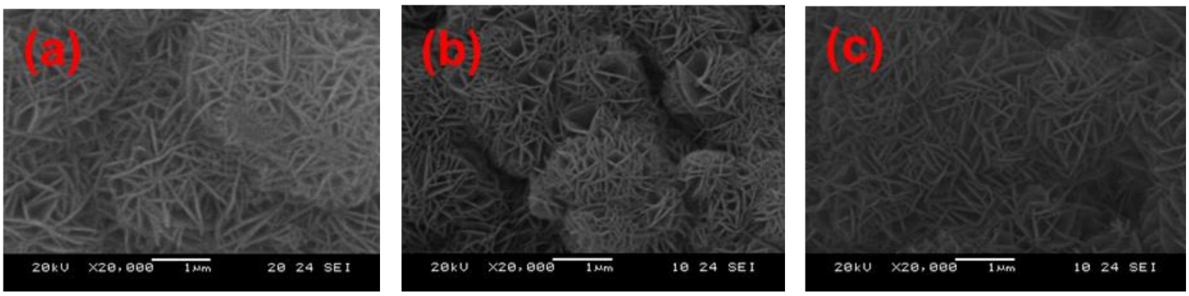

Figure 6.2 SEM images of samples: (a) hydrotalcite (Mg/Al at 4); (b) calcined hydrotalcite (Mg/Al at 4); (c) calcined hydrotalcite (Mg/Al at 3) (Zhang et al., 2021)

According to semi-quantitative EDX analysis of elemental composition, the Mg/Al atomic ratio for samples prepared at 3 and 4 are 3.02 and 3.51, respectively. The Mg/Al ratios of the final products are thus close to the values used in the original stoichiometries.

The TGA and DTG curves for HT samples prepared with Mg/Al ratio of 4, and before calcination, are shown in Figure 6.3. There are three main weight loss peaks appearing, which represent the loss of weakly bonded interlayer water molecules up to around 220 ˚C for the first weight loss peak, and the loss of chemically bonded hydroxyl and carbonate/bicarbonate interlayer anions occurring, from 300 to 600 ˚C, for the second (major) and third (minor) peaks (Constantino and Pinnavaia, 1995). It has been reported that extrinsic water placed in the multilayers on the surface of samples is lost at 60 ˚C, while the intrinsic water starts to be lost above 150 ˚C (Yun and Pinnavaia, 1995). It has also been reported that most of the CO_2 release occurs before 500 ˚C, with 20-30% remaining and being released at 600 ˚C and 900 ˚C (Hibino *et al.*, 1995). However, high temperature CO_2 release is accompanied by migration of Al ions in the calcined material, and thus loss of structure (Hibino *et al.*, 1995). As such, and given the TGA results obtained, all the prepared HT samples were calcined at constant temperature of 500 ˚C to produce CHT. By weighting the synthesized HT samples before and after calcination process, there was around 41-43% weight loss, which agrees with the weight loss observed in the TGA, and can thus be mainly assigned to the release of CO_3^{2-}/HCO_3^{-} and OH groups as $H_2O_{(g)}$ and $CO_{2(g)}$, respectively (Zhang *et al.*, 2021).

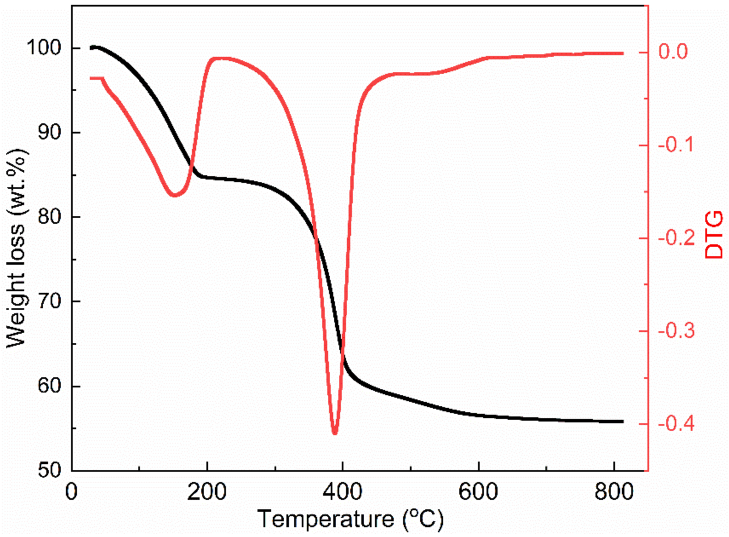

Figure 6.3 TGA-DTG diagram for synthesized hydrotalcite (Mg/Al = 4) before calcination (Zhang et al., 2021).

6.2 Cl removal process

The ion-exchange ability of the CHT prepared is evaluated with the artificial brine to investigate the effect of Mg/Al ratio at different temperatures and solid/liquid ratios. The effect of temperature on Cl^- removal was first investigated under 40 °C and 60 °C with different Mg to Al ratios with a fixed solid to liquid ratio of 0.014 $g \cdot mL^{-1}$; this value was selected to attempt to check the temperature effect slightly outside the optimal condition, and the results are illustrated in Table 6.1. The results indicate that higher temperature can lead to higher Cl^- removal efficiencies at both Mg/Al ratios, which means that higher temperature can help Cl^- ions penetrate the interlayers and attach to the hydrotalcite. Ahmed and Gasser (Ahmed and Gasser, 2012) reported thermodynamic data on the adsorption process of layered double hydroxides, and attributed higher adsorption at higher reaction temperatures to a more negative Gibbs free energy change, which is in agreement with the behaviour of endothermic processes at higher temperatures. Based on these results and reasoning, 60 °C was applied in the subsequent experiments (Zhang *et al.*, 2021).

Table 6.1 Chloride removal efficiency with different synthesised CHT using S/L of 0.014 g·mL^{-1} (Zhang et al., 2021).

Mg/Al ratio	Reaction temperature at 40˚C	Reaction temperature at 60˚C
3	83.1%	87.5%
4	85.3%	88.9%

Solid to liquid ratios ranging from 0.010 to 0.020 g·mL^{-1} were tested with different CHT samples, and results are shown in Figure 6.4 (Zhang *et al*., 2021). These S/L ratios are approximately varied from 0.6 to 1.2 times the stoichiometric amount needed for 0.040 M Cl$^-$ solution. As expected, higher removal efficiencies can be achieved by increasing the CHT mass, and the efficiencies obtained closely correspond to stoichiometry, except at the highest dosage where the efficiency comes close to, but does not reach 100% (Zhang *et al*., 2021). At low S/L ratio, all the active sites are relatively fully exposed for adsorption, but the availability of higher energy sites decreases with higher particle concentration due to competition (Honeyman and Santschi, 1988). Moreover, the CHT prepared with greater Mg/Al ratio showed slightly better Cl$^-$ removal performance. The Mg/Al ratio affects the number of basic sites, according to the research of Nakatuska et al. (Nakatsuka *et al.*, 1979), and basic sites increase with the Mg/Al ratio. MgO content contributes with two types of basic sites, O_2^- and OH^-, on the surface, whereas Al_2O_3 does not contribute to strong basic sites on the surface (St Malinowski and Sloczynski, 1967).

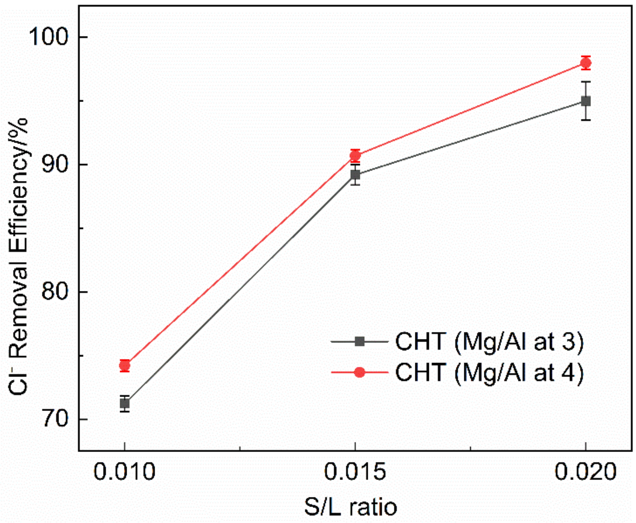

Figure 6.4 Cl removal efficiency with CHTs under different ratios (Zhang et al., 2021).

The BET specific surface area, N_2 adsorption and desorption isotherms, and pore size distribution were analysed at 77K, and data is shown in Figure 6.5 and Table 6.2. The specific surface area expanded after calcination, since the CO_2 release between layers can enlarge the pores of samples. The specific surface area of the sample with Mg/Al ratio at 4 is greater than that at 3, as is its average pore size. The larger pore size of in the mesoporous region and greater specific surface area contributes to the observed higher Cl^- removal efficiency. After the Cl^- removal experiment, the specific surface area reduced, attributing to the Cl^- ions captured between the interlayers, and the average pore size after reaction became smaller compared to before reaction. It can be seen from Table 6.2 that the specific surface area and total pore volume of the reacted sample decreased even lower than that of the original pre-calcination HT (Zhang *et al*., 2021).

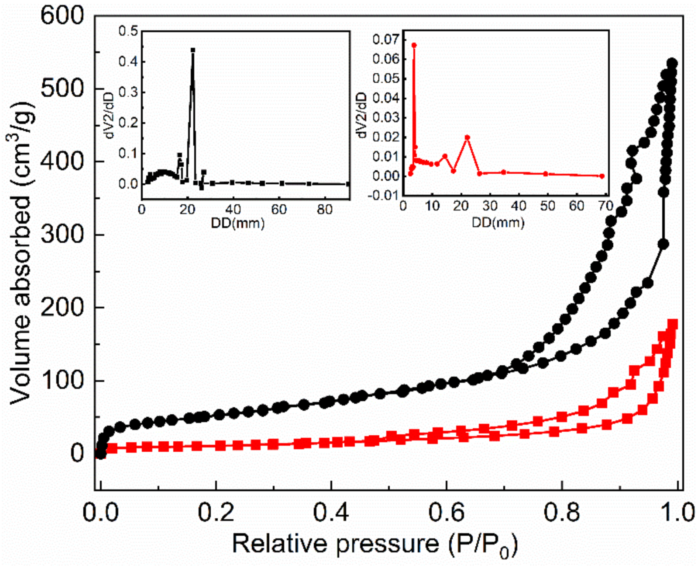

Figure 6.5 N_2 adsorption/desorption isotherms and pore size distribution of hydrotalcite (red, right) and calcined hydrotalcite (black, left) (Zhang et al., 2021).

Table 6.2 Specific surface area and pore size distribution (Zhang et al., 2021).

Sample	Specific surface area (m^2/g)	Total pore volume (cm^3/g)	Average pore size (nm)
Hydrotalcite (Mg/Al= 4)	39.3	0.299	13.67
CHT (Mg/Al=3)	181.4	0.971	12.03
CHT (Mg/Al=4)	191.7	0.858	14.16
CHT (Mg/Al=4) after Cl^- removal reaction	12.4	0.078	9.28

As shown in Figure 6.5, the sample post-calcination exhibits Type II and Type IV isotherm classification in combination with a H3 type hysteresis loop. In contrast, the sample pre-calcination exhibits Type I isotherm at relative pressure (P$_o$/P) lower than 0.5, and turns to Type II isotherm with higher relative pressure with Type H3 loop (Thommes *et al.*, 2015). Figure 6.5 also contains sub-plots of the mesopore size distribution of these two samples, based on BJH calculation method using desorption isotherms. The calcined sample has a sharp peak at around 22 nm, while the sample before calcination displayed a sharp peak at 4 nm and broader mesopores distribution. This means that the thermal treatment promotes larger mesopore formation and influences the pore size distribution (Zhang *et al.*, 2021).

The XRD diffractograms of CHT before and after Cl$^-$ removal reaction is shown in Figure 6.6(left). The XRD pattern of the calcined material was restored to a crystalline structure corresponding to pre-calcination HT after the sample was exposed in the aqueous solution to Cl$^-$, which refers to the ‘memory effect’ property of HT (Cavani *et al.*, 1991). This allows the samples to be regenerated for cyclical usage. Figure 6.6(right) presents an SEM image of sample after Cl$^-$ removal reaction, and it contains plate-like morphology reminiscent of fresh HT (Zhang *et al.*, 2021).

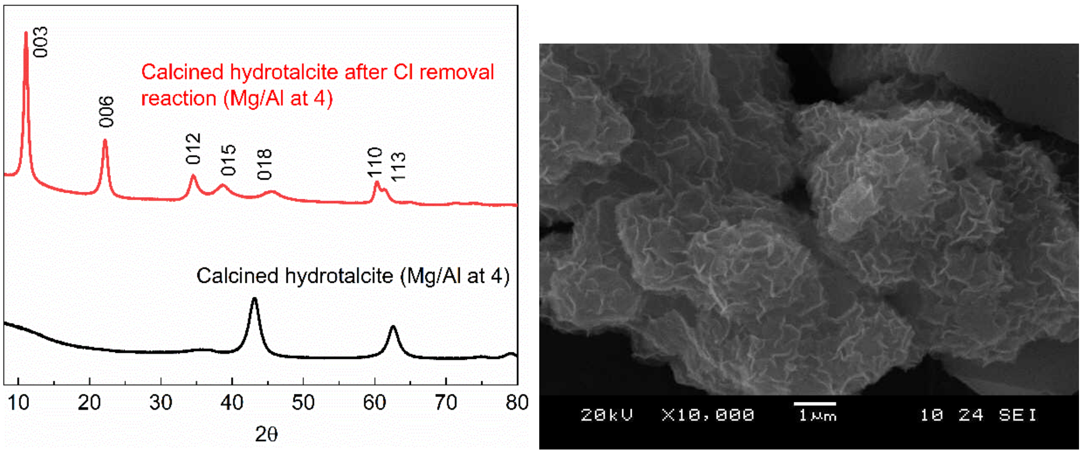

Figure 6.6 XRD diffractograms of CHT before and after Cl$^-$ removal reaction (left) and SEM image of sample after Cl$^-$ removal reaction (right) (Zhang et al., 2021).

The effect of sodium chloride on the absorption process was also investigated, because of its high concentration in desalination brines. The experiment was carried out with the CHT sample with Mg/Al at 4, S/L at 0.020 g·mL^{-1}, under 60 °C, in solution with 0.020 M $CaCl_2$ and 0.60 M NaCl. In the presence 0.6 M NaCl solution, the total amount of chloride anion removal was 2327 ppm, which is greater than the amount of Cl^- (1420 ppm) contributed by the $CaCl_2$ content, and greater than the amount that the same sample under the same S/L ratio achieved in absence of NaCl (Figure 6.4). This shows that CHT is capable of removing Cl^- that originates from Ca^{2+} as well as Na^+, thus extending it applicability to various types of brine (Zhang *et al*., 2021).

6.3 Cycle assessment and regeneration process

The possibility to regenerate and reuse hydrotalcite can significantly decrease the operational costs on the whole process. The crucial property of this material is the so called 'memory effect', which can benefit the regeneration process. TGA/DTG analysis data for a spent sample (after chloride removal) is shown in Figure 6.7. The two main peaks are similar to those in the HT before calcination, however, the first weight loss peak is shifted about 20 ˚C lower compared with the HT (Figure 6.3). This can be explained by the interaction of chloride ions weakening the interlayer water (Zhang *et al*., 2010; Zhang *et al*., 2021).

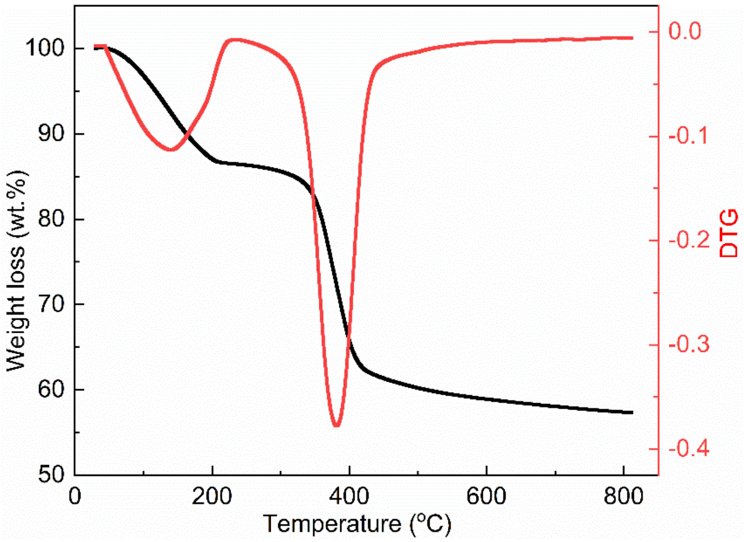

Figure 6.7 TGA/DTG curves for spent HT sample after Cl^- removal reaction (Zhang et al., 2021).

Based on the anion absorption sequence aforementioned, carbonate and bicarbonate anions were deployed to be ion exchangers. Thus, to test recyclability of CHT, five cycles of Cl removal and regeneration with gaseous CO_2 and Na_2CO_3 solution, followed by calcining to 500 °C for 2 hours, were used. The comparative results are presented in Figure 6.8 and Figure 6.9 (Zhang *et al*., 2021).

With the use of Na_2CO_3 solution for regeneration (Figure 6.8), the Cl^- removal efficiency can be maintained above 80% under two S/L ratios tested, 0.015 and 0.020 g·mL^{-1}. It is concluded that regeneration with Na_2CO_3 is promising because of the relatively high pH of Na_2CO_3 solution, allowing the structure to be restored well during the regeneration process. The higher S/L ratio at 0.020 g·mL^{-1} achieves higher Cl^- removal efficiency in the first cycle (98%), and with the increasing number of the experimental cycles, the Cl^- removal efficiency gradually declines, but remains above 83% after five cycles. The Na_2CO_3 regeneration efficiency was not as high with S/L at 0.015 g·mL^{-1}. The reason is that more chloride anions are adsorbed per unit mass of HT, chloride anions occupy more space within the HT interlayers and block pores, which demands stronger ion exchange process to remove them (Zhang *et al*., 2021).

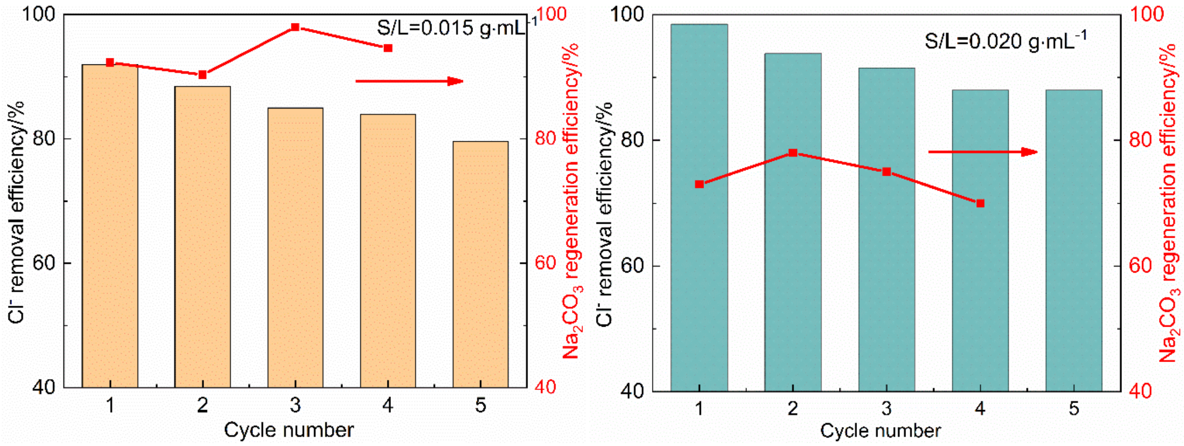

Figure 6.8 Recycling process performance with multiple Na_2CO_3 regeneration cycles of CHT under varying S/L ratios; chloride removal efficiencies (left axes) and Na_2CO_3 regeneration efficiencies (right axes) (Zhang et al., 2021).

The results for the use of CO_2 injection into the HT-Cl solution for regeneration are shown in Figure 6.9. This method can save process cost, and thus energy, because no chemicals are used, and this source of CO_2 can be achieved from the calcination process, as the CO_2 can be used circulated. The Cl^- removal efficiency can also be kept above 90% up the third cycle under higher S/L, as in the case of Na_2CO_3; however, the efficiency of CO_2-regenerated CHT sharply decreases thereafter. Because the CO_2 was injected continuously into the regeneration solution, the pH value eventually became too low after several rounds of experiments. The pH value dropped below 7.0 in the third cycle regeneration, which led to the HT being exposed to acid condition that eventually degraded the structure of the layered double hydroxide. Under this scenario, some mesopores collapse due to the host layers being brucite-like $Mg(OH)_2$, which is basic and can be dissolved in acid circumstance (Bravo-Suárez *et al.*, 2004). This was confirmed from the BJH desorption pore size and pore volume, presented in Table 6.3. As a result, both Cl^- removal efficiency and CO_2 regeneration efficiency drastically decreased in the fourth cycle, and a fifth cycle was not run due to insufficient solids being recoverable from regeneration (Zhang *et al.*, 2021).

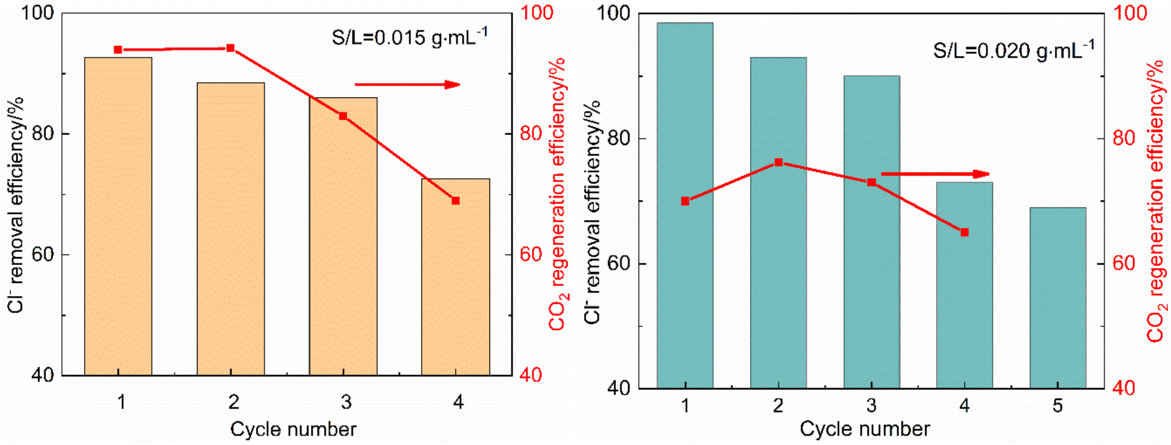

Figure 6.9 Recycling process performance with multiple CO_2 regeneration cycles of CHT under varying S/L ratios; chloride removal efficiencies (left axes) and CO_2 regeneration efficiencies (right axes) (Zhang et al., 2021).

Table 6.3 Surface area and pore size distribution of regenerated CHT samples by CO_2 gas (Zhang et al., 2021).

CHT sample	Specific surface area (m^2/g)	Total pore volume (cm^3/g)	Average pore size (nm)
Mg-Al-O Mg/Al=4	191.7	0.858	14.16
1st regen by CO_2	195.2	0.412	7.26
3rd regen by CO_2	190.9	0.391	5.36

It was found, based on EDX spectra analysis shown in Figure 6.10, that there was significant amount of Cl^- ions remaining on the host layers of regenerated CHT after the fourth cycle: 0.47 wt.% and 0.13 wt.% respectively, for CO_2 and Na_2CO_3 regeneration processes. With the regeneration process not removing the Cl^- content entirely via ion exchange, the Cl^- removal efficiency in the next cycle decreased. In addition, that increase in Ca signal from EDX might be due to CaO, CaO content of the regenerated HT increased over each cycle, given that 1.24 wt.% and 1.63 wt.% of Ca was detected by SEM-EDX after the fourth cycle with CO_2 and Na_2CO_3 regeneration, respectively (Zhang *et al*., 2021). Accumulation of CaO in the HT would lead to formation of $CaCO_3$ during the regeneration process, which then cannot be decomposed with the calcination temperature at 500°C, as this is below the decomposition temperature of calcium carbonates (Santos *et al.*, 2014).

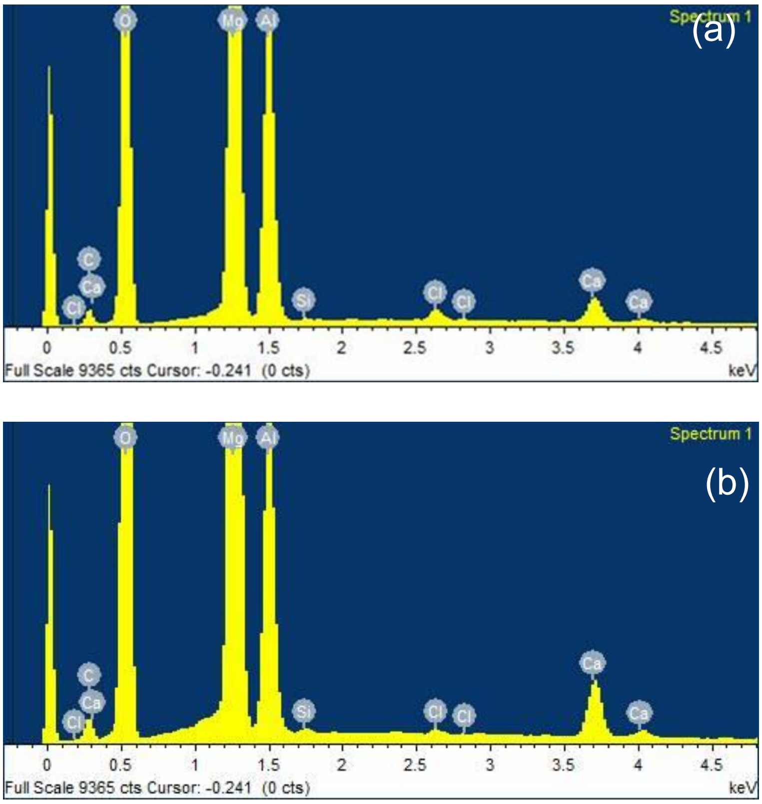

Figure 6.10 (a) EDX spectra regenerated CHT after the fourth cycle of CO_2 regeneration process; (b) EDX spectra regenerated CHT after the fourth cycle of Na_2CO_3 regeneration process (Zhang et al., 2021).

The XRD patterns of spent HT-Cl samples, having undergone various cycles of regeneration via the two approaches discussed are shown in Figure 6.11. The main structural features of hydrotalcites are reconstructed well after each generation, however, the crystallinity degree of the samples decreased with the increasing regeneration cycles. A new peak appears at 29.4° (2θ), which can be assigned to calcite (Kontoyannis and Vagenas, 2000). The intensity of this calcite peak is lower for the samples regenerated with gaseous CO_2 than for the samples regenerated with Na_2CO_3 solution, and in the latter case grow stronger with each passing cycle. In the case of Na_2CO_3 regeneration, the accumulation of calcite attached on the HT occurred due to the higher pH value of the solution during regeneration allowing for precipitation of calcium carbonate. The calcite peak disappeared in the fifth cycle with CO_2 regeneration due to the pH of the solution declining below 6.0 during CO_2 injection, which dissolves the accumulated carbonate back to the solution (Zhang *et al.*, 2021).

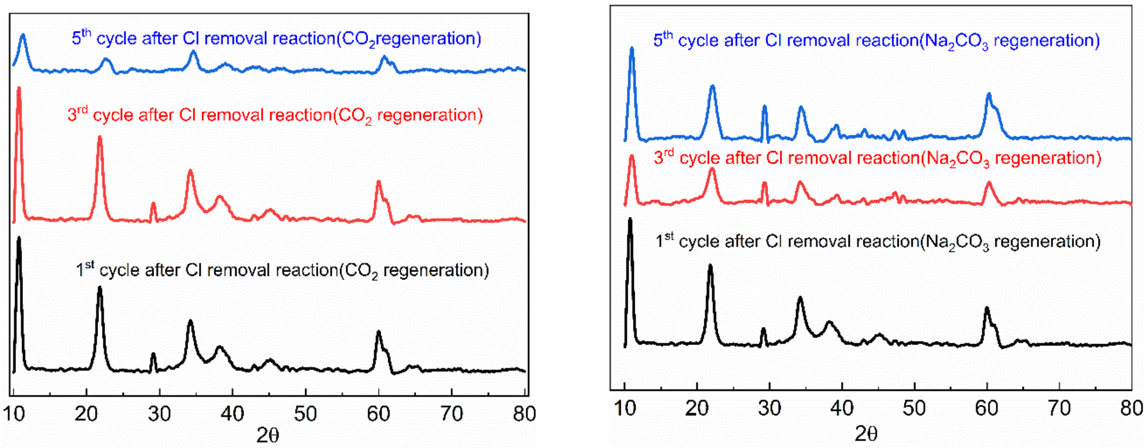

Figure 6.11 XRD patterns of HT-Cl collected after various cycles of regeneration using CO_2 (left) and Na_2CO_3 (right), after Cl^- removal reaction.

The calcite formation, accumulation, and eventual disappearance in the case of CO_2 injection, is also confirmed from the XRD patterns of CHT prior to Cl^- removal reaction, as shown in Figure 6.12. The carbonate was not decomposed during calcination because the temperature is not sufficient. The two main broad peaks in Figure 6.12 are assigned to periclase (MgO) (Hibino *et al.*, 1995), which forms from the heat treatment of the layered double hydroxide (Zhang *et al.*, 2021).

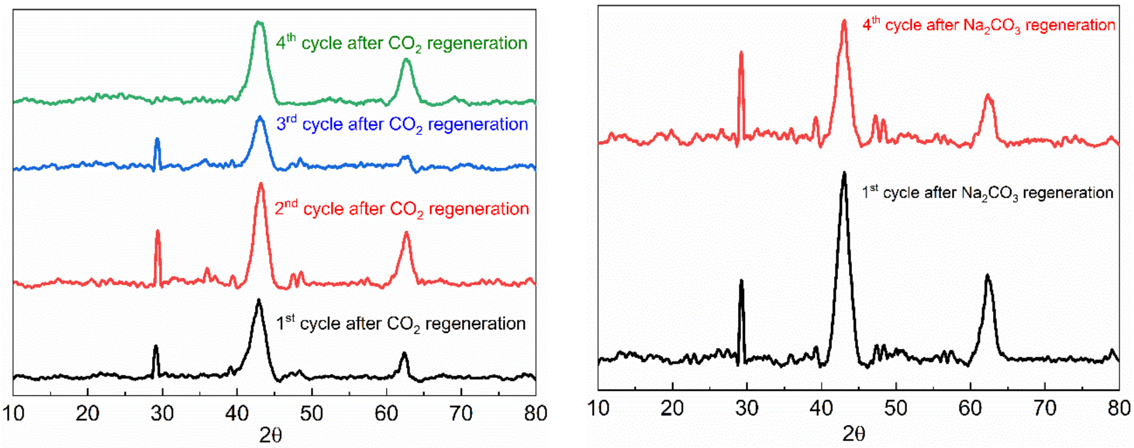

Figure 6.12 XRD patterns of CHT collected after various cycles regeneration using CO_2 (left) and Na_2CO_3 (right), after calcination (Zhang et al., 2021).

SEM images of HT samples after the first and fourth regeneration cycle using gaseous CO_2 are shown in Figure 6.13. It displayed that the structure is plate-like and there were rosette-shaped particles on the surface, but the higher order structure seen for the fresh HT (Figure 6.2) degrades as cycles pass. This indicates that the regeneration process cannot fully reconstruct the original morphology of hydrotalcite, which gradually impacts the Cl^- removal performance (Zhang *et al*., 2021).

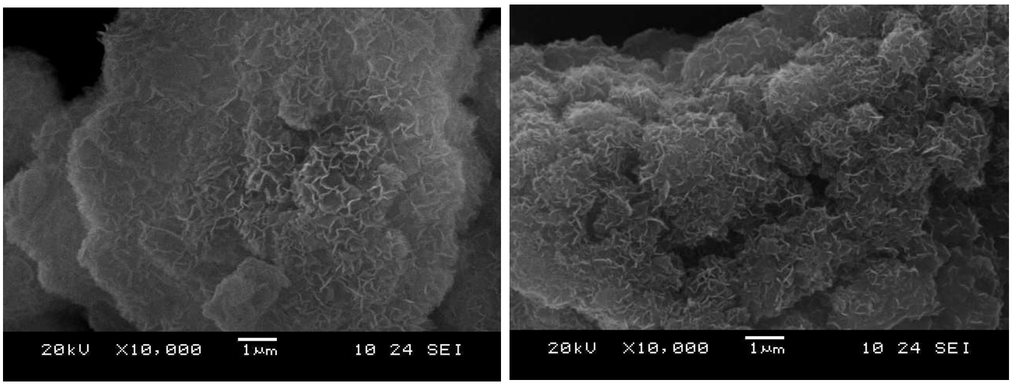

Figure 6.13 SEM images of HT sample after first regeneration (left) and fourth regeneration (right) using gaseous CO_2 (Zhang et al., 2021).

6.4 CO_2 uptake

CO_2 uptake performance of the dechlorinated brine was investigated using a batch reactor and simulated flue gas (12% CO_2). Dechlorinated solution has suitable alkaline pH and contains $Ca(OH)_{2(aq)}$, thus readily reacting with CO_2 to produce $CaCO_3$, as a means of fixing the gaseous CO_2 as a stable solid for permanent storage. The pH values of dechlorinated solutions obtained after each of the five cycles of Cl^- removal, using regenerated CHT, was measured before the mineralisation process, and are shown in Table 6.4. There is a gradual declining trend in pH with the increasing cycles, due to the degradation of HT and its Cl^- removal ability, as previously presented. Yet, in all cases, the pH is sufficiently alkaline to allow for $CaCO_3$ precipitation. The Ca^{2+} concentration in the dechlorinated solutions, before and after mineralisation reaction, was measured by ICP-OES; from these data, CCE was calculated and these values are shown in Table 6.5 (Zhang *et al*., 2021).

Table 6.4 Initial pH values of dechlorination solutions obtained after several regeneration cycles and using two regeneration methods, S/L = 0.020 g·mL^{-1} (Zhang et al., 2021).

Cycle No.	1	2	3	4	5
CO_2 regen	12.4	12.1	12.1	11.8	11.6
Na_2CO_3 regen	12.4	12.3	12.2	11.8	11.8

Table 6.5 CCE values post mineralisation using dechlorinated solution obtain after several regeneration cycles and using two regeneration methods, S/L = 0.020 g·mL^{-1} (Zhang et al., 2021).

Cycle No.	1	2	3	4	5
CO_2 regen	93.7%	93.8%	88.5%	82.3%	80.3%
Na_2CO_3 regen	91.2%	89.8%	90.4%	85.1%	84.0%

The CCE values in Table 6.5 start just below 94% and decrease as the dechlorination performance degrades. The main reason for the CCE limitation under all conditions is that during mineralisation reaction, the pH of the solution drops as the reaction progresses, and once it reaches a value that is too low for $CaCO_3$ precipitation, its dissolution occurs (pH < 8.0, which according to the subsequent discussion is when dissolution of $CaCO_3$ starts). When the starting pH is lower, that limiting pH value is reached sooner, thus with a smaller fraction of Ca^{2+} having precipitated. The pH value plotted against time during a mineralisation reaction is shown in Figure 6.14. This experiment was conducted using the dechlorination solution from the first cycle, thus its initial pH was highest at 12.4. The pH value at first gradually decreases, since sufficient OH^- ions buffer the formation of H^+ ions from carbonic acid dissociation. Once most Ca^{2+} precipitates, the solution loses its ability to buffer the pH, and it dramatically decreases. In this experiment, CO_2 gas flow was shut down after 20 minutes, and it is seen that shortly thereafter the pH rebounded to around 8.0, due to degassing of excess CO_2 from the solution until equilibrium with precipitated $CaCO_3$ is reached. It is evident from this graph that it would make more sense to stop the mineralisation process, and immediately recover the precipitates, once the pH reached the limiting value for $CaCO_3$ precipitation (around 8.0) on the way down, just prior to the 20-minute mark, otherwise it is necessary to wait until past 80 minutes for $CaCO_3$ to re-precipitate. Therefore, the following several cycles of CO_2 mineralisation experiments were all stopped once the pH value reached 8.0 during CO_2 injection, and hence $CaCO_3$ approached equilibrium under the CO_2 partial pressure present (approx. 0.12 atm) (Zhang *et al*., 2021).

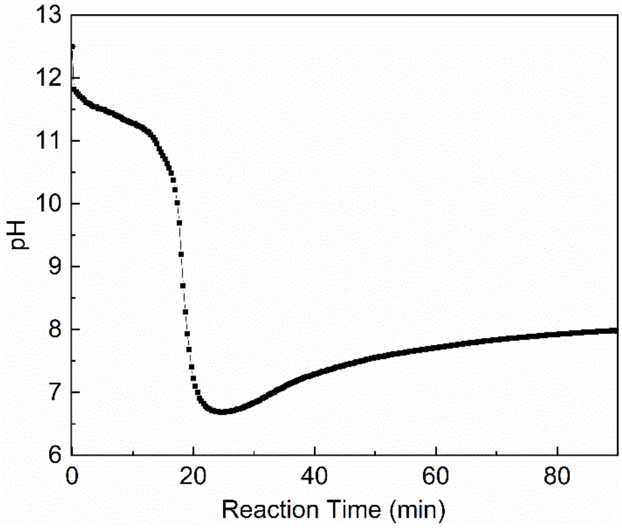

Figure 6.14 pH variation during CO_2 mineralisation process of dechlorinated brine; CO_2 injection stops at 20 minutes, S/L = 0.020 g·mL^{-1} (Zhang et al., 2021).

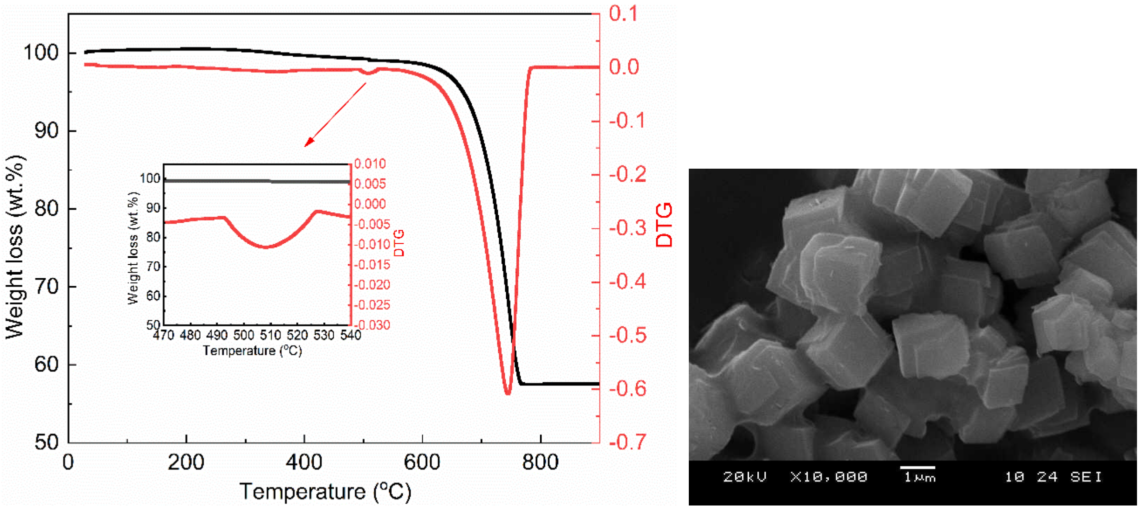

Figure 6.15 TGA/DTG curves (left) and SEM image (right) of a mineralised CO_2 product (Zhang et al., 2021).

Figure 6.15 shows TG/DTG curves of one of the produced precipitated carbonates, and it can be assessed that there are two weight loss peaks, one very minor attributed to traces of $Ca(OH)_2$ and one major attributed to the main $CaCO_3$ phase, at the temperature ranges of 370-480 ˚C and 780-840 ˚C, respectively (Beruto *et al.*, 1980). The SEM image in Figure 6.15 displays the morphology of the product, consisting of pure rhombohedral calcite crystals (Ogino *et al.*, 1987).

6.5. Process design to apply hydrotalcite in CO_2 mineralisation

In this research, the use of calcined hydrotalcite for dechlorination of brine (as opposed to buffering of pH) is investigated. This layered double hydroxide is meant to replace the previous alkaline substances with the aim of recycled usage to reduce the operational process cost and energy demand, thus maximizing net CO_2 sequestration of the process (Zhang *et al*., 2021).

Compared with previous related researches, this study presents a novel regeneration approach of HT after ion-exchange; that is, injecting gaseous CO_2 in the HT solution. In the meantime, the dechlorination solutions obtained from brines can act as an absorbent to fix CO_2 by forming precipitates. Kameda et al. (Kameda *et al.*, 2003) conducted experiments with an analogous feedstock (i.e $CaCl_2$) to react with hydrotalcite, however, much higher $CaCl_2$ concentration solution (0.25 M) was applied, and the results showed that $CaCl_2$ was removed by converting to $Ca(OH)_2$ with the ion-exchange property of HT. However, they did not perform the CO_2 capture reaction with produced $Ca(OH)_2$, and the precipitates were a mixture of HT and $Ca(OH)_2$, which meant that HT could not be reusable. Dindi et al. (Dindi *et al*., 2018) carried out a study to utilise the components in brines to fix CO_2, but aimed to sequester it as solid $NaHCO_3$. Multiple cycles of experiments were run and two regeneration approaches were implemented, and it was concluded that thermal regeneration method was favoured as it produced two products, $NaHCO_3$ and HCl, and required fewer procedures, while the ion-exchange route tested only produced the single chemical $NaHCO_3$ (Dindi *et al*., 2018). Notably their synthetic brine only contained NaCl, which explains why no precipitation of calcium carbonates was seen, as would be expected and is found in this study (Zhang *et al*., 2021).

The schematic of the overall process is displayed in Figure 6.16 and consists of the following steps. First, input calcined hydrotalcite into the brine to implement the first round of Cl^- removal process and raise the pH of the solution sufficiently for CO_2 mineralisation reaction to subsequently occur. The spent HT-Cl material is filtered out and collected from the dechlorinated solution, and sent to be regenerated with gaseous CO_2 or Na_2CO_3 solution. Preferably, the CO_2 source for regeneration can be partially obtained from the calcination process of HT. Flue gas is introduced to the dechlorinated brine to conduct mineralisation reaction, producing solid carbonates that are filtered out and collected. The residual solution from mineralisation, now poor in Cl^- and Ca^{2+}, is used as the solution for the regeneration of spent HT-Cl. This solution following HT regeneration will gain Cl^-, thus becoming acidic, so a low strength HCl solution is produced, and this can be used for industrial purposes. The regenerated HT is sent back to the calcination process, and CHT recycled back to the beginning of the flowsheet. The Cl^- removal efficiency and CO_2 mineralisation performance should be monitored at each cycle to determine the optimal time to replace recycled HT with fresh HT (Zhang *et al*., 2021).

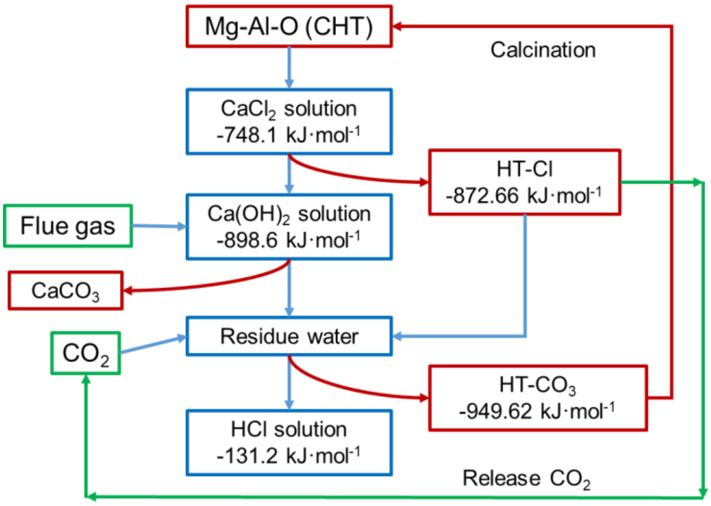

Figure 6.16 Schematic of the process (Zhang et al., 2021).

The general formula of hydrotalcite is $[\mathrm{M^{2+}}_{1-\mathrm{x}}\mathrm{M^{3+}}_{\mathrm{x}}(\mathrm{OH})_2](A^{n-}_{x/n})$, where M^{2+} and M^{3+} represent divalent and trivalent metal ions (herein Mg^{2+} and Al^{3+}) and x is the ratio of $M^{3+}/(M^{2+} + M^{3+})$, which herein is 0.2 under Mg/Al ratio at 4. A^{n-} is the anions that intercalate between the layers, and herein refers to CO_3^{2-}. All the chemical reactions during the whole process are illustrated in Eqs.(6.1) to (6.3). Eq.(6.1) demonstrates the calcination process of double layered hydroxide, which proceed under 500 ˚C to generate CHT. Eq.(6.2) shows the ion exchange reaction occurring in the brine, and the Gibbs free energy change of this reaction is negative according to several research studies (Chabani *et al.*, 2006; Lv *et al.*, 2009; Extremera *et al.*, 2012; Halajnia *et al.*, 2013). This Gibbs free energy change decreases with higher temperature, which can explain why higher temperature can achieve higher chloride removal efficiency, and this related to the absorption of anions being an endothermic process (kumar Allada *et al.*, 2002; Allada *et al.*, 2005). The standard molar Gibbs free energy of formation of hydrotalcite prepared by coprecipitation method can be calculated via Eq.(6.3) to be -949.62 kJ·mol^{-1}, using thermodynamic data obtained from databases (Naumov *et al.*, 1974; Bravo-Suárez *et al.*, 2004). Using this value it is possible to calculate the Gibbs free energy of reaction for the regeneration with CO_2 and with Na_2CO_3, in Eq.(6.3) and Eq.(6.4), as -40.90 kJ·mol^{-1} and -49.35 kJ·mol^{-1}, respectively. As the Gibbs free energy change of the reactions of ion exchange and regeneration processes are all negative, all these reactions are confirmed to occur spontaneously, as experimentally verified (Zhang *et al*., 2021).

$$[Mg_{0.8}Al_{0.2}(OH)_2]CO_{3_{0.1}} \overset{\Delta}{\rightarrow} Mg_{0.8}Al_{0.2}O_{1.1} + 0.1CO_2 + H_2O \quad (6.1)$$

$$Mg_{0.8}Al_{0.2}O_{1.1} + 0.1CaCl_2 + 1.1H_2O \rightarrow [Mg_{0.8}Al_{0.2}(OH)_2]Cl_{0.2} + Ca(OH)_2 \quad (6.2)$$

$$\Delta_f G_m^{\circ}\{298.15K, HT\} = (1-x)\Delta_f G_m^{\circ}\{298.15K, Mg(OH)_2\} + (x)\Delta_f G_m^{\circ}\{298.15K, Al(OH)_3\} + (x/2)\Delta_f G_m^{\circ}\{298.15K, CO_3^{2-}\} \quad (6.3)$$

$$[Mg_{0.8}Al_{0.2}(OH)_2]Cl_{0.2} + 0.1CO_2 + 0.1H_2O \rightarrow [Mg_{0.8}Al_{0.2}(OH)_2]CO_{3_{0.1}} + 0.2HCl \quad (6.4)$$

$$[Mg_{0.8}Al_{0.2}(OH)_2]Cl_{0.2} + 0.1NaCO_3 \rightarrow [Mg_{0.8}Al_{0.2}(OH)_2]CO_{3_{0.1}} + 0.2NaCl \quad (6.5)$$

Conclusions

This chapter presented an alternative process to utilise earth alkaline cations of brines for CO_2 mineralisation based on the benefit of layered double hydroxides exchanging chloride ions to hydroxyl groups. The main advantage of this research is the avoidance of alkali or pH-buffering substances, by using instead a regenerative hydrotalcite for dechlorination. The innovative approach is to remove chloride ions from brine to enable carbonates to subsequently precipitate during carbonation, rather than adding buffers to shift the chemical equilibrium in the system to higher pH. Calcined hydrotalcite compounds (CHT) were synthesised by coprecipitation reaction controlling the pH to be constant, followed by calcination process. This two-step process enhances the specific surface area, from 39 m^2/g to 191 m^2/g, needed for maximising ion-exchange capacity. The optimal, and therefore energy- and cost-effective conditions of CHT utilisation, to achieve chloride removal of 98%, were found to be a solid-to-liquid ratio of 0.020 $g \cdot mL^{-1}$ and a reaction temperature of 60 ˚C. The best performing CHT was prepared using a Mg/Al ratio of 4. The morphology of CHT changed, and its specific surface area declined, after Cl^- removal process (Zhang *et al*., 2021).

Taking advantages of the ‘memory effect’ property of HT, two regeneration methods were tested and compared: one more acidic, using gaseous CO_2, and another more basic, using Na_2CO_3 solution. The results showed that the Cl^- removal efficiency gradually decreased with the increasing regeneration cycles, but the regenerated CHT could still achieve over 70% and 85% Cl^- removal from brine after five cycles with CO_2 and Na_2CO_3 regeneration, respectively. Species irreversibly attached to the HT interlayers (carbonates and chloride) accumulated with every cycle, thus negatively affecting the Cl^- removal from brine and Cl- recovery during regeneration, for both regeneration approaches, though to a lesser extent for Na_2CO_3. For the CO_2 regeneration method, an additional detrimental effect reducing CHT performance was the acidic conditions present during regeneration, which irreversibly degraded the main structure of layered double hydroxide. This study provides an alternative approach to regenerate HT after ion-exchange process (Zhang *et al*., 2021).

The dechlorinated brine, now containing $Ca(OH)_{2(aq)}$ in place of $CaCl_{2(aq)}$, was found to be suitable for direct and rapid reaction with CO_2 at flue gas concentration (12 vol%). This enabled the mineralisation reaction to proceed to near completion, with the calcium conversion efficiency slightly declining with every subsequent cyclical experiment, from 93.7% to 80.3% with CO_2 regeneration and 91.2% to 84.0% with Na_2CO_3 regeneration. Pure precipitated calcium carbonate, rhombohedral calcite, was formed after carbonation reaction (Zhang *et al*., 2021).

Compared to Chapter 4 and 5 on brine carbonation using NaOH and MEA as pH-buffering additives, the method of using the solid adsorbent HT can facilitate the regeneration process, likely reducing processing complexity, cost and energy demand. The NaOH and MEA implemented in previous chapters were disposable chemicals that cannot be reused unless more energy is inputted. In this chapter, a regenerative substitute is employed and that could be recycled multiple cycles with better maintenance by keeping the basic structures of HT. Rapid synthesis method is adopted that can reduce the operational cost (Zhang *et al*., 2021).

In summary, results in Chapter 6 show the feasibility of using regenerative hydrotalcite via cyclical process to treat brines, thus facilitating CO_2 utilisation and sequestration. This process reveals an alternative approach of brine treatment, which is a potential resource that can be reused to achieve a circular industrial economy (Zhang *et al*., 2021).

References

Adachi-Pagano, M., Forano, C. and Besse, J.-P. (2003) 'Synthesis of Al-rich hydrotalcite-like compounds by using the urea hydrolysis reaction-control of size and morphology', *Journal of Materials Chemistry*, 13(8), pp. 1988-1993.

Ahmed, I.M. and Gasser, M.S. (2012) 'Adsorption study of anionic reactive dye from aqueous solution to $Mg\text{-}Fe\text{-}CO_3$ layered double hydroxide (LDH)', *Applied Surface Science*, 259, pp. 650-656.

Allada, R.k., Navrotsky, A. and Boerio-Goates, J. (2005) 'Thermochemistry of hydrotalcite-like phases in the $MgO\text{-}Al_2O_3\text{-}CO_2\text{-}H_2O$ system: A determination of enthalpy, entropy, and free energy', *American Mineralogist*, 90(2-3), pp. 329-335.

Beruto, D., Barco, L., Searcy, A.W. and SPINOLO, G. (1980) 'Characterization of the porous CaO particles formed by decomposition of $CaCO_3$ and $Ca(OH)_2$ in vacuum', *Journal of the American Ceramic Society*, 63(7-8), pp. 439-443.

Bravo-Suárez, J.J., Páez-Mozo, E.A. and Oyama, S.T. (2004) 'Review of the synthesis of layered double hydroxides: a thermodynamic approach', *Química Nova*, 27, pp. 601-614.

Cavani, F., Trifiro, F. and Vaccari, A. (1991) 'Hydrotalcite-type anionic clays: Preparation, properties and applications', *Catalysis today*, 11(2), pp. 173-301.
Chabani, M., Amrane, A. and Bensmaili, A. (2006) 'Kinetic modelling of the adsorption of nitrates by ion exchange resin', *Chemical Engineering Journal*, 125(2), pp. 111-117.

Constantino, V.R. and Pinnavaia, T.J. (1995) 'Basic properties of $Mg^{2+\ 1-x}Al^{3+\ x}$ layered double hydroxides intercalated by carbonate, hydroxide, chloride, and sulfate anions', *Inorganic Chemistry*, 34(4), pp. 883-892.

Dindi, A., Quang, D.V., AlNashef, I. and Abu-Zahra, M.R.M. (2018) 'A process for combined CO_2 utilization and treatment of desalination reject brine', *Desalination*, 442, pp. 62-74.

Extremera, R., Pavlovic, I., Pérez, M.R. and Barriga, C. (2012) 'Removal of acid orange 10 by calcined Mg/Al layered double hydroxides from water and recovery of the adsorbed dye', *Chemical Engineering Journal*, 213, pp. 392-400.

Gazzano, M., Kagunya, W., Matteuzzi, D. and Vaccari, A. (1997) 'Neutron diffraction studies of polycrystalline Ni/Mg/Al mixed oxides obtained from hydrotalcite-like precursors', *The Journal of Physical Chemistry B*, 101(23), pp. 4514-4519.

Halajnia, A., Oustan, S., Najafi, N., Khataee, A.R. and Lakzian, A. (2013) 'Adsorption-desorption characteristics of nitrate, phosphate and sulfate on Mg-Al layered double hydroxide', *Applied Clay Science*, 80-81, pp. 305-312.

Hibino, T., Yamashita, Y., Kosuge, K. and Tsunashima, A. (1995) 'Decarbonation behavior of Mg-Al-CO_3 hydrotalcite-like compounds during heat treatment', *Clays and Clay Minerals*, 43(4), pp. 427-432.

Honeyman, B.D. and Santschi, P.H. (1988) 'Metals in aquatic systems', *Environmental Science & Technology*, 22(8), pp. 862-871.

Kameda, T., Yoshioka, T., Mitsuhashi, T., Uchida, M. and Okuwaki, A. (2003) 'The simultaneous removal of calcium and chloride ions from calcium chloride solution using magnesium–aluminum oxide', *Water Research*, 37(16), pp. 4045-4050.

Kontoyannis, C.G. and Vagenas, N.V. (2000) 'Calcium carbonate phase analysis using XRD and FT-Raman spectroscopy', *Analyst*, 125(2), pp. 251-255.

Kumar Allada, R., Navrotsky, A., Berbeco, H.T. and Casey, W.H. (2002) 'Thermochemistry and aqueous solubilities of hydrotalcite-like solids', *Science*, 296(5568), pp. 721-723.

Lv, L., Sun, P., Gu, Z., Du, H., Pang, X., Tao, X., Xu, R. and Xu, L. (2009) 'Removal of chloride ion from aqueous solution by ZnAl-NO_3 layered double hydroxides as anion-exchanger', *Journal of Hazardous Materials*, 161(2-3), pp. 1444-9.

Nakatsuka, T., Kawasaki, H., Yamashita, S. and Kohjiya, S. (1979) 'The Polymerization of β-propiolactone by calcined synthetic hydrotalcite', *Bulletin of the Chemical Society of Japan*, 52(8), pp. 2449-2450.

Naumov, G.B., Ryzhenko, B.N. and Khodakovsky, I. (1974) 'Handbook of thermodynamic data', *" Handbook of Thermodyanic Data" Moscow, Atomizdat., 1971*.

Ogino, T., Suzuki, T. and Sawada, K. (1987) 'The formation and transformation mechanism of calcium carbonate in water', *Geochimica et Cosmochimica Acta*, 51(10), pp. 2757-2767.

Reichle, W., Kang, S. and Everhardt, D. (1986) 'The nature of the thermal decomposition of a catalytically active anionic clay mineral', *Journal of Catalysis*, 101(2), pp. 352-359.

Santos, R.M., Chiang, Y.W., Elsen, J. and Van Gerven, T. (2014) 'Distinguishing between carbonate and non-carbonate precipitates from the carbonation of calcium-containing organic acid leachates', *Hydrometallurgy*, 147-148, pp. 90-94.

St Malinowski, S.S. and Sloczynski, J. (1967) 'Magnesium Oxide as a Catalyst', *Journal of Catalysis,* 7, pp. 67-75.

Thommes, M., Kaneko, K., Neimark, A.V., Olivier, J.P., Rodriguez-Reinoso, F., Rouquerol, J. and Sing, K.S. (2015) 'Physisorption of gases, with special reference to the evaluation of surface area and pore size distribution (IUPAC Technical Report)', *Pure and Applied Chemistry*, 87(9-10), pp. 1051-1069.

Tichit, D., Bennani, M.N., Figueras, F. and Ruiz, J.R. (1998) 'Decomposition processes and characterization of the surface basicity of Cl^- and CO_3^{2-} hydrotalcites', *Langmuir*, 14(8), pp. 2086-2091.

Wang, S.-L. and Wang, P.-C. (2007) 'In situ XRD and ATR-FTIR study on the molecular orientation of interlayer nitrate in Mg/Al-layered double hydroxides in water', *Colloids and Surfaces A: Physicochemical and Engineering Aspects*, 292(2-3), pp. 131-138.

Yun, S.K. and Pinnavaia, T.J. (1995) 'Water content and particle texture of synthetic hydrotalcite-like layered double hydroxides', *Chemistry of Materials*, 7(2), pp. 348-354.

Zhang, J., Xu, Y.F., Qian, G., Xu, Z.P., Chen, C. and Liu, Q. (2010) 'Reinvestigation of dehydration and dehydroxylation of hydrotalcite-like compounds through combined TG-DTA-MS analyses', *The Journal of Physical Chemistry C*, 114(24), pp. 10768-10774.

Zhang, N., Santos, R.M. and Šiller, L. (2021) 'CO_2 mineralisation of brines with regenerative hydrotalcites in a cyclical process', *Chemical Engineering Journal*, 404, p. 126450.

Chapter 7. Conclusions and Future Work

CO_2 utilisation process via mineralisation route is an efficient approach to mitigate the effect of greenhouse gas by converting CO_2 into solid phase to store it permanently. The resource containing alkaline earth metal (Ca, Mg) used to trap CO_2 can be derived directly from the saline aquifer or desalination plant, which is a vast capacity facilitating aqueous mineralisation technology used to address CO_2 emissions and wastewater treatment. However, the commercial deployment of mineral carbonation processes has been slow over decades, since many processes have been shown to suffer from limited reaction rate, poor energy efficiency or high energy requirement. Therefore, the aim of this thesis project is to develop a continuous process with low energy demand systematic process to proceed aqueous mineralisation, which is favoured by the industry that can accelerate the process of employing mineralisation with brines into commercial scale. A helically coiled tubular reactor is designed to conduct the experiments of CO_2 and alkaline brine, and various alkaline substances (i.e. NaOH, BF slag and MEA) are applied to neutralise the acidification causing by CO_2 dissolution coupled with alkaline earth metal precipitation and chloride ions accumulation (Zhang *et al*., 2019; Zhang *et al*., 2020; Zhang *et al*., 2021). Moreover, a one-dimensional time-dependent three-phase plug-flow model in Chapter 5 is developed acting as a scale-up tool that incorporates transport and chemical speciation equations enabling to predict the species and other process parameters as the function of the tubular reactor length (Zhang *et al*., 2020). The model is capable of reactor design that can be used to scale up. The unique features of this work include using a continuous tubular reactor with three-phase slug flow pattern, and introducing a nickel nanoparticle catalyst to accelerate the carbonation reaction. In Chapter 6, considering the high investment on alkaline substances, a regenerative material which can convert chloride ions to hydroxyl groups by ion exchange is introduced, namely hydrotalcite (HT). The main advantage of HT is its recyclable property that enables multiple usages by the HT's 'memory effect' (Cavani et al., 1991). Overall, for the scalable process of mineralisation with brine is partially achieved, and future work is needed in order to improve and integrate all processes.

7.1 Summary of significant conclusions

Chapter 2 briefly summarised the state of the art of the research in mineralisation and is mainly focused on the current advances in aqueous mineralisation technology.

In Chapter 4, a tubular reactor is implemented for the continuous process of CO_2 mineralisation with alkaline brines. Main conclusions are presented below (Zhang *et al*., 2019):

- A 20.9-meter silicone helically coiled tubular reactor was built, and NaOH and BF slags applied as alkaline additives.
- The optimal conditions, which refers to the highest calcium conversion efficiency (100%), was achieved at the liquid to gas ratio at 80/35 with 3.8 vol.% (1M) NaOH at 50 °C. Higher gas flow rate results in greater CO_2 dissolution and mass-transfer of gas and liquid is enhanced, and then higher CCE is achieved with sufficient alkaline supplement.
- The effect of temperature on CCE was investigated under 25 °C and 50°C, and it was found that there was no significant difference between these two temperatures as there is a trade-off between the solubility of CO_2 and mass transfer of ions. However, the morphologies of precipitated calcium carbonates obtained at these temperatures showed differences: needle-like aragonite is visible under 50 °C, while spherical vaterite is evident in the low temperature. Rhombohedral calcite appeared in both temperatures.
- With the addition of BF slags, higher CCE could be obtained, and also the amount of used NaOH was reduced.
- The catalyst NiNPs can improve the rate of mineralisation process with a low concentration of 30 ppm, and CCE can be increased up to 10% under certain process conditions.
- CCE is slightly reduced by 5% in the presence of 0.8M NaCl and decreased from 100% to 83% with the addition of 0.012 $MgCl_2$ at optimal conditions. The morphologies of particles obtained under other ions are also varied.
- Chapter 4 reveals the feasibility of employing the tubular reactor for continuous CO_2 mineralisation with brines to sequester CO_2.

In Chapter 5, the subsequent study was conducted to further improve the mineralisation process with a tubular reactor. Based on the previous research achievement, an alternative chemical additive, MEA solution was implemented to replace NaOH (Zhang *et al*., 2020). Moreover, a model was built up to comprehensively explain the reactions occurred in the reactor and enable scale up this technology (Zhang *et al*., 2020). The main results are listed below (Zhang *et al*., 2020):

- A 7-meter smooth metallic tubing was built to reduce the influence of the precipitate (NiNPs and carbonates) stick on the internal surface.
- A lower L/G ratio with increasing gas flow rate is beneficial for higher CCE with a broader range of MEA concentrations (< 5 vol.%). It was found that CCE was reduced when the MEA concentration is over 1 vol.%, as high MEA concentration did not result in high CCE. This is a different result compared to the previous chapter with the NaOH solution.
- The influence of temperature was investigated and the results showed that higher temperature could significantly lead to higher CCE, which is also different from the research with NaOH because the carbonation effect in MEA solution is predominant.
- 30 ppm NiNPs addition can increase the CCE from 59% to 68% under specific processing conditions.
- The morphologies of precipitates under different temperatures are studied and it turns out that spherical vaterite is formed at 30 °C and aragonite is found at higher temperature.
- The modelling results provide the evidence of the ongoing reactions in an invisible reactor which facilitate the reactor design and species prediction.
- The outlet of pH values, bubble sizes and Ca^{2+} concentration are the main parameters to validate the model and the results show that the experimental data and model are in good agreement.
- The primary parameter of the model is the interfacial overall mass transfer coefficient K, and the model illustrates that K values are linearly correlated with the gas flow rate.

In Chapter 6, calcined hydrotalcite as a dechlorination agent, which presents a cost-effective approach to address the challenge of the repetitive usage of alkaline substances is used to implement mineral carbonation process (Zhang *et al*., 2021) The reacted hydrotalcite is easy to be regenerated and novel regeneration process is developed. The achieved high pH dichlorination solution is used to sequestrate CO_2 by forming carbonates. Overall, a cyclical CO_2 mineralisation process with regenerative hydrotalcite was demonstrated to reduce the cost of alkali. The main results are presented below and they have been published (Zhang *et al*., 2021):

- Hydrotalcites with different Mg/Al ratios were synthesised with the coprecipitation method, and the specific surface area was dramatically increased with the thermal decomposition at 500 °C, from 39 m^2/g to 191 m^2/g.
- Higher temperature and higher solid-to-liquid ratio can benefit the performance of chloride removal of brines. Chloride removal efficiency reached 98% under optimal experimental parameters: a solid-to-liquid ratio of 0.020 $g \cdot mL^{-1}$ and a reaction temperature of 60 ˚C.
- Taking advantage of the memory effect of HT, gaseous CO_2 and Na_2CO_3 solution as recharging agents were tested to displace Cl^-.
- The chloride removal efficiency of regenerative hydrotalcite could be maintained at over 70% with gaseous regeneration process and 85% with Na_2CO_3 regeneration approach because HT is favoured at the basic solution to maintain the layered structure.
- The dechlorinated brine is reacted with the flue gas component, CO_2, and carbonate conversion efficiency of over 90% Ca^{2+}, from the brine was achieved in the first cycle and slightly decreased with more cycles run. The precipitates are calcite under room temperature formation.
- Compared to Chapter 4 and 5, the utilisation of HT provides a process with the lowest cost and energy requirement. Moreover, HT can be applied in a wider range of brines or salty solutions with its ion-exchange property to proceed CO_2 mineralisation.

7.2 Future Work

This thesis provides the framework for future research on scalable mineralisation process. According to the results obtained in this project, future work should focus on the large-scale deployment with the pilot plant.

The theoretical model should be built up for a large-scale plant. The current model matches the experimental results well, but further development of the model should be introduced for large-scale deployment and validated on the pilot plant.

Nickel nanoparticles implementation can improve the mineralisation in some specific conditions, however, the optimal conditions in the tubular reactor are still under development and further investigation should be taken. Moreover, the exact mechanism of this catalyst in the mineralisation process remains to be further determined in tubular reactor process, due to either the acceleration of CO_2 hydration reaction (Bhaduri et al., 2015; Verma et al., 2016) as proposed in batch reactor process or the seed introduction or the synergistic effect. The choice of using NiNPs in aqueous carbonation reaction depends on the ability to recover and re-use the nanoparticles, or embed them within fixed support (Han *et al.*, 2015) within the reactor. Different process parameters should be explored, such as pressure variation and tubing size, in order to further enhance the process in the tubular reactor.

Future work should focus on how to deploy the process at commercial scale. Computational models can be used to conduct environmental impact, economic and energetic assessment, such as life cycle assessment and techno-economic assessment.

In the present study, simulated brine was used to perform experiments; a real desalination brine could result in unpredicted effects on carbonation kinetics, conversion or product quality; thus, this should be studied in future using our developed tubular reactor process. Although 100% complete calcium conversion efficiency is achieved in this thesis, the other ions in the brines should be tested in combination with Ca. Especially magnesium ions, because Mg is also another alkaline earth metal ion that is in high concentration in brine which can be carbonated via mineralisation.

However, the mineralisation of Mg^{2+} is more challenging compared to Ca^{2+}. Perhaps by adjusting the multi-step processes, Mg-carbonates and Ca-carbonates could be obtained separately and this would be an essential ongoing research to employ real brines to this technology.

HT shows its potential application on anions removal by ion-exchange property that means it can be applied also in a wider range concentration of brines to convert them to base solution enabling CO_2 mineralisation. The method of using the solid adsorbent HT can facilitate the regeneration process, likely by reducing processing complexity, cost and energy demand. These engineering and economic analyses are intended in future piloting studies. Before that, further experimentation of a wider range of brine composition, and geochemical modelling, is needed to identify the brine carbonation applications, in terms of brine composition, that are energetically feasible. Further study should also investigate strategies to improve the performance of gaseous CO_2 regeneration process, deemed preferable from cost and process integration perspectives, by buffering the pH during HT regeneration to avoid structure collapse and maintain high efficiency for more than five cycles.

Once the primary mineralisation process has been optimised and intensified, then the integrated process should be the next stage research to fully utilise the resources and combine the multiple ‘green’ CCUS processes (Gabrielli *et al.*, 2020).

The optimal process development involves extensive experimental work to be conducted. With the improvement of automation technology (Fabry *et al.*, 2016; Schweidtmann *et al.*, 2018), machine learning-based design of process and process optimisation have risen much attention to reduce the number of experiments and free up researchers from repetitive work. Depending on different processes, various algorithms could be implemented to achieve the optimal process parameters (Zhang, 2008; Osuolale and Zhang, 2016; Clayton *et al.*, 2020) and this could be a promising research direction enabling technology that can be deployed much faster in future.

References

Bhaduri, G.A., Alamiry, M.A.H. and Šiller, L. (2015) 'Nickel Nanoparticles for Enhancing Carbon Capture', *Journal of Nanomaterials*, 2015, pp. 1-13.

Cavani, F., Trifiro, F. and Vaccari, A. (1991) 'Hydrotalcite-type anionic clays: Preparation, properties and applications', *Catalysis today*, 11(2), pp. 173-301.

Clayton, A.D., Schweidtmann, A.M., Clemens, G., Manson, J.A., Taylor, C.J., Niño, C.G., Chamberlain, T.W., Kapur, N., Blacker, A.J., Lapkin, A.A. and Bourne, R.A. (2020) 'Automated self-optimisation of multi-step reaction and separation processes using machine learning', *Chemical Engineering Journal*, 384.

Fabry, D.C., Sugiono, E. and Rueping, M. (2016) 'Online monitoring and analysis for autonomous continuous flow self-optimising reactor systems', *Reaction Chemistry & Engineering*, 1(2), pp. 129-133.

Gabrielli, P., Gazzani, M. and Mazzotti, M. (2020) 'The Role of Carbon Capture and Utilisation, Carbon Capture and Storage, and Biomass to Enable a Net-Zero-CO_2 Emissions Chemical Industry', *Industrial & Engineering Chemistry Research*, 59(15), pp. 7033-7045.

Han, X., Williamson, F., Bhaduri, G.A., Harvey, A. and Šiller, L. (2015) 'Synthesis and characterisation of ambient pressure dried composites of silica aerogel matrix and embedded nickel nanoparticles', *The Journal of Supercritical Fluids*, 106, pp. 140-144.

Osuolale, F.N. and Zhang, J. (2016) 'Energy efficiency optimisation for distillation column using artificial neural network models', *Energy*, 106, pp. 562-578.

Schweidtmann, A.M., Clayton, A.D., Holmes, N., Bradford, E., Bourne, R.A. and Lapkin, A.A. (2018) 'Machine learning meets continuous flow chemistry: Automated optimisation towards the Pareto front of multiple objectives', *Chemical Engineering Journal*, 352, pp. 277-282.

Verma, M., Sravan Kumar, K.B. and Deshpande, P.A. (2016) 'Computational Insights into the Activity of Transition Metals for Biomimetic CO_2 Hydration', *The Journal of Physical Chemistry C*, 120(10), pp. 5577-5584.

Zhang, J. (2008) 'Batch-to-batch optimal control of a batch polymerisation process based on stacked neural network models', *Chemical Engineering Science*, 63(5), pp. 1273-1281.

Zhang, N., Santos, R.M., Smith, S.M. and Šiller, L. (2019) 'Acceleration of CO_2 mineralisation of alkaline brines with nickel nanoparticles catalysts in continuous tubular reactor', *Chemical Engineering Journal*, 377, p. 120479.

Zhang, N., Santos, R.M. and Šiller, L. (2020) 'Rapid CO_2 capture-to-mineralisation in a scalable reactor', *Reaction Chemistry & Engineering*, 5(3), pp. 473-484.

Zhang, N., Santos, R.M. and Šiller, L. (2021) 'CO_2 mineralisation of brines with regenerative hydrotalcites in a cyclical process', *Chemical Engineering Journal*, 404, p. 126450.